Optics and acoustics with a single nano-object : environment effects

Fabio Medeghini

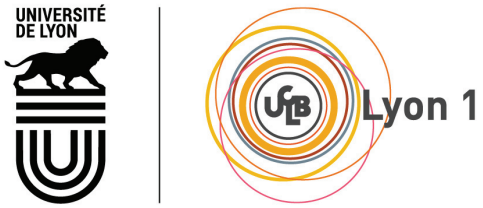

N° d'ordre NNT : 2018LYSE1026

THÈSE DE DOCTORAT DE L'UNIVERSITÉ DE LYON
opérée au sein de
l'Université Claude Bernard Lyon 1

École Doctorale ED01
Physique et Astrophysique

Spécialité de doctorat : Physique

Soutenue publiquement le 26/02/2018, par :
Fabio Medeghini

Optics and acoustics with a single nano-object: environment effects

---

Devant le jury composé de :

De Wilde Yannick, Directeur de Recherche, CNRS - ESPCI	Rapporteur
Ruello Pascal, Professeur des Universités, Le Mans Université	Rapporteur
Roubin Pascale, Professeure des Universités, Aix-Marseille Université	Examinatrice
San Miguel Alfonso, Professeur des Universités, UCBL	Examinateur
Vallée Fabrice, Directeur de Recherche, CNRS - UCBL	Directeur de thèse
Del Fatti Natalia, Professeure des Universités, UCBL	Co-directrice de thèse

Contents

Introduction

The physical properties of nanoparticles have been largely investigated over the last decades as a result of important developments in their synthesis, detection and modeling. It has been shown that nanosized materials, as compared to their bulk counterpart, exhibit new optical, electrical, magnetic, mechanical and thermal properties, due in particular to their high surface to volume ratio. From an optical point of view, noble metal nanoparticles show an extinction spectrum dominated by the surface plasmon resonance (SPR), responsible for the bright colors of nanoparticle colloids that are apparent in the stained-glass windows of medieval cathedrals. SPR is associated to the collective oscillation of electrons excited by the incident electromagnetic field, enhancing the electric field in and around the particle. It is influenced by the nanoparticle size, shape, composition and environment, whose control during fabrication has been improved during the last decades, increasingly allowing experimental and theoretical investigations on single nano-objects and their use in various applications such as sensing, energy harvesting and photothermal therapy.

This thesis, organized in three chapters, aims to extend the knowledge and understanding of environmental effects on the optical and acoustic properties of single metal nanoparticles.
The first chapter theoretically compares the physical properties of noble metals in the bulk state and at the nanoscale. The cases of spherical and elongated nanoparticles are discussed in details, allowing to connect SPR properties (spectral position, linewidth and area) with the nano-object features (size, shape, composition, environment). A final section deals with the spatial modulation spectroscopy (SMS) technique, consistently employed to optically detect single nanoparticles in far-field and quantitatively measure its extinction spectrum.
The second chapter investigates experimentally and theoretically how the SPR of a single metal nanoparticle is affected by extreme conditions, i.e. by strongly modifying the pressure of the external environment. After the description of the diamond anvil cell (DAC) apparatus suitable for yielding a controlled high-pressure environment, its non-trivial combination with the SMS microscope is explained.

The experimental results on the SPR properties evolution with increasing pressure are presented in details. In particular, the SPR spectral position redshift with pressure is successfully modeled both numerically, using the finite-element method (FEM), and analytically, under simplifying assumptions to provide further physical insights. The SPR spectral area dependence on pressure is explained through a simple model and the spectral linewidth change justified by considering the pressure dependence of its multiple contributions.
The last chapter describes how the acoustic behavior of a single nanoparticle is affected by its morphology and interaction with the environment. After a theoretical introduction of the vibrational properties of single nano-objects, the principle of acoustic FEM simulations is explained. It follows the description of the investigated samples, composed of isolated gold nanodisks on a sapphire substrate, among which the most circular have been selected and investigated by SMS. The combination of the SMS microscope with a *pump&probe* (P&P) setup is introduced, allowing investigations of the ultrafast response of a gold nano-object. By focusing on the acoustic component of the P&P signal from single nanodisks, specific vibrational modes are characterized, with particular attention to the dependence of their damping rate on nanodisk morphology. FEM modeling results are compared to the data in order to unveil the origin of the observed phenomena, associated to a reduction of acoustic energy tranfer to the environment through the disk/substrate interface.

Chapter 1

Optical and electronic properties of metal nano-objects

Optical properties of metals are directly related to their electronic properties at both bulk and nanometric level. In this chapter, it is firstly presented the connection between electronic and optical properties for bulk metals with a focus on noble metals, widely used for plasmonics applications. Afterwards, the optical response of metallic nano-objects with simple geometries is described, with particular regard for their surface plasmon resonance (SPR). The last part deals with the optical detection of single nanoparticles via the spatial modulation spectroscopy (SMS) technique.

1.1 Electronic properties of bulk metals

Gold, silver and copper are noble metals. They are constituted by monovalent atoms with a resembling electronic configuration, comprehending the full electronic level $(n-1)d$ and the level ns occupied by a single electron reported in Tab. (1.1). In bulk materials, these atoms are organized in a faced cubic centered

METAL	CONFIGURATION	a (Å)	n_e ($\times 10^{22}$ cm^{-3})
Gold (Au)	[Xe]$4f^{14}5d^{10}6s^1$	4.07	5.90
Silver (Ag)	[Kr]$4d^{10}5s^1$	4.08	5.86
Copper (Cu)	[Ar]$3d^{10}4s^1$	3.61	8.47

Table 1.1: Electronic configuration, lattice periodicity a and electron density n_e of noble metals [1, 2].

structure with lattice periodicity a, as illustrated in Fig. (1.1). Isolated atoms

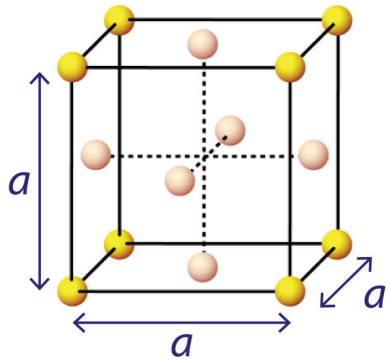

Figure 1.1: Schematic of a FCC structure with lattice periodicity a.

have quantized electronic levels, each one representing an orbital. In a solid, interactions between atoms induce a broadening of the energy levels, leading to a continuum of electronic states, called *electronic bands*.
The band structure of crystalline materials is theoretically described by the Bloch theorem (that allows to solve the Schrödinger equation of a free electron in a potential with periodicity defined through a). An ensemble of energy bands $E_p(\vec{k})$ quantized by p emerges. Core electrons are weakly influenced by the presence of other atoms, while the electrons in the highest energy levels ($(n-1)d$, ns and np) are strongly affected. At $T=0\,\mathrm{K}$, the energy bands are filled until the Fermi energy E_F, corresponding to the energy of the electronic state with highest energy.
Two energy bands are particularly important to understand the materials physical properties: the *valence band*, the highest energy band completely filled with electrons, and the *conduction band*, the lowest energy band partially filled. A sketch of the band structure of a metal is presented in Fig. (1.2). Each atom contributes to the conduction band with an electron (ns^1), and thus, the conduction electrons density is defined as

$$n_e = N_A \frac{\rho}{MM}\,, \tag{1.1}$$

where N_A is the Avogadro number, ρ is the density and MM the molar mass.
The electrons of the conduction band may be considered as free electrons with effective mass m^*, according to the dispersion relationship

$$E(\vec{k}) = \frac{\hbar k^2}{2m^*}\,. \tag{1.2}$$

The density of states $g(E)$ of conduction electrons for a tridimensional system of volume V is therefore given by

$$g(E) = \frac{V}{2\pi^2}\left(\frac{2m^*}{\hbar^2}\right)^{\frac{3}{2}}\sqrt{E}\,. \tag{1.3}$$

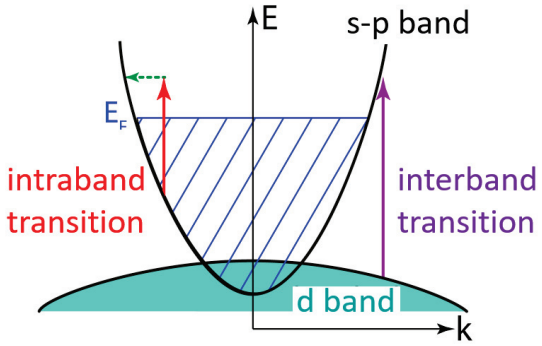

Figure 1.2: Sketch of the band structure of a metal with a low-dispersed valence band (d band) and a partially filled conduction band (s-p band). Photon absorption by a d-electron may cause a transition towards the s-p band. The electron in the conduction band can realize intraband transitions with the assistance of a phonon (dashed arrow) or another electron.

Thus, the Fermi energy is defined by the free electron density n_e via

$$E_F = \frac{\hbar^2}{2m^*} (3\pi n_e)^{\frac{2}{3}} \tag{1.4}$$

from which two constants can be deduced: the Fermi temperature $T_F = E_F/k_B$ (with k_B the Boltzmann constant) and the Fermi velocity $v_F = \sqrt{\frac{2E_F}{m^*}}$. The main quantities of the free electrons model are summarized in Tab. (1.2).
It follows that the volumetric heat capacity of free electrons is defined (under the hypothesis $T_e \ll T_F$) as

$$c_e(T_e) = \frac{1}{V} \int_0^{+\infty} E\, g(E) \frac{\partial f(E)}{\partial T_e} dE = \frac{\pi^2 n_e k_B}{2T_F} T_e = a_e T_e \,, \tag{1.5}$$

METAL	m^*	E_F (eV)	T_F ($\times 10^4$ K)	v_F ($\times 10^6$ ms^{-1})
Gold (Au)	1	5.53	6.42	1.39
Silver (Ag)	1	5.49	6.38	1.39

Table 1.2: Effective mass (m^*) ($m^* = 1$ indicate a particle with mass equal to one electron mass $m_e = 9.11 \times 10^{-31}$ kg), Fermi energy (E_F), Fermi temperature (T_F) and Fermi velocity (v_F) for gold and silver [2].

where f is the Fermi-Dirac distribution, describing the occupation probability of an energy state with energy E:

$$f(E) = \frac{1}{e^{(E-E_F)/(k_B T_e)} + 1} \tag{1.6}$$

(where the chemical potential has been posed equal to E_F, accordingly with the condition $T_e \ll T_F$). In the gold and silver case, the proportionality constant results $a_e = \frac{\pi^2 n_e}{2T_F} k_B \approx 65\,\mathrm{J\ m^{-3}\ K^{-2}}$.

1.2 Optical properties of bulk metals

In metals, optical properties are governed by the response of electrons to external electromagnetic fields.

1.2.1 Electromagnetism in a metal

The interaction between an electromagnetic field $\vec{E}(\omega)$ of angular frequency ω and a material is described by the dielectric function $\epsilon(\omega) = \epsilon_1(\omega) + i\epsilon_2(\omega)$ (being $\epsilon_1(\omega) = \mathrm{Re}\{\epsilon\}$ and $\epsilon_2(\omega) = \mathrm{Im}\{\epsilon\}$) or using the complex refractive index $\tilde{n} = n + i\kappa$ (with $\tilde{n}^2 = \epsilon$, $n = \mathrm{Re}\{\tilde{n}\}$ and $\kappa = \mathrm{Im}\{\tilde{n}\}$). They link the electronic induction $\vec{D}$ to the electric field

$$\vec{D} = \epsilon_0 \epsilon \vec{E} = \epsilon_0 (1 + \chi) \vec{E} \tag{1.7}$$

where ϵ_0 is the vacuum permittivity and χ the electric susceptibility. Fig. (1.3) shows the dependence of $\epsilon_{1,2}$ as a function of photon energy for gold and silver.

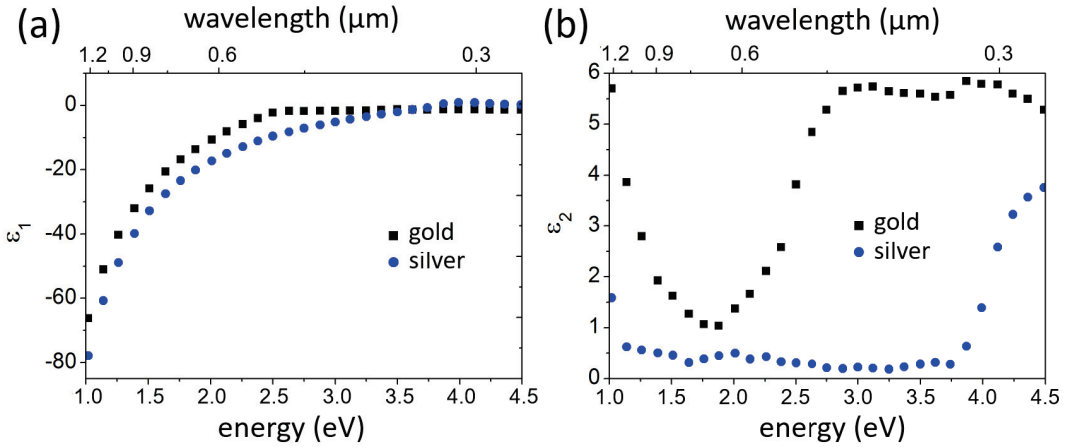

Figure 1.3: Real (a) and imaginary (b) part of the dielectric function of gold and silver experimentally measured [3].

Supposing isotropy (ϵ scalar) and a monochromatic electric field $\vec{E}(\vec{r},t)=\vec{E}_0\,e^{-i\omega t}+$ *c.c.*, the Helmholtz equation applies

$$\nabla^2\vec{E}_0+\frac{\omega^2}{c^2}\epsilon(\omega)\vec{E}_0=0\,. \tag{1.8}$$

Considering the propagation along the axis z, the electric field becomes $\vec{E}(\vec{r},t)=\vec{E}_0(\vec{r})e^{i\omega t\left(\frac{\tilde{n}}{c}z-t\right)}$. The field intensity ($I\sim|\vec{E}|^2$) has the form

$$I(z)=I_0\,e^{-\alpha z}\,, \tag{1.9}$$

where $\alpha(\omega)=2\,\omega\,\kappa(\omega)/c$ is the absorption coefficient. In metals, the dielectric function can be separated in two terms $\epsilon=\epsilon^D+\epsilon^{ib}$, each one associated to different electron-photon mechanisms. Photons may be absorbed by conduction electrons leading to *intraband transitions* (internal to the conduction band), or by valence electrons yielding *interband transitions* (between valence and conduction band). Classically, intraband transitions are described through the Drude model, based on the quantities ϵ^D and χ^D, while interband transitions are governed by ϵ^{ib} and χ^{ib}, related to ϵ by

$$\epsilon=\epsilon^{ib}+\epsilon^D=1+\chi^{ib}+\chi^D\,, \tag{1.10}$$

having defined $\epsilon^{ib}=1+\chi^{ib}$ and $\epsilon^D=\chi^D$.

1.2.2 Intraband transitions: the Drude model

The Drude model [4] allows to calculate the dielectric function associated to intraband transitions ϵ^D. It considers the quasi-free electrons of metals as free independent electrons interacting with their surrounding by scattering processes, described through the viscous force $\vec{F}=-m_e\gamma\vec{v}$, with γ the scattering rate. The dynamics of an electron undergoing an electric field $\vec{E}(t)=\vec{E}_0e^{-i\omega t}+c.c.$, is thus described by

$$m_e\frac{d^2\vec{r}}{dt^2}=-m_e\gamma\frac{d\vec{r}}{dt}-e\vec{E}\,, \tag{1.11}$$

where $\vec{r}$ is the position vector. The Drude component of dielectric function ϵ^D is defined through the polarization vector $\vec{P}_{NP}=-n_e e\vec{r}=\epsilon_0\chi^D\vec{E}$, where n_e is the conduction electrons density. It follows

$$\epsilon(\omega)=\epsilon^{ib}(\omega)+\epsilon^D(\omega)=1+\chi^{ib}(\omega)+\chi^D(\omega)=\epsilon^{ib}(\omega)-\frac{\omega_p^2}{\omega(\omega+i\gamma)}\,, \tag{1.12}$$

where $\omega_p=\sqrt{\frac{n_e e^2}{m_e\epsilon_0}}$ is the plasma frequency, resulting $\hbar\omega_p\approx 9\,\text{eV}$ in gold and silver. The real ϵ_1^D and imaginary part ϵ_2^D of the Drude contribution result as

$$\begin{cases}\epsilon_1^D=-\frac{\omega_p^2}{\omega^2+\gamma^2}\approx-\frac{\omega_p^2}{\omega^2}\\ \epsilon_2^D=\frac{\omega_p^2\gamma}{\omega(\omega^2+\gamma^2)}\approx\frac{\omega_p^2\gamma}{\omega^3}\end{cases}\qquad\text{for}\quad\gamma\ll\omega\,. \tag{1.13}$$

In noble metals, this approximation is valid in the optical frequency domain ($\omega/\gamma \sim 10$).
In the case $\omega = 0$, γ is the scattering rate between electrons and lattice (electron-phonon scattering) or other electrons (electron-electron scattering), and thus is restricted to two-bodies interaction processes. When $\omega \neq 0$, γ takes into account the absorption of a photon with frequency ω by a conduction electron. As the momentum of a photon is negligible, this intraband absorption requires the presence of a third body (electron or phonon) in order to satisfy the energy and momentum conservation (see Fig. (1.2)).
Fig. (1.4) shows the intraband transitions contribution, computed using the Drude model for the gold dielectric function. The agreement is good for large wavelengths, conversely, for photon energies $E > 2\,\mathrm{eV}$, the interband transitions contribution becomes dominant.

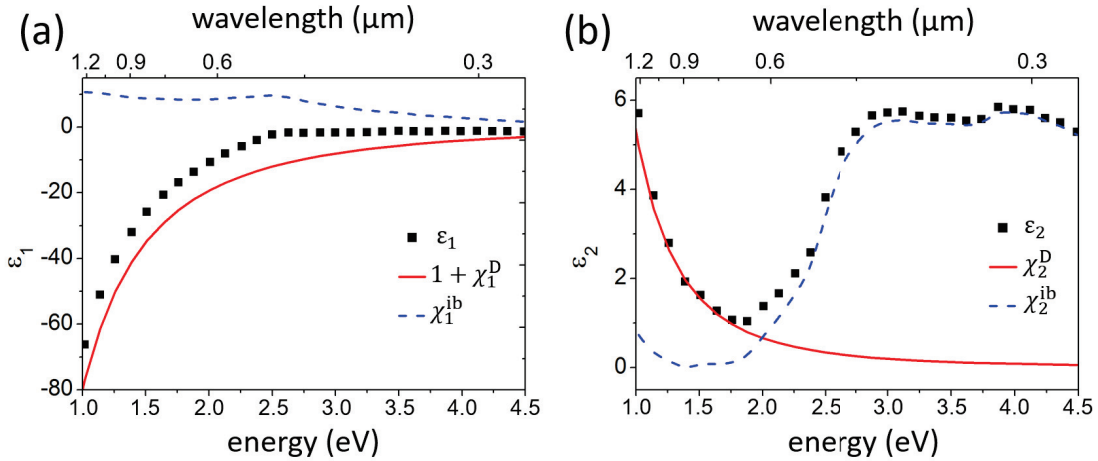

Figure 1.4: Real (a) and imaginary (b) part of the dielectric function of gold. The differences between measured $\epsilon_{1,2}$ (black dots) [3] and the calculated contributions of the Drude model $\chi^D_{1,2}$ (solid lines) dielectric function allows to extract the interband contributions $\chi^{ib}_{1,2}$ (dashed lines).

1.2.3 Interband transitions

In noble metals, interband transitions occur between core electrons of d-bands and the empty states in the conduction band (Fig. (1.2)). The energy threshold $\hbar\omega_{ib}$ for this process is $\approx 2\,\mathrm{eV}$ in gold and $\approx 4\,\mathrm{eV}$ in silver [5, 6]. The energy threshold $\hbar\omega_{ib}$ correspond to the step increase in ϵ_2 (Fig. (1.4b)).

1.3 Optical properties of metal nano-objects

Metallic nanoparticles are small systems consisting of few tens to thousands or millions of atoms, whose optical response is dominated by the presence of an extinction resonance induced by the dielectric confinement, called surface plasmon resonance (SPR). Its properties (spectral position, linewidth and area) depend on the nanoparticle size, shape and environment, and are briefly discussed in this section.

1.3.1 Energetic considerations

When an electromagnetic wave $\vec{E}_0(t) = \vec{E}_0 e^{-i\omega t}$ shines a nanoparticle, as illustrated in Fig. (1.5), the nanoparticle electrons oscillates along the light polarization at the frequency ω.

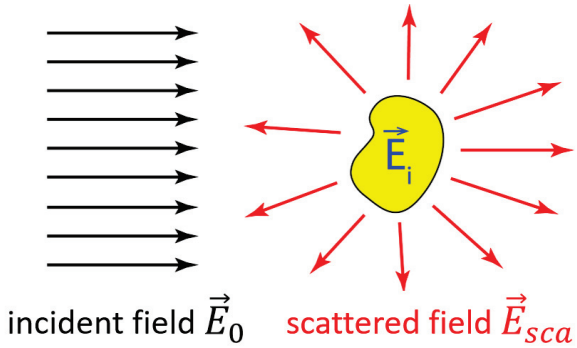

Figure 1.5: Nanoparticle illuminated by an incident electromagnetic wave $\vec{E}_0$. Interaction with the particle yields a scattered field $\vec{E}_{sca}$ and an internal one $\vec{E}_{int}$.

This electronic periodic movement induces an electric field inside the nanoparticule, $\vec{E}_{int}(t)$, and a scattered one, $\vec{E}_{sca}(t)$, propagating through the external matrix (from the nanoparticles towards every direction). Absorbed electromagnetic energy can also be transformed in thermal energy via Joule effect.
In an homogeneous environment, the power absorbed by the nanoparticle, W_{abs},

$$W_{abs} = -\oint_S \vec{P} \cdot \vec{n}\, dS\,, \tag{1.14}$$

is determined by the flux through the nanoparticule surface S (with $\vec{n}$ the unitary vector normal to the surface and directed towards the exterior) of the Poynting vector $\vec{P}$, defined as a function of the total external electric field $\vec{E}_m(t) = \vec{E}_0(t) + \vec{E}_{sca}(t)$ and total external magnetic field $\vec{H}_m(t) = \vec{H}_0(t) + \vec{H}_{sca}(t)$

$$\vec{P} = \frac{1}{2}\mathrm{Re}\{\vec{E}_m \times \vec{H}_m^*\}\,. \tag{1.15}$$

Considering a transparent environment, the development of the electric and magnetic fields yields [7, 8, 9]

$$W_{abs} + W_{sca} = W_{ext}\,, \tag{1.16}$$

where

$$\begin{cases} W_{sca} = \frac{1}{2}\mathrm{Re}\left\{\oint_S [\vec{E}_{sca} \times \vec{H}^*_{sca}] \cdot \vec{n}\, dS\right\} \\ W_{ext} = -\frac{1}{2}\mathrm{Re}\left\{\oint_S [\vec{E}_0 \times \vec{H}^*_{sca} + \vec{E}_{sca} \times \vec{H}^*_0] \cdot \vec{n}\, dS\right\} \end{cases} . \tag{1.17}$$

The incident power loss (extinction), W_{ext}, in the propagation direction is caused by the sum of the absorbed power W_{abs} and scattered power W_{sca} by the nanoparticle.

Convenient definitions are the extinction, absorption and scattering cross-sections of the nanoparticle. They are defined as the ratio of the powers over the average intensity I_0 ($I_0 = n_m\, c\, \epsilon_0 \langle E_0 \rangle^2/2$, with n_m the refractive index of the medium and c the speed of light) of the incident beam on the nano-object [9].

$$\begin{cases} \sigma_{ext} = \frac{W_{ext}}{I_0} \\ \sigma_{abs} = \frac{W_{abs}}{I_0} \\ \sigma_{sca} = \frac{W_{sca}}{I_0} \end{cases} , \tag{1.18}$$

and therefore

$$\sigma_{ext} = \sigma_{abs} + \sigma_{sca} \tag{1.19}$$

Analytic computation of the cross-sections are possible in simple cases (spheroids in homogeneous matrix), while for more complicated geometries a numerical approach is required.

1.3.2 Optical response of a nanosphere in the quasi-static approximation

Consider the configuration illustrated in Fig. (1.6), where a sphere of diameter D and dielectric function $\epsilon(\omega) = \epsilon_1 + \epsilon_2$ is embedded in a transparent medium of dielectric function ϵ_m and shined by the incident plane wave $\vec{E}_i = E_0 e^{i(\vec{k}\cdot\vec{r} - \omega t)}$ with $k = n_m \omega / c$. As shown in Fig. (1.7), if the sphere diameter is of the order of the incident wavelength ($D \sim \lambda$), electric field is not uniform within the particle, creating an inhomogeneous charge distribution, inducing multipolar electron oscillations. On the other hand, if the particle is very small as compared to the optical wavelength ($D \ll \lambda$), the field is uniform inside the particle and the charge distribution approaches that of an oscillating dipole (dipolar approximation). The

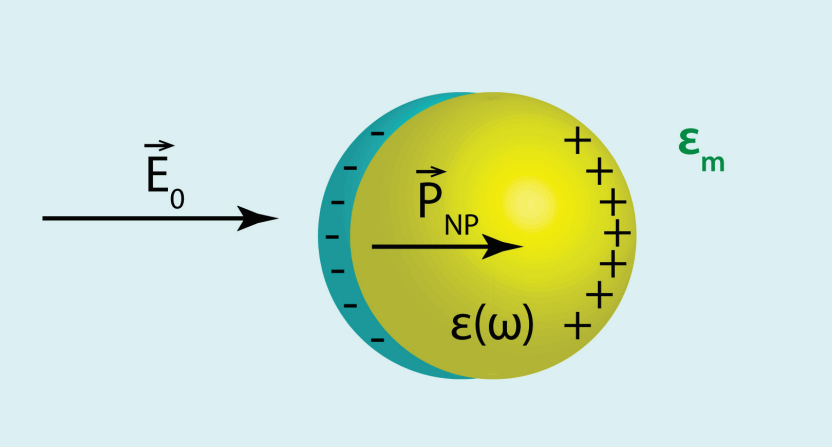

Figure 1.6: Nanosphere (yellow sphere) of dielectric function ϵ under an electric field $\vec{E}_0$ in a medium characterized by ϵ_m. $\vec{E}_0$ induces a polarization $\vec{P}_{NP}$ corresponding to electronic movement (blue sphere).

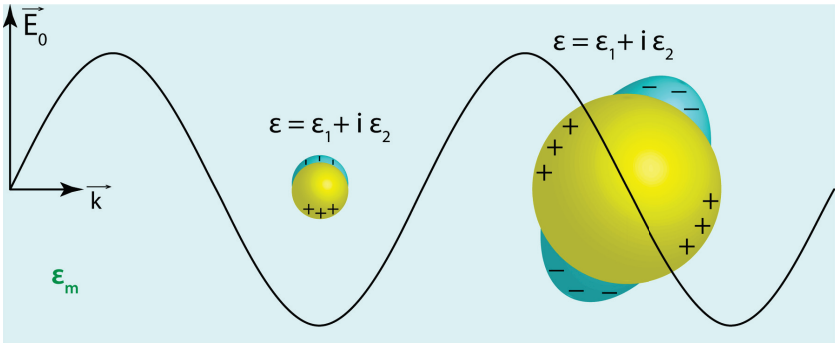

Figure 1.7: Charge distribution in the case $D \ll \lambda$ (left) and $D \sim \lambda$ (right).

latter case corresponds to the electrostatic problem of the polarization of a sphere in a uniform field, which can be solved by Poisson equation with proper boundary conditions. The incident field induces a polarization p_s within the sphere and a polarization p_0 in the surrounding medium; applying field continuity conditions at the interface, the internal field E_{int} is shown to be proportional to the incident field through a dielectric confinement factor [10]

$$\vec{E}_{int} = \frac{3\epsilon_m}{\epsilon + 2\epsilon_m}\vec{E}_0\,, \tag{1.20}$$

The polarizability α of the nanoparticle can be deduced from $\vec{P}_{NP} = \alpha\epsilon_0\epsilon_m\vec{E}_0$ [10]

$$\alpha = 3V\frac{\epsilon - \epsilon_m}{\epsilon - 2\epsilon_m}\,, \tag{1.21}$$

where $V = \frac{1}{6}\pi D^3$ is the volume of the sphere. As a first approximation, the particle response to an incident field can thus be identified with the response of a dipole placed in its center. Analytical expressions for σ_{ext} and σ_{sca} can then be obtained as a function of the absolute value of polarizability and its imaginary part [10, 11]

$$\sigma_{ext}(\omega) = k\,\mathrm{Im}\{\alpha\} = \frac{9V\omega\,\epsilon_m^{3/2}}{c}\,\frac{\epsilon_2(\omega)}{\left(\epsilon_1(\omega)+2\epsilon_m\right)^2+\epsilon_2^2(\omega)}\,, \tag{1.22}$$

$$\sigma_{sca}(\omega) = \frac{k^4}{6\pi}\,|\alpha|^2 = \frac{3V^2\,\omega^4\epsilon_m^2}{2\pi c^4}\,\frac{\left(\epsilon_1(\omega)-\epsilon_m\right)^2+\epsilon_2^2(\omega)}{\left(\epsilon_1(\omega)+2\epsilon_m\right)^2+\epsilon_2^2(\omega)}\,. \tag{1.23}$$

The scattering cross section σ_{sca} varies with λ as $1/\lambda^4$ (Rayleigh scattering) ($\lambda = 2\pi c/\omega$ being the wavelength in vacuum) and the ratio between scattering and extinction cross sections is proportional to $(D/\lambda)^3$. In the approximation $D \ll \lambda$, extinction is therefore dominated by absorption

$$\sigma_{ext} \approx \sigma_{abs} \gg \sigma_{sca}\,. \tag{1.24}$$

The extinction cross section is enhanced at the frequency $\omega = \omega_R$ minimizing the denominator in Eq. (1.22). Supposing a relatively small and weakly dispersed imaginary part ϵ_2 of the metal dielectric constant in this optical region, the resonant condition can be simplified as

$$\epsilon_1(\omega_R) + 2\epsilon_m = 0\,. \tag{1.25}$$

The occurrence of this condition is associated with the appearance of a resonance in the extinction optical spectrum of the metal nanoparticle: the surface plasmon resonance (SPR). Accordingly to Eq. (1.20), the SPR corresponds to an enhancement of the optical response of the confined nanosphere resulting from the exaltation of the internal field E_{int} as compared to the incident field E_0, phenomenon customarily called dielectric confinement effect. The SPR can be classically associated to a collective oscillation of the metal electrons relative to the lattice, resonantly driven by the external electromagnetic field. In the frame of the quasi-static approximation, the resonant frequency ω_R is given by the expression

$$\omega_R = \frac{\omega_p}{\sqrt{\epsilon_1^{ib}(\omega_R) + 2\epsilon_m}}\,, \tag{1.26}$$

obtained by injecting Eq. (1.12) and (1.13) in Eq. (1.25). When the SPR lies far from the interband transitions threshold, as in the simple case of a silver sphere, it can be spectrally described by a quasi-Lorentzian profile centered around ω_R. The extinction spectrum of a silver nanosphere embedded in water ($\epsilon_m = 1.33^2$) and evaluated by Eq. (1.22) is reported in Fig. (1.8). It shows a quasi-Lorentzian

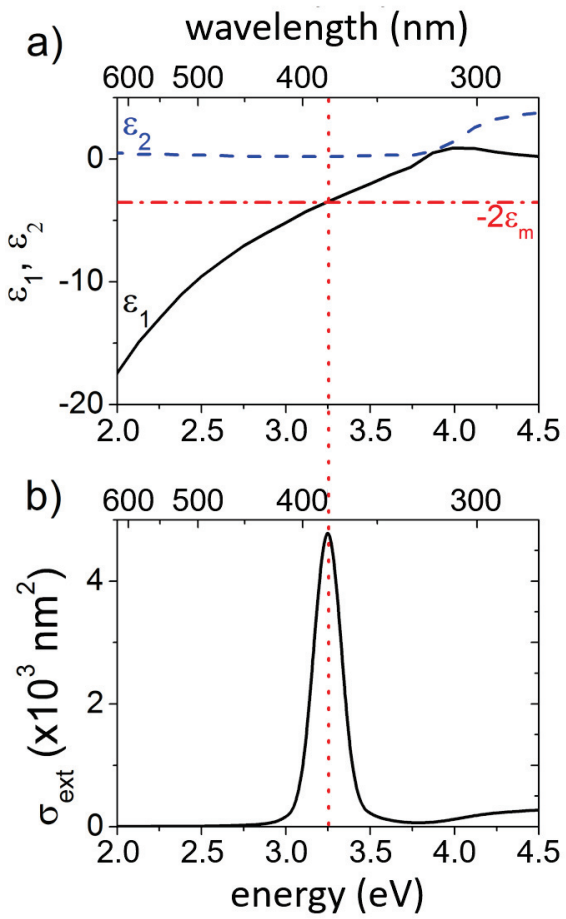

Figure 1.8: (a) Real (solid line) and imaginary (dashed line) part of the silver dielectric function. The intersection between ϵ_1 and $-2\epsilon_m$ (dash-dot) determines the SPR peak position (b), being $\hbar\omega_R \approx 3.3\,\text{eV}$ for a silver nanosphere of diameter $D = 20\,\text{nm}$ in water ($\epsilon_m = 1.33^2$).

SPR about 3.3 eV, where the resonance condition is satisfied. Conversely, the SPR of a gold nanosphere in water (Fig. (1.9a)), located around 2.4 eV, exhibits weaker amplitude and asymmetry caused by the presence of interband transitions, which induce an important optical response for energies $E > \hbar\omega_{ib} \approx 2\,\text{eV}$. In addition, SPR spectral position depends on the matrix through ϵ_m. As shown in Fig. (1.9b), the SPR undergoes a redshift for increasing values of ϵ_m together with an amplitude increase mostly due to the $\epsilon_m^{3/2}$ prefactor in Eq. (1.22).

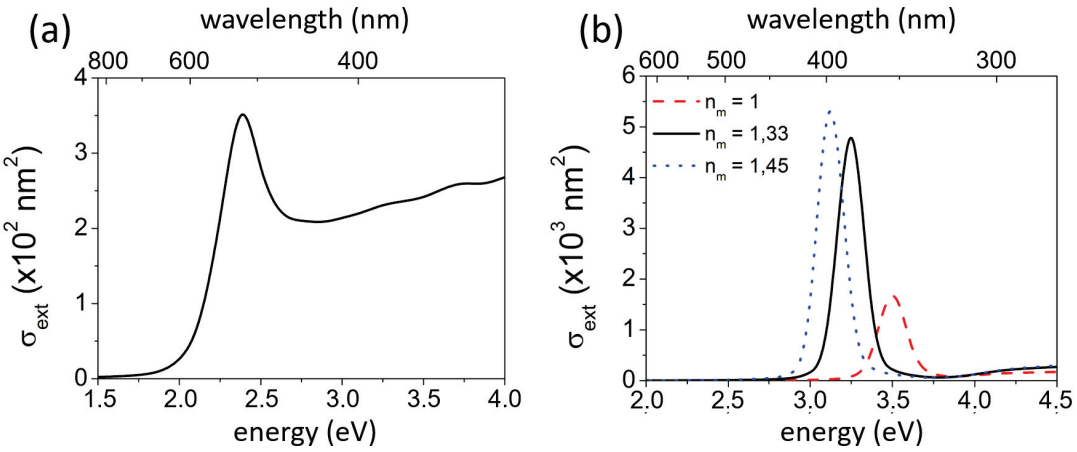

Figure 1.9: (a) Extinction spectrum of a gold nanosphere of diameter 20 nm in water ($\epsilon_m = 1.33^2$) in quasi-static approximation ($D \ll \lambda$). (b) Extinction spectrum of a silver nanosphere of diameter 20 nm in vacuum ($\epsilon_m = 1^2$), water ($\epsilon_m = 1.33^2$) and glass ($\epsilon_m = 1.45^2$) in quasi-static approximation ($D \ll \lambda$).

1.3.3 Optical response of a nanosphere beyond the quasi-static approximation: Mie theory

For large nanosphere sizes ($D \geq \lambda$), the dipolar approximation is not justified, since the spatial heterogeneity of the field within the particle and the consequent appearance of delay effects cannot be disregarded [8, 10].
Exact calculation of the optical response of a sphere has been developed by G. Mie [12, 13]. In the case of a non-absorbing medium (real ϵ_m), the cross-sections of a sphere of radius R write as

$$\sigma_{ext} = \frac{2\pi R^2}{u^2} \sum_{n=1}^{\infty} (2n+1)\, \mathrm{Re}\{a_n + b_n\}\,, \tag{1.27}$$

$$\sigma_{sca} = \frac{2\pi R^2}{u^2} \sum_{n=1}^{\infty} (2n+1)\left(|a_n|^2 + |b_n|^2\right), \qquad \sigma_{abs} = \sigma_{ext} - \sigma_{sca}\,, \tag{1.28}$$

with

$$a_n = \frac{m\psi_n(mu)\psi_n'(u) - \psi_n(u)\psi_n'(mu)}{m\psi_n(mu)\xi_n'(u) - \xi_n(u)\psi_n'(mu)}, \quad b_n = \frac{\psi_n(mu)\psi'(u) - m\psi_n(u)\psi_n'(mu)}{\psi_n(mu)\xi_n'(u) - m\xi_n(u)\psi_n'(mu)}\,, \tag{1.29}$$

where $m = (\epsilon/\epsilon_m)^2$, $u = kR = 2\pi n_m R/\lambda$, ψ_n and ξ_n are the Riccati-Bessel and Hankel functions, respectively. The index n corresponds to the multipolar expansion order (dipolar for $n = 1$, quadripolar for $n = 2$, etc...). Fig. (1.10) shows a comparison between the extinction spectra of single gold nanospheres computed using

the Mie theory and the quasi-static approximation. For small sphere diameters ($D < 30$ nm and $u \ll 1$), the dipolar is a good approximation of the Mie theory (Fig. (1.10a)). In fact, a first order development of Eq. (1.27) leads to Eq. (1.22) of the quasi-static case. Increasing the nanosphere size progressively induces a redshift and broadening of the SPR (Fig. (1.10b,c)) and the introduction of additional resonances related to quadrupolar modes (Fig. (1.10d)) [14, 15, 16, 17].

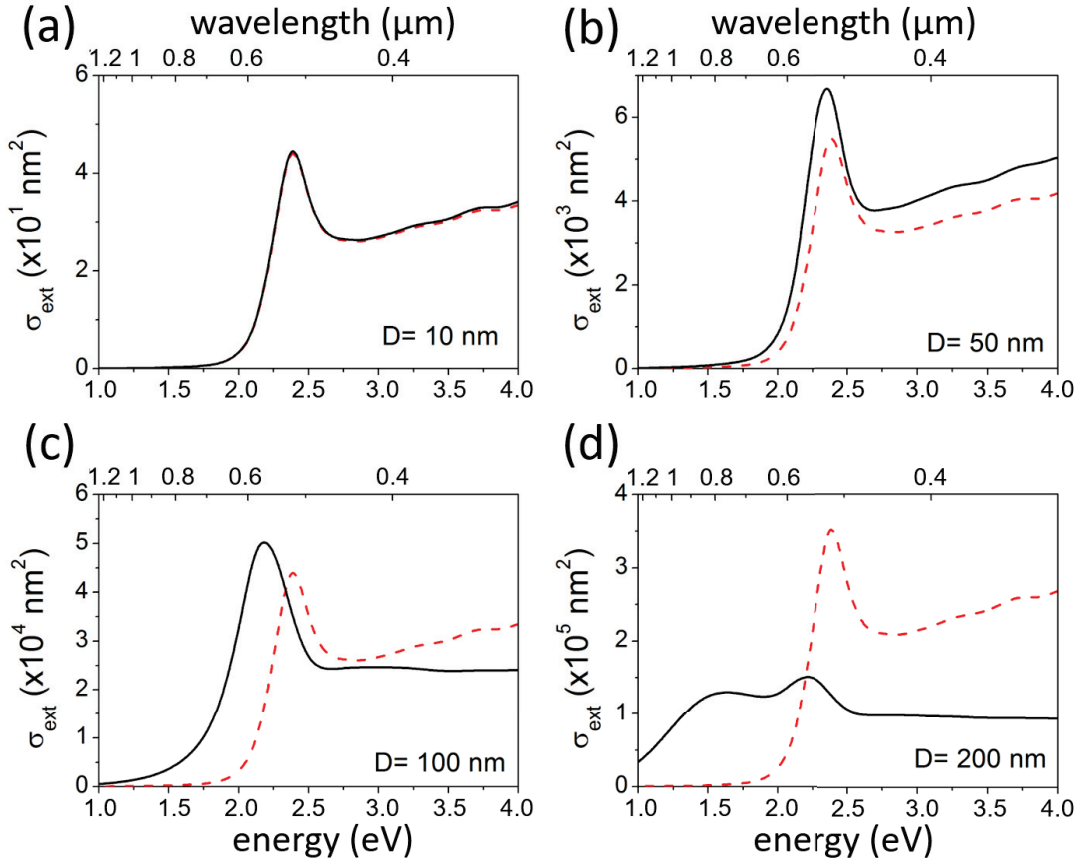

Figure 1.10: Extinction spectra of a gold nanosphere in water ($\epsilon_m = 1.33^2$) accordingly to the Mie theory (solid line) and to the quasi-static approximation of Eq. (1.22) (dashed line) for different diameters D.

The optical response of a nano-object is also strongly influenced by its shape [18]. In most cases, no analytical solution is achievable, exception made for high symmetric configurations, such as core-shell spheres, ellipsoids and infinite cylinders.

1.3.4 Optical response of an ellipsoid and more complex shapes

Consider a prolate ellipsoid of semi-axes a, b and c ($a>b=c$), characterized by a complex dielectric function $\epsilon=\epsilon_1+\epsilon_2$ and embedded in a medium of real dielectric constant ϵ_m, as the one illustrated in Fig. (1.11).

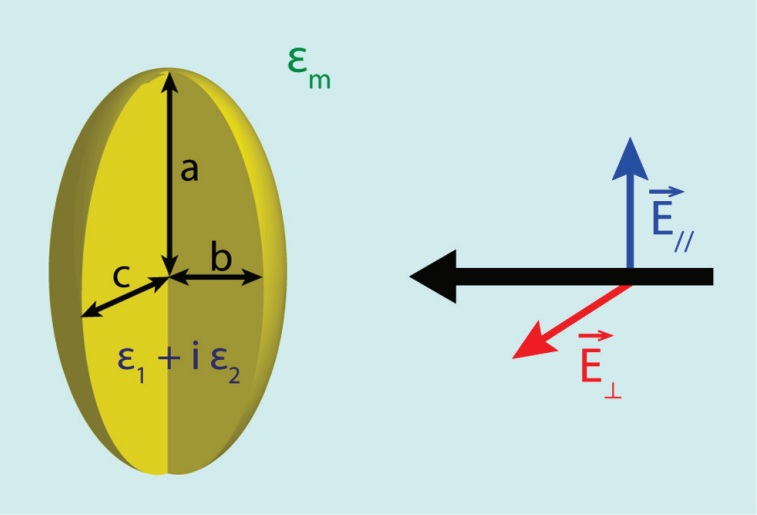

Figure 1.11: Prolate ellipsoid ($a > b = c$) of dielectric function ϵ illuminated by an electromagnetic wave (of components $\vec{E}_{\|}$ along a and $\vec{E}_{\perp}$ orthogonal to a) propagating in a medium of dielectric function ϵ_m.

For such an elongated particle, absorption cross-section strongly depends on the incoming light polarization. In the frame of the quasi-static approximation, for a light polarization along the principal axes $i = a, b, c$, the extinction-cross section has been expressed by R. Gans as [7, 8, 19, 20]

$$\sigma_{ext}^{i} = \frac{V(H_i[\eta]+1)^2\,\omega\epsilon_m^{3/2}}{c}\,\frac{\epsilon_2(\omega)}{\left(\epsilon_1(\omega)+H_i[\eta]\epsilon_m\right)^2+\epsilon_2^2(\omega)}\,, \tag{1.30}$$

where $V=4/3\pi abc$ is the volume of the ellipsoid, while $H_i[\eta]$ is a geometrical factor dependent on the aspect ratio $\eta=a/b$ accordingly to

$$H_i = \frac{1-L_i}{L_i} \qquad (i=a,b,c)\,, \tag{1.31}$$

$$L_a = \frac{1-e^2}{e^2}\left(\frac{1}{2e}\ln\left(\frac{1+e}{1-e}\right)-1\right)\,, \quad L_b = L_c = \frac{1-L_a}{2}\,, \quad e=\sqrt{1-\eta^2} \tag{1.32}$$

Except for the additional factor H_i, this relation is similar to the one obtained for a sphere (Eq. (1.22)) and the resonance condition may be similarly determined

$$\epsilon_1(\omega_R[i]) + H_i\epsilon_m = 0\,, \tag{1.33}$$

if ϵ_2 is weakly dispersed around $\omega_R[i]$. Considering Eq. (1.12) and (1.13)

$$\omega_R[i] = \frac{\omega_p}{\sqrt{\epsilon_1^{ib}(\omega_R[i]) + H_i\epsilon_m}} \tag{1.34}$$

Fig. (1.12a) shows the extinction spectra of an ellipsoid of aspect ratio $\eta = 2$ for different polarization orientations: two separate resonances appear which are referred to as longitudinal and transversal SPR. The first one is induced by an incident electric field ($\vec{E}_{\parallel}$) polarized along the major axis a, while the second one by a field ($\vec{E}_{\perp}$) with orthogonal polarization in respect to a. As illustrated in Fig. (1.12b), increasing the ellipsoid aspect ratio η redshift the longitudinal SPR in respect to the transversal one.

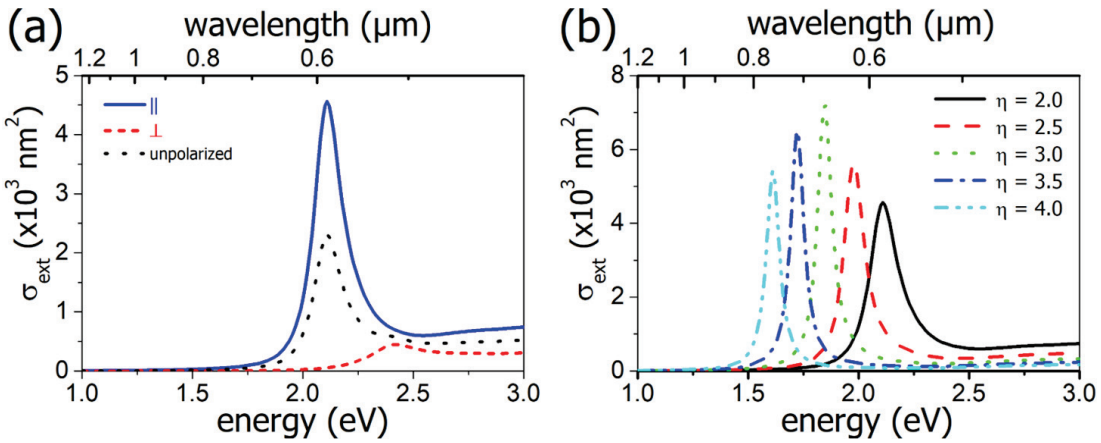

Figure 1.12: (a) Extinction spectra of a prolate Au ellipsoid of aspect ratio $\eta = a/b = 2$ and long semi-axis $a = 20$ nm for incident waves of different polarizations. (b) Extinction spectra of a prolate ellipsoid with long semi-axis $a = 20$ nm and several aspect ratio for a light polarization along a. All the calculations have been realized in water ($\epsilon_m = 1.33^2$).

The origin of the quasi-Lorentzian profile of the longitudinal SPRs in elongated nanoparticles (with a central frequency ω_R) can be understood in the framework of the dipolar response of ellipsoidal nano-objects ($\omega_R = \omega_R[a]$). A first order expansion in $(\omega - \omega_R)$ of the extinction cross-section of Eq. (1.30), assuming a weak and/or weakly dispersed ϵ_2 around ω_R (as for gold in the red and infrared

range, see Fig. (1.3)), yields the longitudinal SPR:

$$\sigma_{ext}(\omega) = \frac{V(H+1)^2\,\omega\epsilon_m^{3/2}}{c}\frac{\epsilon_2(\omega)}{\left[\frac{\partial\epsilon_1}{\partial\omega}\Big|_{\omega_R}(\omega-\omega_R)\right]^2+\epsilon_2^2(\omega)}\,, \tag{1.35}$$

where H is the geometrical factor associated to the long axis ($H=H_a$). In experiments described in this thesis, the longitudinal SPR position is always located far from interband transitions, so that $\partial\epsilon_1/\partial\omega|_{\omega_R}\sim 2\omega_p^2/\omega_R^3$ using the Drude dielectric function of Eq. (1.13). This leads to a Lorentzian extinction profile of the type

$$\sigma_{ext}(\omega) = \frac{A}{\pi}\frac{\left(\frac{\hbar\Gamma}{2}\right)}{(\hbar\omega-\hbar\omega_R)^2+\left(\frac{\hbar\Gamma}{2}\right)^2}\,. \tag{1.36}$$

Such a profile is fully characterized by three independent parameters: peak position ω_R, integrated area A and spectral linewidth Γ. The energy peak position

$$\hbar\omega_R = \frac{\hbar\omega_p}{\sqrt{\epsilon_1^{ib}(\omega_R)+H\epsilon_m}} \tag{1.37}$$

depends on nano-object shape, composition and local environment (Eq. (1.34) with $\omega_R[i]=\omega_R[a]$). The spectral area

$$A = \frac{\pi(1+H)^2\,\epsilon_m^{3/2}\,V\,\omega_R^4}{2\,c\,\omega_p^2} \tag{1.38}$$

is proportional to the particle total number of electrons through the volume V and also depending on its shape, environment and SPR peak position. The SPR linewidth

$$\Gamma = \gamma + \frac{\omega_R^3}{\omega_p^2}\epsilon_2^{ib} \approx \gamma \tag{1.39}$$

is the electronic damping rate in Drude model (see Eq. (1.13)) extended to the confined nano-object case. The discussion here does not include the radiative (Γ_{rad}), chemical (Γ_{chem}) and electron-surface scattering (γ_s) contributions to Γ: they will be introduced in Section (2.2.3) of Chapter (2) in order to discuss about the SPR broadening of gold nanoparticles with bipyramidal shape induced by pressure.
The previous calculations demonstrate that ω_R and A are affected by physical parameters different from those influencing Γ. In particular, plasmon damping rate controls Γ but does not affect ω_R and A, which is of key importance as Γ can be significantly altered by surface effects. These parameters can be extracted from the experimental data by fitting the SPR line, as shown in Fig. (1.13b), and subsequently compared to theoretical predictions if nanoparticle size is known, as it

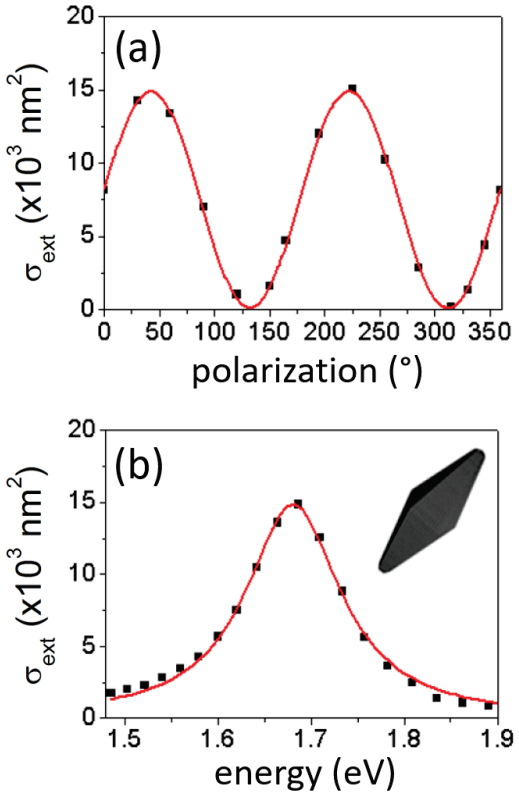

Figure 1.13: (a) The polarization dependence of the extinction cross-section measured for a gold bipyramid at 1.68 eV is reproduced by a sinusoidal function (Eq. (1.40)). (b) Its absolute extinction cross-section for light polarized along the long axis of the nano-object is fitted by a Lorentzian function (Eq. (1.36)).

is done in the following chapters.

The optical response of elongated nano-objects strongly depends on the polarization of the incident light. This dependence, which is partially lost by orientational averaging in ensemble measurements, can be highlighted in single particle experiments. The extinction cross-section of a nanoparticle illuminated by a linearly polarized plane wave can be generally written as [21]

$$\sigma_{ext}(\theta,\omega) = \sigma_{\parallel}(\omega)\cos^2(\theta-\theta_0) + \sigma_{\perp}(\omega)\sin^2(\theta-\theta_0) \tag{1.40}$$

where θ is the incident light polarization angle and θ_0 the particle long axis angle, with respect to a reference laboratory frame. The polarization response measured in an elongated bipyramid is well reproduced by Eq. (1.40), showing a very high contrast ratio $\sigma_{\perp}/\sigma_{\parallel} \sim 0$ between the maximum amplitude corresponding to polarization along the nanoparticle long axis, and the minimum for a perpendicular

polarization (Fig. (1.13b)). These measurements provide the absolute orientation of the nano-object on the substrate.

In the general case of an arbitrary shape, such as penta-twinned bipyramids (which will be studied in Chapter 2) or finite cylinder (analyzed in Chapter 3) the optical response can only be computed numerically by different methods, as discrete dipole approximation (DDA), or finite element methods (FEM). In this thesis work, FEM has been consistently used to interpret experimental data and their operating principles will be explained later, in Section (2.2.1) of Chapter 2) (optical domain simulations) and in Section (3.1.4) of Chapter 3 (acoustic domain simulations).

1.4 Optical detection of single nano-objects: spatial modulation spectroscopy (SMS)

Nanoparticles have been largely investigated over the last decades because of their distinctive properties and potential use in technological (nonlinear photonic devices [22], data storage [23], energy harvesting [24]) and biomedical applications (photothermal therapy [25], biological imaging [26] and sensing [27]). In this context, optical techniques are powerful tools, yielding information on the intrinsic features of a nanoparticle (size, shape, and composition) and on its local environment. As these parameters can strongly fluctuate from object to object, conventional ensemble experiments prevent obtaining quantitative information. In this perspective, the development of optical techniques for detecting and characterizing single nano-objects has greatly increased the knowledge in this field over the past few years.

In the first part of this section, the principal methods for the detection of single nano-objects are presented. The following part will focus on the description of the spatial modulation spectroscopy (SMS) technique exploited in this thesis.

1.4.1 Overview of single-particle characterization techniques

In these last years, several experimental techniques [28, 29] have been developed with the aim of investigating optical properties of single metallic nano-objects. These can be classified into two categories: far-field (where sources and detectors are far from the nanoparticle with respect to the wavelength) and near-field methods (based on illumination or detection typically closer than one wavelength from the nanoparticle).
A summary of the relevant techniques, with relative advantages and disadvantages, can be found in Tab. (1.3). Historically, scanning near-field optical microscopy

	Technique	Measured Quantity	Advantages	Limitations
Near-field	Scanning near-field optical microscopy (SNOM)	Scattering	- High resolution (~ 10 nm) - Electric field mapping in proximity of the nano-object - Suitable for liquid environment	- Complex interpretation - Perturbation by the tip - Long scan times
Far-field	Dark-field spectroscopy	Scattering	- Simple setup - Dynamic nanoparticle tracking - Short scan times	- No absolute cross-section - Nanoparticle sizes > 40 nm - Background scattering from other objects - Diffraction-limited
	Photothermal imaging (PHI)	Absorption	- Detection of very small particle sizes (~ 1 nm) - Suitable for liquid and biological environments	- No absolute cross-section - High laser powers - Complex setup (two beam alignment) - Diffraction-limited
	Spatial modulation spectroscopy (SMS)	Extinction	- Absolute extinction cross-section - Detection of small particles sizes (≥ 5 nm) - Low laser powers	- No quantitative measurements for large nanoparticle sizes ($\sigma_{sca} \sim \sigma_{abs}$) - Diffraction-limited

Table 1.3: Overview of the main optical single nanoparticle detection techniques [28].

(SNOM) was one of the first methods to be introduced [30]. Based on a nanometric tip maintained at a few nanometers from the sample, the technique provides a high spatial resolution (~ 10 nm, depending on the tip [31]), however the signal strongly depends on the tip-nanoparticle interaction and it interpretation requires a complex modeling of the near-field around the tip [32].
Far-field techniques are characterized by a limited spatial resolution, being intrinsically diffraction-limited, but are free from the spurious influence of the observation apparatus. The most commonly used far-field techniques are dark-field microscopy, photothermal imaging (PHI) and spatial modulation spectroscopy (SMS).
Dark-field microscopy is based on the selective collection of the scattered light from an illuminated nano-object [33, 34, 35]. Simple to apply, it does not provide a quantitative measurement of σ_{sca} (since only a fraction of the scattered light is detected) and is limited to relatively large nanoparticle sizes (typically > 40 nm, being $\sigma_{sca}/\sigma_{ext} \sim V$ accordingly to Eq. (1.22), (1.23) and (1.25).
PHI is based on the local heating of the nano-object environment through the absorption of a modulated "pump" laser beam that modifies its refractive index and on the propagation of a "probe" beam [36, 37, 38]. In absorbing environment this high sensitive technique allows the detection of small nanoparticle sizes (~ 1 nm), although a quantitative determination of σ_{abs} remains difficult.

Conversely, SMS permits a quantitative measurement of σ_{ext} in nano-objects sizes larger than $\sim$5 nm (Au) or $\sim$2 nm (Ag) [39] deposited on transparent or absorbing substrates. This technique, employed in this thesis, will be explained in detail in the next section.

1.4.2 Principle of SMS

When a laser beam is focused on a nano-object, a part of the incident power W_0 is lost through absorption and scattering (see Section (1.3.1)). Consider a punctiform particle of cross-section σ_{ext}, expressed by Eq. (1.22), located in (x_0, y_0) and shined by a beam with full-width-at-half-maximum $FWHM$ and intensity profile $I(x, y)$ in the nanoparticle plane, as illustrated in Fig. (1.14).

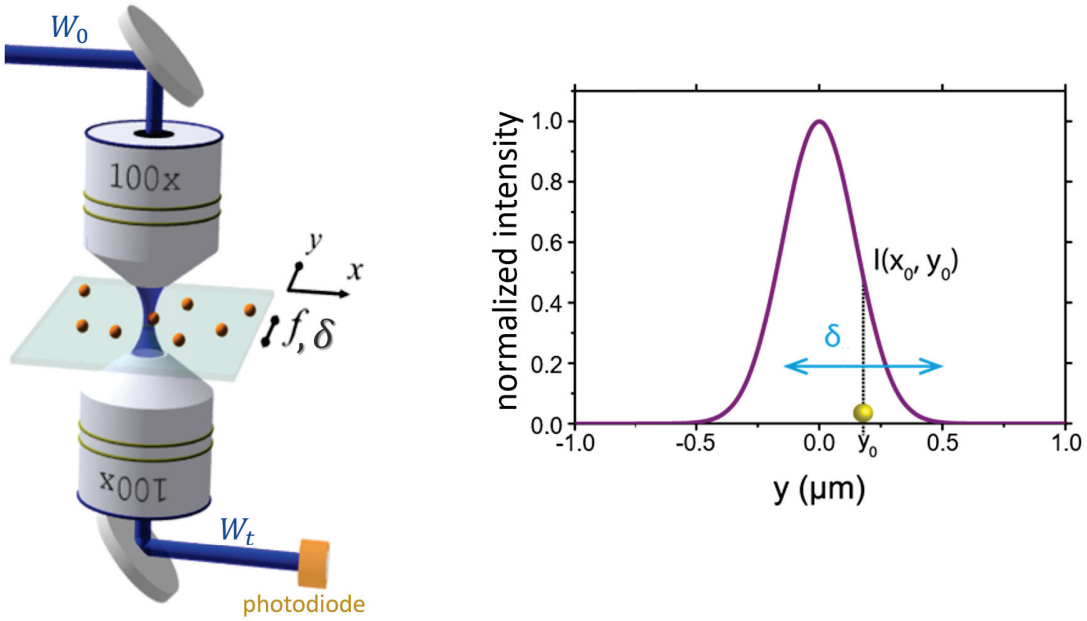

Figure 1.14: SMS principle: a laser beam is focused on a sample containing nanoparticles. Sample position is modulated along y at frequency f and amplitude δ.

The transmitted power W_t writes as

$$W_t = W_0 - \sigma_{ext}\, I(x_0, y_0)\,, \tag{1.41}$$

meaning the incident beam attenuation $\Delta W = W_0 - W_t$ is

$$\Delta W = \sigma_{ext}\, I(x_0, y_0)\,. \tag{1.42}$$

For small nanoparticle sizes direct measure of ΔW is very challenging. For instance, in a sphere of diameter 20 nm illuminated by a diffraction-limited Gaussian beam,

$$\frac{\Delta W}{W_0} \sim 10^{-3}\,, \tag{1.43}$$

the signal being dominated by the power fluctuations of the laser source.
To overcome this limitation, a general solution consists in purposely introducing a periodic modulation of ΔW through the modulation of the laser wavelength [40], the light polarization [41], or the illuminated nano-object position [39, 42], and detecting the oscillating component of ΔW at the same frequency.
The latter approach has been developed by the team. Typically, the sample is mounted on a piezoelectric shaker which modulates the nanoparticle y position according to $y(t)=y_0+\delta\sin(2\pi ft)$, where δ is the oscillation amplitude and f the frequency. Thus, the power loss becomes time-dependent

$$\Delta W(t) = \sigma_{ext}\, I(x_0, y_0+\delta\sin(2\pi ft))\,. \tag{1.44}$$

Assuming the oscillation amplitude is much smaller than the beam size, $\delta \ll FWHM$, Eq. (1.44) can be developed

$$\Delta W(t) = \Delta W_0 + \Delta W|_f \sin(2\pi ft) + \Delta W|_{2f} \cos(4\pi ft) + o(\delta^2)\,, \tag{1.45}$$

where

$$\begin{cases} \Delta W_0 = \sigma_{ext}\left[I(x_0,\, y_0) + \dfrac{\delta^2}{4}\right] \\ \Delta W|_f = \sigma_{ext}\delta \left.\dfrac{\partial I}{\partial y}\right|_{x_0,y_0} \\ \Delta W|_{2f} = -\dfrac{1}{4}\sigma_{ext}\delta^2 \left.\dfrac{\partial^2 I}{\partial y^2}\right|_{x_0,y_0} \end{cases}. \tag{1.46}$$

Therefore, the power modulation $\Delta W(t)$ contains constant and sinusoidal terms, all proportional to σ_{ext}. Furthermore, the components oscillating at f and $2f$ are respectively proportional to the first and second derivative of the beam profile $I(x, y)$ with respect to the coordinate y along the vibrational axis and evaluated in (x_0, y_0).

Practically, power modulations $\Delta W|_{f,2f}$ are detected as a voltage $\Delta V|_{f,2f}$ using a photodiode followed by a lock-in amplifier (LIA) to measure relative power changes. The detection of the LIA allows to select the component of $\Delta W(t)$ at a specific frequency $(f, 2f)$, i.e. filtering out all the other frequencies and increasing the signal/noise ratio. The same setup is used to measure, for normalization, the power

W_0 of the incident beam when modulated as a square wave at the same frequency $(f, 2f)$ by a mechanical chopper, producing $V_0\,|_{f,2f}$ (alternatively a digital multimeter can be used to continuously monitor the incident power). The SMS signal $\mathbb{S}_{f,2f}$ is thus

$$\mathbb{S}_{f,2f} = \frac{\Delta V|_{f,\,2f}}{V_0\,|_{f,2f}} = \frac{\pi}{2}\frac{\Delta W|_{f,\,2f}}{W_0} \qquad \text{with} \qquad W_0 = \iint\limits_{\mathbb{R}^2} I(x,\,y)\,dxdy\,, \tag{1.47}$$

where the factor $\pi/2$ takes into account the temporal shape of the normalization signal (square wave). This allows to achieve a high sensitivity ($\min\{\mathbb{S}_{f,2f}\} \sim 10^{-5}$), permitting the detection of nano-objects with cross-section of the order of a few nm^2 [39].

In the general case, beyond the condition $\delta \ll FWHM$, Eq. (1.44) can be developed using the Fourier theory

$$\mathbb{S}_f(x_0, y_0) = \frac{\pi}{2}\frac{\Delta W|_f}{W_0}(x_0, y_0) = \frac{\pi\sigma_{ext}}{W_0}\frac{1}{T}\int\limits_{-T/2}^{T/2} I(x_0, y_0 + \delta_y \sin(2\pi f t))\sin(2\pi f t)\,dt\,, \tag{1.48}$$

$$\mathbb{S}_{2f}(x_0, y_0) = \frac{\pi}{2}\frac{\Delta W|_{2f}}{W_0}(x_0, y_0) = \frac{\pi\sigma_{ext}}{W_0}\frac{1}{T}\int\limits_{-T/2}^{T/2} I(x_0, y_0 + \delta_y \sin(2\pi f t))\cos(2\pi(2f t))\,dt\,. \tag{1.49}$$

Fig. (1.15a,b,c) presents the results of numerical computations of $\mathbb{S}_f(x_0, y_0)$ and $\mathbb{S}_{2f}(x_0, y_0)$ supposing a Gaussian intensity profile centered in $(0, 0)$ of form $I(x, y) = \exp\left(-2\frac{x^2+y^2}{w^2}\right)$ with $FWHM = \sqrt{2\ln 2}w = 0.7\lambda$ (typical experimental condition in the wavelength range $500-1100\,\mathrm{nm}$). The nanoparticle position is moved through the windows $1\times 1\,\mu\mathrm{m}^2$, being spatially modulated with $\delta = 325\,\mathrm{nm}$ and $f = 1500\,\mathrm{Hz}$ (typical experimental parameters). The extinction cross-section has been arbitrary fixed at $\sigma_{ext} = 10^3\,\mathrm{nm}^2$.
In Fig. (1.15d,e) it should be noticed that along the vibrational axis y the detected profile at f $(2f)$ is similar, but not coincident, to the first (second) derivative of the intensity profile, accordingly with Eq. (1.46), being $\delta \approx FWHM$.
In the case of a detection at f the signal is zero when the particle is in the center of the beam, i.e. at $(x_0, y_0) = (0, 0)$, while at $2f$ the signal is maximized. Additionally, the position of the maximum does not change with the wavelength. For these reasons the $2f$ detection is experimentally preferred.

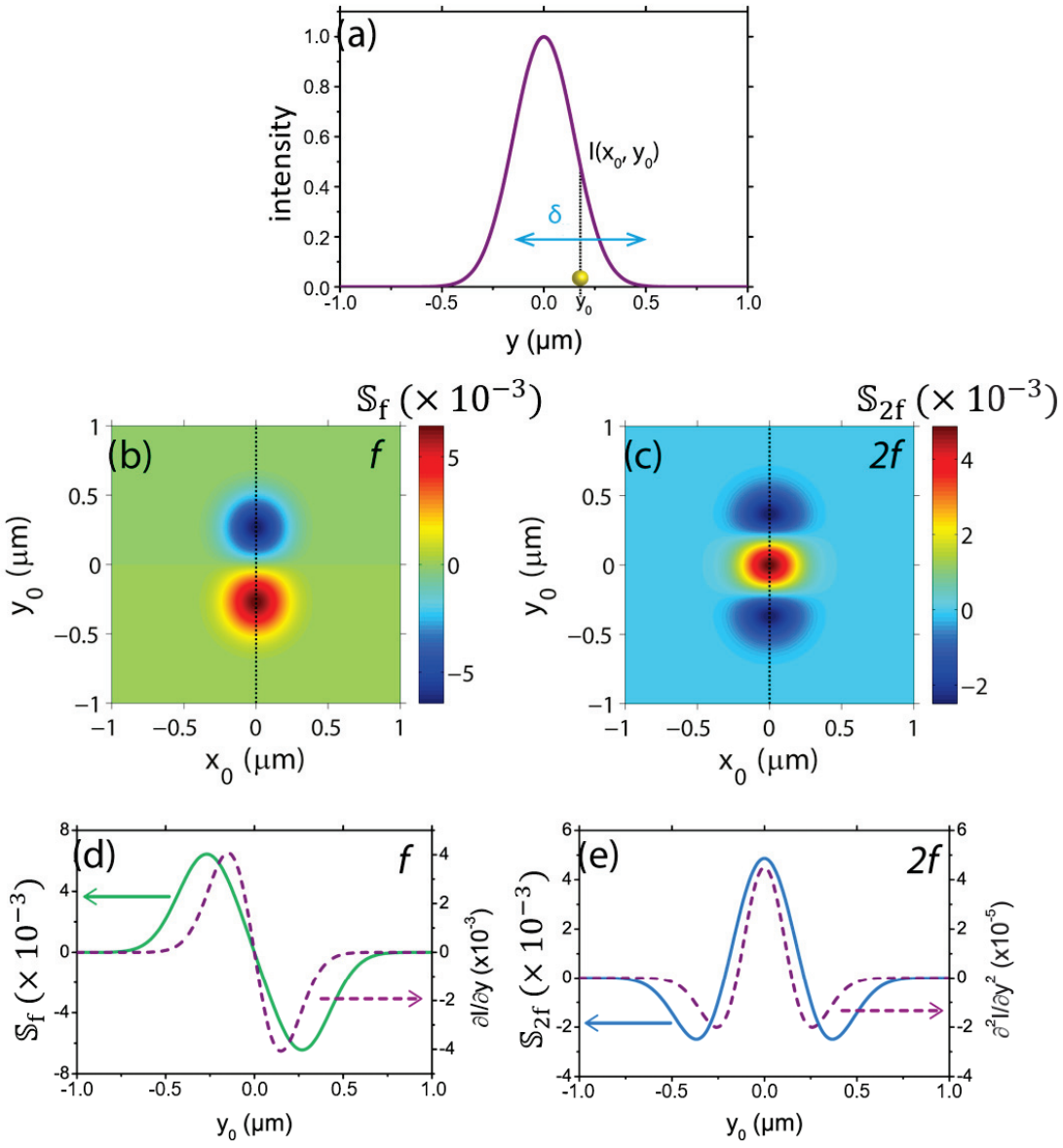

Figure 1.15: (a) Gaussian intensity profile ($FWHM$=370 nm) and spatially modulated nanoparticle (δ=325 nm and $\sigma_{ext} = 10^3$ nm^2). SMS signal simulated at f (b) and $2f$ (c) for 1×1 µm^2 scan of a nanoparticle located at $(x_0, y_0) = (0, 0)$. SMS signal profiles along the vibration direction (solid lines) at f (d) and $2f$ (e). A comparison with the first and second derivatives of the Gaussian beam (dashed lines) shows that a broadening appears when the amplitude of oscillation δ is not negligible as compared to the $FWHM$.

ABSOLUTE EXTINCTION CROSS-SECTION MEASUREMENT

The maximal signal amplitude $\mathbb{S}_{2f}(x_0, y_0)$ can be optimized by varying w and δ. For a particle in the center of the Gaussian beam $(x_0, y_0) = (0, 0)$, the analytical solution of Eq. (1.49) writes as

$$\mathbb{S}_{2f}(0,0) = \sigma_{ext} \cdot \frac{2}{w^2}\, b_{j1}\left(\frac{\delta^2}{w^2}\right) \exp\left(-\frac{\delta^2}{w^2}\right) = \sigma_{ext} \cdot R_{2f}(\delta, w)\,, \tag{1.50}$$

where b_{j1} is the modified Bessel function of first kind and first order. The proportionality coefficient R_{2f} relating the raw SMS signal $\mathbb{S}_{2f}$ to the absolute extinction cross-section σ_{ext} is completely determined by the Gaussian beam waist w (or $FWHM$) and the vibrational amplitude δ (experimentally tunable parameter). Fig. (1.16) shows the effect of δ and $FWHM$ on R_{2f}. Note that it exists an optimal oscillating amplitude maximizing R_{2f}, occurring at about $\delta \sim FWHM$.

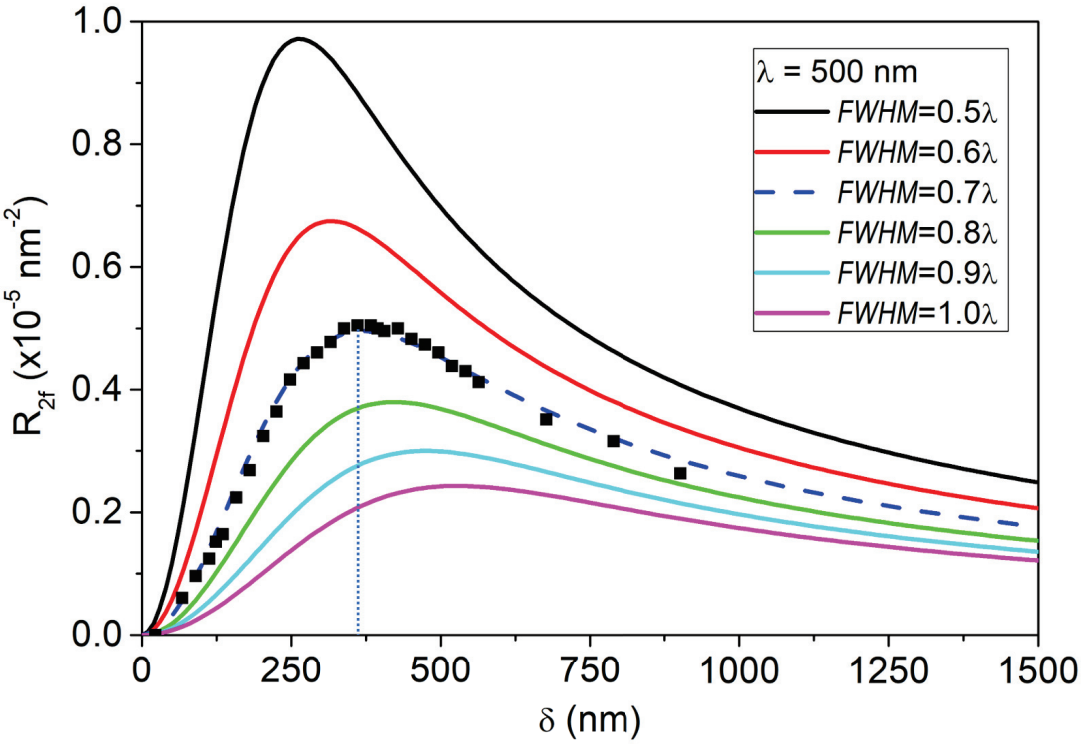

Figure 1.16: R_{2f} as a function of the oscillation amplitude δ. Different curves correspond to different focal spot sizes at fixed wavelength $\lambda = 500\,\text{nm}$. Black squares are the normalized experimental $\mathbb{S}_{2f}(0,0)$ values for a small gold nanoparticle (diameter 30 nm) illuminated by a beam of $\lambda = 500\,\text{nm}$ and $FWHM = 0.7\lambda \approx 350\,\text{nm}$ for different modulation amplitudes δ ($f = 1500\,\text{Hz}$). Under these conditions the experimental signal is maximized by $\delta \approx 350\,\text{nm}$ (dotted line).

EXPERIMENTAL SETUP

The SMS microscope setup, used in the work of Chapter 3, has been introduced in Fig. (1.14). In standard conditions, it consists of apochromatic objectives of high magnification $100\times$ and numerical aperture $N.A.=0.75$ which focus and recollect a tunable laser beam on an individual nanoparticle deposited on a substrate. Using a piezo shaker, the sample is forced to oscillate along the y direction, typically with frequency $f=1500\,\mathrm{Hz}$ and amplitude $\delta=325\,\mathrm{nm}$. A second piezo is employed to perform XYZ movements, allowing to move single nano-objects within the beam focus and realize sample cartographies of $100\times100\,\mu\mathrm{m}$ range.
The beam $FWHM$ can be directly measured considering a linecut along x of the SMS signal map, as the modulation is absent along this direction, and thus, the signal x profile will reproduce the beam intensity profile, accordingly to Eq. (1.42). It exhibits an Airy intensity profile close to the diffraction limit

$$FWHM=\frac{0.515}{N.A.}\,\lambda\approx 0.7\,\lambda$$

similar, in first approximation, to a Gaussian profile (see Appendix (A)). However, in all the reported experiments, the solution of the integral of Eq. (1.49), that for a Gaussian spot yields the analytical expression of Eq. (1.50), has been numerically computed for the Airy profile in order to obtain a more accurate conversion from SMS raw signal to absolute extinction cross-section.
In the following chapter it will be presented in detail the developments of the SMS microscope setup that were necessary to realize high-pressure measurements.

Chapter 2

Optics of a single metal nano-object under high pressure

Up to now, nanoparticle properties alterations as a function of the pressure have been studied only in ensemble experiments [43, 44, 45]. However, in order to obtain more reliable and meaningful results, an individual nano-object characterization is required. In this context, a setup to analyze single nano-objects under extreme conditions has been conceived, implemented and improved. This new apparatus is tailored not only to investigate optical properties modifications of metal nanoparticles under high pressure, but can also be used in other contexts (e.g. to study the evolution and collapse of an isolated carbon nano-tube (CNT)). In this chapter are firstly described all the steps necessary to realize and characterize the optical microscopy measurements on individual nanostructures under high pressure. Afterwards, the main experimental results obtained on a single elongated gold nanoparticle, as well as the modeling studies are reported.
Such a setup is based on the SMS technique combined with a diamond anvil cell (here abbreviated to the acronym "DAC"), a device that makes possible the generation of a hydrostatatic high-pressure environment around the sample. These are domains of expertise of our FemtoNanoOptics group, and of the group of prof. A. San Miguel at iLM, in collaboration with whom this work has been realized.

2.1 High-pressure microscopy setup

The setup for optical characterization on individual nanostructures under high pressure is based on the SMS technique which allows to locate a single nano-object and study its optical properties, such as the extinction cross-section, as a function of wavelength and polarization (see Section 1.4.2 of Chapter 1). Moreover, it exploits the diamond anvil cell, a structure that permits the generation

of a uniform and controlled high-pressure surrounding. As we are interested in a setup designed to investigate an individual nanostructure under high pressure, the combination of these two experimental methods is required. The far-field nature of the SMS technique is suitable for the adaptation of a DAC, but two relevant and challenging problems were encountered (and solved) during the setup realization: optical focusing of the beam and mechanical vibration of the DAC.

2.1.1 Generalities on the diamond anvil cell (DAC)

The DAC is a high-pressure apparatus consisting of two opposing diamonds with a sample compressed between two plane surfaces, the polished culets (diamond tips). This enables the compression of sub-millimeter sized samples to extreme pressures, typically around 100 GPa, although pressures close to 800 GPa can be reached [46, 47]. An example of laser-heated DAC device is shown in Fig. (2.1). The combination of high pressure and high temperature (generated by IR lasers penetrating the diamonds) has allowed the simulation of the planetary interiors, [48, 49, 50] the discovery of new structures and phases in elements and the synthesis of novel hard materials [51, 52]. What makes the DAC so suitable is that the

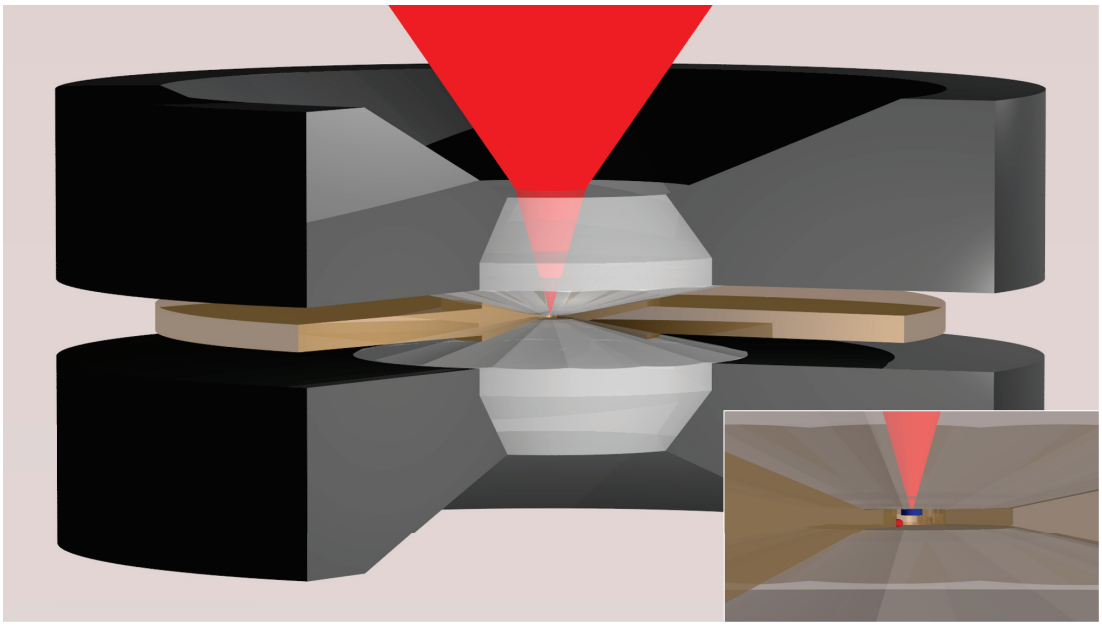

Figure 2.1: Schematic of a DAC. The object under investigation (blue disk in the center of the inset) is surrounded by a pressure medium, contained by a metallic gasket (yellowish), and heated with an IR laser. The fluorescence (excited by a blue or green laser light) from a small ruby ball (red sphere) located in the unheated part of the pressure chamber is used for pressure measurement.

new materials can be identified and characterized in situ. Remarkable examples includes the non-molecular ice X, [53] polymeric nitrogen, [54] metallic phases of xenon, [55] and potentially hydrogen [56].

In a DAC, two diamond anvils are used to compress the pressure chamber (a sub-millimeter thickness metallic gasket with a hole drilled in its center by spark erosion [57]). Diamonds have a truncated conical shape with large external surfaces typically 3-4 mm in diameter, 16 facets, with 1/8 to 1/3 carat weight and cost about $1000. The diamond culets face each other, and must be polished and perfectly parallel in order to produce uniform pressure and to prevent dangerous strains. For this reason a proper alignment must be accomplished, procedure based on the removal of Newton interference fringes produced by the relative tilt of the anvils [57].
In order to bring the diamonds closer, an external force-generating device must be introduced. This can rely on a lever arm, tightening screws, pneumatic or hydraulic pressure applied to a membrane [57]. In all cases the force is uniaxial and is applied to the external sides of the two diamond anvils. The operation of DAC is based on the principle $p = F/A$ where p is the pressure, F the applied force and A the area. Typical culet sizes for diamond anvils are 100–400 µm, such that a very high pressure is achieved by applying a moderate force on the much larger external diamond surfaces. Diamond is a very hard and virtually incompressible material even at high temperatures [58] and thus it minimizes the deformation and breakup of the apparatus.
The pressure chamber contains a pressure-transmitting medium (abbreviated with "PTM"), a high-pressure sensor and the object under investigation. The uniaxial pressure provided by the DAC may be transformed into uniform hydrostatic pressure using a fluid PTM, such as helium, neon, argon, nitrogen, paraffin oil or a mixture of methanol and ethanol [59]. The PTM must be chemically inert, as to not interact with the sample and must be stable under high pressures, in order to stay hydrostatic and ensure uniform compressibility of the sample. If the sample is heated with a laser, the PTM should not absorb the laser radiation and should have low thermal conductivity in order to keep the temperature constant (diamond anvils possess high thermal conductivity). In this case, ideal PTM are noble gases.
Pressure are measured by a high-pressure sensor, a reference material whose behavior under high pressure is known. This can be a structurally simple material with a known equation of state, such as copper or platinum, monitored by X-ray diffraction [60] or an unheated ruby ball, where its fluorescence lines are tracked [61, 62]. More details on the DAC and its alignment can be found in [57].

2.1.2 Employed diamond anvil cell and pressure handling

The DAC employed in this work, reproduced in Fig. (2.2), was conceived to allow increasing the pressure environment up to 10 GPa and to permit the optical characterization of an individual nanostructure using strongly focusing microscope objectives (magnification 100x and numerical aperture 0.7).

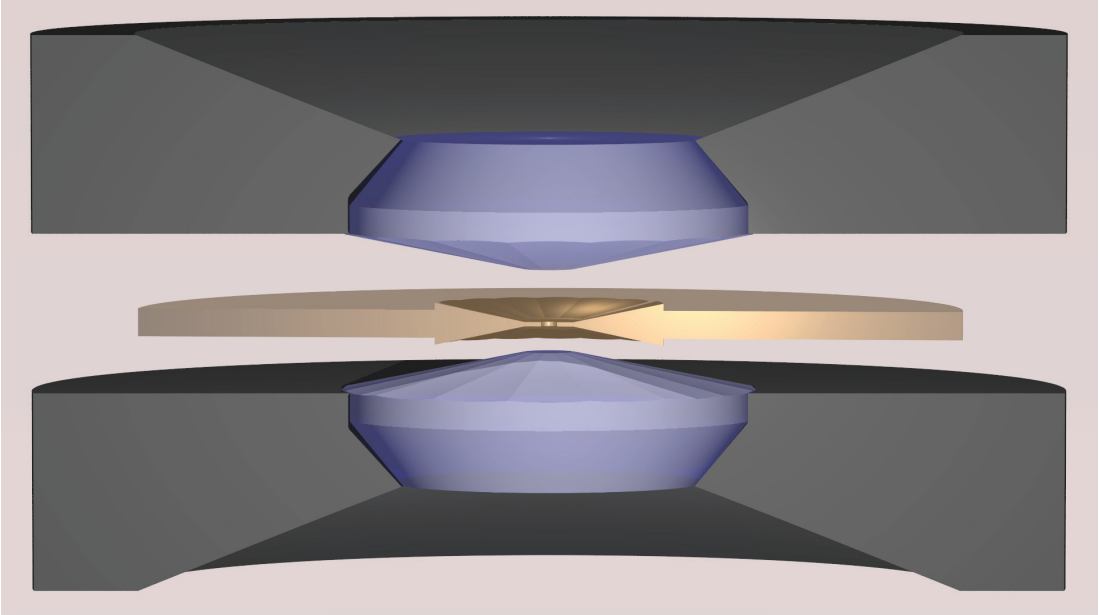

Figure 2.2: Schematic of the employed DAC. Two Boehler-Almax diamond anvils are supported by a tungsten-carbide seat and separated by a Cu-Be gasket.

The two parts are Boehler-Almax design anvils made from rough diamonds. This geometry was introduced in 2004 by R. Boehler and compared to conventional anvils offers a superior alignment stability, larger aperture, and smaller size [63]. The external diameter measures 3.30 mm, while the unpolished thickness is 1.44 mm, the smallest available. A small diamonds thickness is required in optical microscopy to minimize beam absorption. In order to produce the culets, they are polished following the [100] crystal orientation for the highest strength, which allows to tolerate a maximal pressure of 50 GPa. The culet has no bavels and measure 0.4 mm in diameter, with a thickness after polishing of 1.385 mm. The anvils geometry is reproduced in Fig. (2.3).
The two diamonds differ in quality: the upper one is a type IIas (~ 1 ppm of nitrogen defects), while the lower one is a type Ia ($\sim 2\times10^3$ ppm of nitrogen defects). The upper diamond must be purer because the excitation of the sample and the corresponding optical processes (Raman spectroscopy, fluorescence, SMS) sensitively dependent on the quality of the exciting beam. Another difference consists in a more accurate polishing necessary on the upper diamond culet to remove

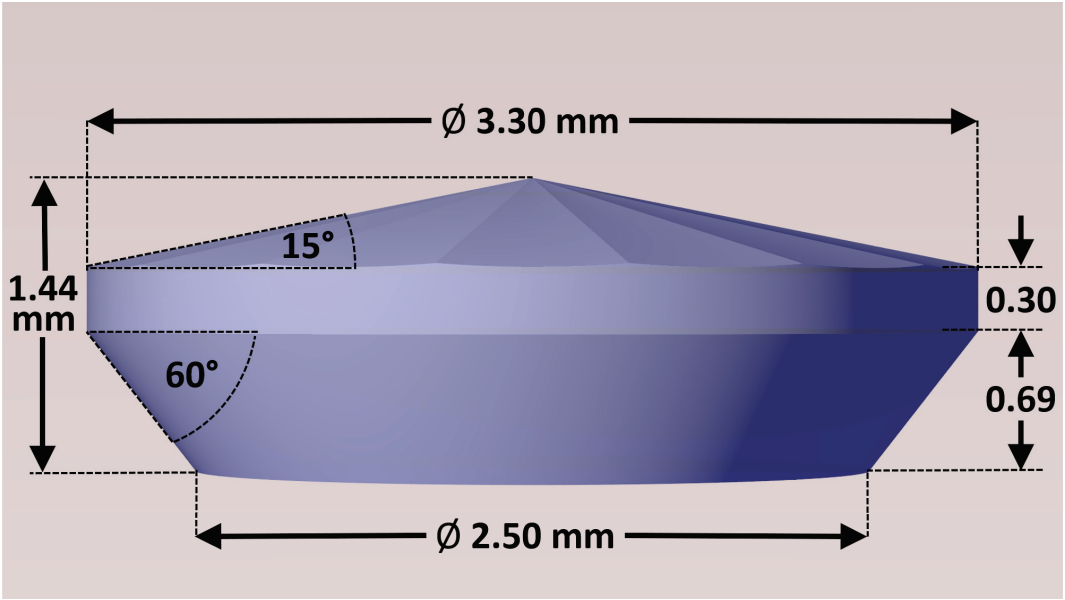

Figure 2.3: Boehler-Almax geometry has high conical aperture and low thickness, valuable features to realize a microscopy system. In this picture the diamond tip is still uncut. The reported length are measured in mm.

nano-scratches that can emerge during a long testing period. Those nano-flaws were extending a few tens nanometers into the diamond and were identified by looking at the secondary electrons of a scanning electron microscope (SEM), as one can see in Fig. (2.4). Their effect was a slight, but intolerable modification of the SMS signal from an individual nanoparticle. The practical result of this polishing is a newfound thickness of 1.385 mm for the upper anvil.

The external thickness of each anvils is glued to tungsten-carbide seats with large aperture (85°) allowing optical spectroscopy measurements (as well as X-ray diffraction). A stretchy membrane, screwed on the external support of the superior diamond, pushes down the upper diamond by swelling up. This process is reversible and controlled by a pneumatic inflator that pumps helium towards the membrane. An example of how the external membrane pressure influences the sample chamber pressure is illustrated in Fig. (2.5). Note that the pressure within the chamber is about 10^3 times higher than the external pressure applied with the inflator.

A pierced Cu-Be gasket is placed in between the diamonds. The Cu-Be alloy was preferred to other stiffer material like steel, because, although it can stand relatively modest pressures (up to 10 GPa), its malleability permits to seal the DAC at very low pressures (in practice, to characterize the sample at 0 GPa). To

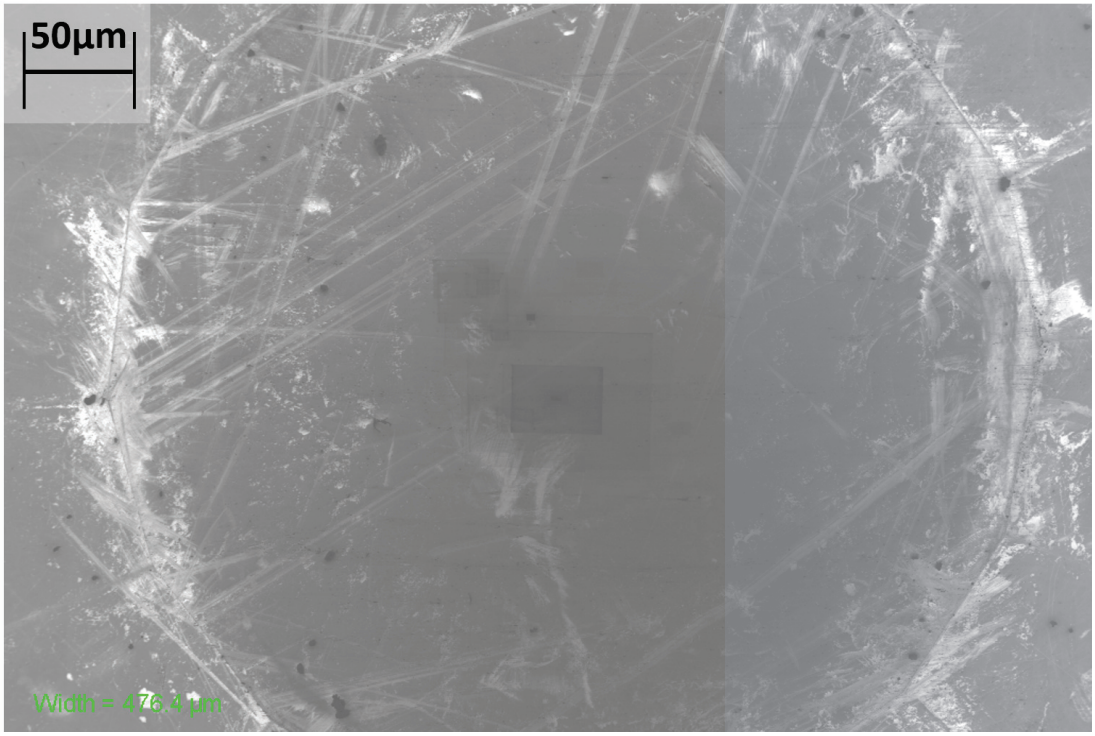

Figure 2.4: Secondary electron SEM scan realized on the upper diamond culet. Nano-scratches deep a few tens of nanometers are visible.

avoid leaking at high pressure the gasket hole must be drilled regular and circular. On the other hand, in order to avoid leaking at very low pressure, seems to be essential the removal of debris around the perforation by acetone. Before drilling the hole, the Cu-Be plate must be indented using the DAC. This allows to choose the starting thickness for the pressure chamber and to make the gaskets perfectly fit the space between the anvils. The real hole is drilled in the center of this indentation by spark erosion, and its diameter will be determined by the size of the tip used. Typical sample space is given by the gasket thickness (typically 50 µm) and the central hole diameter (routinely 130 µm). The chamber thickness is selected on the basis of the sample and sensor size and of the maximal pressure desired, while the diameter should be around the 30-50% of the culet extension for avoiding leaking and leaving enough space for the sample. It is vital that the chamber thickness remains always larger than the pressure sensor, otherwise an uniaxial pressure is applied on the sensor giving falsified results.

In case one wants to work with nano-objects deposited on a diamond substrate, they can be deposited on one of the anvil culets via spin-coating method. It is preferable to use the upper diamond, because optical modeling as well as ex-

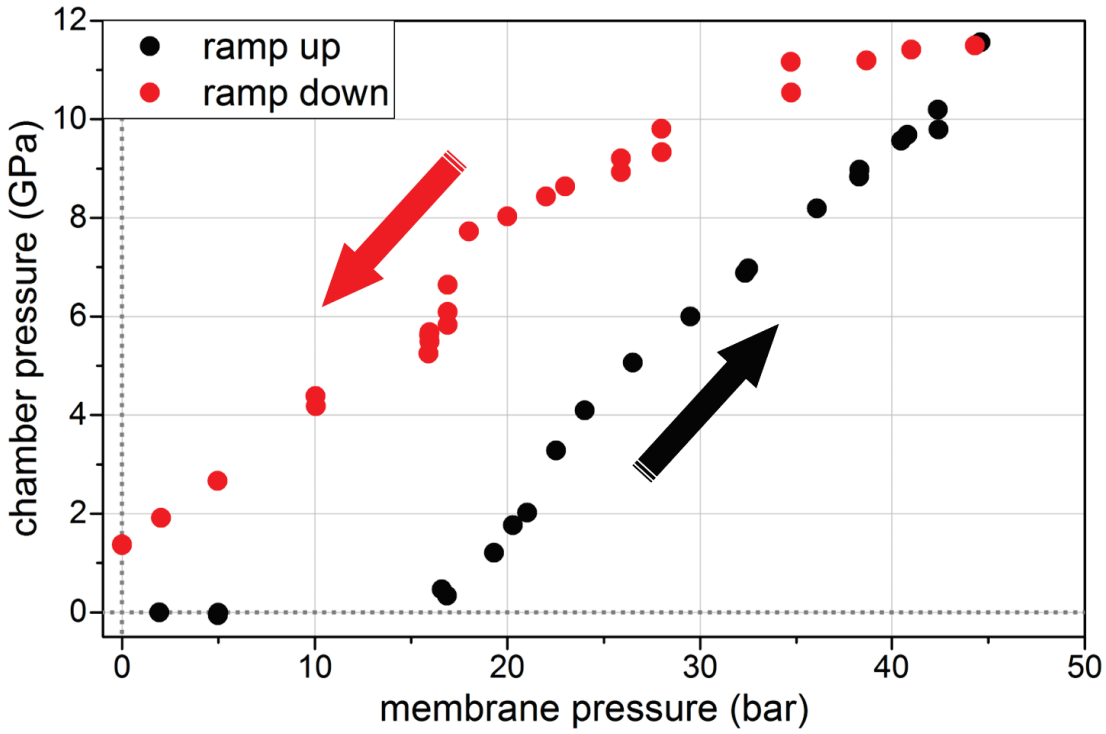

Figure 2.5: Typical external-internal pressure plot, highlighting a strong hysteresis.

perimental calibrations are more reliable. Since diamond surfaces are naturally lipophilic and hydrophobic, it is important to gently clean the culets before realize the spin-coating. This can be done using an optical paper soaked in methanol (the acetone is to avoid because it dissolves the glue that keep the diamond attached to the seat). Alternatively, one can introduce in the pressure chamber an external substrate with nanostructures on it. This enables to change the substrate material provided that it supports the high pressure and also to realize electron microscopy measurements on the sample before and after the experiment. Diamond or silica substrates with a few µm of thickness are currently in phase of realization (by A. San Miguel group and our collaborator L. Marty in Grenoble at Institut NÉEL).

The PTM composition is 4Me:1Et, an alcoholic and transparent mixture which remains quasi-hydrostatic until 10.4 GPa, where the solidification, displayed in Fig. (2.6), occurs [64]. This liquid is volatile, therefore it must be added quickly before sealing the DAC. In order to avoid air bubbles formation inside the pressure chamber it is useful to prepare the PTM a few hours earlier, letting it some time to rest; filling the chamber with one droplet that should be gently deposed on the gasket beside its hole, instead of make it fall directly into it; closing the cell in a smooth and continuous manner, without low-and-overs.

The pressure inside the cell is directly measurable by the ruby fluorescence method (see the end of the section), introducing in the pressure chamber one or several spherical ruby balls with diameter typically below 10 µm. To avoid contaminations, the ruby balls should be placed on the anvil culet without the sample. As shown in Fig. (2.6), the ruby balls should preferably be placed close to the gasket edge in order be far from the center of the sample. Even if ruby and nano-objects are placed on different culets, but are not well separated in the XY direction, a distortion in the SMS signal will occur. Once one adds the PTM droplet to fill the chamber, the nano-objects are not moving due to van der Waals forces, whereas the ruby balls are easily dragged away. To avoid this, it is extremely useful to introduce a first PTM droplet on the cleaned culet, then adding the rubies on this wet surface and immediately after them adding a new PTM droplet on it. With this procedure the chances of a successful sealing are much higher.

Closing the DAC produces a typical pressurization of $0.02 - 0.05$ GPa. In order to measure this starting pressure, it is essential to measure the reference ruby flu-

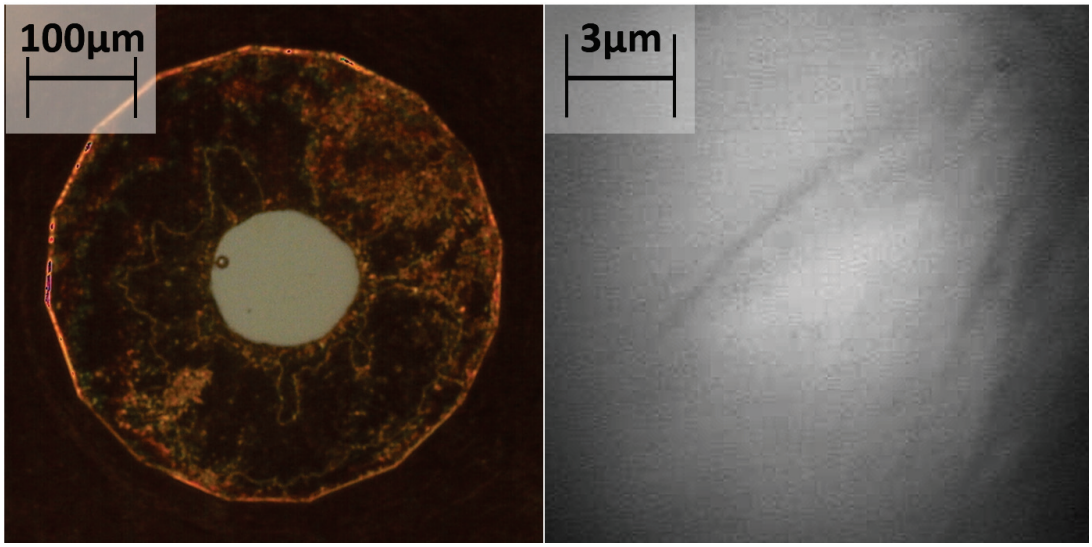

Figure 2.6: Left: microscope image of a Cu-Be gasket indentation after a high-pressure experiment. The shape of the hole is dangerously asymmetrical. Close to its left edge it is possible to recognize the ruby ball used as pressure probe. Right: a TV screen capture of a culet portion taken during an experiment. The picture outlines the appearance of crystals in the PTM by increasing the pressure. The phenomenon, called vitrification, is caused by an excessive pressure or by the presence of impurities in the PTM. In the reported case an incorrect ratio in the PTM preparation was the origin (1Me:1Et rather than 4Me:1Et), decreasing the solidification pressure from 10.4 to about 8 GPa.

orescence with the DAC open ($1\,\mathrm{Atm} \approx 1\,\mathrm{bar} \approx 10^{-4}\,\mathrm{GPa} \sim 0\,\mathrm{GPa}$), before or after the experiment [1]. This starting value can be stabilized by swelling the membrane a little (usually introducing a quantity of He generating 4 bars of pressure into the membrane and a pressure of the order of 0.05 GPa inside the chamber). In this low-pressure configuration the DAC may be affected by a slow leaking which empties the chamber in a few hours. For this reason the time available for the low pressure measurement is limited. However, once the pressure approaches 0.5 GPa (applying 15 bars into the membrane), the apparatus becomes very stable and it can remain pressurized for days. This steadiness persists at high pressure, until the vitrification of the 4Me:1Et. In this regime of pressure close to 10 GPa (40−45 bar in the membrane) there is a high risk of leaking due to an asymmetrical deformation of the gasket hole. Consequently, it is useful to have an optical system which permits to monitor the gasket shape and thickness during the experiment (in addition, measuring the gasket thickness allows to verify that the ruby ball is not crushed between the two approaching anvils).
The pressure can be released by gently emptying the membrane. In this phase the pressurization is stable, permitting experiments to investigate reversibility. Unfortunately, going back to the initial pressure is not possible because of a considerable hysteresis in the relation between the applied load (membrane) and the pressure obtained. An example of the phenomenon is reported in Fig. (2.5). The residual pressure is usually around 1−2 GPa, is stable, and mainly depends on the starting Cu-Be gasket thickness and on the maximal pressure reached.
In order to monitor the gasket behavior during the experiment, images of the pressure chamber at different spatial coordinates must be acquired. In the setup, the DAC is mounted on a XYZ piezo nanopositioning stage, with a close loop travel of 100×100×100 µm, a close loop resolution of 0.8 nm due to capacitive integrated sensors [2]. The piezo stage, in turn, is placed on a manual XY micrometer stage for coarser movements. To monitor the gasket, the DAC must be moved under a focusing objective, which focuses an incoherent white light in the pressure chamber, passing through the upper diamond anvil. When the focal plane falls on an internal surface, like the gasket or a culet plateau, the backscattered light is recollected by the same objective and redirected to a CCD camera, reproducing the image of the sample plane on a TV screen. A schematic of the setup is displayed in Fig. (2.7).
In Fig. (2.8) the culet surfaces has been fully imaged by joining several TV screen captures along the whole XY range of the piezo stage. In Fig. (2.6) is shown a microscope image of a gasket indentation after an experiment. The shape of the hole

[1] Ruby fluorescence characterization in air should be accomplished in every experiment, since every ball show a slightly different fluorescence spectrum.

[2] The piezo stage is not essential in this monitoring phase, but is useful in maximizing the fluorescence signal from the ruby ball and essential in localizing and studing single nano-objects.

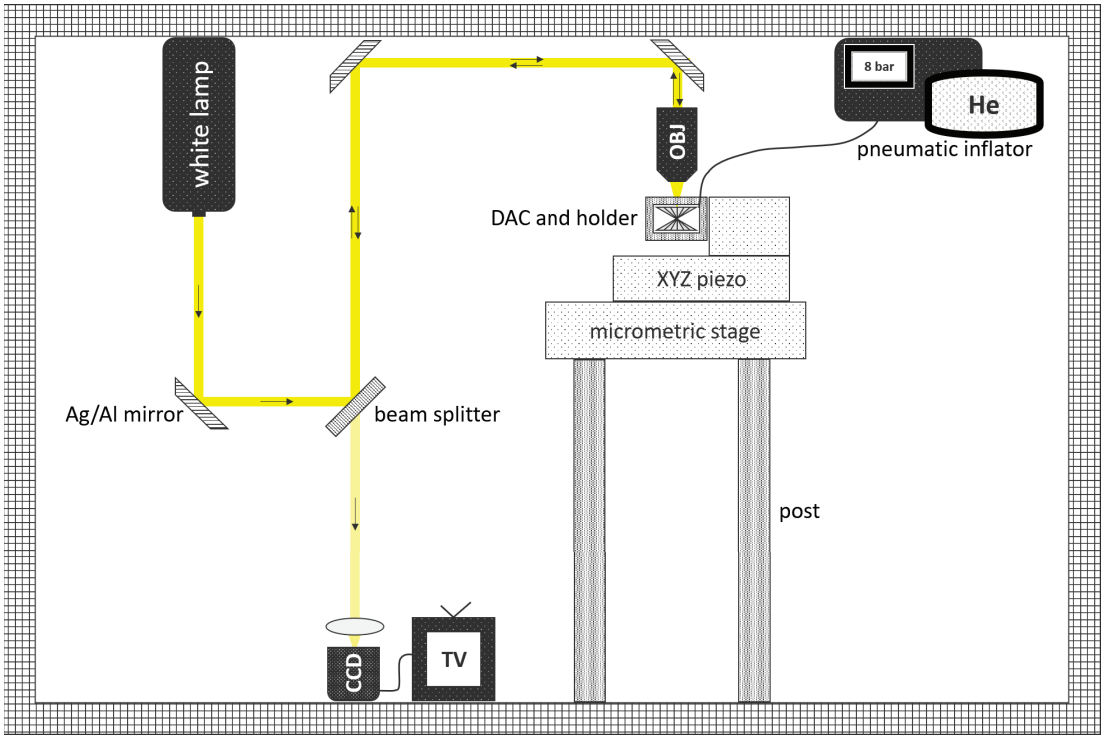

Figure 2.7: "Culet imaging setup" (front view of the setup, the instruments lying on the optical table): the white light is focused on a diamond culet by an objective; the backscattered light is detected by a CCD camera connected to a TV screen.

appears asymmetrical, which indicates that a higher pressure may have induced the breakdown. By this imaging, one can check the surface state before and after nanoparticles deposition, verify the vitrification absence of Fig. (2.6), the circular shape of the gasket, measure its diameter along the X and Y directions by moving the micrometric screws, as well as its thickness by looking at the Z coordinates corresponding to the two culets well-focused.

Typically, until 3 GPa, the gasket evolution consists in an initial diameter decrease. This is due to the malleability of the Cu-Be, forced to penetrate into the chamber. Beyond this point, the pressure inside the hole is enough to cause an overall increase in diameter. During this widening, it is important to check the integrity and the shape of the gasket: an excessive asymmetry induces a structural weakening and a subsequent leaking. An example of gasket evolution until its breakdown, occurred at 6 GPa, is shown in Fig. (2.9). With the pressure rising, the chamber thickness experiences a linear reduction until the breakdown, where it keeps dropping despite the internal pressure remains constant. Therefore, it is important to monitor the gap between the culets and release the pressure before

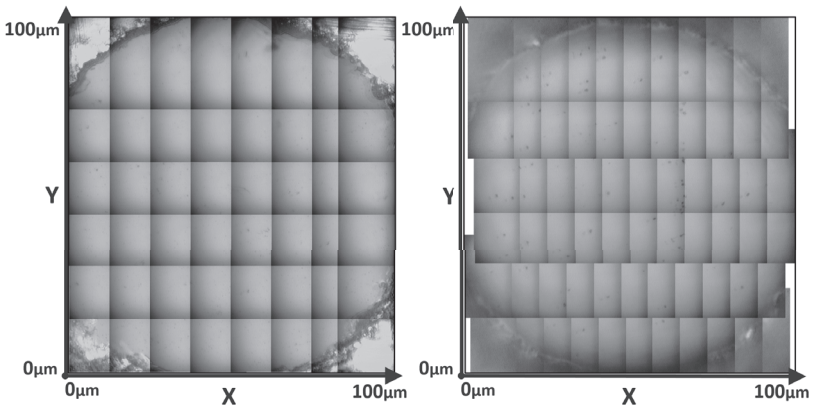

Figure 2.8: Collages of TV screen captures reproducing the upper culet (on the left) and the lower culet (on the right). Every rectangle correspond to a screen capture. The small grey spots appearing on the surfaces are microdusts or big nanoclusters introduced during the ruby ball placement, the DAC sealing and the spin-coating process. These particles are very stable and can be exploited to orientate on the surfaces. The bright rounded border that covers the upper culet (left) corresponds to the superior part of the gasket reflecting the white light, while the circular shadow that blots out the lower culet (right) represents the bottom of the gasket obstructing the light path.

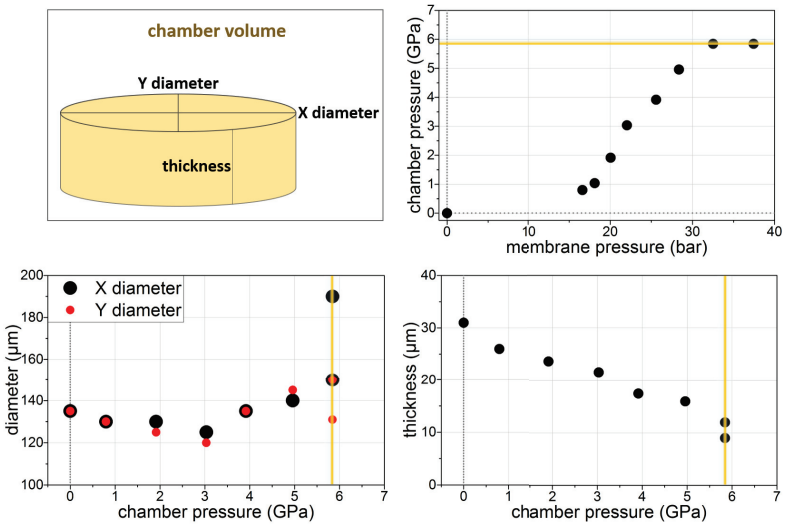

Figure 2.9: Example of gasket deformation until its breakdown. In the ideal case (no breakdown), the chamber pressure is supposed to increase linearly with the external load (membrane pressure); the diameter should grow slowly beyond 3 GPa; the thickness should decrease linearly. Here all the trends are suddenly interrupted around 6 GPa.

the breakdown occurs. In this phase, the gasket does not change significantly its dimension, although a modest decrease in thickness could be noticed. Consequently, a new pressure ramp up with the same gasket can not reach the same high pressures anymore. The gasket should be replaced after a high-pressure cycle.

In order to measure the chamber pressure a ruby fluorescence calibration system must be implemented. As illustrated in Fig. (2.10), its essential elements are

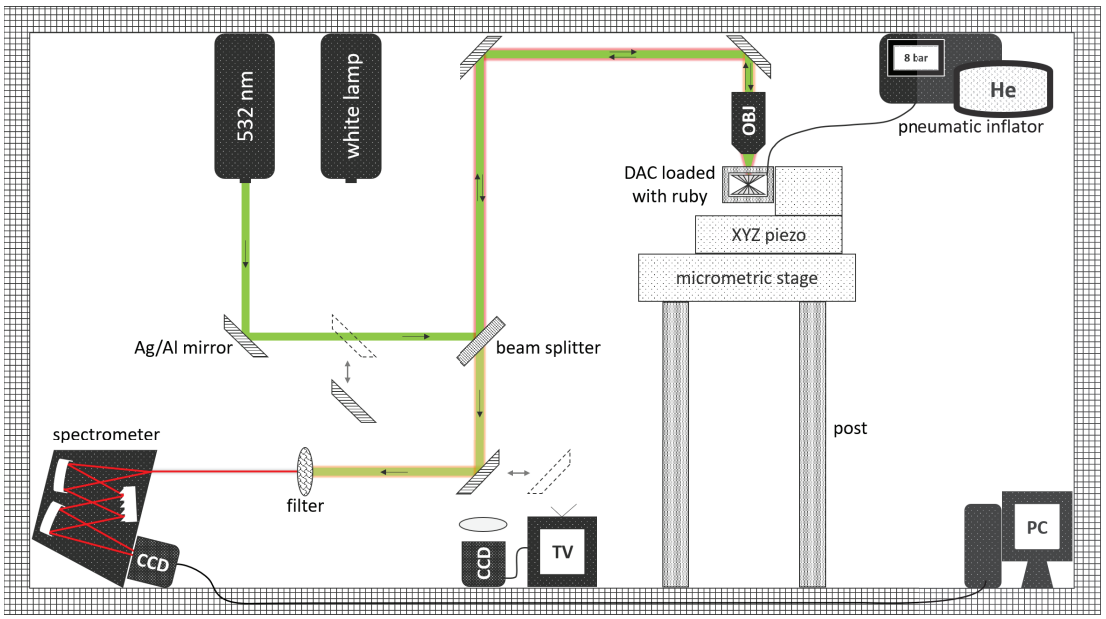

Figure 2.10: "Ruby luminescence setup": a monochromatic green laser is focused on a ruby ball placed on a diamond culet; the yielded fluorescence (red line), filtered from the backscattered green light by a long-pass filter, is analyzed with a spectrometer. Translating a pair of mirrors allows to quickly recovered the "culet imaging setup" of Fig. (2.7).

a laser source to excite the fluorescent radiation and a spectrometer for spectral analysis. The exciting light is generated by a 531.92 nm continuous wave solid state laser (Nd:YAG doubled), with a full output power of 50 mW. The use of a long working-length objective is essential to focus the laser on a micron size spot within the pressure chamber, after passing through the diamond anvil [66]. The excited fluorescent radiation is collected by the same objective and separated from the backscattered laser light introducing a 532 nm ultrasteep long-pass edge filter. In this way a spectrometer can be used to detect the fluorescence signal. The spectrometer is a Horiba *i*HR320 with a grating of 1800 grooves and blazed wavelength of 400 nm. The pressure determination requires the measurement of the fluorescence spectrum at ambient pressure (~ 0 GPa) and at high pressure.

The correlation of the measured wavelength shift $\Delta\lambda$ (or frequency change $\Delta\nu$) with applied pressure is the basis for pressure determination.

The ruby, Cr^{3+} doped α-Al_2O_3, is a well established high-pressure sensor and does not undergo phase transitions up to 100 GPa. Suitable ruby balls contain $3000 - 5500$ ppm of Cr^{3+} and are around 10 µm in diameter. Ruby fluorescence under blue-green excitation is dominated by an intense doublet with sharp band components centered at 694.2 nm (14402 cm^{-1}) and 692.8 nm (14432 cm^{-1}), respectively named R1 and R2 line [57, 67, 68]. The lines exhibit a pronounced redshift with the applied pressure, making the ruby fluorescence a good pressure gauge. Barnett (1973) and Piermarini (1975) calibrated the wavelength shift through the Decker equation of state of the NaCl up to 20 GPa and found a linear pressure dependency given by

$$\frac{\Delta\lambda}{\Delta P} = 0.365\,\frac{\text{nm}}{\text{GPa}}. \tag{2.1}$$

Later, Mao (1978, 1986) and Bell (1986) improved this result by a calibration through the equation of state of several metals under quasi-hydrostatic and non-

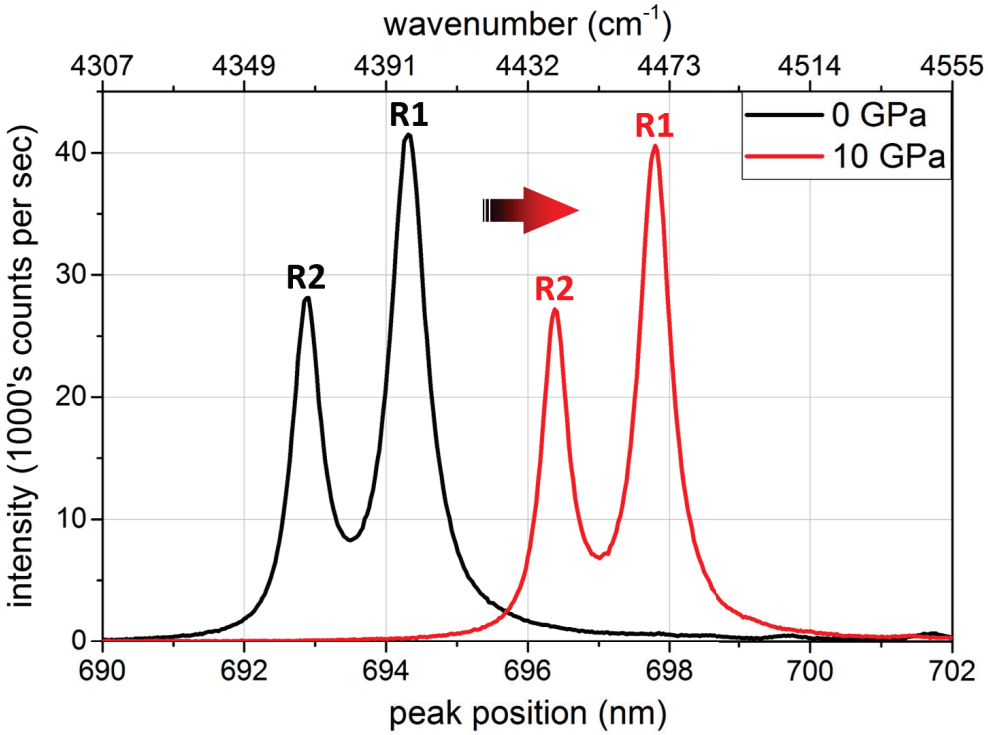

Figure 2.11: Typical response of a ruby ball observed in the setup. The process is exploited for pressure measurements using Eq. (2.2). On the top axis the frequency shift from the 532 nm carrier is indicated.

hydrostatic pressure condition up to 180 GPa and, for the R1 line, found the empirical quasi-linear relation

$$P = \frac{A}{B}\left[\left(\frac{\lambda}{\lambda_0}\right)^B - 1\right], \tag{2.2}$$

where $A = 1904$ and $B = 7.665$ for quasi-hydrostatic and $B = 5$ for non-hydrostatic conditions. The incertitude on the calibration introduces an error on the pressure of $4\% \times P$ [69]. An example of the ruby's fluorescence evolution with the pressure is reported in Fig. (2.11). To extract the R1 line position a double-Lorentzian fit should be performed.

As shown in Fig. (2.12), the R1-R2 lines splitting remains almost constant in a hydrostatic pressure environment. It was found that the R1 line shifts remarkably in a non-hydrostatic environment, while the R2 line shifts negligibly [70, 71]. Furthermore, the widths of the fluorescence lines increase with increasing non-hydrostaticity [61, 65]. Therefore the R1-R2 line separation and their linewidths can be monitored to verify the hydrostaticity of the pressure environment.
The ruby lines positions are however influenced by the temperature. Specifically,

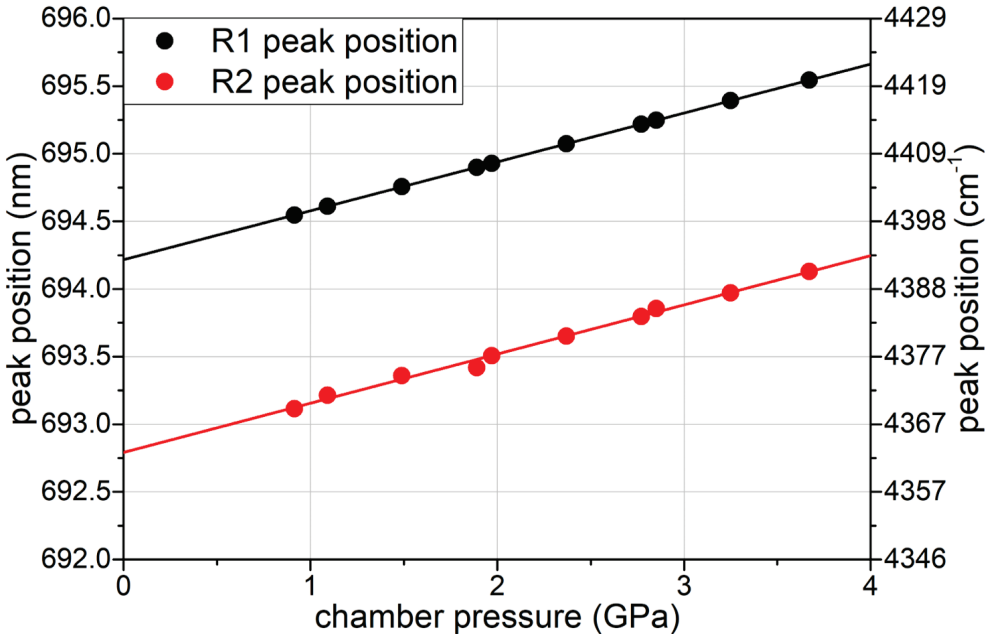

Figure 2.12: R1-R2 lines quasi-linear shifts observed in the setup. The continuous lines are fits of the experimental points. At ambient pressure, the R1-R2 lines are located at 694.2 nm and 692.8 nm respectively. The pressure dependency is in accordance with Eq. (2.1) and the distance between the lines remains constant with the pressure ($1.42\,\text{nm} = 29.46\,\text{cm}^{-1}$), indicating a hydrostatic environment.

the R1 line follows the empirical third-order polynomial [72, 73]:

$$\Delta\lambda = 6.591\times10^{-3}\,\Delta T + 7.624\times10^{-6}\,\Delta T^2 - 1.733\times10^{-8}\,\Delta T^3\,, \tag{2.3}$$

where $\Delta\lambda$ and T are expressed in nm and K respectively. By linearizing this formula to $\Delta\lambda/\Delta T \approx 6.2\times10^{-3}\,\mathrm{nm/K}$ and comparing with Eq. (2.1), it results that a temperature change of 6 K is equivalent to a pressure variation of 0.1 GPa. Therefore the heating effect due to the laser absorption in the ruby ball can be a source of systematic error in the pressure determination, mainly for powers greater than 40 mW [57], and should be minimized using low power ($\sim$1 µW in this work).

2.1.3 SMS and DAC combination: optical development

The setup for optical characterization on individual nano-objects under high pressure requires the application of the SMS technique to the DAC system mentioned above. This means: focusing at the diffraction-limit inside the DAC and kHz mechanical shaking of the whole DAC. This was achieved by carefully developing both optical and mechanical aspects.
From an optical point of view, an efficient SMS system requires a tunable laser source that must be focused on an individual nanostructure at the diffraction limit. Concerning the laser source, a mode-locked Ti:Sa laser is employed enabling quick wavelength changes in the range $680-1080\,\mathrm{nm}$ [3]. The main obstacle to focus the laser light at the diffraction limit is the presence of the diamond. This is connected to the diamond's high index of refraction of 2.4 [74, 75]. The problem can be easily explained treating the diamond as a plane-parallel plate. In case it is crossed by a collimated beam, no aberrations are introduced into the system. On the other hand, when the same parallel plate is placed in a converging or diverging beam, a series of aberrations including spherical and astigmatism are introduced. Since the SMS technique is performed with a single laser wavelength at the time (quasi-monochromatic regime), the chromatic aberration is not relevant. On the other hand, the spherical aberration shall be corrected, as discussed here.
When a plane-parallel plate is traversed by a converging beam, its focal plane is longitudinally retarded. The displacement Δz, illustrated in Fig. (2.13), is due to the change in refractive index and in the paraxial region is given by [76]:

$$\Delta p = \left[\frac{n-1}{n}\right] h\,, \tag{2.4}$$

where n is the diamond refractive index and h is the parallel plate thickness. Considering the thickness of the used top diamond anvil (1.385 mm after the pol-

[3] The use of a pulsed laser source is not relevant for the purposes of linear SMS technique. On the other hand it becomes fundamental to further implement nonlinear methods within the same setup, like the *pump&probe* technique or the second-harmonic generation.

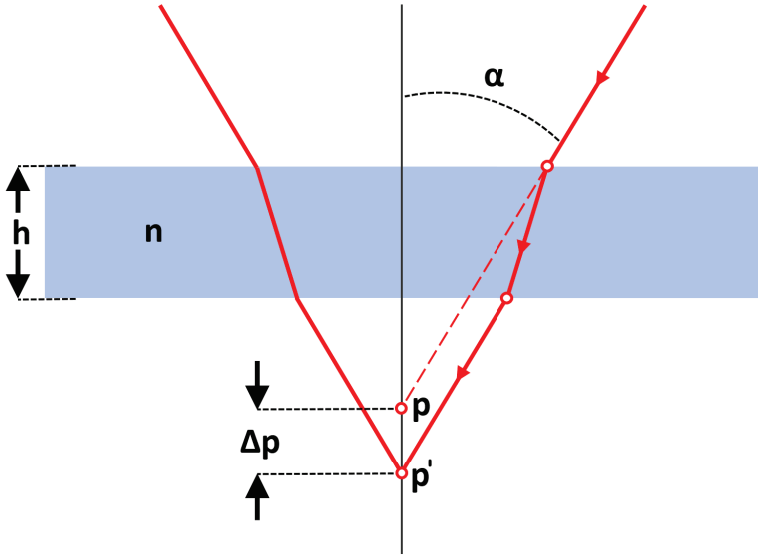

Figure 2.13: Longitudinal displacement of image by plane-parallel plate.

ishing) the longitudinal displacement measures 0.8 mm. Eq. (2.4) applies to the paraxial region only. Outside this region, a more complex relation applies [77]:

$$\Delta m = \left[1 - \sqrt{\frac{1-\sin^2\alpha}{n^2-\sin^2\alpha}}\right] h = \left[1 - \sqrt{\frac{1-N.A.^2}{n^2-N.A.^2}}\right] h\,, \tag{2.5}$$

where $N.A.$ is the numerical aperture. Assuming an objective with a numerical aperture in air of $N.A. = sin\alpha = 0.7$, Δm results 0.9 mm. Therefore, the longitudinal spherical aberration, defined as the difference between Δm and Δp, is 0.1 mm. Moreover, the blur diameter for the spherical aberration is given by [77]:

$$B_{spher} = \left[\frac{n^2-1}{32n^3N^3}\right] h\,. \tag{2.6}$$

For the considered objective, $B_{spher} = 0.029$ mm, which is too high as the necessary condition to investigate single nanoparticles by SMS is the focusing of the beam down to diffraction limit ($\leq 1\,\mu$m).
Typically, spherical aberration are compensated by using a commercial focusing objective with a correction collar. Unfortunately, for the DAC case, the aberration is too important to be adjusted in such a way, posing a considerable challenge in individual nano-object imaging. In order to overcome these aberrations a custom made pre-compensated microscope objective has been conceived on purpose for the specific diamond thickness. It was realized by Mitutoyo (Japan), it has a 100x magnification, 0.7 as numerical aperture and 30 mm working distance, high enough

to be compatible with the DAC geometry constrains.

Introducing the tunable laser source and the pre-compensated objective in the setup of Fig. (2.10) yields the "transmission SMS setup" of Fig. (2.14) that permits to implement the SMS technique and characterize the focused beam.

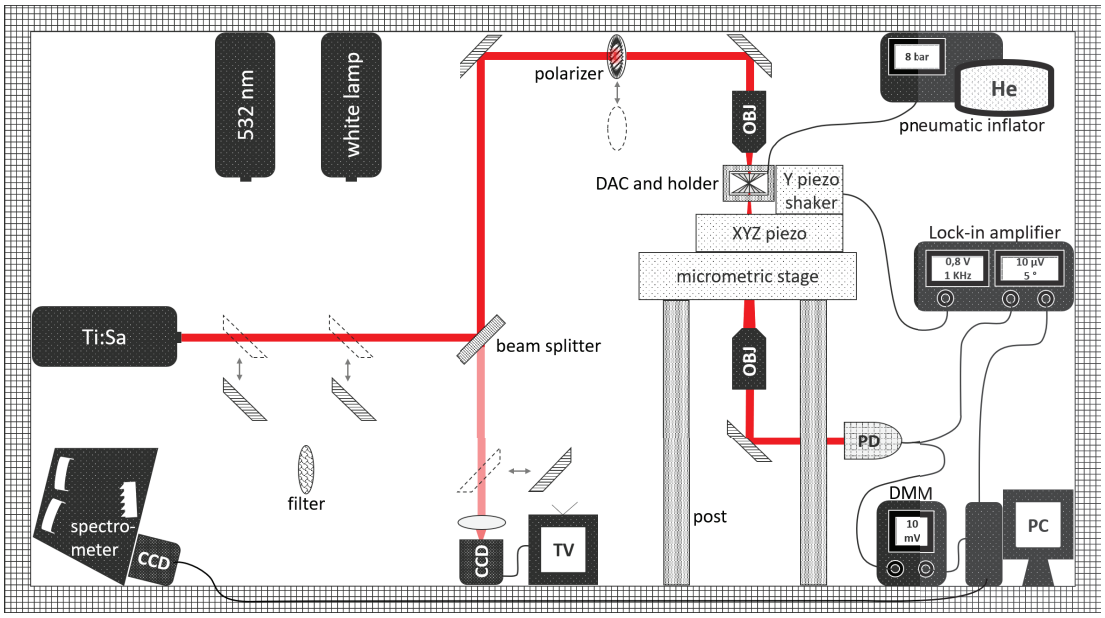

Figure 2.14: "Transmission SMS setup": a tunable laser beam is polarized and then focused into the pressure chamber through a pre-compensated objective; the DAC is forced to oscillate by a Y piezo shaker and the outcoming modulated power is detected using a lock-in amplifier. Moving a few mirrors on magnetic supports allows to quickly switch between the "transmission SMS setup", the "ruby luminescence setup" of Fig. (2.10) and the "culet imaging setup" of Fig. (2.7).

In this configuration the laser source is polarized and focused on a culet surface, where the nanostructures are typically deposed. The DAC is screwed to an aluminum holder, which in turn is fixed on an Y electric piezo shaker, mounted on the top of the XYZ piezo stage. The XYZ stage allows XY cartographies, while keeping the laser beam focused. The Y piezo shaker (with a capacitive integrated sensor) produces a sinusoidal oscillation in the nano-object Y-coordinate. In order to perform spatial modulation, amplitude and frequency of vibration are controlled by the function generator of a lock-in amplifier (LIA). After transmission through the lower anvil, the modulated transmitted light beam is detected by a silicon photodiode. The photodiode signal is read in parallel by a DMM (digital multimeter), which monitors the average transmitted power in absence of the nano-object W_0, and to the LIA, that detects the modulated transmitted power ΔW at twice the

frequency of oscillation. These two instruments are connected to a computer allowing to map the "SMS signal", proportional to the relative variation in transmitted power $\Delta W/W_0$, over the spatial XYZ coordinates. The SMS signal can be easily converted in absolute extinction cross-section σ by knowing the amplitude of oscillation and the beam shape and size. In general, the absolute extinction cross-section σ of a nano-object is a function of the light wavelength and polarization. These two parameters are controlled by the tunable laser source and by the polarizer angle. A change in wavelength slightly modifies the focal distance of the beam, but can be easily compensated with the XYZ piezo stage.
A qualitative beam characterization can be performed enlightening the CCD camera with the backreflected laser light. In Fig. (2.15) are reported two TV captures realized with a standard objective and with the pre-compensated one. Both of them have 100x magnification, 0.7 numerical aperture and 30 mm working dis-

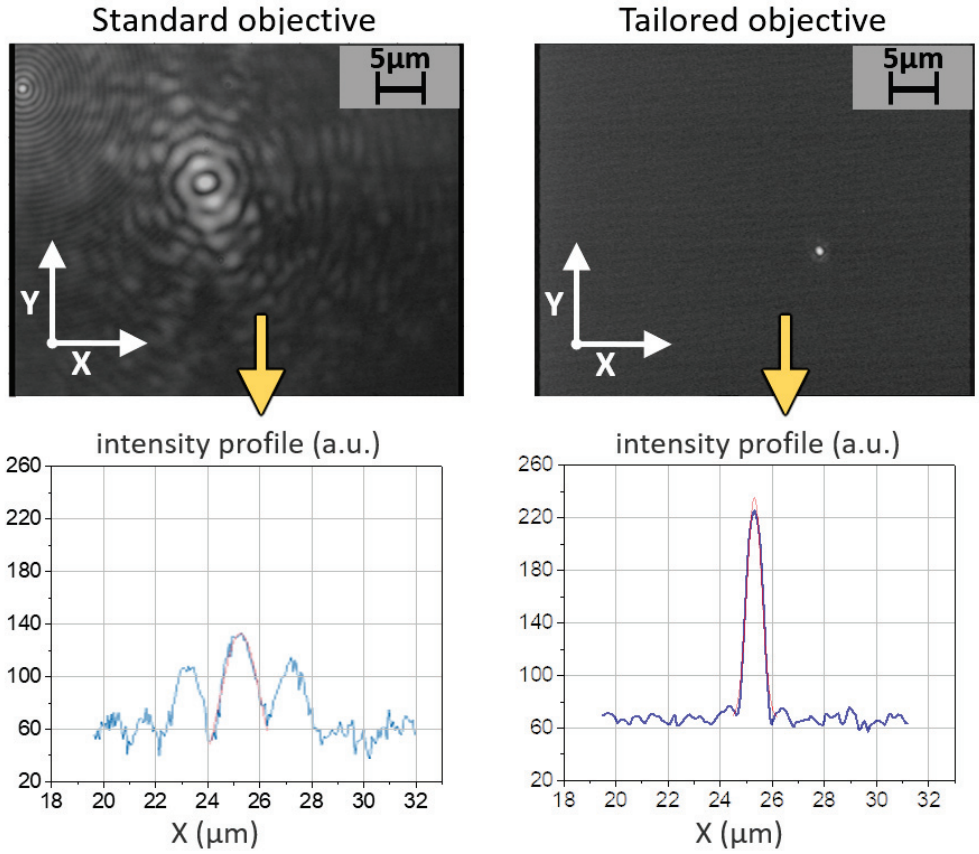

Figure 2.15: Qualitative beam spot comparison performed using a CCD camera. Left: the standard objective introduces serious aberrations. Right: the pre-compensated objective enables to reach diffraction limit.

tance. As clearly seen in the image, the spot corresponding to the pre-compensated objective is narrower and has a Gaussian profile, while the one generated by the standard objective is wider and presents strong aberrations, making it inappropriate for focusing purposes. A standard objective has been used to collect the transmitted light, although a second pre-compensated objective would be the best solution.
A quantitative beam characterization has been performed once the mechanical development (see Section (2.1.4)) was carried out and the "Transmission SMS setup" of Fig. (2.14) was fully operational. As explained in Section (1.4.2), a proper SMS image realized using a particle much smaller than the beam size allows a precise beam characterization. When this condition is respected the SMS image profile along the oscillation movement (Y) tends to the second derivative of the beam profile for small amplitudes (the LIA detection was always realized at the second harmonic), while across the orthogonal direction (X) it simply coincides with the beam profile. In order to produce an SMS image, a nano-bipyramid was deposed on the culet of the superior diamond anvil and the laser beam (with $\lambda = 800\,\text{nm}$) focused on it.
As shown in Fig. (2.16), the SMS image at the focal point may present asymmetries and rings. This is a consequence of the spot displacement and defocussing occurring when a plane-parallel plate is tilted relative to the optical axis. This effect can be minimized rotating the DAC in its holder with the aim of yielding a symmetric 3-lobe SMS image, as illustrated in Fig. (2.16).

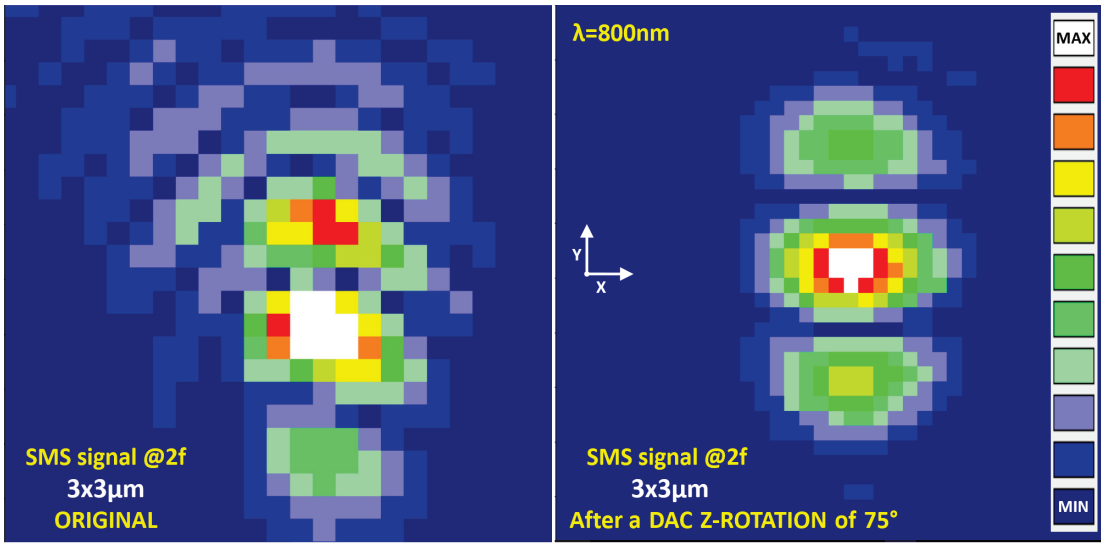

Figure 2.16: DAC tilt correction made by optimization of the SMS image map.

As displayed in Fig. (2.17), the image spot profile is well fitted by the Gaussian distribution, and even better by the Airy pattern (Eq. (A.2) and (A.3) of Ap-

pendix (A)). This is not surprising as the Gaussian beam is deliberately strongly truncated by the pupil of the pre-compensated objective, the incoming light being well-approximated by a plane wave. The truncation effects in the focusing and the quantitative treatment of the diffraction limit can be found in Appendix (A). In an Airy pattern profile, the *FWHM* of the focused spot is limited by

$$FWHM = \frac{K\lambda}{N.A.} \qquad \text{with} \quad K{=}0.515\,. \tag{2.7}$$

When $\lambda = 800\,nm$ and $N.A. = 0.7$, Eq. (2.7) gives $FWHM(800\,\text{nm}) = 590\,\text{nm}$, while the Airy fit of Fig. (2.17) gives $FWHM(800\,\text{nm}) = (625 \pm 20)\,\text{nm}$, which is slightly larger than the diffraction limit.
According to Eq. (A.6) of Appendix (A), fitting an Airy-like spot profile with a Gaussian (max-free) function, rather than a Bessel function, underestimates the *FWHM* (reducing the constant K of Eq. (2.7) giving diffraction limit to $K_{Gauss} = 0.496$). This is due to the fact that the Gaussian fit of a Bessel distribution is too large at the base and consequently narrower at the the *FWHM* to compensate, as shown in Fig. (2.17). This is consistent with the experimental case, as $K_{Gauss} = 0.496$ yields a theoretical diffraction limit $FWHM(800\,\text{nm}) = 570\,\text{nm}$ and the Gaussian fit of Fig. (2.17) gives $FWHM(800\,\text{nm}) = 605\,\text{nm}$ (again 35 nm larger than theoretical limit). This suggest that the image spot profile is the Airy pattern main lobe, despite the fact that outer rings are not visible. Their absence is due to some residual spherical aberration that generates some spikes, clearly visible for $x < 0.5\,\mu\text{m}$ in Fig. (2.17). The spot size larger than the diffraction limit and the presence of some aberrations are limited inconveniences and not an obstacle to perform SMS experiments. These imperfections are probably due to the difference between the diamond thickness after the polishing (1.385 mm) and the nominal thickness compensation of the objective (1.5 mm).
In the available range of laser wavelength, $680 - 1080\,\text{nm}$, the *FWHM* is proportional to λ, in accordance with Eq. (2.7). This means that the objective correctly focuses the beam and no significant aberration are occurring in this wavelengths range. Repeating the analysis of Fig. (2.17) for several wavelengths at a specific pressure as illustrated in Fig. (2.18a) yields a more reliable estimation of K_{exp} for the experimental *FWHM* formula

$$FWHM_{exp} = \frac{K_{exp}\,\lambda}{N.A.} \tag{2.8}$$

Experimentally K_{exp} is also a function of the pressure P, as the latter affects the diamond refractive index and thickness, as well as the PTM refractive index. Indeed the beam is focused and studied at the nano-particle level, whose center is located in the pressure chamber, 30–40 nm under the culet of the superior diamond anvil. The PTM refractive index n_{PTM} grows with the pressure, as illustrated in

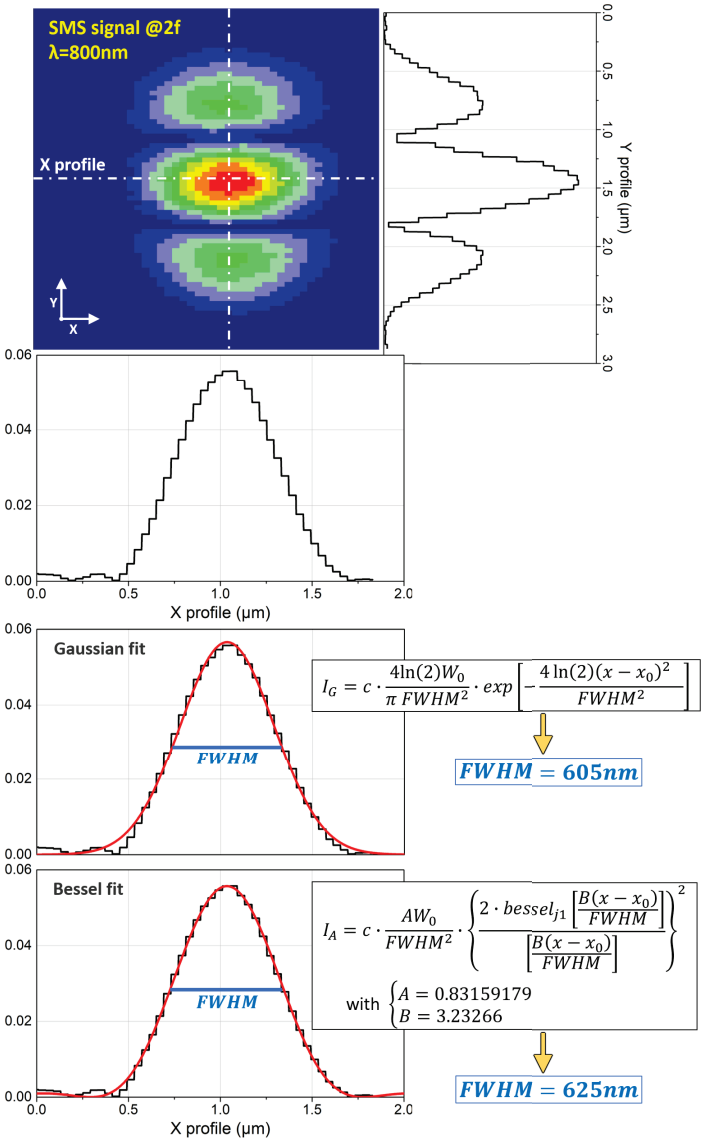

Figure 2.17: Quantitative image spot analysis realized through the SMS technique performed with a 2f detection. If the oscillating particle is smaller than the beam, then the X profile of the signal corresponds to the beam intensity profile; if the amplitude of oscillation is much smaller than the beam size, then the Y profile approaches the second derivative of the beam intensity profile. The X profile is well fitted by a Gaussian function (although the base is too large and the linewidth too narrow), and even better through a Bessel function (first kind, order one) corresponding to an Airy pattern. The key parameter is the fitted $FWHM$ (W_0 identifies the total beam power and c is an experimental parameter, converting the arbitrary SMS signal into absolute cross-section).

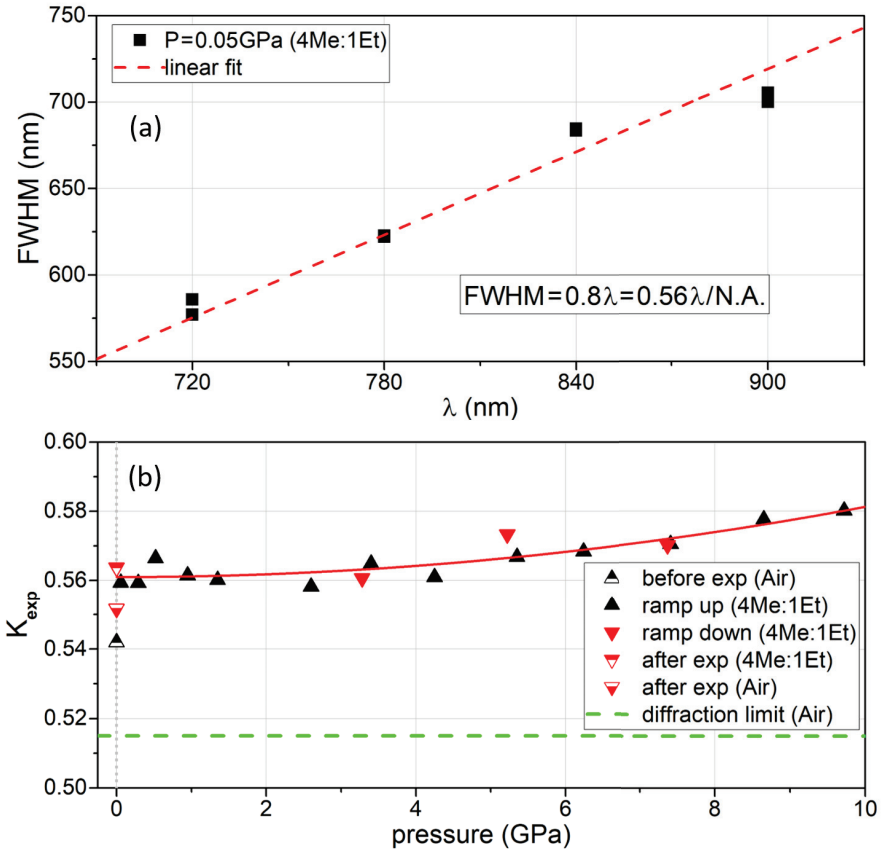

Figure 2.18: (a) For a specific pressure, the FWHM measured via SMS (squares) shows a linear dependence with the wavelength. (b) The experimental K_{exp} dependence on pressure (triangles) is well fitted by a parabola (solid red curve). Its increment in the $0-10$ GPa range corresponds to a *FWHM* widening of $20-30$ nm.

Fig. (C.2) of Appendix (C)). Conversely, the refractive index of the diamond n_d decreases linearly with the pressure, as shown in Fig. (B.2) of Appendix (B)). Furthermore, even the diamond thickness h decreases linearly when the pressure is incremented, as displayed in Fig. (B.3) of Appendix (B)). For a variation of 10 GPa the changes in h are negligible (-12 µm over 1.385 mm), while the variation of n_d (-5×10^{-3}) may have a significant impact due to the important thickness of the anvil. Overall, during the pressure ramp-up, the light path is modified (n_{PTM} increases, n_d and h decrease), eventually inducing non-corrected aberrations. The image spot *FWHM* has been measured at several wavelengths in air and in 4Me:1Et during an entire pressure experiment. The phenomenological relation between K_{exp} and the pressure is quasi-parabolic as shown in Fig. (2.18b). It can be expressed

as

$$K_{exp} = 0.56 + 2{\times}10^{-4}\, P^2\,, \tag{2.9}$$

where the pressure P is in GPa. In conclusion, the $FWHM$ is simply given taking Eq. (2.8) with $N.A.{=}0.7$

$$FWHM_{exp} = \left(0.8 + 3{\times}10^{-4}\, P^2\right)\lambda\,, \tag{2.10}$$

where P is expressed in GPa.

In the "Transmission SMS setup" of Fig. (2.14) nano-objects deposed on the superior diamond culet can be localized through an SMS cartography. Despite the initial gasket diameter is around 130 µm only an inner circular area with lower diameter can be examined. This is a consequence of the numerical aperture of the objective, as is illustrated in Fig. (2.19). The useful diameter in air can be expressed as

$$\oslash_{SMS} = \oslash_{gasket} - 2h_{gasket}\tan\left(\arcsin\left(N.A.\right)\right)\,. \tag{2.11}$$

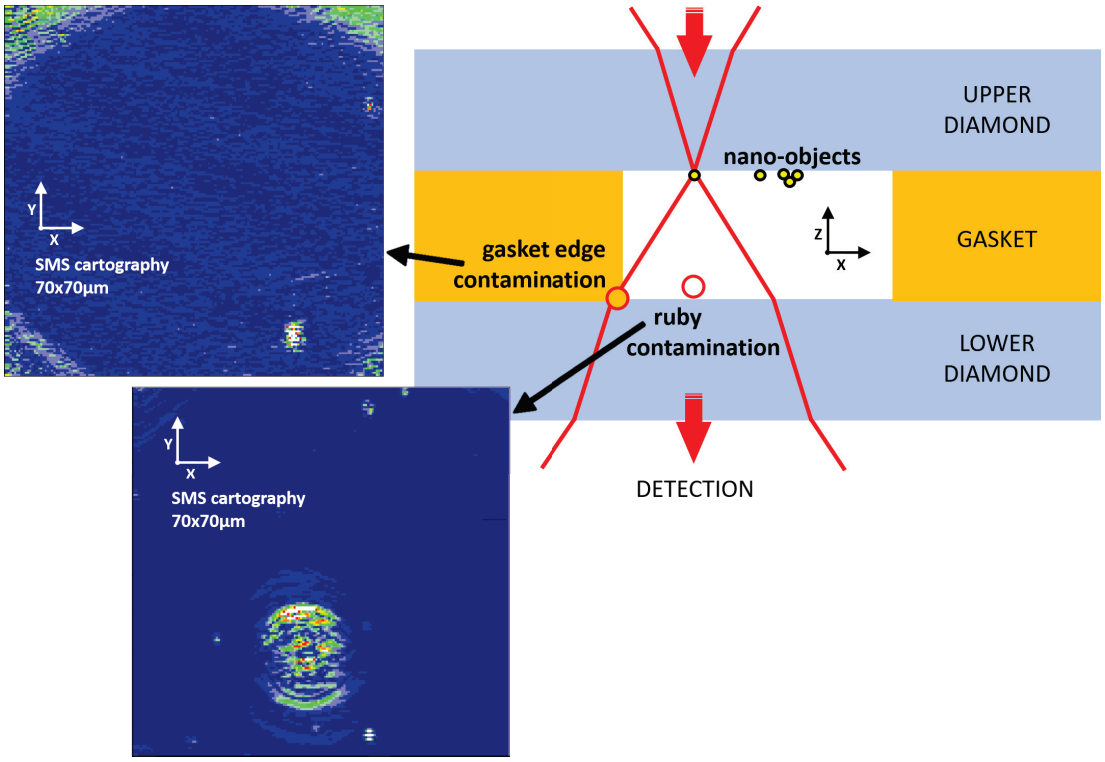

Figure 2.19: SMS signal contamination induced from the gasket borders (outer green ring in the upper cartography) and from a ruby deposed on the opposite culet (circular blur in the lower cartography). The simplistic diagram explains the origin of the problem.

For a gasket thickness $h_{gasket} = 30\,\mu m$ and $N.A. = 0.7$, this results in $\oslash_{SMS} \sim 70\,\mu m$. Another source of SMS signal distortion comes from the ruby on the opposite culet. The contaminated area is a circle of diameter $20-30\,\mu m$, as shown in Fig. (2.19). In conclusion, only the nano-objects far enough from the contamination sources should be studied.

From an optical point of view, the knowledge of the image spot profile and size are the keys elements to realize a proper quantitative SMS experiment. Using the pre-compensated objective, the spot shape is well described by an Airy pattern whose size is governed by Eq. (2.10). The optical part characterized, in order to realize SMS experiments, an appropriate mechanical oscillation must now be applied and quantified.

2.1.4 SMS and DAC combination: mechanical development

From a mechanical point of view, an efficient SMS system should be able to precisely control in time the XYZ coordinates of an individual nano-object. The particle must be kept into the focused laser beam, while it oscillates along the Y-direction with a proper amplitude and frequency. The vibration amplitude should be comparable to the beam spot size in order to have a strong SMS signal, while the working frequency should be high enough to reduce the $1/f$ noise coming from laser power fluctuations and electronics, but not too elevated either, otherwise mechanical coupling will appear and odd XYZ vibration could occur. To this respect, for a sample of a few tens of grams the operating working frequency lies around 1500 Hz. Unfortunately diamond anvil cells are pretty heavy and, even after important improvements, the employed DAC still weights 0.4 Kg. This strongly reduces the amplitude of oscillations and generates mechanical resonances at relatively low frequencies. In order to characterize and improve the mechanical apparatus, a simple model based on an interferometric study has been realized.

In the "Transmission SMS setup" of Fig. (2.14) the XYZ position of a nano-object can be manually controlled via a micrometric stage which is fixed to the optical table through 4 posts. For a finer positioning, a XYZ piezo nanopositioning stage with a capacitive integrated sensor is mounted at the top of the micrometric stage. In order to generate the sinusoidal oscillation, a Y piezo shaker is installed on the XYZ piezo nanopositioning stage (mass of piezo 0.16 Kg, maximum displacement 12 µm, presence of a capacitive integrated sensor). The base of the Y

shaker is fixed on the movable part (top) of the XYZ stage (see also Fig. (2.22) at page (56)). The DAC is screwed to a cylindrical holder made of aluminum (mass of DAC with holder 0.6 Kg), which is in turn fixed on the top of the Y piezo shaker. Two vertical springs are hooked up to the holder in order to statically compensate the weight force of the DAC. The voltage for controlling the position of the Y piezo shaker is provided by the internal LIA (lock-in amplifier) function generator, which generates a sinusoidal voltage of amplitude V_{LIA}, frequency f and phase ϕ_{LIA}

$$v_{LIA}(t) = V_{LIA}\sin(2\pi ft + \phi_{LIA})\,, \tag{2.12}$$

forcing a periodic expansion in the Y piezo shaker that can be followed through its capacitive integrated sensor on an oscilloscope

$$v'_Y(t) = V'_Y\sin(2\pi ft + \phi'_Y)\,, \tag{2.13}$$

where the prime symbol ($'$) indicates quantities measured through the capacitive integrated sensors. The voltage amplitude V'_Y (measured in Volt) can be directly converted in spatial amplitude A'_Y (in µm) using the calibration factor $C_Y = 12\,\mu\text{m/V}$ of the Y piezo shaker:

$$Y'_Y(t) = A'_Y\sin(2\pi ft + \phi'_Y)\,. \tag{2.14}$$

Ideally, the Y piezo shaker and the DAC (with the nano-objects contained in the pressure chamber) should move as one. If this is the case, the system can be modeled by a forced harmonic oscillator, where the only limitation in frequency would come from the Y piezo shaker push-pull force capacity, that is equal to $F = 20\,\text{N}$. According to this, $M_{DAC}\,\ddot{Y}_Y(t) < F\ \forall t$ with $M_{DAC} = 0.6\,\text{Kg}$, the maximal available amplitude of oscillation being inversely proportional to the frequency square and quantified in Fig. (2.20). The graph highlights the need of choosing a frequency below 1.5 kHz, where the vibration amplitudes can attain at least half of the beam spot *FWHM* in the infrared, and hence yield an intense SMS signal.

Unfortunately the system oscillates in such an ideal movement only for low frequencies, beneath 100 Hz, where the noise from laser fluctuations is way too large for the SMS technique. In fact, the DAC important weight causes some mechanical couplings between the DAC, the Y piezo shaker and the XYZ piezo stage, making the apparatus more akin to a forced system of three coupled harmonic oscillators, rather then a single one. As a consequence, the real amplitude of oscillation of the DAC is insufficient to generate a perceptible SMS signal for most of the accessible frequencies, whereas for three specific frequencies dangerous resonances show up. Therefore, in order to perform the SMS technique, an optimal working frequency range must be found, hence requiring a mechanical system characterization.

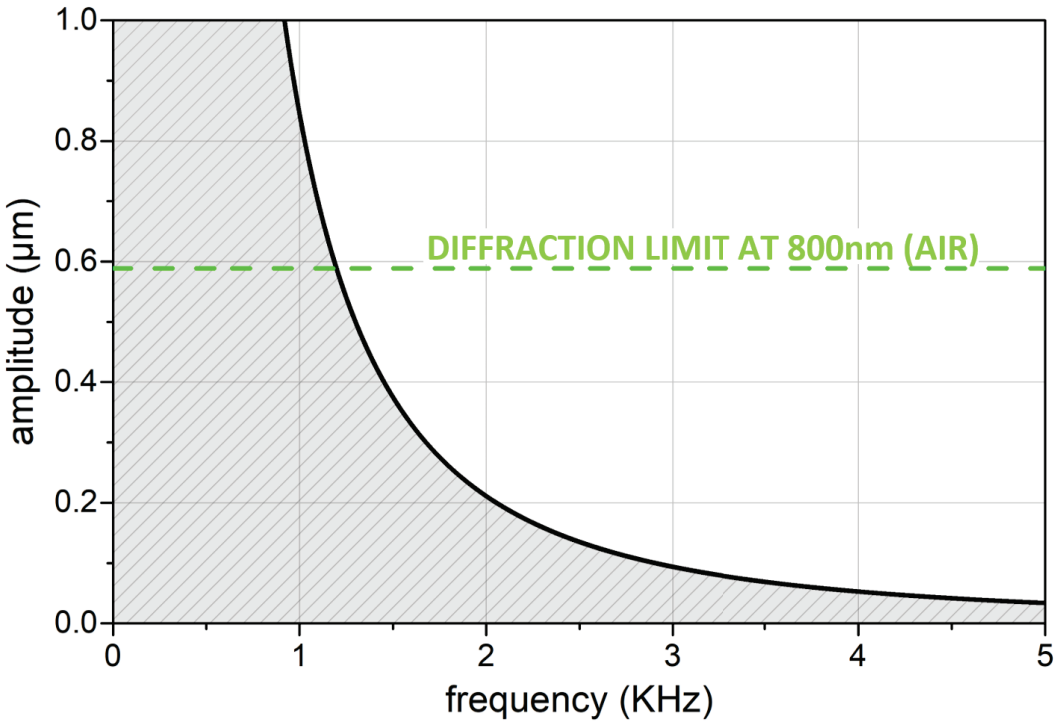

Figure 2.20: Maximum amplitude of oscillation as a function of the frequency, accordingly to the push-pull limit of the Y piezo shaker. Amplitudes can be reached only for $f < 1.5\,\mathrm{kHz}$, region where they are comparable to the beam spot size.

The capacitative sensors integrated in the piezos allow to monitor the motion of the system components with respect to the element they are attached to, and what discussed for the Y piezo shaker applies to the XYZ piezo stage too. In the Y direction a periodic movement shows up due to the coupling with the Y shaker

$$Y'_{XYZ}(t) = A'_{XYZ}\sin(2\pi ft + \phi'_{XYZ})\,, \tag{2.15}$$

while along the X and Z direction the movement is always negligible (unless in the case of a strong resonance).

To study the absolute movement of the system components (with respect to the optical table) a home-made interferometer has been assembled. Outlined in Fig. (2.21), it is based on an optical mirror mounted on the mechanical component to characterize and enables to detect the absolute movements along the Y direction of the DAC holder

$$Y_{holder}(t) = A_{holder}\sin(2\pi ft + \phi_{holder})\,, \tag{2.16}$$

of the XYZ piezo stage

$$Y_{XYZ}(t) = A_{XYZ}\sin(2\pi ft + \phi_{XYZ}) \tag{2.17}$$

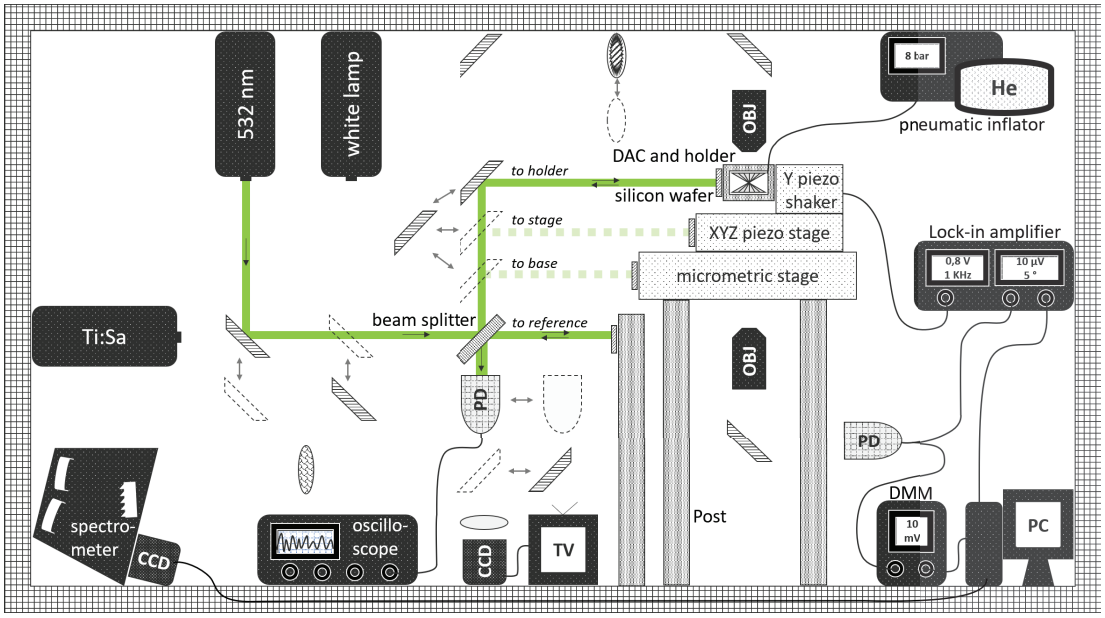

Figure 2.21: "Interferometer setup": a monochromatic green laser beam is separated in two arms using a beam splitter; the first line is reflected by a mirror that is fixed with respect to the laboratory reference system; the second line reflected by a small silicon wafer (acting as a light mirror) glued on the DAC holder, on the XYZ piezo stage, or on the micrometric stage. The two beam paths are recombined and sent to a silicon photodiode connected to an oscilloscope, that allows to study their interference as a function of time. Translating a few mirrors allows to quickly recover the "Transmission SMS setup" of Fig. (2.14), the "ruby luminescence setup" of Fig. (2.10) or the "culet imaging setup" of Fig. (2.7).

and of the micrometric stage

$$Y_{base}(t) = A_{base}\sin(2\pi f t + \phi_{base}) \sim 0\,. \tag{2.18}$$

The latter resulted negligible, yielding an equivalence between relative and absolute movement of the XYZ piezo stage (Eq. (2.15) and Eq. (2.17)). Absolute (measured by the interferometer) and relative (sensor) movement of the system components are summarized in Fig. (2.22).

When amplitudes and phases are deduced from piezo sensors, they are obtained directly by the sinusoidal signal in the oscilloscope, proportional to the internal mouvement. However, when they are measured through the interferometer, a more complex signal occurs. Basically, the more fringes are detected per period, the greatest the oscillation amplitude is, but the sinusoidal motion makes the fringes denser in time when the oscillation speed is maximal. To be more quantitative, the intensity of the interference between the path 1 (reflected by the fixed mirror)

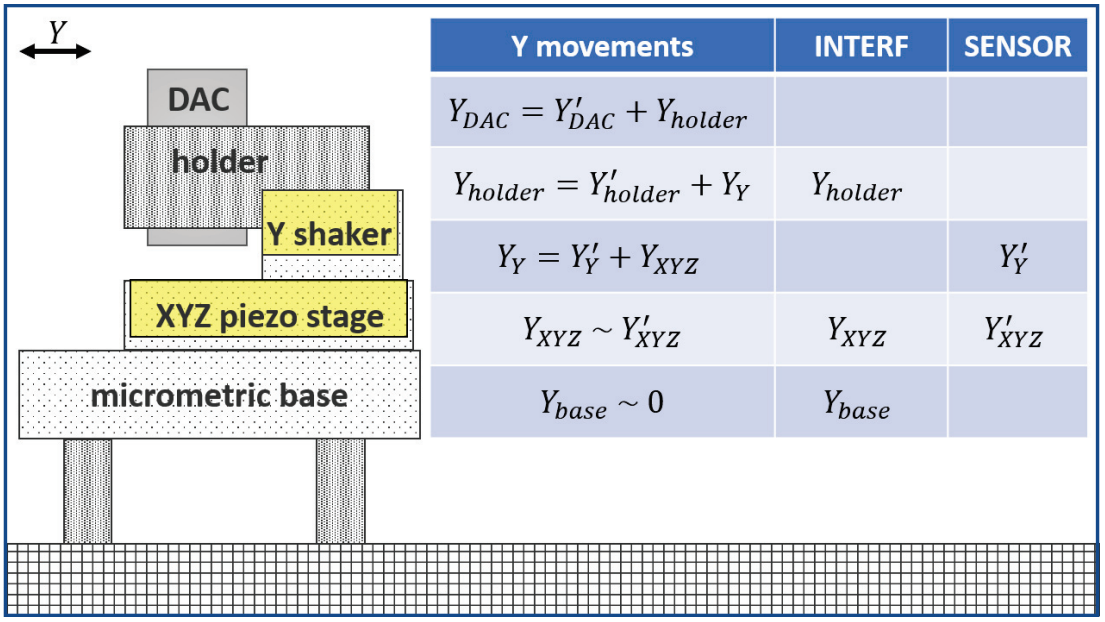

Y movements	INTERF	SENSOR
$Y_{DAC} = Y'_{DAC} + Y_{holder}$		
$Y_{holder} = Y'_{holder} + Y_Y$	Y_{holder}	
$Y_Y = Y'_Y + Y_{XYZ}$		Y'_Y
$Y_{XYZ} \sim Y'_{XYZ}$	Y_{XYZ}	Y'_{XYZ}
$Y_{base} \sim 0$	Y_{base}	

Figure 2.22: Sketch of the system components (movable piezoelectric parts in yellow). Table: absolute and relative movements along Y are summarized in column "Y movements". Absolute movements (i.e. with respect to the optical table) are measured by the interferometer ("INTERF"). Relative movements (i.e. movement of the piezo component with respect to its base) are measured by piezo internal sensor ("SENSOR").

and the path 2 (reflected by the oscillating component) takes the form

$$I_{int}(t) = I_1 + I_2 + 2\sqrt{I_1 I_2}\cos\left[\frac{4\pi}{\lambda}\left(L_2 - L_1 + A\cos(2\pi f + \phi)\right)\right], \qquad (2.19)$$

where λ is the laser wavelength, I_1 and I_2 are the intensities along the path 1 and 2 respectively, L_1 is the distance between the beam-splitter and the reference mirror, $L_2 + A\cos(2\pi f + \phi)$ is the distance between the beam splitter and the mirror on the moving part, A, f and ϕ are the amplitude, frequency and phase of oscillation. The intensity $I_{int}(t)$ is detected through a photodiode, measured on an oscilloscope and fitted using Eq. (2.19). An example of the interference signal and its fit is reported in Fig. (2.23).

The main results on the mechanical vibration characterization are presented in Fig. (2.24), showing the Y amplitudes divided by the excitation voltage amplitude (e.g. A_{holder}/V_{LIA}) and normalized to the amplitude at very low frequencies and the dephasings. As a preliminary remark, it should be notice that, in the ideal case (verified at very low frequencies), the driving force should only make the holder and the DAC vibrate ($Y_{DAC} = Y_{holder} = Y_Y \neq 0$), while supporting components are

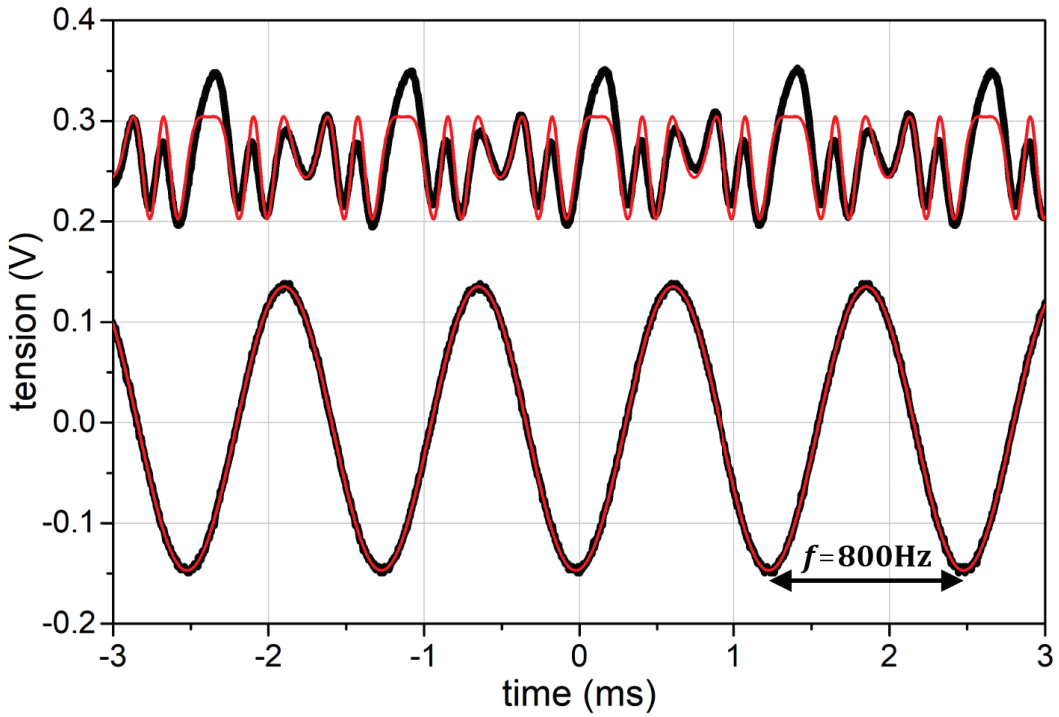

Figure 2.23: Example of signals monitored on the oscilloscope for interferometric analysis. The lower black curve is the voltage introduced by the LIA that drives the Y shaker; in red its sinusoidal fit; the upper black curve is the voltage proportional to the interference induced by the DAC holder oscillation; in red the fit based on Eq. (2.19). This fit curve slightly deviates from the experimental one, as the photodiode acts like a low-pass frequency filter, reducing the amplitudes of the signal when it varies faster. However, it was verified that this signal distortion does not affects the relevant fit parameters (amplitude and phase).

not supposed to move ($Y_{base} = Y_{XYZ} = 0$). As illustrated in Fig. (2.22), the DAC holder was characterized via interferometer only, the Y piezo shaker through the capacitative sensor, the XYZ piezo stage with the two methods, albeit only the capacitative sensor data are reported (the other data being similar). Three resonances dominate: "R_3" $\sim$100 Hz, "R_1" $\sim$770 Hz and "R_2" $\sim$1770 Hz, each one being attributed to the proper frequency of the three equivalent oscillator. The XYZ piezo stage introduces the resonance "R_3". Indeed, its nominal unloaded resonant frequency is 190 Hz($\pm$20%) that becomes 140 Hz($\pm$20%) with a load of 0.33 Kg (data from manufacturer). Thus, it can be associated to an equivalent oscillator with unloaded mass 0.4 Kg and spring constant 5.7×10^6 N/m. A mass load of 0.76 Kg (DAC, holder and Y shaker) would thus produce a resonant frequency close to 110 Hz.
The Y shaker and its load (DAC plus holder) introduce the two resonances "R_1"

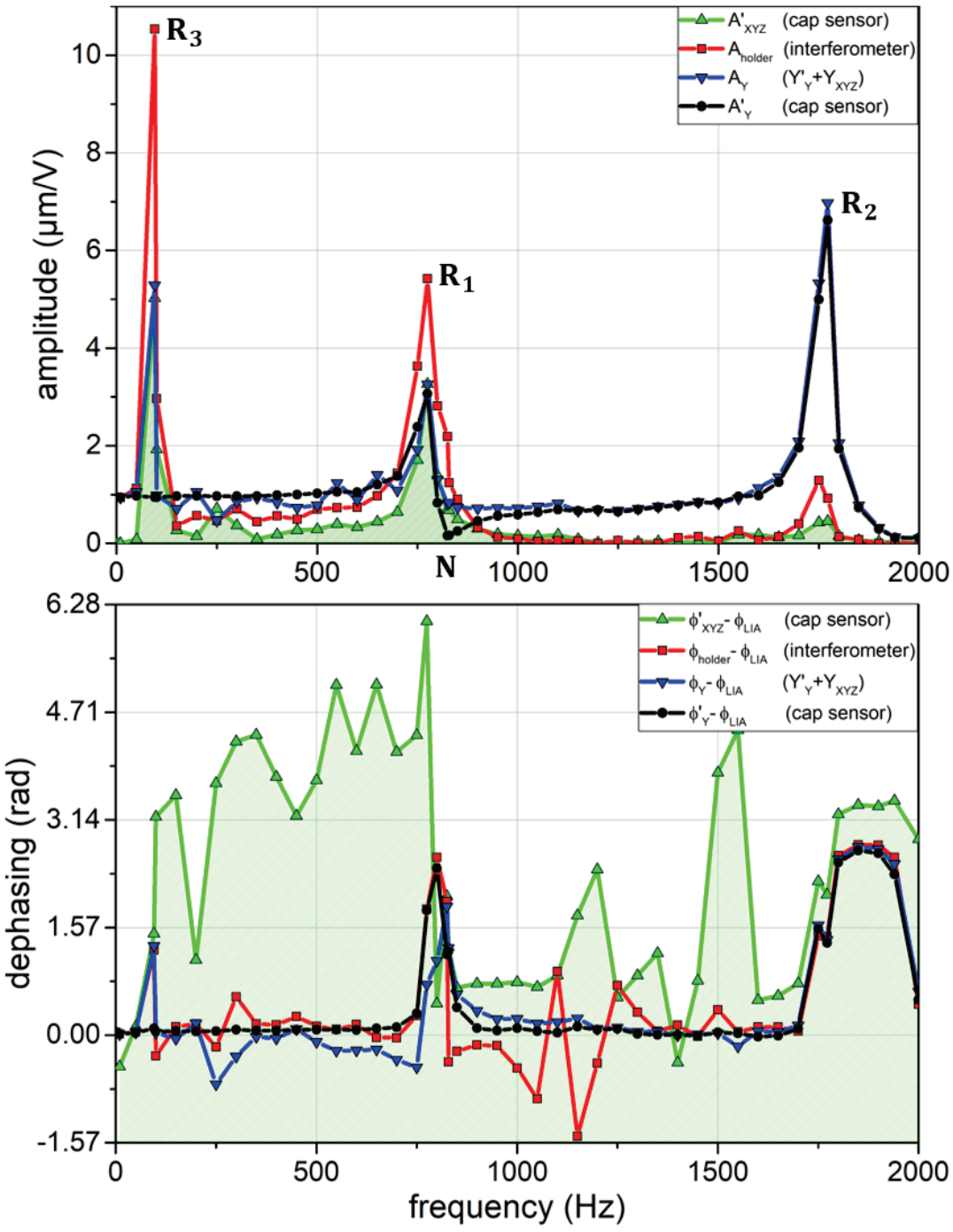

Figure 2.24: Main results from the system experimental characterization. Green triangles correspond to the motion of the XYZ piezo stage (measured through its integrate capacitative sensor); red squares indicate the absolute motion of the DAC holder (measured by the interferometer); black dots are the relative motion of the Y piezo shaker (sensor); blue reversed triangles represent the absolute motion of the Y piezo shaker (obtained from $Y_Y = Y'_Y + Y_{XYZ}$). Note that the XYZ piezo stage is approximately in phase with the driving force in the intervals [0 Hz, "R_3"] and ["R_1", "R_2"], while they are in antiphase in the regions ["R_3", "R_1"] and ["R_2", 2000 Hz].

and "R_2" at higher frequencies. Indeed, the Y shaker nominal unloaded resonant frequency is 5600 Hz($\pm$20%) and its nominal stiffness 45×10^6 N/m($\pm$20%). Therefore, it can be associated to an equivalent oscillator with unloaded mass 0.036 Kg and spring constant 45×10^6 N/m. A mass load of 0.6 Kg (DAC and holder) would produce a resonant frequency at about 1350 Hz.

The amplitudes reported in Fig. (2.24) show that in the frequency range [1000$-$1500 Hz] the Y shaker is oscillating, but the XYZ piezo stage and the DAC holder are not moving. Therefore, this range can not be used for SMS experiments, as the sample would not vibrate. A possible working frequency could be the nodal point at 825 Hz, indicated as "N" in Fig. (2.24), where $A'_Y \sim 0$. Here $A_{holder} \sim A_Y$ and therefore relatively high oscillation amplitudes of the DAC can be produced. However, "N" is located in the proximity of "R_1", where the dephasing are strongly varying with the frequency. For stability reasons, it is preferable to work at frequencies where all the system components are in phase with the driving force.
In order to better understand the behavior of the dephasing around "N", the relative movements of the DAC holder ($Y_{holder} - Y_{XYZ}$) and Y shaker ($Y_Y - Y_{XYZ}$) with respect to the XYZ piezo stage has been modeled through a forced two-spring system along the Y direction

$$\begin{cases} M_1\ddot{Y}_1 = -k_1Y_1 + k_2(Y_2 - Y_1) - \beta_1\dot{Y}_1 + F_1\sin(2\pi ft) \\ M_2\ddot{Y}_2 = -k_2(Y_2 - Y_1) - \beta_2\dot{Y}_2 \end{cases}, \tag{2.20}$$

where a sinusoidal force of amplitude F_1 is applied to the first oscillator tied to a wall, while the second oscillator is connected to the first one. The first

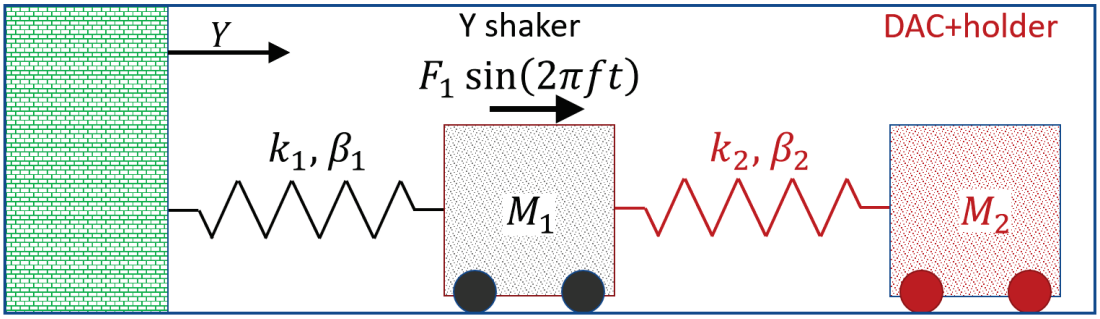

Figure 2.25: Forced two-spring model adopted to understand the dephasing behavior of the system components: a sinusoidal force of amplitude F_1 and frequency f is applied to M_1 to simulate the LIA driving force applied on the Y shaker. This mass is attached to the wall (replacing the XYZ piezo stage) through a spring of constant k_1 and dissipative parameter β_1. On the other side, it is connected to a second oscillator (simulating the DAC and its holder) characterized by M_2, k_2 and β_2.

resonator represents the Y piezo shaker, while the second one the load (DAC plus holder), as illustrated in Fig. (2.25). The system of Eq. (2.20) can be analytically solved assuming that the solutions are sinusoidal functions with frequency f. The solutions are:

$$\begin{cases} Y_1 = A_1 \sin(2\pi f t + \phi_1) \\ Y_2 = A_2 \sin(2\pi f t + \phi_2) \end{cases} , \tag{2.21}$$

where

$$A_1 = \frac{F_1}{M_1} \frac{\sqrt{(2\pi f)^4 + [(\beta_2/M_2)^2 - 2k_2/M_2]\,(2\pi f)^2 + (k_2/M_2)^2}}{\sqrt{p^2+q^2}} , \tag{2.22}$$

$$A_2 = \frac{F_1}{M_1} \frac{k_2/M_2}{\sqrt{p^2+q^2}} , \tag{2.23}$$

$$\phi_1 = -\arctan\left[\frac{q-rp}{p+rq}\right] , \tag{2.24}$$

$$\phi_2 = -\arctan\left[\frac{q}{p}\right] , \tag{2.25}$$

$$p = (2\pi f)^4 - \left(\frac{k_1+k_2+\beta_1}{M_1} + \frac{k_2+\beta_2}{M_2}\right)(2\pi f)^2 + \frac{k_1 k_2}{M_1 M_2} , \tag{2.26}$$

$$q = -\left(\frac{\beta_1}{M_1} + \frac{\beta_2}{M_2}\right)(2\pi f)^3 + \left(\frac{k_1\beta_2 + k_2\beta_2 + k_2\beta_1}{M_1 M_2}\right)(2\pi f) , \tag{2.27}$$

$$r = \frac{\beta_2(2\pi f)}{k_2 - M_2(2\pi f)^2} . \tag{2.28}$$

In Fig. (2.26) are plotted experimental amplitudes and dephasings of $Y''_{holder} = Y_{holder} - Y_{XYZ}$ and $Y'_Y = Y_Y - Y_{XYZ}$ and their fits, realized using Eq. (2.22), (2.24) and (2.23). Imposing $k_1 = 4.5\times10^7$ N/m (so that the first spring constant is close to the nominal stiffness per unit length of the Y piezo shaker) and fitting the amplitudes and the dephasing concomitantly determines all the model parameters (F_1, M_1, M_2, k_1, k_2, β_1, β_2). The model reproduces the main features of the experimental data "R_1", "R_2", "N", showing that around 1500 Hz the amplitude of oscillation of the DAC holder is smaller than the Y shaker one. Varying the model parameters pointed out that the nodal point "N" occurs every time that an oscillator of mass M_1 is placed between two elements with higher masses (M_2 and the wall). More importantly, comparison of fitted curves (Fig. (2.27)), enlightens that the Y shaker is in phase with the driving force in the interval ["N", "R_2"], while they are in antiphase in the regions ["R_1", "N"], making the frequencies higher

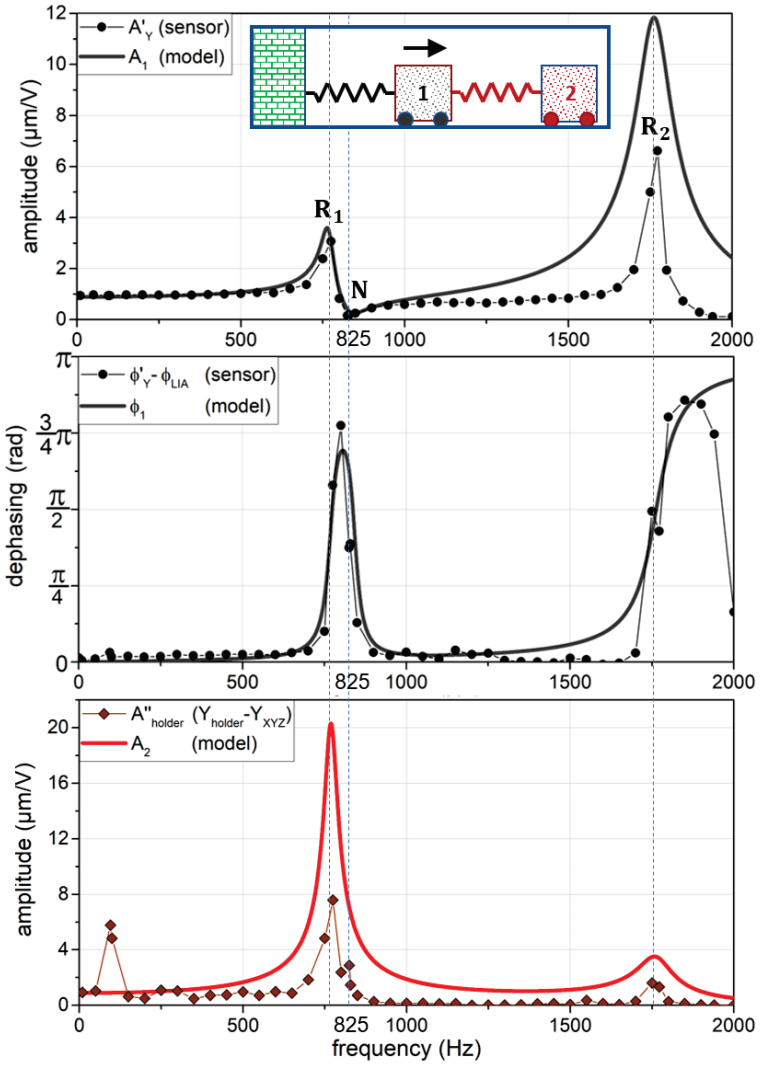

Figure 2.26: System simulation with the forced two-spring model and comparison to experiments. Black dots represent the movement (amplitude and phase) of the Y shaker relative to the XYZ piezo stage (Y'_Y) (see also Fig. (2.24)). Black lines are amplitude and phase (A_1 and ϕ_1) derived by the fit of all the points with the forced two-spring model. Red diamonds correspond to motion of the DAC holder relative to the XYZ piezo stage ($Y''_{holder} = Y_{holder} - Y_{XYZ}$). Red line is amplitude A_2 from the fit. In these fits, k_1 was taken equal to the Y shaker stiffness, $k_1 = 4.5 \times 10^7$ N/m; F_1 was chosen so that at low frequency the oscillation amplitudes where of 1 µm/V, $F_1 = 40$ N; the equivalent sum of masses of $M_1 + M_2$ should be close to the masses sum of DAC, holder and Y shaker (0.76 Kg). Fitting yields $M_1 = 0.44$ Kg and $M_2 = 0.25$ Kg; the other parameters were completely determined from the fits, resulting $k_2 = 7 \times 10^6$ N/m, $\beta_1 = 300$ Kg/s and $\beta_2 = 60$ Kg/s.

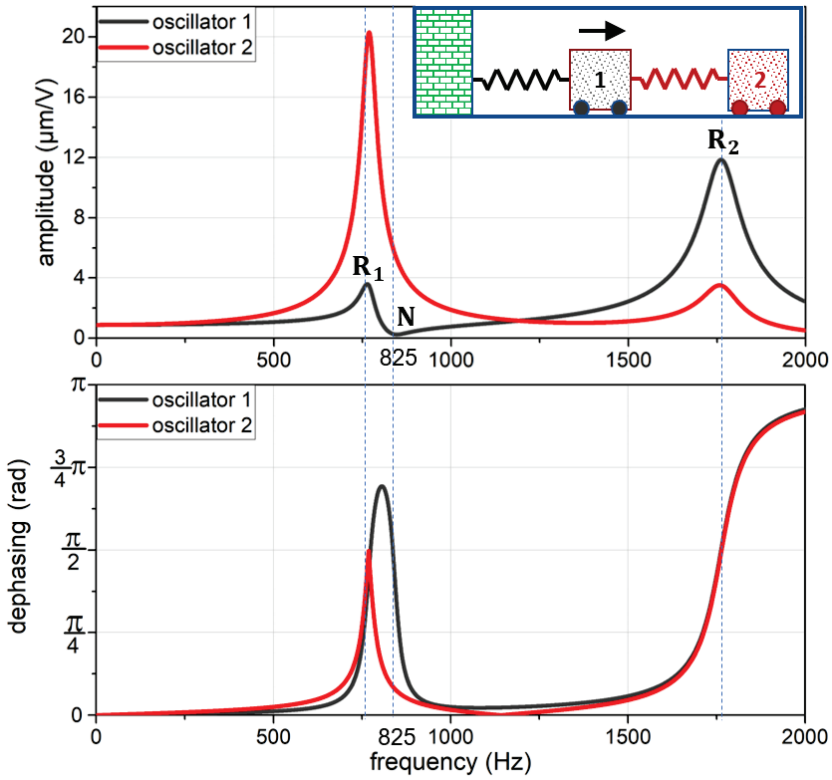

Figure 2.27: Oscillation amplitudes and dephasing obtained through the forced two-spring model (Eq. (2.22), (2.23), (2.24) and (2.25)) considering the parameters obtained from the data fit illustrated in Fig. (2.26). Notice that at frequencies slightly lower than "N" the oscillators are not in phase, while at slightly higher frequencies they are both in phase with the driving force.

than "N" more appropriate to work with.

In conclusion, it is necessary to work at a frequency in the range $700\,\text{Hz} < f < 1500\,\text{Hz}$ to have a reasonable signal-over-noise ratio (large frequencies) and to avoid mechanical breakdowns (occurring at too high frequencies). In this range, the DAC can oscillate with an amplitude comparable to the size of the beam spot, the dephasing between the oscillators and the applied force is small and has not discontinuities.
A good choice would be to work close to the nodal point "N" (825 Hz), where the internal movement of the Y piezo shaker is negligible ($Y'_Y \sim 0$) and the amplitude of its movement with respect to the optical table is comparable to the DAC holder one $Y_Y \sim Y_{holder}$. For this reason the choice $f = 825\,\text{Hz}$ was initially made. Even better is to work at slight higher frequencies than "N" ($\sim 840\,\text{Hz}$) in order to have all the components almost in phase with the driving force.

In order to improve the signal-over-noise ratio, the working frequency should be increased. In the model, this can be done by changing the parameters M_1, M_2, k_1, k_2. Indeed, decreasing M_1 would mainly increase the frequency for "R_1"; increasing k_1 would increase "R_1", "R_2" and slightly "N"; decreasing M_2 or increasing k_2 would increase "R_1", "R_2" and "N".
In practice, a modification of the connection (removal of part of a mechanical adapter mass) between the base of the Y piezo shaker and the top of the XYZ piezo stage (corresponding to a modification of M_1 and K_1) has enabled to shift the working frequency at $f = 940\,\mathrm{Hz}$, which is the one used in the pressure experiments presented in this chapter.
The application of the SMS technique requires the determination of the DAC amplitude of oscillation at $f = 940\,\mathrm{Hz}$. This oscillation amplitude is a linear function of the amplitude of the applied sinusoidal voltage, then can be written in the form

$$\delta(940\,\mathrm{Hz}) = c \cdot V_{LIA}\,. \tag{2.29}$$

The coefficient c, measured in µm/V, has been determined applying the SMS technique on a gold nanoparticle deposed on the culet of the superior diamond. If the beam shape and size are well known this kind of measurement is more reliable than the interferometric one, because it gives the movement of the nanoparticle ot the center of the DAC, while the interferometer measures the vibrations of the outer part of the holder (indeed even the holder and the DAC are not completely moving as one). It results $c = (0.52 \pm 0.02)\,\mu\mathrm{m/V}$. To have a strong SMS signal, the LIA voltage was tuned yielding $\delta(940\,\mathrm{Hz})$ of the order of the beam size described by Eq. (2.10). The following experiments has been performed with $V_{LIA} = 1.13\,\mathrm{V}$ corresponding to a spatial modulation of

$$\delta(940\,\mathrm{Hz}) = (0.52 \pm 0.02)\mu\mathrm{m\ V^{-1}} \times 1.13\,\mathrm{V} = (590 \pm 25)\,\mathrm{nm}\,. \tag{2.30}$$

From a mechanical point of view, determination and optimization of the sample oscillation amplitude is the key element to realize a proper SMS experiment. The apparatus improvement and characterization have made it possible to work with the desired amplitude, at a reasonably high frequency. At this point, the SMS technique was operational and high-pressure experiments could be carried out.

2.2 A single metal nanoparticle under high pressure

The implementation and characterization of a setup for optical microscopy measurement on individual nano-objects under high pressure allowed to realize the first quantitative experiments, which are presented in this section.

Up to now, the studied nanostructures are elongated gold nanoparticles: nanobipyramids (BPs) directly deposed on a diamond culet and then immersed in hydrostatic 4Me:1Et (properties of this PTM can be found in Appendix C). The choice of working with this kind of nanoparticles was made on the basis of the solid knowledge of their optical properties (experiments and modeling) already established at standard pressure [78, 79]. Examples of BPs experimental extinction cross-section spectra, $\sigma(\omega)$, dominated by a quasi-Lorentzian SPR are illustrated in Fig. (2.28). In the current section are reported the successful measurements realized on gold BPs, starting from the most recent one ("BP1") and ending with the first measured ("BP5"). In order to describe them, it is convenient to introduce the following terminology: "*ramp-up*", which indicates the experiment part where the pressure is increased; "*ramp-down*", which corresponds to the phase where the pressure is decreased and "*pressure cycle*", hence the union of a *ramp-up* with the following *ramp-down*. Furthermore, when the word "*complete*" is added, it means that the whole available pressure range $[0-10\,\mathrm{GPa}]$ was investigated.

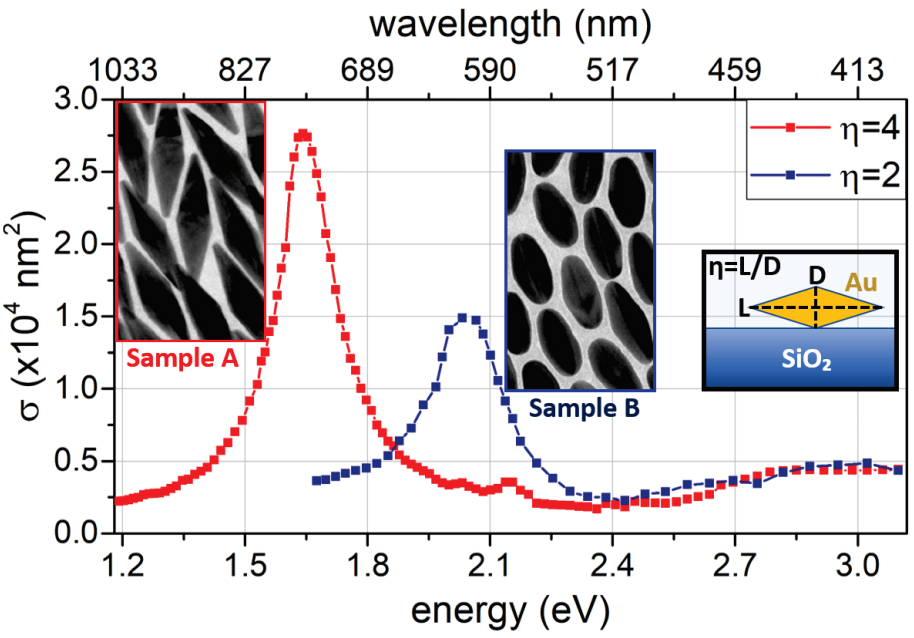

Figure 2.28: Extinction cross-section of individual gold BPs deposed on a silica substrate. The red curve is associated to a BP from sample A, constituted by sharp BPs with aspect-ratio $\eta \sim 4$. It exhibits a quasi-Lorentzian longitudinal SPR centered at 1.64 eV and a smaller peak at 2.15 eV related to the presence of sharp tips. The blue curve corresponds to a BP extracted from sample B, composed by rounded BPs with $\eta \sim 2$. It shows a quasi-Lorentzian longitudinal SPR located at higher energy 2.04 eV. Interband transitions increase the extinction cross-section σ beyond 2.5 eV.

The investigated nanoparticles are synthesized in collaboration with chemists (Prof. L.M. Liz-Marzán in San Sebastián and Prof. M. Tréguer-Delapierre in Bordeaux) and they are available in liquid solution which can be directly deposited on a culet of a diamond anvil via spin-coating. As illustrated in Fig. (2.29), transmission electron microscope (TEM) images show that all the BPs from the same solution have very similar dimensions, which are summarized in Tab. 2.1. This is important for modeling, as a morphological characterization by electron microscopy of the BPs deposited on the anvil substrate (1.4 mm thick) is not possible.
Some attempts have been made using scanning electron microscopy (SEM), but the insulator character of the diamond makes the electrons accumulate on the interface causing a strong blur, as shown in Fig. (2.30).
In Tab. 2.2 on page 79 are summarized the working conditions and the main features of each experiment (from the most recent "BP1" to the first attempts "BP5"). Here, the experiment "BP1" is discussed in detail, while for the others only the final results and some peculiarities are reported.

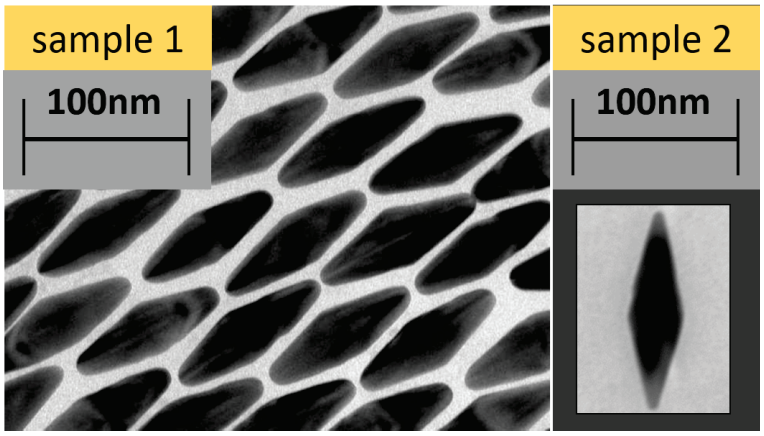

Figure 2.29: TEM images realized on standard TEM grids. at the left is presented the sample 1 (very low size and shape dispersion); at the right sample 2.

	sample 1	sample 2
SAMPLE	Au-BP @PEG	Au-BP @PEG
LONG AXIS (nm)	100.5 ± 4.5	100 ± 11
SHORT AXIS (nm)	32 ± 3	31.0 ± 3.5

Table 2.1: Summary of the solutions containing gold BPs with PEG as surfactant. The reported dimensions come from TEM images. Sample 1 has a very low size and shape dispersion, while sample 2 is more polydisperse and contains also gold spheres.

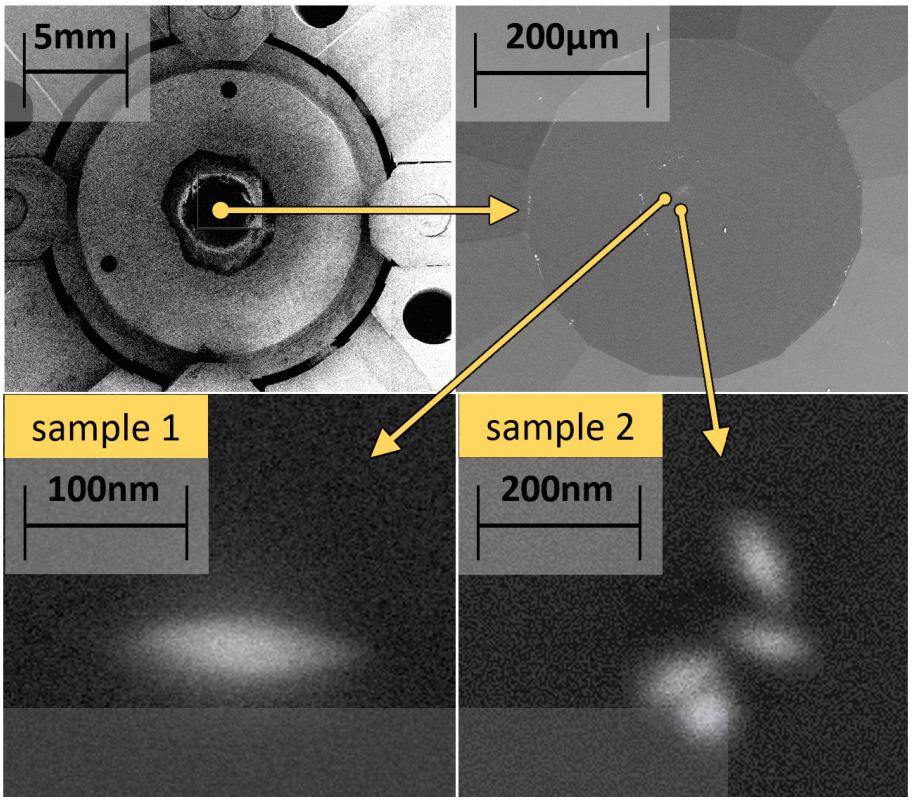

Figure 2.30: SEM images realized on the culet of the superior anvil: at the top left the diamond anvil glued on its tungsten-carbide seat; at the top right the culet plateau where the BPs are deposed via spin-coating; at the bottom left a BP from sample 1; at the bottom right a cluster from sample 2.

BP1

During experiment "BP1", the particle under investigation was an individual gold BP from sample 1 placed on the superior diamond anvil. Typically, after the spin-coating, isolated BPs are searched on the culet at 0 GPa, without PTM. This is accomplished through the SMS technique, which allows to measure the extinction spectrum dominated by the SPR and the polarization response of each detected particle. The longitudinal SPR of a single BP shows up as a Lorentzian shape, while the light polarization dependence is sinusoidal and drops to zero for light polarized orthogonally to the long axis. These are key points to distinguish an isolated BP from a spherical particle or a cluster, which present several resonances or a polarization response not going to zero. As this mapping and selection of the nano-object may take some hours, it is realized without PTM (avoiding evaporation). The characterization of an analyzed BP in air is presented in Fig. (2.31).

The *ramp-up* begins after the introduction of a ruby ball on the clean culet (the one with no nanoparticles deposited) and of the PTM in the pressure chamber. The pressure is already increased by a small amount when loading the DAC. For the studied BP, the starting point was 0.055 GPa and the maximal value 9.72 GPa. Afterwards, the *ramp-down* was started, dropping the chamber pressure until a

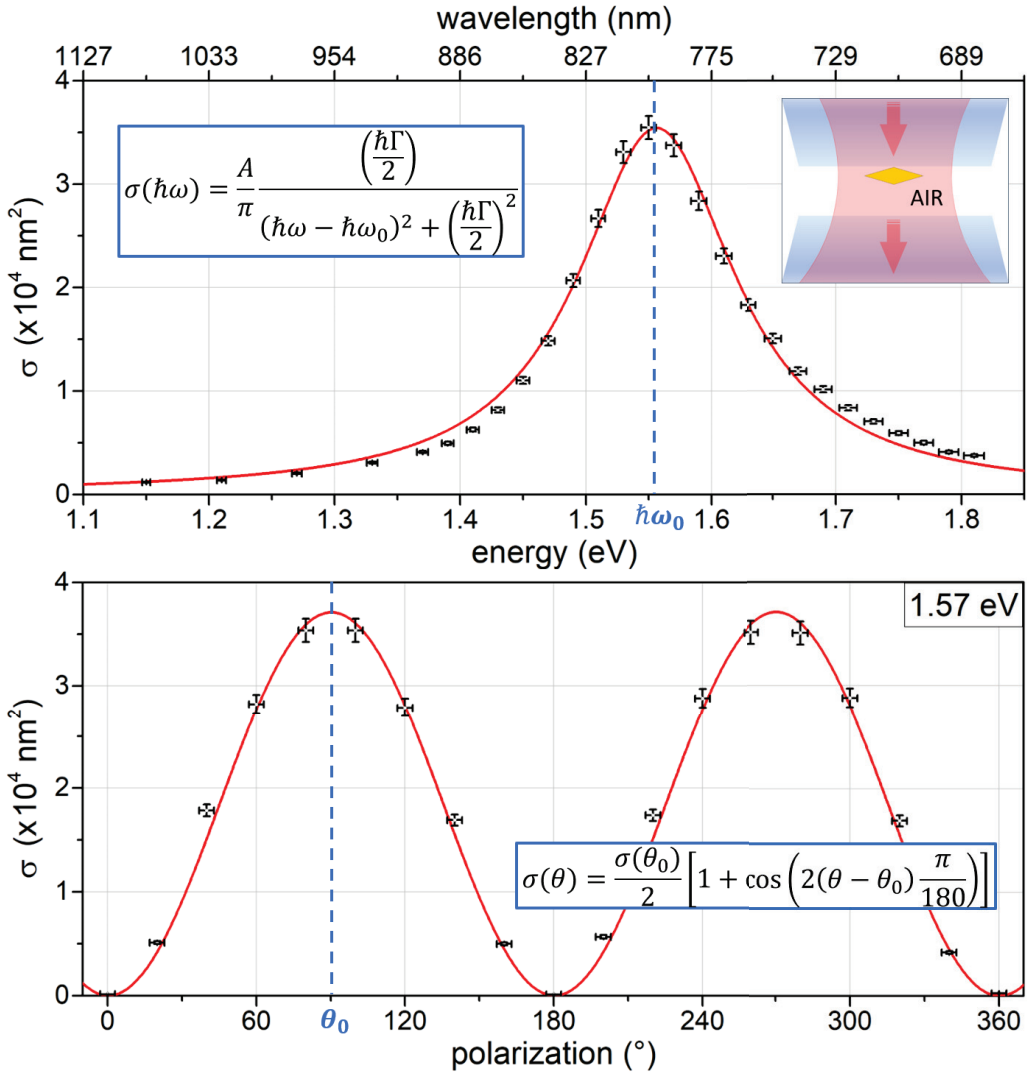

Figure 2.31: Extinction cross-section σ of "BP1" placed on the upper culet and surrounded by air. Top: the longitudinal SPR spectrum is fitted through a Lorentzian function centered at the photon energy $\hbar\omega_0$, with linewidth Γ and area A (Eq. (1.36) of Section (1.3.4)). Bottom: the polarization response at $\lambda = 800$ nm is fitted using a sinusoidal function with maximum $\sigma(\theta_0)$ at θ_0 and passing through zero at θ_0+90° (Eq. (1.40) of Section (1.3.4) with $\sigma_\perp = 0$).

residual value of 1.82 GPa. During the whole *pressure cycle*, the longitudinal SPR of the BP was measured and its polarization response verified. Lastly, the BP is characterized again in air, at 0 GPa. The beam spot *FWHM* was also characterized as a function of wavelength and pressure, yielding the pressure and wavelength dependence of Eq. (2.10) and allowing to convert the raw SMS signals in absolute cross-section, measured in nm^2.

Measuring the polarization response enables to monitor the orientation of the BP long axis. As illustrated in Fig. (2.32), it never changed during the pressure experiments. No modification of BP orientation has ever been detected in any *pressure cycle*, due to the strength of the van der Waals forces between nanoparticles and diamond. The SPR measured during the *ramp-up* and their Lorentzian fits are plotted in the graphs of Fig. (2.33). The main role of the *ramp-down* is to study the reversibility, by coming back to some pressure points already measured, as checked for this particular BP at 7.37 GPa. This extinction spectrum is displayed in Fig. (2.34) together with its counterpart of the *ramp-up*, exhibiting perfect reversibility. Unfortunately, during *ramp-down* after 7.37 GPa, the SPR started to redshift and broaden in time without any pressure modification. The reasons for this out-of-control behavior are unclear and may be ascribed to permanent modifications of the nano-object shape and/or its surface degradation.

The Lorentzian distribution fit function is completely determined by three parameters: peak position (SPR energy), linewidth and area, whose evolution are

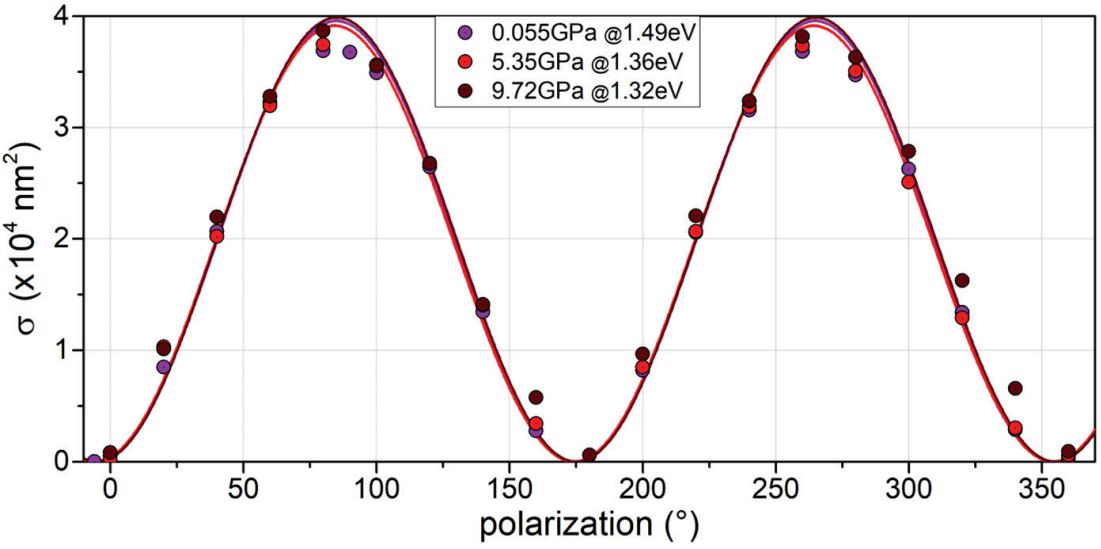

Figure 2.32: The polarization response of "BP1" remained unchanged during the experiment.

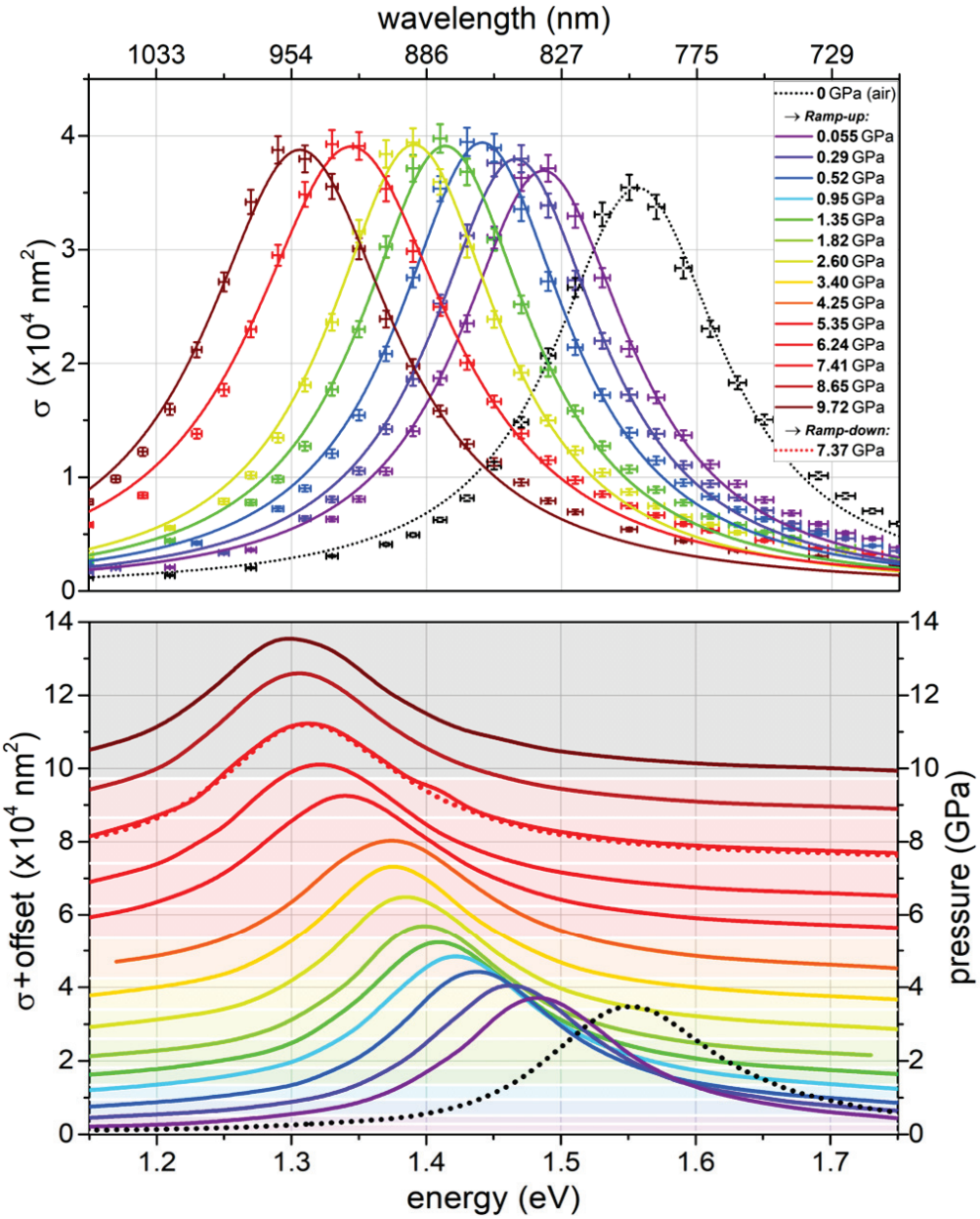

Figure 2.33: In the upper graph some of the measured extinction spectra of "BP1" are presented as well as their Lorentzian fits. In the lower graph, all experimental curves are shown, vertically shifted adding a constant proportional to the related pressure (the offsets are indicated by white lines below each curve and intersect the right axis at the corresponding pressure). The strong redshift experienced from 0 to 0.055 GPa is mainly due to the introduction of PTM. The reversibility of the process has been verified at 7.37 GPa (dashed red line).

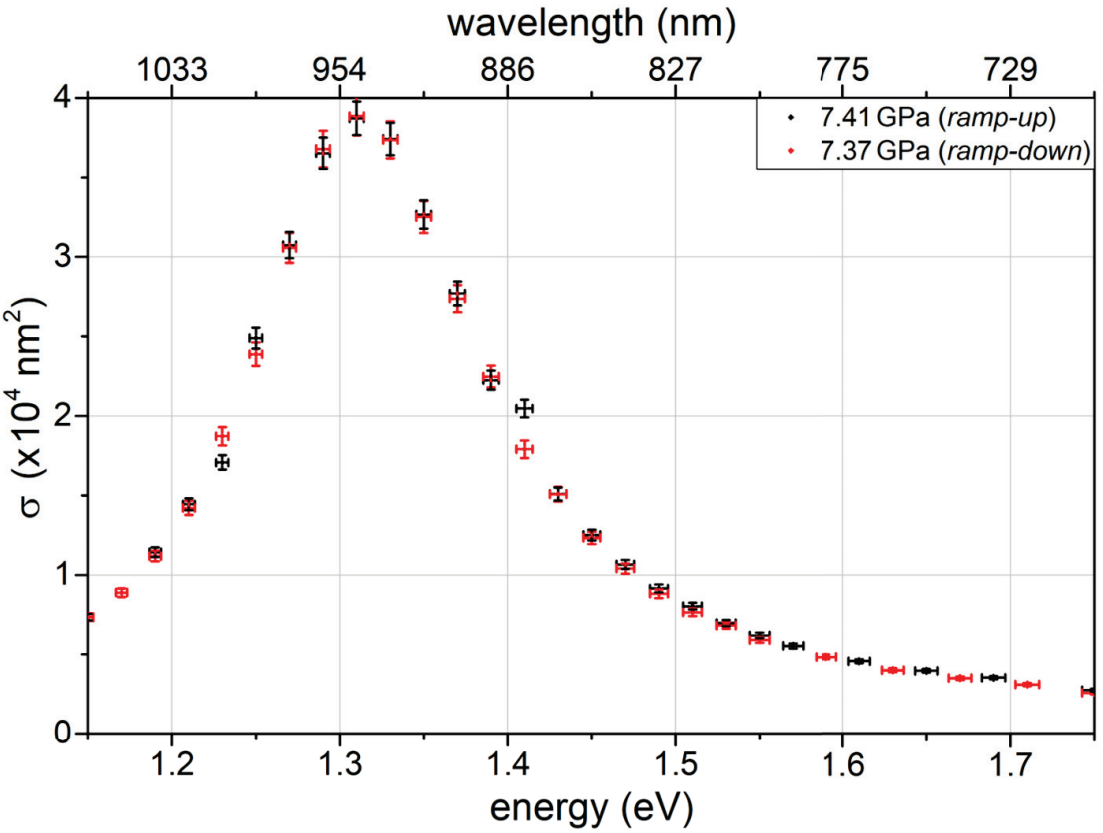

Figure 2.34: Extinction spectra during *ramp-up* and *ramp-down* show perfect reversibility at 7.4 GPa for "BP1".

illustrated in Fig. (2.35). The peak position of the resonance undergoes a non-linear monotonic redshift. These are the most precise data (smallest error bars) of all the pressure cycles and show a variation of about $\Delta E \sim -0.18\,\text{eV}$ (redshift of $\Delta E/E \sim -12\%$ for 10 GPa increase). Linewidth and area have more important vertical error bars, however they both exhibit an increase with pressure: spectral SPR broadening $\Delta(\hbar\Gamma) \sim 15\,\text{meV}$ ($\Delta\Gamma/\Gamma \sim 10\%$) and SPR area increase $\Delta A \sim 1500\,\text{eV nm}^2$ ($\Delta A/A \sim 15\%$) for 10 GPa increase. To confirm these trends, other single BPs are reported. Note that the sharp redshift and broadening that occurs around 5 GPa has been observed only in "BP1".

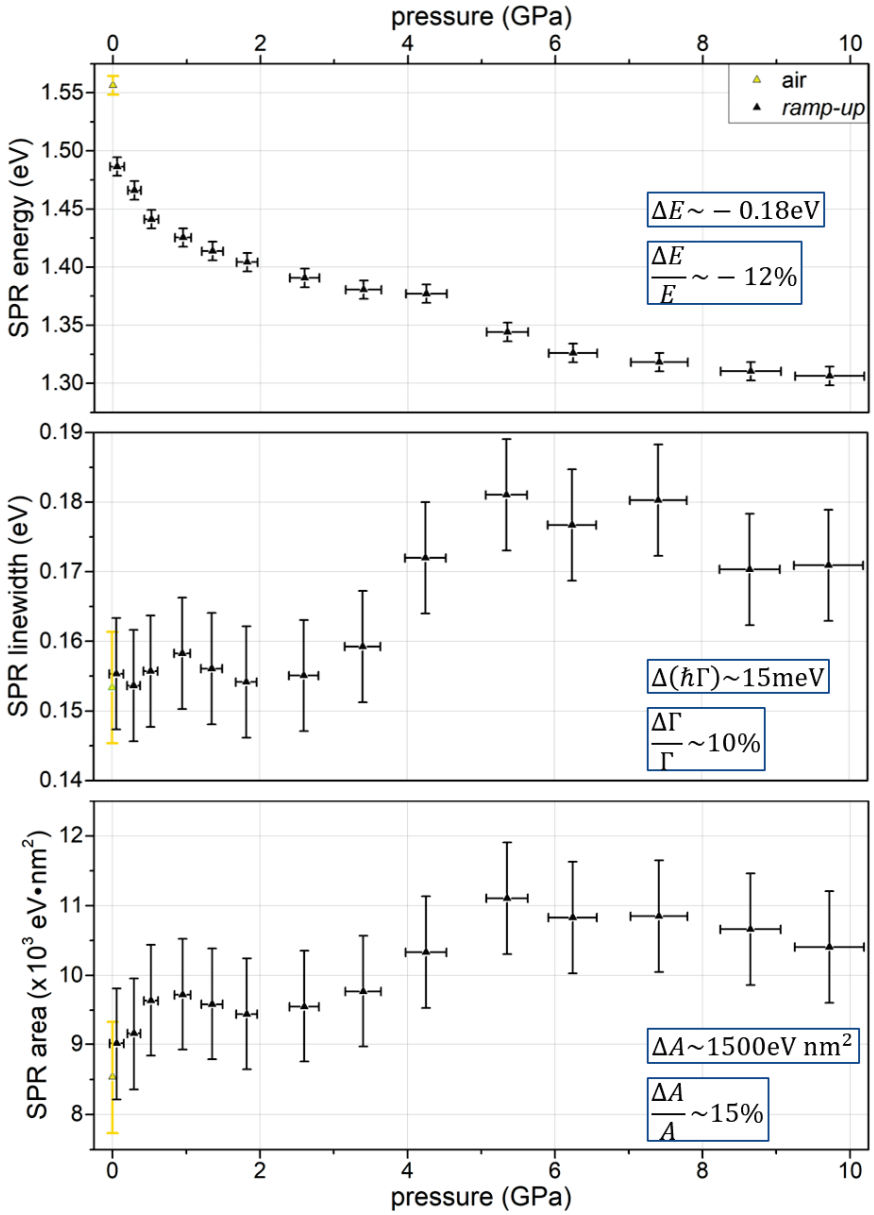

Figure 2.35: Evolution of the "BP1" Lorentzian fit through the *ramp-up*. The horizontal error bars are established looking at the pressure fluctuations during every SPR measurement, plus the intrinsic incertitude related to Eq. (2.11) estimated at 4% of the pressure, plus a standard error of 0.06 GPa, which takes into account eventual heterogeneity in the ruby ball as well as changes in temperature governed by Eq. (2.3). The vertical errors bars are determined by changing the fit parameter of interest while letting other fit parameters free to move until the Lorentzian function no longer fits experimental data.

BP2

The studied "BP2" particle was again an individual gold BP from sample 1 placed on the superior diamond anvil. Firstly, the BP was characterized in air. The *ramp-up* began at 0.058 GPa and ended at 9.52 GPa. Afterwards, a *complete ramp-down* took place, dropping the chamber pressure until the residual 1.59 GPa. Lastly, the BP was characterized in air, at 0 GPa.
During this experiment, the beam spot *FWHM* was not directly characterized, but, as the working conditions were the same as "BP1", Eq. (2.10) was exploited to convert the raw SMS signals in absolute extinction cross-sections. This transformation seems successful as the obtained SPR curves are symmetrical and Lorentzian-like. One reason why the *FWHM* was not directly measured is that the beam spot was somehow unusual, having two focus positions maximizing the SMS signal from the BP. Later on, it was understood that other particles present on the opposite culet could contaminate the SMS signal, similarly to what illustrated in Fig. (2.19) for the ruby ball case.
During the *complete pressure cycle*, the polarization response was repeatedly measured, and as shown in Fig. (2.36) the resonance goes always to zero at the same angle, demonstrating no re-orientation of the elongated nano-object.
The extinction spectra σ were fitted with the Lorentzian distribution. The evolution of peak position, linewidth and area are illustrated in Fig. (2.37). The peak position of the resonance undergoes a redshift that resembles to the one seen in "BP1", although no discontinuities occur. The *complete ramp-down* reveals the

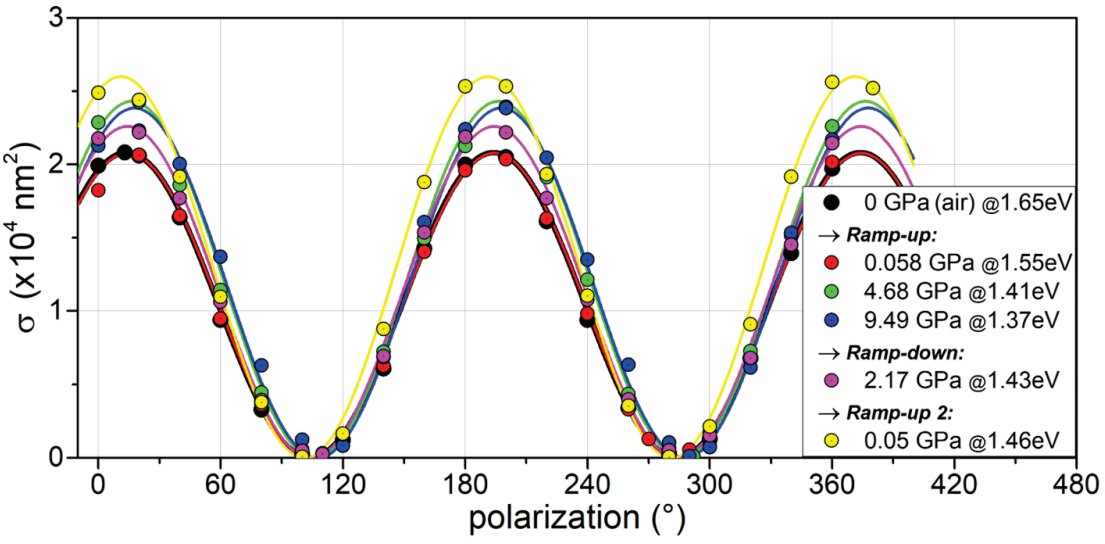

Figure 2.36: The polarization response of "BP2" remained unchanged during the experiment.

reversibility of this parameter. The peak position shows a non-reversibility only when measured in air, but this is probably due to a change in the environment refractive index after putting the BP back to air at the end of the cycle, as SPR is

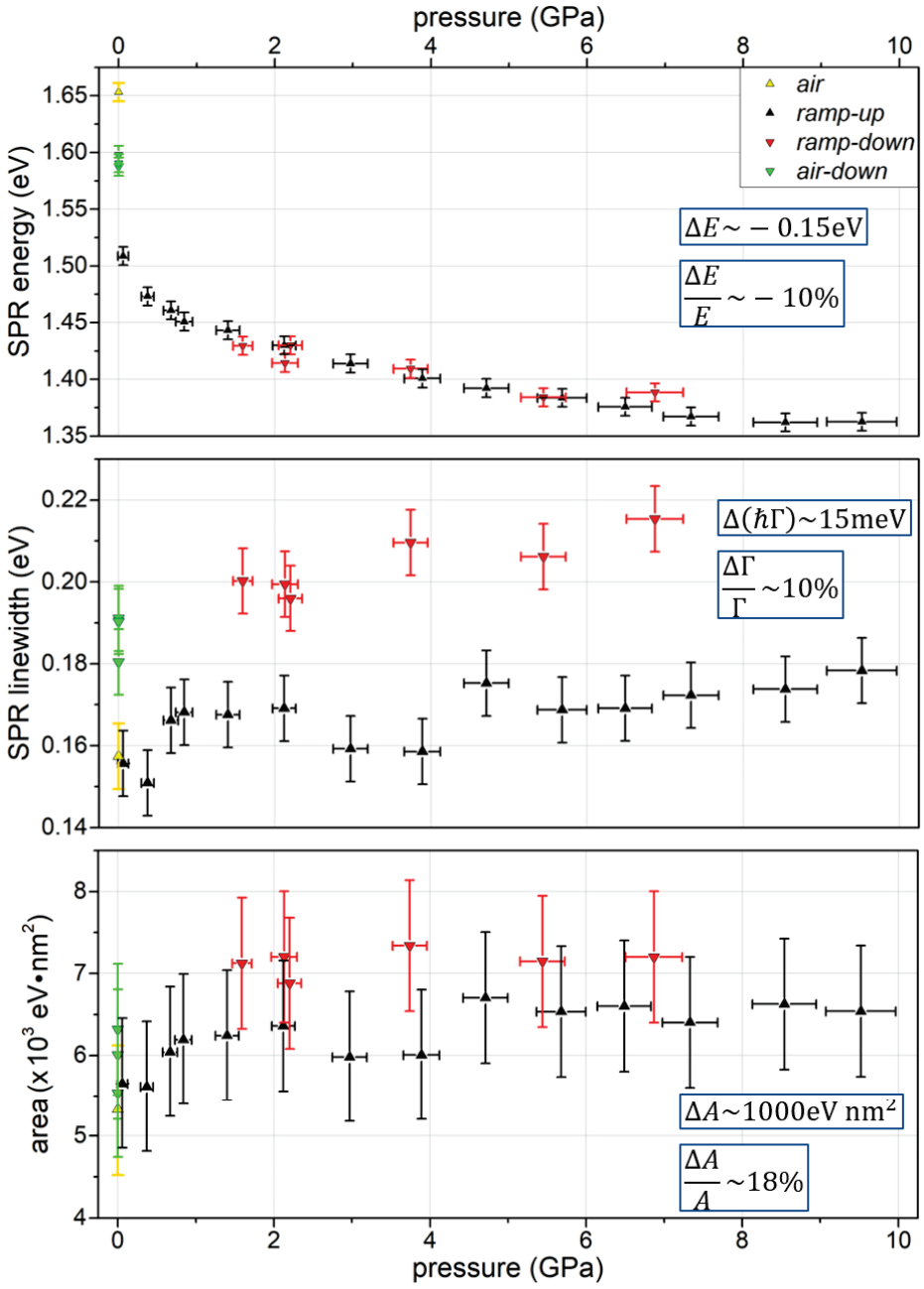

Figure 2.37: Evolution of the Lorentzian fit through the *complete pressure cycle* of "BP2".

very sensitive to residual liquid or water vapor. Linewidth and area undergo a soft augmentation throughout the *complete ramp-up*. During the *complete ramp-down* these parameters seem to decrease and come back. However, between these two measurements an additional broadening shows up. This unexpected behavior was observed only in "BP2" and its origins are unknown. One possibility is a systematic error introduced through a wrong focusing of the beam during the *ramp-down* experiments. The amplitudes of the induced pressure changes are very similar to those measured for "BP1": red shift $\Delta E \sim -0.15\,\text{eV}$ (with $\Delta E/E \sim -10\%$), broadening $\Delta(\hbar\Gamma) \sim 15\,\text{meV}$ (with $\Delta\Gamma/\Gamma \sim 10\%$), and enhancement area $\Delta A \sim 1000\,\text{eV nm}^2$ (with $\Delta A/A \sim 18\%$), the three presenting a non-linear dependence on pressure.

BP3

During experiment "BP3", the studied object was a cluster composed by two aligned nano-objects from sample 1, placed on the superior diamond anvil. Firstly, the BPs were characterized in air. At that time, the ruby ball was not characterized in air, at 0 GPa. Therefore the first pressure point of the *ramp-up* was not precisely measured. Supposing that the DAC loading produces a starting pressure similar to the one of "BP1" and "BP2", the *ramp-up* then started at 0.05 GPa and ended at 8.54 GPa. Afterwards, a *complete ramp-down* took place, dropping the chamber pressure until the residual 0.33 GPa. Lastly, the BP was studied again in air, at 0 GPa.
Over the course of the experiment "BP3", the beam spot *FWHM* was not directly characterized. However, as the working conditions were the same as "BP1", Eq. (2.10) was exploited to convert the raw SMS signals to absolute extinction cross-section.

The measured extinction spectra present two SPR peaks and are well fitted by a double-Lorentzian distribution. Supposing that the two nano-objects are two BPs subjected to the same broadening, the two linewidths are fitted with the same value, while the two peak positions and areas are kept independent. As illustrated in Fig. (2.38), this kind of fit is satisfactory until the end of the *ramp-down*, where the SPR second peak is not recognizable anymore. During the *complete pressure cycle*, the polarization response was repeatedly measured and the signal is always minimized at the same angle, as showed in Fig. (2.39).
The peak position of the two resonances undergo a redshift that resembles to the one seen in "BP1" and "BP2", despite a very little discontinuity can be noticed about 7 GPa (see Fig. (2.40)). The *complete ramp-down* reveals the reversibility of the position with a redshift of $\Delta E \sim -0.14\,\text{eV}$ ($\Delta E/E \sim -10\%$) upon 10 GPa. However, fitting with a double-Lorentzian distribution with the same linewidth adds additional parameters which increases the error bars. Consequently, the

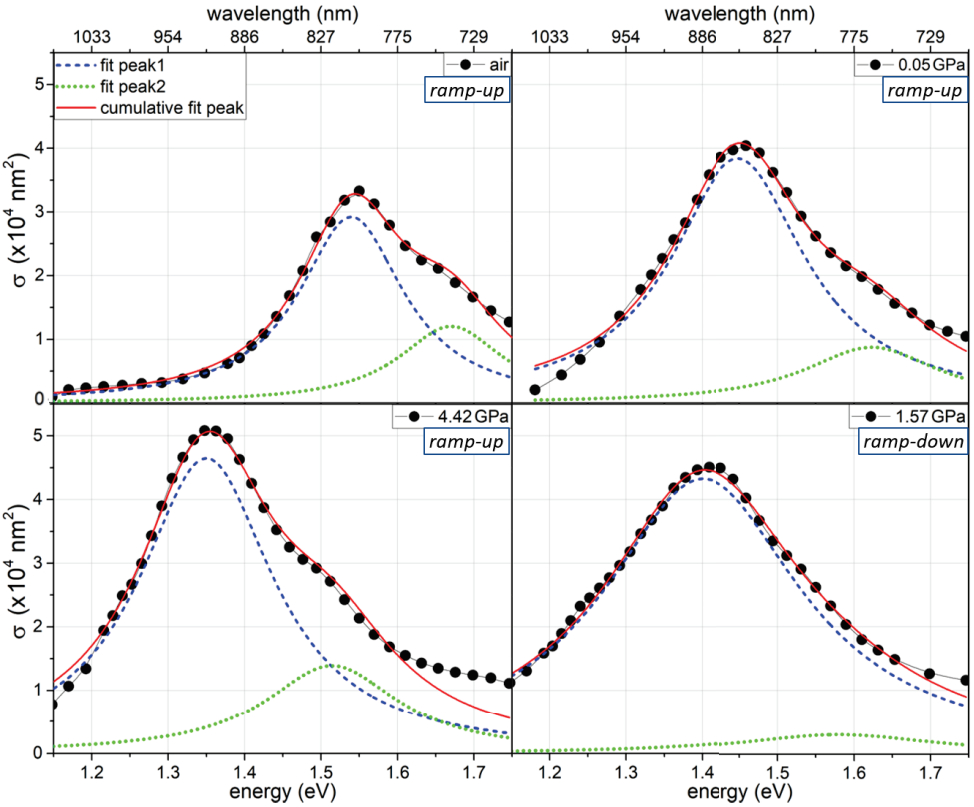

Figure 2.38: Double-Lorentzian fit curves allow to reproduce the SPR shape of "BP3" cluster until 4 GPa of the *ramp-down*, where only one peak remains.

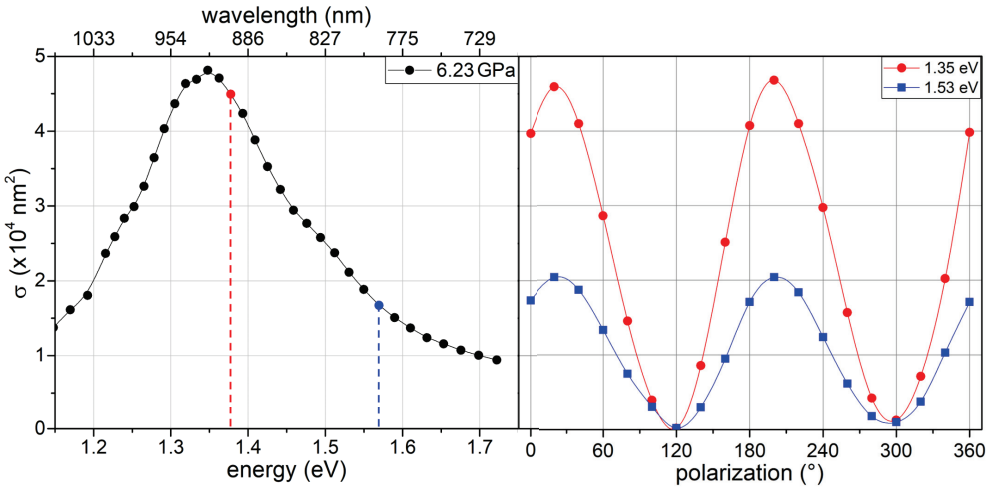

Figure 2.39: Polarization responses for "BP3" cluster measured at 6.2 GPa of the *ramp-down* for two different wavelengths.

linewidth and the area should not be examined, though a general trend similar to the previous ones seems to occur.

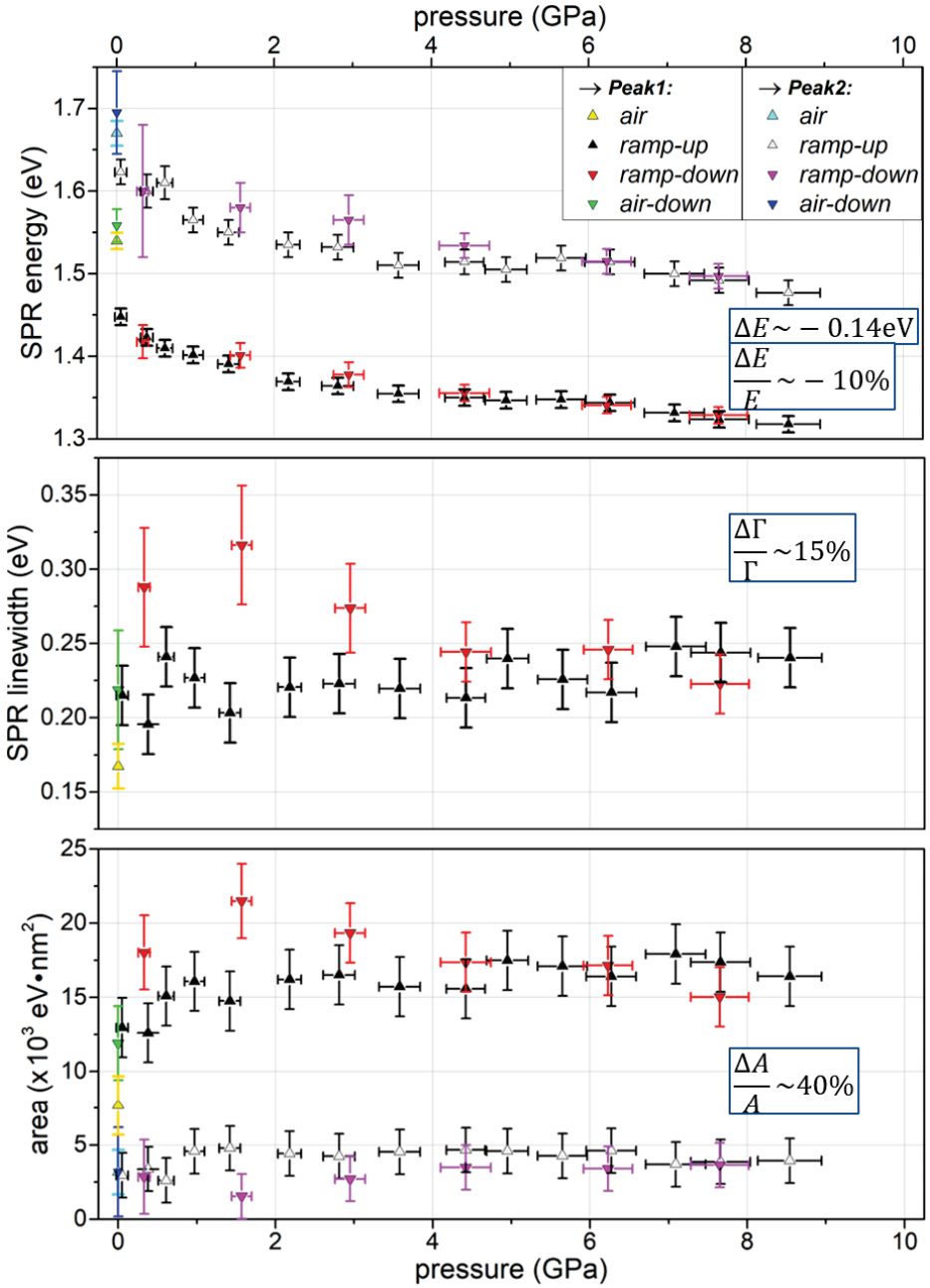

Figure 2.40: Evolution of the double-Lorentzian fit through the *complete pressure cycle* of "BP3". Vertical error bars become larger starting from 3 GPa of the *ramp-down* because the second peak is very weak and its characterization becomes uncertain.

BP4

During experiment "BP4", the studied particle was a gold BP from sample 2, placed on the inferior diamond anvil. The ruby ball was not characterized in air (0 GPa) and, as in the case of "BP3", the *ramp-up* is supposed to start at 0.05 GPa, ending at 7.61 GPa. Afterwards, a *complete ramp-down* took place, dropping the chamber pressure until the residual 1.75 GPa. During the *complete pressure cycle*, the polarization response was repeatedly measured and the signal goes to zero always at the same angle.
During the experiment "BP4", the beam spot size and the BP amplitude of oscillation were unknown, preventing from a conversion of the raw SMS signal to an absolute cross-section quantitative value.
Even without conversion, the observed SPRs can be satisfactorily reproduced by a Lorentzian distribution. Note that, when the raw SMS signal is directly fitted (instead of absolute extinction cross-section), peak position and linewidth are still reliable (however with introduction of a modest systematic error that can be estimated of the order of -0.01 eV and therefore can be corrected). On the other hand the area, measured in $\mathrm{eV}\cdot\mathrm{nm}^2$, cannot be quantified. Original and retrieved data are illustrated in Fig. (2.41). The typical redshift is dominating, while a small broadening shows up. Data indicate that a pressure change of 10 GPa induces a redshift $\Delta E \sim -0.12$ eV (with $\Delta E/E \sim -9\%$) and a broadening $\Delta(\hbar\Gamma) \sim 30$ meV (with $\Delta\Gamma/\Gamma \sim 16\%$). The *complete ramp-down* of "BP4" counts several pressure points, because the aim was to verify the reversibility of the SPR. During the *complete pressure cycle*, no discontinuity was observed.

BP5

During experiment "BP5", the studied particle was a gold BP from sample 2, placed on the inferior diamond anvil. The *ramp-up* began at 0.5 GPa and ended at 7.5 GPa. Afterwards, the gasket hole became asymmetrical (as seen in Fig. (2.6)) and a PTM leaking forced to abort the experiment.
During experiment "BP5", beam spot size and amplitude of oscillation were unknown, making impossible to convert the raw SMS signal to absolute extinction cross-section. Over the course of the *ramp-up*, the polarization response was repeatedly verified.
When the raw SMS signal is directly fitted, peak position and linewidth are still reliable, despite the introduction of a modest systematic error, that has been corrected. This is illustrated in Fig. (2.41), confirming the typical redshift with a soft broadening that, over a pressure change of 10 GPa, is about $\Delta E \sim -0.09$ eV (with $\Delta E/E \sim -7\%$) and $\Delta(\hbar\Gamma) \sim 40$ meV (with $\Delta\Gamma/\Gamma \sim 23\%$).

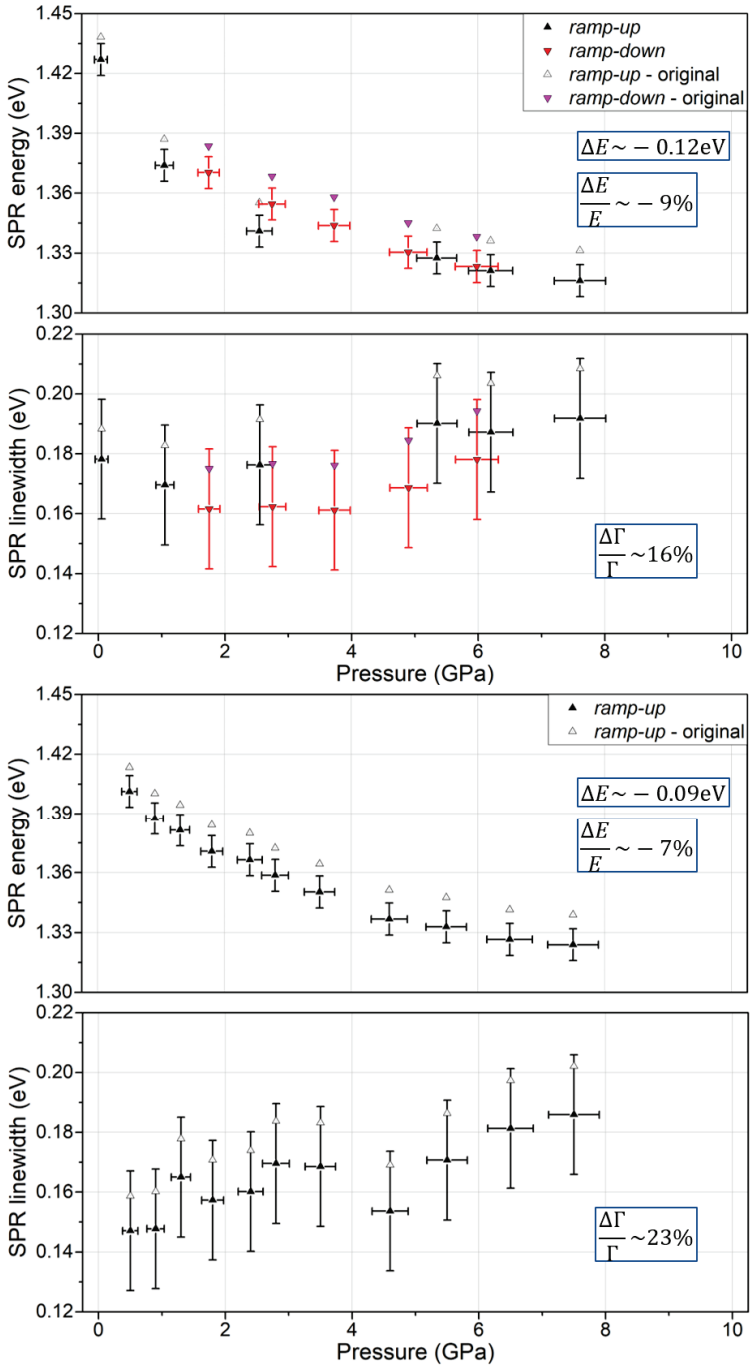

Figure 2.41: Evolution of the Lorentzian fit through the *complete pressure cycle* of "BP4" in the two upper graphs and through the *complete pressure cycle* of "BP5" in the lower ones.

	BP1	BP2	BP3	BP4	BP5
SAMPLE	individual Au-BP @PEG sample 1; upper culet, 4Me:1Et.	individual Au-BP @PEG sample 1; upper culet, 4Me:1Et.	cluster of 2 Au-BP @PEG sample 1; upper culet, 4Me:1Et.	individual Au-BP @PEG sample 2; lower culet, 4Me:1Et.	individual Au-BP @PEG sample 2; lower culet, 4Me:1Et.
SMS	quantitative: $f = 940$ Hz; $\delta = 590$ nm; *FWHM* measured (yielding Eq. (2.10)).	quantitative: $f = 940$ Hz; $\delta = 590$ nm; *FWHM* from Eq. (2.10).	quantitative: $f = 940$ Hz; $\delta = 590$ nm; *FWHM* from Eq. (2.10).	qualitative: $f = 825$ Hz.	qualitative: $f = 825$ Hz.
PRESSURE	*complete ramp-up* & beginning *ramp-down.*	*complete pressure cycle.*	*complete pressure cycle.*	*complete pressure cycle.*	*ramp-up.*
RESULTS	redshift & broadening; reversibility until 7 GPa in *ramp-down.*	redshift & broadening; *complete* reversibility.	redshift & broadening; *complete* reversibility.	redshift & broadening; *complete* reversibility.	redshift & broadening; reversibility not verified.
OTHER EFFECTS	enhanced redshift & broadening @ 5 GPa *ramp-up.*	additional broadening @ beginning *ramp-down.*			

Table 2.2: Brief summary of the characteristics of the various experiments, identified by the columns "BP1", "BP2", "BP3", "BP4", "BP5". The line "SAMPLE" introduces the studied nanostructures and their environment; "SMS" reports the main working parameters and specifies if the optical study was "quantitative" or "qualitative", i.e. if the absolute cross-section in nm^2 was retrieved or not; "PRESSURE" describes the range of pressure investigated; "RESULTS" contains the main effects of the pressure *ramp-up* and states their eventual reversibility; the line "OTHER EFFECTS" reports additional observations in the SPR position or linewidth while the pressure was changing.

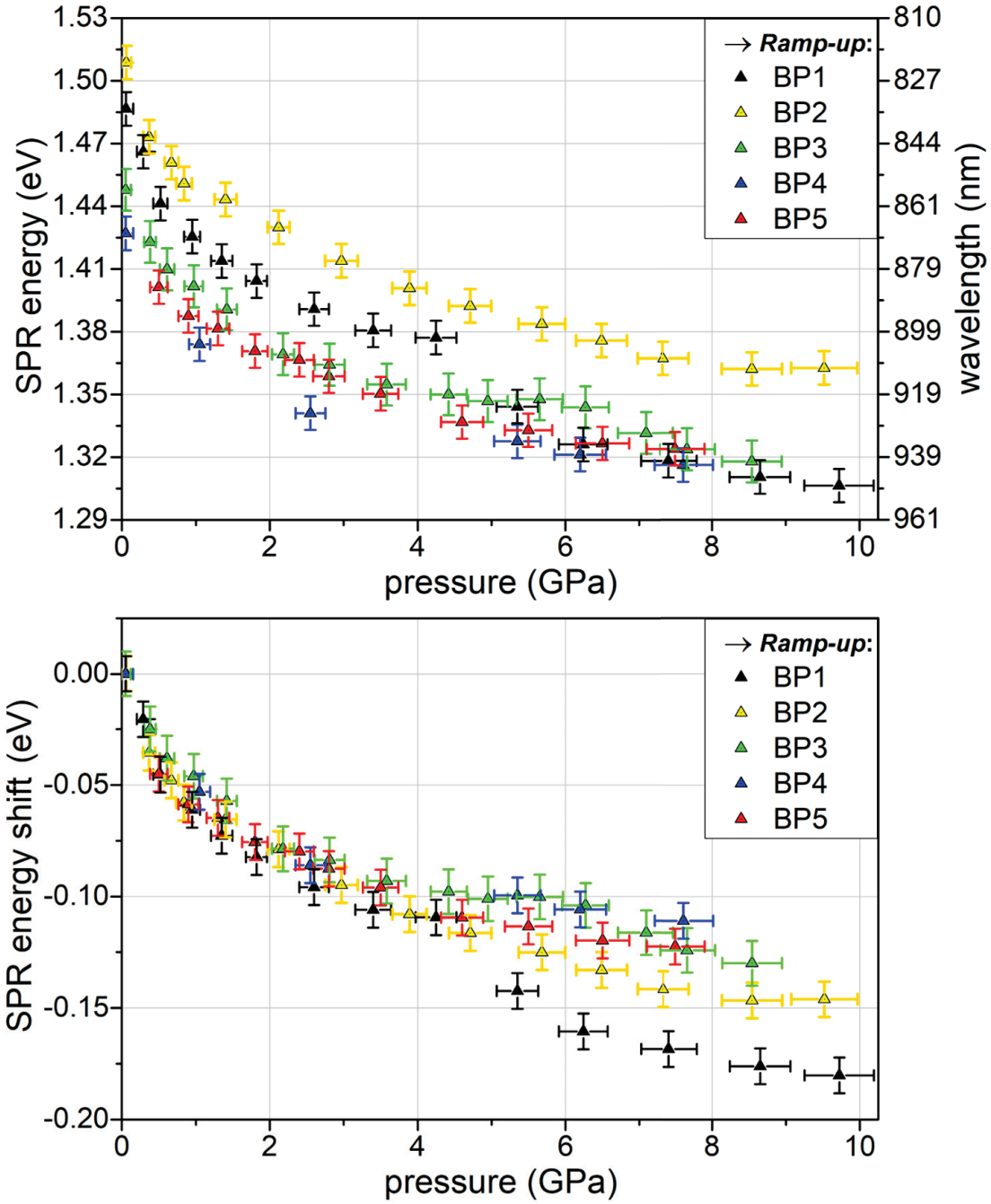

Figure 2.42: Upper graph: SPR energy measured from ramp-up experiments realized on individual gold BP placed on the diamond substrate. Lower graph: SPR energy shift induced by pressure increase.

2.2.1 Pressure dependence of the SPR spectral position

As seen in the previous section, the pressure ramp-up produces a redshift in the SPR position which is modeled in the current section. Firstly, complete numerical simulations based on the finite elements modeling (FEM) and taking into account the real geometry of the experiment are presented. Afterwards, a simplified analytical model is developed with the aim of enlightening the main physical origins of the observed evolution.

The experimental SPR energy data of all BPs are summarized in the upper graph of Fig. (2.42), while the lower one directly shows the SPR energy shifts with respect to initial position. This peak translation is not linear with the pressure, and is modeled in the current section. Moreover, until 5 GPa the curves are overlapped, while they separate at higher pressures. In particular, "BP1" present a strong shift at 5 GPa that can not be explained through a simple model. The reasons of these deviations at high pressure will be discussed later (Section (2.2.3)).

NUMERICAL MODEL

The FEM has been realized in the configurations reported in Fig. (2.43), where an individual Au-BP of volume V, aspect-ratio η and 30 nm short axis, is separated from a diamond substrate by distance d, which could be introduced to take into account the presence of surfactants. The nanoparticle is characterized

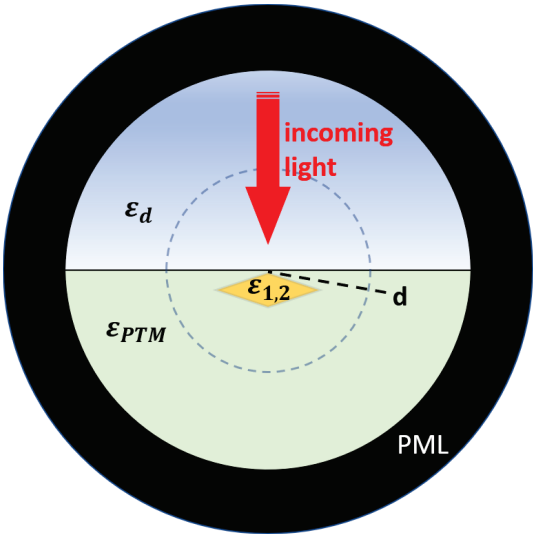

Figure 2.43: Configuration adopted for the FEM.

volumetrically by the compressibility of bulk gold and optically through the pressure dependent dielectric functions of gold, whose real and imaginary parts are

$\epsilon_{1,2}(\omega) = \epsilon^D_{1,2} + \epsilon^{ib}_{1,2}$, where $\epsilon^D_{1,2}$ indicates the Drude components and $\epsilon^{ib}_{1,2}$ the inter-band contributions. The BP environment consists of the diamond substrate and the 4Me:1Et as surrounding liquid, which are respectively modeled by the real dielectric functions $\epsilon_d(\omega) = n_d^2$ and $\epsilon_{PTM}(\omega) = n_{PTM}^2$, whose imaginary parts are negligible for red and near-IR photons, as explained in Appendix (B) and (C). A polarized and monochromatic Gaussian wave of intensity I_0, passes through the diamond and illuminates the BP, exciting its longitudinal SPR at the photon frequency ω. Computations in this geometry yield the spatial distribution of the electromagnetic field from which absorption and scattering cross-section are deduced. The absorption component is calculated integrating the differential form of the Joule heating equation over the nano-object volume

$$\sigma_{abs} = \frac{1}{I_0} \int Re\{\vec{j} \cdot \vec{E}^*\} dV \,, \tag{2.31}$$

where $\vec{j}$ is the current density and $\vec{E}$ is the electric field. The scattering part is computed from the flux of the Poynting vector of the scattered field over a virtual sphere surrounding the nanoparticle

$$\sigma_{sca} = \frac{1}{I_0} \oint \frac{1}{2} Re\{\vec{E}_{sca} \cdot \vec{H}^*_{sca}\} dS \,. \tag{2.32}$$

In order to avoid artifacts coming from the boundaries back-reflected radiation, a perfectly-matched layer (PML) has been introduced between two wider spherical boundaries, of radii 200 and 260 nm. At a fixed frequency ω, the computed extinction cross-section is

$$\sigma_{ext} = \sigma_{abs} + \sigma_{sca} \,. \tag{2.33}$$

By varying ω, the entire σ_{ext} spectrum can be calculated. A change in pressure P affects both the volume of the gold nanoparticle and the optical properties of the nanoparticle and environment ($\epsilon^D_{1,2}$, ϵ_d and ϵ_{PTM}, through relations: Eq. (1.13) of Chapter 1 , Eq. (B.4) of Appendix (B) and Eq. (C.4) of Appendix (C). These effects are taken into account in the numerical simulations, which provide the longitudinal SPR spectrum for each desired pressure.

As illustrated in Fig. (2.44), the FEM simulations with horizontal BPs in contact with the diamond substrate ($d = 0$ nm) show an excellent agreement with the experimental SPR shift observed in all the BPs, meaning that the considered ingredients (pressure dependence of dielectric functions and volume) are responsible for the observed response. The aspect-ratio η of each nanoparticle has been chosen to reproduce the SPR of the measured cross-section σ at the initial lowest pressure value. This aspect-ratio, coherent with TEM measurements of the initial solution, is kept constant for all the applied pressures. The numerical simulations

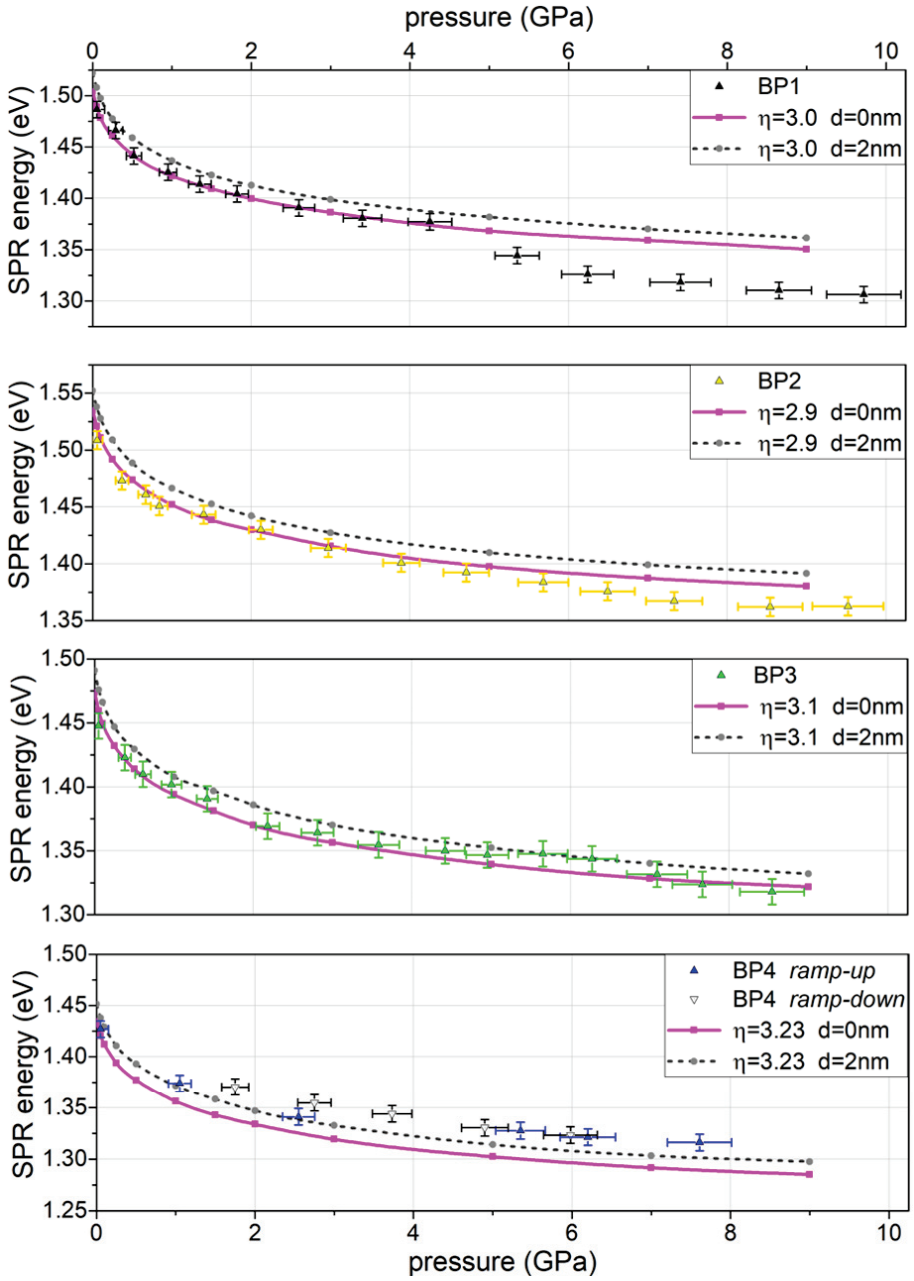

Figure 2.44: Reproduction of the experimental data through the FEM approach. Experimental data are points with error bars. Lines identify the SPR peak position obtained from the FEM realized on an horizontal BP of aspect ratio η: the violet solid line corresponds to a perfect contact between BP and diamond ($d = 0\,\text{nm}$); gray dotted lines correspond to the configuration where the BP is separated from the diamond because of the surfactant presence ($d = 2\,\text{nm}$).

also allows to take into account different configurations, such as the presence of the surfactant layer around the nanoparticle, introducing a distance d between particle and substrate from 0 to 2 nm [79]. As displayed in Fig. (2.44), considering $d \neq 0$ does not change the curvature of the simulated shift. The main consequence is a uniform blueshift (+0.01 eV if $d = 2$ nm), which can be compensated by slightly increasing η (from 3 to 3.05, consistent with the uncertainty of the morphological characterization), thus recovering a good fit of the low pressure spectrum. The simulation on experiment "BP5" has not been reported as experimental data overlap with the ones of "BP4".

SEMI-ANALYTICAL MODEL

The semi-analytical model is a powerful tool to provide a physical insight into the observed pressured-induced effects.
In dipolar approximation, when the SPR lies far from the interband transition threshold, as in the case of an elongated Au-BP, the SPR is spectrally described by a quasi-Lorentzian profiled centered around

$$\omega_R = \frac{\omega_p}{\sqrt{\epsilon_1^{ib} + H\epsilon_{PTM}}}, \tag{2.34}$$

where

$$\omega_p = \sqrt{\frac{Ne^2}{Vm\epsilon_0}} \tag{2.35}$$

is the plasma frequency of gold. Eq. (2.34) is an extension of Eq. (1.26) and (1.34) of Chapter 1, valid for a sphere and elongated ellipsoid in an homogeneous environment, for an arbitrary nano-object in a generic environment. Here, H is a geometric factor depending on the BP aspect-ratio η and on the configuration considered (shape, size, environment, substrate distance). For an ellipsoidal shape, analytical expressions can be used to calculate H. For the general case, as the present one, numerical FEM simulations have been performed for a BP of aspect-ratio η deposited on diamond and embedded in PTM (see Fig. (2.43)). Once the aspect-ratio identified for each BP, its extinction spectrum is computed for different values of ϵ_{PTM}. From Eq. (2.34) it follows

$$(\omega_R/\omega_p)^{-2} = H\epsilon_{PTM} + \epsilon_1^{ib} \tag{2.36}$$

which has been exploited to retrieve H, as illustrated in Fig. (2.45).

The following approximations are made in the semi-analytical model presented here: the dipolar regime applies (i.e. the nanoparticle sizes are small with respect to the light wavelengths); the SPR is located far away from the gold interband

transition frequencies ($\omega_R \ll \omega_{ib}$), being a quasi-Lorentzian with position independent from ϵ_2; the interband component of the gold real dielectric function has negligible dispersion in frequency $\epsilon_1^{ib} \approx \epsilon_1^{ib}(\omega_R)$; the nanoparticle has an elongated shape with aspect-ratio η (but it is not an ellipsoid) and $H(\eta)$ can be numerically determined performing FEM simulations; the product $H\epsilon_{PTM}$ allows to take into account the impact of the global environment (including both PTM and diamond substrate) on the BP resonance position ω_R at $P = 0\,\text{GPa}$; only the pressure dependence of the PTM is considered because the pressure changes of the diamond refractive index are 60 times smaller than the PTM ones in the $0-10\,\text{GPa}$ range (Appendix (B) and (C)); the frequency dependence of ϵ_{PTM} can be neglected (as shown Fig. (C.2) of Appendix (C)); in the interval $0-10\,\text{GPa}$, the BP volumetric compression is governed by the linear relation

$$V = V_0(1 - k_{Au}P)\,, \tag{2.37}$$

where V is the BP volume at the pressure P, V_0 is the BP volume at 0 GPa and $k_{Au} = 5.77\times10^{-3}\,\text{GPa}^{-1}$ is the bulk gold isothermal compressibility at 300 K [80].

Considering Eq. (2.34), the pressure shift of ω_R may be seen as a consequence of the pressure variations of ω_p, ϵ_{PTM} and ϵ_1^{ib}

$$\frac{d\omega_R}{dP} = \frac{\partial\omega_R}{\partial\omega_p}\frac{\partial\omega_p}{\partial P} + \frac{\partial\omega_R}{\partial\epsilon_{PTM}}\frac{\partial\epsilon_{PTM}}{\partial P} + \frac{\partial\omega_R}{\partial\epsilon_1^{ib}}\frac{\partial\epsilon_1^{ib}}{\partial P} \tag{2.38}$$

which can be developed as follows

$$\frac{d\omega_R}{dP} = \frac{\omega_R}{2}k_{Au} - \frac{\omega_R}{2}H\left(\frac{\omega_R}{\omega_p}\right)^2\frac{\partial\epsilon_{PTM}}{\partial P} - \frac{\omega_R}{2}\left(\frac{\omega_R}{\omega_p}\right)^2\frac{\partial\epsilon_1^{ib}}{\partial P}\,. \tag{2.39}$$

The first term has been rearranged considering $\partial\omega_R/\partial\omega_p = \omega_R/\omega_p$ (from Eq. (2.34)) and $\partial\omega_p/\partial P = \partial\omega_p/\partial V \times \partial V/\partial P = -\omega_p/(2V)\times(-k_{Au}V)$, following from the plasma frequency dependence on volume (Eq. (2.35)) and from Eq. (2.36). Transformation of the second and third terms follows from Eq. (2.34).
Considering $\hbar\omega_R \sim 1.55\,\text{eV}$, it results $(\omega_R/\omega_p^0)^2 \sim 3\times10^{-2}$ (ω_p^0 being the gold plasma frequency calculated at V_0: $\hbar\omega_p^0 = 9\,\text{eV}$), while $H \sim 10$, $d\epsilon_{PTM}/dP \sim 1\times10^{-1}\,\text{GPa}^{-1}$ and $d\epsilon_1^{ib}/dP < 4\times10^{-2}\,\text{GPa}^{-1}$, meaning the last term of Eq. (2.39) is negligible compared to the first two, yielding the non-linear differential equation in $\omega_R = \omega_R(P)$

$$\frac{d\omega_R}{dP} - \frac{k_{Au}}{2}\omega_R + \frac{H}{2}\frac{d\epsilon_{PTM}}{dP}\frac{\omega_R^3}{\omega_p^2} = 0\,, \tag{2.40}$$

where ω_p depends on P according to Eq. (2.35) and (2.37). Its solution depends on the value of H, which is determined numerically, as discussed above. Importantly,

for both full-numerical (FEM) and semi-analytical modeling, an initial numerical computation is needed to determine aspect ratio η, or equivalently H, by comparison of numerically generated and experimental spectra for a specific pressure.
Note that the differential equation (Eq. (2.40)) can also be obtained starting from ω_R general dependency on environment index (ϵ_m) and gold dielectric functions ($\epsilon^D_{1,2}$ and $\epsilon^{ib}_{1,2}$) under the same assumptions made here, as detailed in Appendix (D).

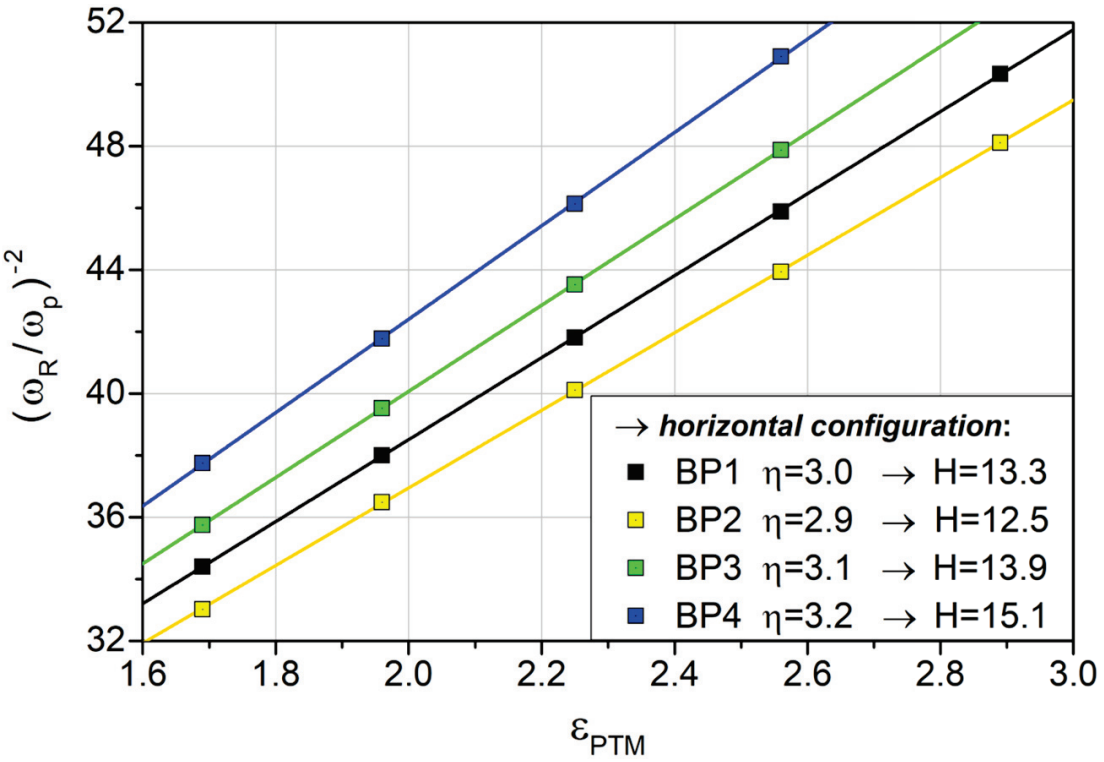

Figure 2.45: Determination of the factor H through linear fits of the numerically computed SPR position of BP in different conditions: in each curve, related to a particular aspect-ratio η, the slopes are equal to H.

Eq. (2.40) has been numerically solved using, as boundary condition, the experimental point at the lowest measured pressure for "BP1" and "BP2", and the second lowest measured pressure for "BP3" and "BP4". Results of this simplified approach, reported together with the experimental data in Fig. (2.46), are almost identical to the ones obtained through the complete FEM simulations. This proves that the main effects responsible for the observed SPR shift are the pressure induced modifications of the environment refractive index (especially of the PTM one) and of the metal (real part of its dielectric function).

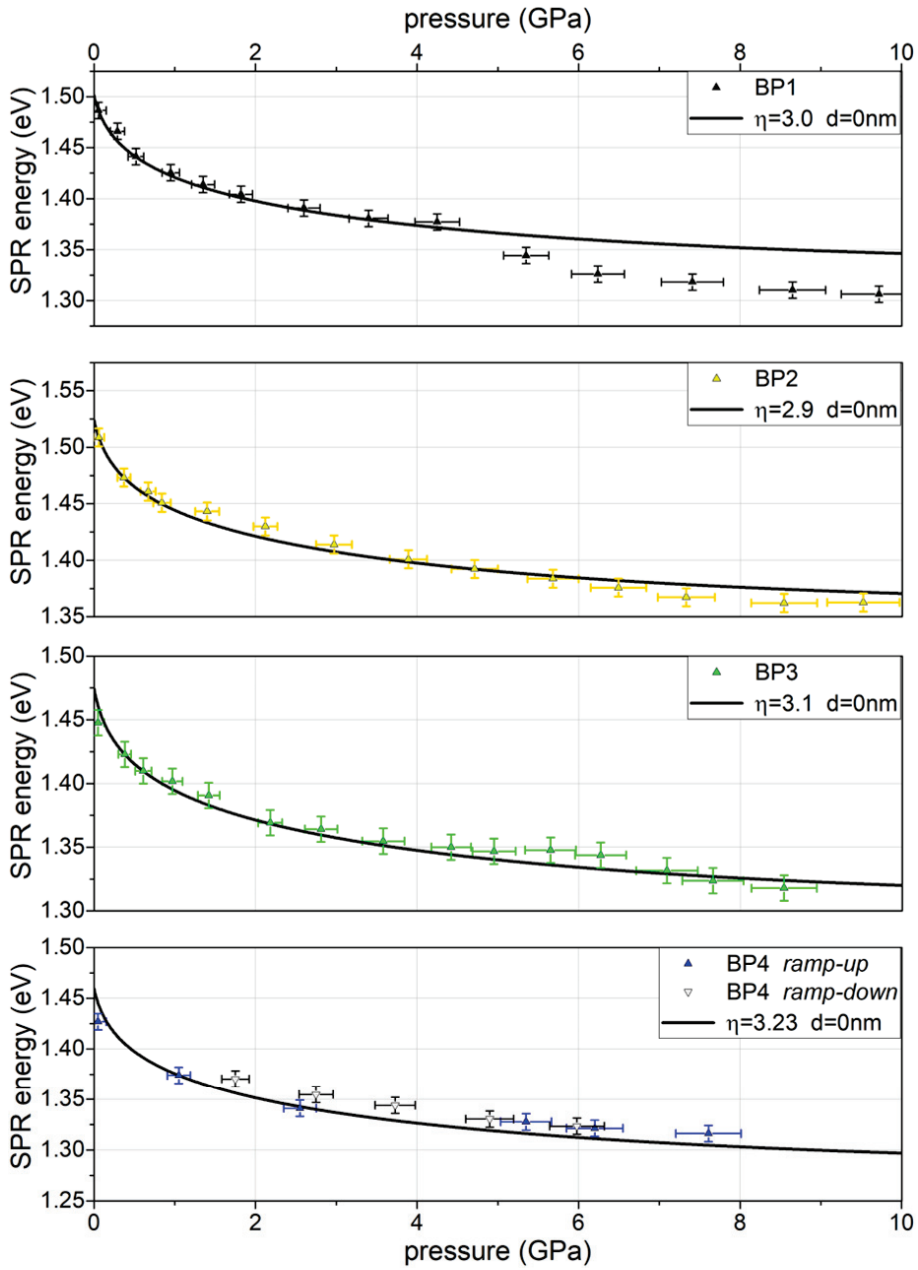

Figure 2.46: Reproduction of experimental data through the numerical resolution of differential equation Eq. (2.40), based on the Mie theory and the Drude model. These results are basically identical to the ones obtained through the FEM approach with $d = 0\,\text{nm}$ (Fig. (2.44)).

In order to go further into the physical mechanisms behind the SPR shift, an analytical study of the non-linear Eq. (2.40) is proposed, based on an iterative approach. A small pressure increment from $P_0 = 0\,\mathrm{GPa}$ to P_1 will shift the resonant frequency from ω_R^0 to $\omega_1 = \omega_R^0 + \Delta\omega_1(\omega_R^0)$, where

$$\Delta\omega_1(\omega_R^0) = \omega_R^0 \int_{P_0}^{P_1} \left[\frac{k_{Au}}{2} - \frac{H}{2} \frac{(\omega_R^0)^2}{(\omega_p^0)^2} \frac{\partial \epsilon_{PTM}}{\partial P} \right] dP = \omega_R^0 \left[\frac{k_{Au}}{2} \Delta P - \frac{H}{2} \frac{(\omega_R^0)^2}{(\omega_p^0)^2} \Delta_1 \epsilon_{PTM} \right] , \tag{2.41}$$

with

$$\begin{cases} \Delta P = P_1 - P_0 \\ \Delta_1 \epsilon_{PTM} = \epsilon_{PTM}(P_1) - \epsilon_{PTM}(P_0) \end{cases} . \tag{2.42}$$

Note that the pressure dependence of $1/\omega_p^2$ introduces a correction that will be neglected here ($\hbar\omega_p^0 = 9\,\mathrm{eV}$). Eq. (2.41) has been evaluated at the starting frequency ω_0, and is valid only for small increments in pressure. The new resonant frequency becomes

$$\omega_1 = \omega_R^0 \left[1 + \frac{k_{Au}}{2} \Delta P - \frac{H}{2} \frac{(\omega_R^0)^2}{\omega_p^2} \Delta_1 \epsilon_{PTM} \right] . \tag{2.43}$$

Subsequently, the pressure can be raised from P_1 to $P_2 = P_1 + \Delta P$, producing a new resonance at $\omega_2 = \omega_1 + \Delta\omega_2(\omega_1)$ that is obtained integrating at ω_1 fixed. As the dependence of $\omega_1(\omega_R^0)$ on ω_R^0 has a known expression (Eq. (2.43)), $\omega_2(\omega_1)$ can be expressed as a function of ω_R^0. After N steps, one obtains

$$\omega_R(P = N\Delta P) = \omega_R^0 + \lim_{\Delta P \to 0} \sum_{i=1}^{N} \Delta\omega_i = \omega_R^0 + \Delta\omega_1 + ... + \Delta\omega_N \, . \tag{2.44}$$

where the expression of the frequency shift results

$$\Delta\omega_i = \omega_{i-1} \left[\frac{k_{Au}}{2} \Delta P - \frac{H}{2} \frac{\omega_{i-1}^2}{(\omega_p^0)^2} \Delta_i \epsilon_{PTM} \right] , \tag{2.45}$$

with

$$\Delta_i \epsilon_{PTM} = \epsilon_{PTM}(P_i) - \epsilon_{PTM}(P_{i-1}) \, . \tag{2.46}$$

Neglecting the terms beyond the second order in ΔP (keeping ΔP^2, $\Delta P \Delta\epsilon_{PTM}$ and $\Delta\epsilon_{PTM}^2$) will bring, after N integrals, to

$$\begin{aligned} \omega_N \approx \omega_R^0 \Bigg[1 + \frac{k_{Au}}{2} \sum_{i=1}^{N} \Delta P - H_0 \sum_{i=1}^{N} \Delta_i \epsilon_{PTM} + H_0^2 \sum_{i=1}^{N} \left(\Delta_i \epsilon_{PTM} \sum_{j=1}^{i-1} \Delta_j \epsilon_{PTM} \right) + \\ - H_0 \frac{k_{Au}}{2} \Delta P \sum_{i=1}^{N} \left(\Big((N-1) + 2(i-1) \Big) \Delta_i \epsilon_{PTM} \right) + \frac{N(N-1)}{2} \left(\frac{k_{Au}}{2} \Delta P \right)^2 \Bigg] , \end{aligned} \tag{2.47}$$

where

$$H_0 = \frac{H}{2}\frac{(\omega_R^0)^2}{(\omega_p^0)^2}\,. \tag{2.48}$$

As N is a big number, Eq. (2.47) can be rewritten as

$$\begin{aligned}\omega_N \approx \omega_R^0\Bigg[1 + \frac{k_{Au}}{2}N\Delta P - H_0\Big(\epsilon_{PTM}(NP) - \epsilon_{PTM}(0)\Big) + \\ + H_0^2\sum_{i=1}^{N}\left(\Delta_i\epsilon_{PTM}\Big(\epsilon_{PTM}((i-1)P) - \epsilon_{PTM}(0)\Big)\right) \\ - H_0\frac{k_{Au}}{2}\Delta P\sum_{i=1}^{N}\left((N+2i)\Delta_i\epsilon_{PTM}\right) + \frac{1}{2}\left(\frac{k_{Au}}{2}N\Delta P\right)^2\Bigg]\,.\end{aligned} \tag{2.49}$$

Considering the limit of Eq. (2.44) the sums are transformed into integrals, yielding an expression of the resonance frequency at the pressure P

$$\begin{aligned}\omega_R(P) \approx \omega_R^0\Bigg[1 + \frac{k_{Au}}{2}P - H_0\Big(\epsilon_{PTM}(P) - \epsilon_{PTM}(0)\Big) + \\ + H_0^2\int_0^P\Big(\epsilon_{PTM}(P') - \epsilon_{PTM}(0)\Big)\frac{\partial\epsilon_{PTM}}{\partial P'}dP' \\ - H_0\frac{k_{Au}}{2}\int_0^P\Big(P + 2P'\Big)\frac{\partial\epsilon_{PTM}}{\partial P'}dP' + \frac{1}{2}\left(\frac{k_{Au}}{2}P\right)^2\Bigg]\,.\end{aligned} \tag{2.50}$$

Finally, by defying the variation of PTM dielectric function as

$$\Delta\epsilon_{PTM}(P) = \epsilon_{PTM}(P) - \epsilon_{PTM}(0)\,, \tag{2.51}$$

the resonance position can be expressed as a function of P and $\Delta\epsilon_{PTM}$ as follows

$$\begin{aligned}\omega_R(P) \approx \omega_R^0\Bigg[1 + \frac{k_{Au}}{2}P - H_0\Delta\epsilon_{PTM}[P] + H_0^2\int_0^P\Delta\epsilon_{PTM}(P')\frac{\partial\Delta\epsilon_{PTM}}{\partial P'}dP' + \\ - H_0\frac{k_{Au}}{2}P\Delta\epsilon_{PTM}(P) - H_0k_{Au}\int_0^P P'\frac{\partial\Delta\epsilon_{PTM}}{\partial P'}dP' + \frac{1}{2}\left(\frac{k_{Au}}{2}P\right)^2\Bigg]\,.\end{aligned} \tag{2.52}$$

In Eq. (2.52), the term $+k_{Au}P/2$ results from the volumetric compression of gold, which increases the density of conduction electrons, and hence ω_R through ω_p (numerator of Eq. (2.34), the plasma frequency dependence term). It is always

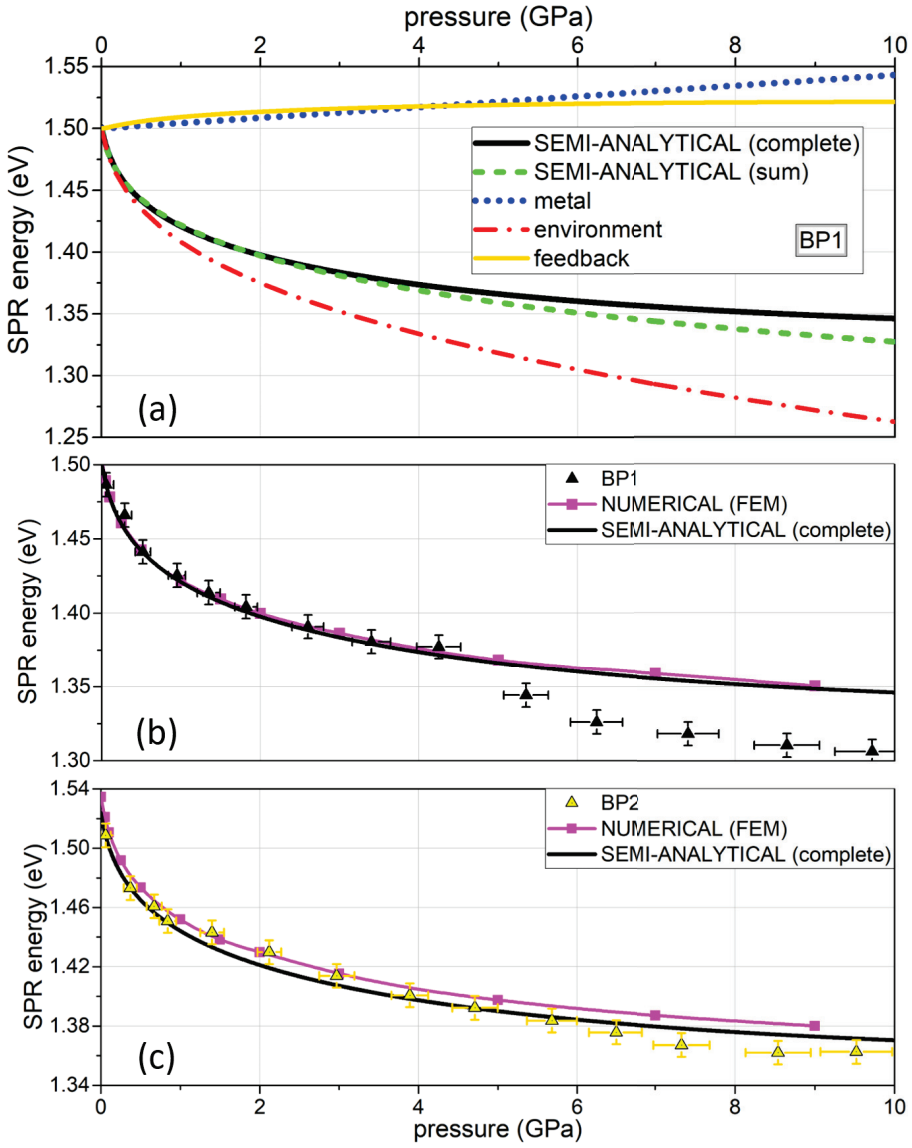

Figure 2.47: (a) The three components of Eq. (2.52) are separately plotted; their sum (dashed green curve) is compared to the full solution of Eq. (2.40) (solid black curve). Comparison between simplified analytical model and complete numerical approach in the case of experiment "BP1" (b) and "BP2" (c). Numerical and semi-analytical solutions always have similar shapes. A vertical shift of the order of the experimental incertitude is visible in the case "BP2". This difference comes from errors in the numerical determination of aspect ratio by fitting the lowest pressure σ_{ext} spectrum with FEM model. This uncertaintly translates into an offset in all the SPR energy – pressure curve of the order of 0.01 eV.

positive and proportional to the pressure, and therefore introduces a blueshift.
The element $-H_0\Delta\epsilon_{PTM}(P)$ originates from the grow of PTM refractive index with pressure. It is always negative and dominates at lower pressure, where ϵ_{PTM} changes quickly. Consequently it provokes a redshift (through the denominator of Eq. (2.34), the environment dependence term).
The remaining four terms results from a retroactive process. They are introduced to take into account that, when the resonance is modified by the previous two mechanisms, the frequency $\omega = \omega_R$ at which $\frac{\partial\omega_R}{\partial\epsilon_{PTM}}$ and $\frac{\partial\omega_R}{\partial\epsilon_1^{ib}}$ are evaluated changes, modifying in turns the SPR position. As, between these corrective contributions, $+H_0^2\int_0^P \Delta\epsilon_{PTM}[P']\frac{\partial\Delta\epsilon_{PTM}}{\partial P'}dP'$ is dominant and always positive, additional blueshift shows up.
Altogether, at lower pressure the PTM influence strongly dominates, since ϵ_{PTM} increases fast, while at higher pressure the change of the gold dielectric function becomes more and more important.

In Fig. (2.47a), the resonance position as a function on the pressure defined by Eq. (2.52) is plotted. The contribution from the gold compression ($+k_{Au}P/2$), from the environment ($-H_0\Delta\epsilon_{PTM}[P]$), and from the feedback terms (sum of the last four terms) are reported separately. Their sum is compared to the full solution of Eq. (2.40). In the lower graphs, the comparison between this solution and the complete numerical model shows a very similar dependence, confirming that the main ingredients at the origin of the SPR shift of a single elongated metal nanoparticle under high pressure are the modifications of the metal dielectric function (the real part of the Drude term) and the environment refractive index.
From experiments, other characterization of the SPR can be analyzed, providing insightful views of physical phenomena. In the following, the integrated spectral area of the measured cross-section spectra and their spectral width will be discussed.

2.2.2 Pressure dependence of the SPR area

The spectral area under the experimental BP cross-section at different pressure is discussed here. Only experiments "BP1" and "BP2" provide quantitative values of the optical cross-section of a single BP, which is obtained from experimental data after the calibration procedure. Results are summarized in Fig. (2.48).
Even if error bars are large, in the two situations the spectral area slightly increases with pressure, in a nonlinear way. To understand the possible physical origin of this effect, one can analyze the optical response of a model elongated nanoparticle, i.e. a prolate spheroid of volume V, aspect-ratio η, embedded in a medium of dielectric function $\epsilon_m(\omega)$. As already mentioned in the previous section, an ellip-

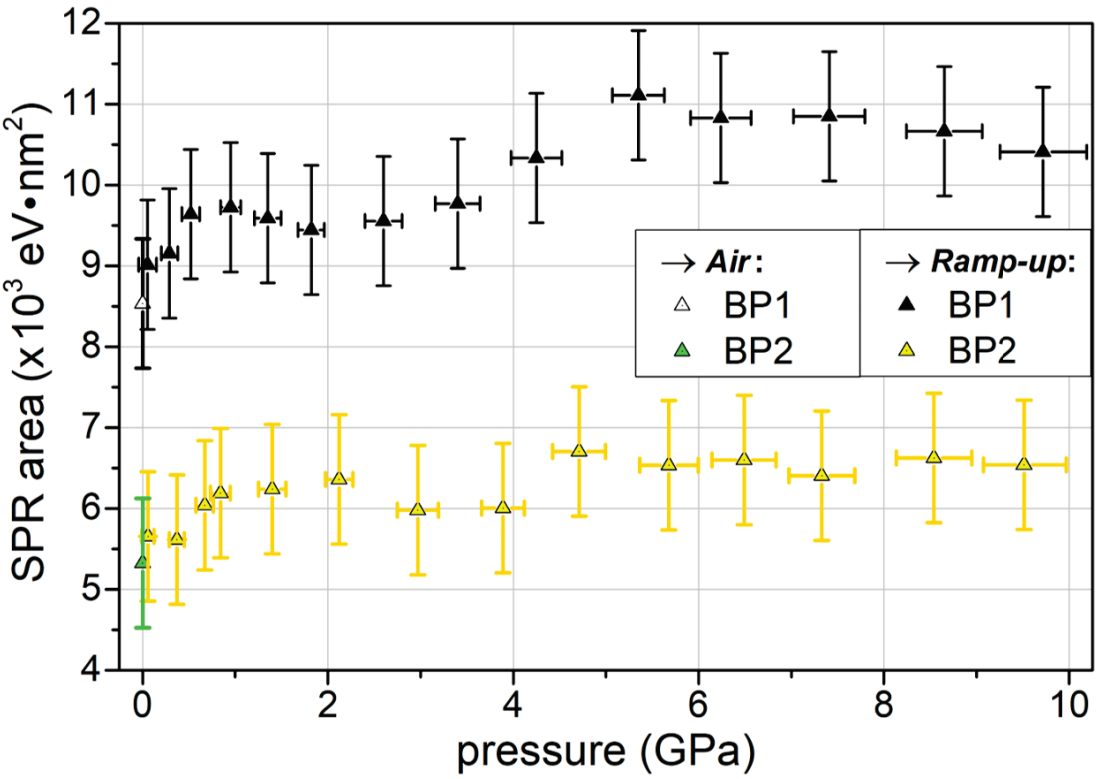

Figure 2.48: Evolution of the spectral area of the optical single nanoparticle cross-section as a function of the pressure. Note that for "BP1" a discontinuity in the SPR position occurs about 5 GPa.

soid in an homogeneous environment is well-adapted to mimic the configuration of the horizontal BP seen in Fig. (2.43), where the exact geometry is taken into account through the H parameter. In the frame of the quasi-static approximation, where the optical response is dominated by absorption, Eq. (2.34) applies and the spheroid cross-section $\sigma(\omega)$ becomes a Lorentzian distribution. For light polarized along the longer ellipsoid axis, the area under $\sigma(\omega)$ writes as

$$A = \frac{\pi(1+H)^2\,\epsilon_m^{3/2}\,V\,\omega_R^4}{2\,c\,\omega_p^2} = \frac{\pi(1+H)^2\,m\,\epsilon_0}{2\,c\,N\,e}\,\epsilon_m^{3/2}\,V^2\,\omega_R^4\,. \tag{2.53}$$

Here, the elements affected by the pressure are ϵ_m, V and ω_R. Therefore, for small changes, the relative variation of the area is expected to be

$$\frac{\Delta A}{A_0} = \frac{(A-A_0)}{A_0} \approx \frac{3}{2}\frac{\Delta\epsilon_m}{\epsilon_m(0)} + 2\frac{\Delta V}{V(0)} + 4\frac{\Delta\omega_R}{\omega_R(0)}\,, \tag{2.54}$$

where the zeros enlightens the quantities evaluated at standard pressure. One obtains

$$A(P) = A_0 \left(1 + \frac{3}{2}\frac{\Delta\epsilon_{PTM}}{\epsilon_{PTM}(0)} + 4\frac{\Delta\omega_R}{\omega_R(0)} - 2k_{Au}P\right) , \tag{2.55}$$

where $\Delta\omega_R(P) = \omega_R(P) - \omega_R(0)$ is given by the numerical solution of Eq. (2.40) computed in the precedent section for "BP1" and "BP2". Note that at the zero order approximation (Eq. (2.43)) the volumetric contribution vanishes, giving

$$A(P) \approx A_0 \left[1 + \left(\frac{3}{2} - \frac{2H\omega_R^2\,\epsilon_m(0)}{\omega_p^2}\right)\frac{\Delta\epsilon_m}{\epsilon_m(0)}\right] \tag{2.56}$$

which is consistent with the fact that the total absorption in a metal nanoparticle is proportional to the number of its gold electrons, that remains constant at different pressures (only their density is modified). Therefore, the main area modifications come, once again, from the change with pressure of the environment, affecting the nanoparticle polarizability. This analysis explains the non-linear increase of the area with pressure, being directly proportional to the pressure dependence of the PTM dielectric function $\Delta\epsilon_{PTM}(P)$.

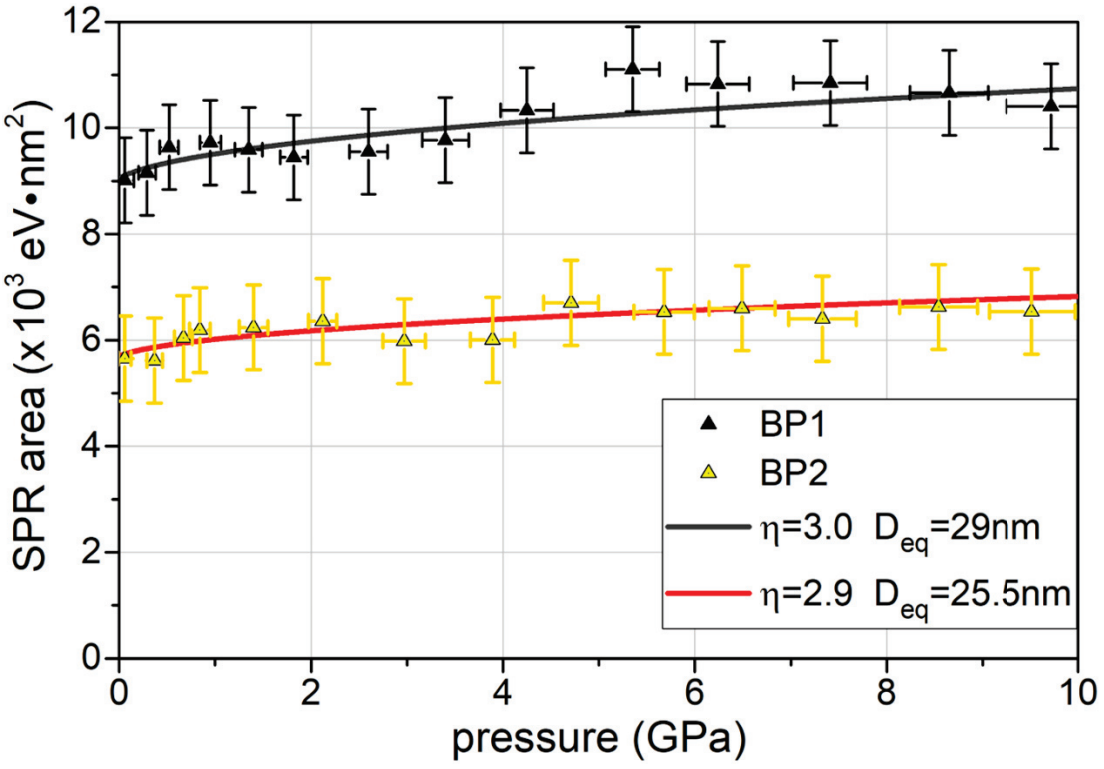

Figure 2.49: Fits of the experimental area of "BP1" and "BP2" optical cross-section using Eq. (2.55). The only free parameter is D_{eq}, the ellipsoid equivalent short-axis.

More quantitatively, Eq. (2.55) allows to calculate the spectral area of the ellipsoid cross-section. Considering the values of H and η used in the previous section, the only free parameter is the initial volume of the equivalent ellipsoid: $V = \frac{\pi}{6}\eta D_{eq}^3$. The choice of a good value for D_{eq}, the ellipsoid short-axis, permits to reproduce the experimental areas evolution and also to reproduce their absolute values, as displayed in Fig. (2.49).

2.2.3 Perspectives: SPR linewidth and discontinuities

The SPR linewidth dependence on the pressure has been quantitatively studied for single BP in the experiments "BP1", "BP2", "BP4" and "BP5", all showing a broadening of the order of $10-15\%$ in the range $0-10\,\mathrm{GPa}$ (see Fig. (2.35) and (2.37)). The analysis of the SPR spectral linewidth provides useful informations on the electronic processes. The SPR linewidth Γ is the sum of indipendent contributions

$$\Gamma(\omega_R) = \frac{\omega_R^3}{\omega_p^2}\epsilon_2^{ib}(\omega_R) + \Gamma_{rad}(\omega_R) + \Gamma_{chem} + \gamma_e(\omega_R) + \gamma_{ph}(\omega_R) + \gamma_s(\omega_R)\,, \qquad (2.57)$$

including an interband ($\frac{\omega_R^3}{\omega_p^2}\epsilon_2^{ib}$), a radiative ($\Gamma_{rad}$), a chemical ($\Gamma_{chem}$), an electron-electron (γ_e), an electron-phonon (γ_{ph}) and an electron-surface scattering (γ_s) term. The interband contribution to damping is here absent ($\epsilon_2^{ib}(\omega_R)=0$), as the considered spectral region is far from interband transitions ($\omega_R \ll \omega_{ib}$).

The radiative term at the frequency ω_R scales as

$$\Gamma_{rad} = 2\hbar k_{rad}(\omega_R)V \qquad (2.58)$$

and is important only at large sizes (typically $>30\,\mathrm{nm}$). Previous measurements on lithographed gold nanodisks and gold-silver nanoboxes, as well as discrete-dipole approximation calculations, show that $k_{rad}(\omega_R) \sim n_m$ [81]. Consequently, $\Gamma_{rad} \sim n_m V$ and its relative variation in $10\,\mathrm{GPa}$ should be $\frac{\Delta\Gamma_{rad}}{\Gamma_{rad}} \approx \frac{\Delta n_m}{n_m} + \frac{\Delta V}{V} \approx +22\% - 6\% = +16\%$.

For surfactant stabilized nanoparticles, the presence of molecules at the matrix interface introduces the so called chemical damping Γ_{chem}. Increasing the pressure could progressively densify the surfactant layer in contact with the nanoparticle, modifying Γ_{chem}. This term is difficult to quantify and model, however it only weakly affects the SPR linewidth in BPs. The main contribution to the linewidth of the SPR optical absorption comes from the conduction band electronic scattering rates, where the absorption of a photon at ω_R is assisted by unklapp electron-electron, electron-phonon and electron-surface scattering processes.

The scattering between umklapp electrons at optical frequencies yields [82]

$$\gamma_e(\omega_R) = \omega_p \left(\frac{K_B T_e}{\hbar\omega_p}\right)^2 \left[1 + \left(\frac{\hbar\omega_R}{2\pi K_B T_e}\right)^2\right], \tag{2.59}$$

that, in the domain $K_B T_e \ll \hbar\omega_R$, becomes

$$\gamma_e(\omega_R) \approx \omega_p \left(\frac{\omega_R}{2\pi\omega_p}\right)^2. \tag{2.60}$$

Consequently, $\gamma_e(\omega_R) \sim V^{\frac{1}{2}}\omega_R^2$ and its relative variation of $\gamma_e(\omega_R)$ in 10 GPa should be $\frac{\Delta\gamma_e(\omega_R)}{\gamma_e(\omega_R)} = \frac{1}{2}\frac{\Delta V}{V} + 2\frac{\Delta\omega_R}{\omega_R} \approx$-3%-22%=-25% . However, the term $\gamma_e(\omega_R)$ only weakly contributes to the linewidth of the SPR, as $\gamma_e(\omega_R) \ll \gamma_{ph}(\omega_R)$. The two following terms, $\gamma_{ph}(\omega_R)$ and $\gamma_s(\omega_R)$, are the dominant ones for small size nanoparticles. Their quantitative pressure dependence is not known, and these first studies may contribute to sheld light on such processes at nanoscale. Even if further investigations will be required for a complete analysis, the following qualitative elements can already be discussed.

The absorption of a photon of energy $\hbar\omega_R$ mediated by electron-phonon scattering generates [83, 84, 85, 86, 87]

$$\gamma_{ph}(\omega_R) = \frac{G_{e\text{-}ph}}{\hbar\omega_R}\int_0^\infty \sqrt{E}\sqrt{E+\hbar\omega_R}\, f_{FD}(E)\left(1 - f_{FD}(E+\hbar\omega_R)\right) dE\,, \tag{2.61}$$

for parabolic energy dispersion and $\hbar\omega_R \ll K_B T_e$. Consequently, $\gamma_{ph}(\omega_R)$ is related to the electron-phonon coupling, $G_{e\text{-}ph}$, which could be affected by the pressure. Ultrafast *pump&probe* experiments performed by the team on silver nanoparticles embedded in glass at high pressure have demonstrated that the electron-phonon energy relation time γ_{ph} is weakly modified by the pressure [44]. Although the optical $\gamma_{ph}(\omega_R)$ and the ultrafast γ_{ph} are not the same physical quantity, they are related to $G_{e\text{-}ph}$, and thus, one can exploit this dependence to get an idea of the possible variation in 10 GPa range $\frac{\Delta\gamma_{ph}(\omega_R)}{\gamma_{ph}(\omega_R)} \leq 10\%$.

The electron-surface scattering term writes as [88]

$$\gamma_s(\omega_R) = g_s(\omega_R)\frac{v_F}{L_{eff}}\,. \tag{2.62}$$

The confinement factor $g_s(\omega_R)$ has been recently quantitatively investigated at single particle level, both experimentally [89, 90, 91] and theoretically [92, 93].

It has been correlated with the extent of the electronic spillout tail and a detailed recent study [92] has shown that it is proportional to the refractive index of the environment $n_m(\omega_R)$. No quantitative experimental evidence of this dependence has been proved, and such pressure investigations, where this refractive index can be modified in a controlled way by pressure could bring the first quantitative demonstration of this quantum effect. The effective confinement length L_{eff} is tied to the nanoparticle size and geometry. In the case of a nanorod $L_{eff} = \sqrt{LD} \sim \eta^{\frac{1}{2}} D \sim \eta^{\frac{1}{2}} V^{\frac{1}{3}}$, where L and D are its long and short axis, while $\eta = L/D$ is the aspect-ratio [91]. Considering the volumetric dependence of the Fermi velocity, $v_F \sim V^{-\frac{1}{3}}$, it results $\gamma_s \sim n_m \eta^{-\frac{1}{2}} V^{-\frac{2}{3}}$ and its relative variation in 10 GPa should be $\frac{\Delta\gamma_s}{\gamma_s} \approx \frac{\Delta n_m}{n_m} - \frac{2}{3}\frac{\Delta V}{V} \approx +22\% + 4\% = +26\%$.

This simple analysis is qualitatively in line with the observed broadening. In fact, the only negative variation comes from $\gamma_e(\omega_R)$, which gives a marginal contribution to the total Γ, as $\frac{\gamma_e(\omega_R)}{\gamma_e(\omega_R)+\gamma_{ph}(\omega_R)} \approx 10\%$ [94]. Furthermore, as in the case of SPR shift, the environment matrix change plays here an important role.
In order to be more quantitative, the knowledge of the percentage contribution of each term in Eq. (2.57) is needed. This has been previously investigated in the group [78] for smaller Au-BP (76 nm × 24 nm). The pressure induced modifications of the SPR linewidth therefore write as $\gamma_e \approx 6\%\Gamma$, $\gamma_{ph} \approx 56\%\Gamma$, $\gamma_s \approx 22\%\Gamma$, $\Gamma_{rad} \approx 2.4\%\Gamma$ and $\Gamma_{chem} \approx 13.6\%\Gamma$. In this case one can write

$$\frac{\Delta\Gamma}{\Gamma} = 0.024\frac{\Delta\gamma_{rad}}{\gamma_{rad}} + 0.136\frac{\Delta\Gamma_{chem}}{\Gamma_{chem}} + 0.06\frac{\Delta\gamma_e}{\gamma_e} + 0.56\frac{\Delta\gamma_{ph}}{\gamma_{ph}} + 0.22\frac{\Delta\gamma_s}{\gamma_s}\,, \quad (2.63)$$

that, in the case $\frac{\Delta\Gamma_{chem}}{\Gamma_{chem}} = 0$ leads to a total relative variation at 10 GPa between +6 and +12%. As expected, the relevant contribution comes from γ_{ph} and γ_s, that would introduce a broadening of $\leq +6\%$ and +6% respectively. Considering that the present Au-BP are slightly larger, one would expect that the weight of $\frac{\Delta\gamma_{rad}}{\gamma_{rad}}$ is larger at the expense of $\frac{\Delta\gamma_s}{\gamma_s}$, so the global broadening should be little modified. Overall, these consideration agrees well with the variation observed in the experimental linewidth.

This open the ways to more studies in order to better understand and quantify the physical mechanisms at the origin of the SPR broadening at different pressures. For instance a single particle *pump&probe* investigation under high pressure could help to understand the behavior of $\gamma_{ph}(\omega_R)$ as a function of the pressure [44]. Changing the size and aspect-ratios will help to investigate $\gamma_s(\omega_R)$ and distinguish its contribution from the electron-phonon bulk one. Moreover, performing experiments on single gold BP with different environments (e.g. changing PTM or using surfactant-free encapsulated in SiO_2 BPs) will possibly shed light on this quantum

confinement effect and, for the first time, its dependence on the environment.

Another aspect to investigate is the presence of some discontinuities in the optical behaviors ot high pressure (>5 GPa), as for instance the jump in peak position or linewidth occurring in some experiments. The most notable cases are "BP1" at 5 GPa for the peak position and "BP2" at about 10 GPa for the broadening. This may come from exceeding the elastic limit of the nanoparticle metal that could abruptly modify the particle lattice (changing $\gamma_{ph}(\omega_R)$) and aspect-ratio (modifying $\omega_R(\eta)$ and $\gamma_s(\omega_R)$). The gold elastic limit measures only 0.2 GPa in the bulk case [95], but it increases reducing the size [96]. The threshold for the investigated Au-BPs is unknown, but plastic deformation could be a source of discontinuity and irreversibly. To shed light on this point, the particles should be deposed on adequate substrates, in order to perform SEM or TEM microscopy before and especially after a *complete pressure cycle*.

Later on, these experiments will be extended to isolated carbon nanotubes. An in-depth experimental analysis (that will rely on combinations of different techniques at high pressure: SMS, Raman spectroscopy and *pump&probe*) will give an enhanced understanding of the CNTs properties evolutions under extreme conditions, with special regard to the collapse phenomenology.

Chapter 3

Mechanical properties of a single nano-resonator: damping of acoustic vibrations

The vibrational properties of nano-objects can be experimentally addressed using optics-based methods in the frequency (e.g. Raman spectroscopy) or time (e.g. *pump&probe* spectroscopy) domains and have been the object of many investigations in the last 20 years. The main outcome of such experiments are specific vibrational modes which are detected as damped oscillations with period T and damping time τ. The way vibrational periods depend on nano-object size, shape, environment and encapsulation, has now been clarified [102]. In particular, it has been demonstrated that they are accurately described by continuum mechanics even for ultrasmall ($\sim$1 nm) nanoparticles [97, 98]. However, many questions still remain open on the damping mechanisms, which are subtler to determine since small structural, morphological and environmental changes provoke dramatical alterations of the vibrational modes lifetime. The greater complexity of their study as compared to that of frequencies has two origins. First, in contrast with vibrational periods which are predominantly determined by intrinsic nano-object properties (e.g., composition, morphology and crystallinity) in most experimental cases [102], damping times are very sensitive to the properties of the nano-object/environment interface, which determine the efficiency with which acoustic energy is transmitted from the former to the latter. Additionally, damping investigations by ensemble experiments is precluded by the size and shape dispersion of the nanoparticles, meaning that experimenal techniques with single-particle sensitivity have to be used for such studies. In this regard, ensemble studies do not allow a precise investigation of the relaxation processes, due to the unavoidable inhomogeneous effects (dephasing between the vibrations of nanoparticles induced by small differences in their morphology) that they introduce. As illustrated in

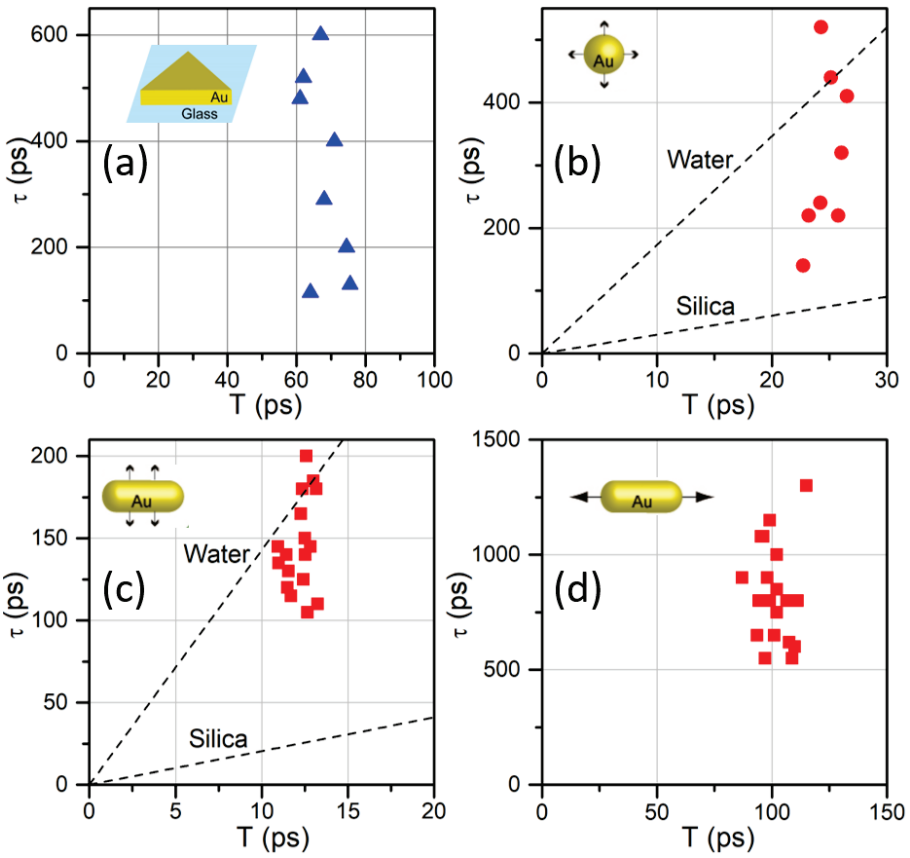

Figure 3.1: Statistics on periods T and damping times τ of the modes detected in previous P&P experiments on single nanoparticles [99, 100]. For each graph, the investigated particle geometry is displayed. Lithographed or deposited on a glass substrate (a) nanotriangles (aspect ratio 2.4); (b) spheres (radius 40 nm) and (c)(d) rods (axes 25×60 nm) have been studied. All the reported oscillations are associated to a breathing mode, apart from the last one (d) which is an extensional mode. Each data point correspond to a different nano-object of a given sample. Green dashed lines (b)(c) are the results of continuum mechanics computations for spheres and infinite cylinders in the indicated homogeneous environments [102]. These curves enlighten the important dispersion in τ.

Fig. (3.1), even studies on single nanoparticles produce an important dispersion in the modes damping times. In fact, while the periods present a weak dispersion (mostly reflecting the size dispersion in the samples used), their lifetimes strongly fluctuate from a particle to another, an effect that was initially ascribed only to large variations of nanoparticle-substrate coupling [99, 100, 101] (note that the impact of nanoparticle geometry, which constitutes the main finding of this chapter, had not been invoked).

In order to shed light on these aspects, and in particular to investigate a possi-

ble dependence of damping rate on nano-objects morphology, a systematic study on individual nanodisks produced by electron lithography was carried out. The choice of this kind of geometry relies on the simple shape characterized by two dimensions only (diameter and thickness) and on the relatively large contact with the substrate. Furthermore, lithography avoids the presence of ligand molecules and residual solvent occurring for deposed, chemically synthesized nano-objects. Making use of the experimental *pump&probe* (P&P) technique, the damping times were successfully correlated with the disks aspect ratio, while simulations based on finite elements method (FEM) helped to clarify the general physical origin of the observed behavior.
This chapter opens with some elements of the elasticity theory and a description of the numerical simulation modus operandi. Afterwards, the analyzed samples are described in details and the experimental investigations, as well as their analysis, are illustrated. The experimental results are compared with the outcomes of the numerical modeling and the consequential conclusions are drawn.

3.1 Fundamentals on vibrational properties of single metal nanoparticles

A continuous solid can be treated as a network of points with equilibrium position $\vec{L}$, whose motion is described by the new position $\vec{l}$ of each point, or, alternatively, by the displacement field $\vec{u}$, as shown in Fig. (3.2) [103].

$$\vec{u}(\vec{L},t) = \vec{l}(\vec{L},t) - \vec{L}\,, \tag{3.1}$$

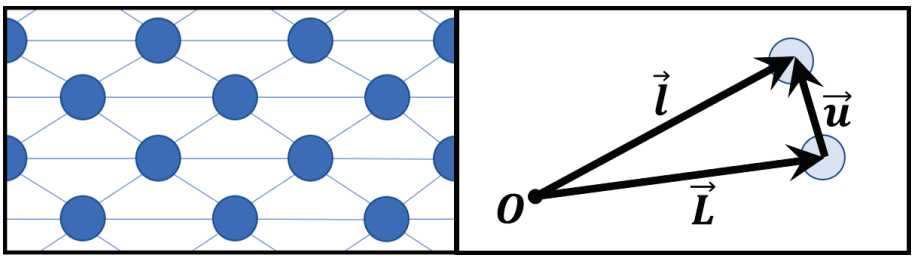

Figure 3.2: Left: idealization of a solid as a web of points. Right: local displacement of an element.

In order to describe a material deformation, it is convenient to consider the differential form

$$\Delta = \Big[dl(\vec{L},t)\Big]^2 - \Big[dL\Big]^2 . \tag{3.2}$$

Considering a three dimensional coordinate system with axis $i=x,y,z$, vectors $\vec{u}_i$, and small displacements, so that $\vec{r}\approx\vec{L}\approx\vec{l}$, the deformation Δ can be expressed through the strain matrix $\mathbf{S}$ as

$$\Delta = \sum_{i,j=1}^{3} S_{i,j} dr_i dr_j \,, \tag{3.3}$$

where $\mathbf{S}$, in linear approximation, consists in a symmetric tensor

$$S_{i,j} = \frac{\partial u_i}{\partial r_j} + \frac{\partial u_j}{\partial r_i}\,; \qquad \text{written in compact form as:} \quad \mathbf{S} = \nabla_{sym}\vec{u}\,. \tag{3.4}$$

A deformation is produced by some forces which can be of volume ($\vec{F}$), like the gravity, or of surface ($\vec{T}$) that are transmitted in the volume through elastic forces. The traction forces acting on the surface of normal vector $\vec{n}$ are described introducing the stress matrix $\mathbf{T}$, defined as

$$\vec{T}_n = \mathbf{T}\cdot\vec{n}\,. \tag{3.5}$$

The Newton principle allows to relate the force fields ($\vec{F}$, $\vec{T}$) with the displacement field ($\vec{u}$) as follows

$$\rho\frac{\partial^2\vec{u}}{\partial t^2} = \nabla\cdot\vec{T} + \vec{F}\,, \tag{3.6}$$

where ρ is the material density. In the regime of linear elastic deformation the Hooke law applies, giving rise to the elastic constitutive equation

$$T_{i,j} = \sum_{k,l} c_{ijkl}\ S_{kl}\,; \qquad \text{written in compact form as:} \quad \mathbf{T} = \mathbf{c} : \mathbf{S}\,, \tag{3.7}$$

where the stiffness tensor $\mathbf{c}$ has 3^4 components, of whom only 21 are independent.[1] For cubic crystals the components of the stress tensor $\mathbf{c}$ can be summarized through a 6×6 matrix containing c_{11}, c_{12} and c_{44}. Besides, if there is elastic isotropy (polycrystalline case),

$$c_{11} = c_{12} + 2c_{44} \tag{3.8}$$

and the material elasticity is described by only two independent elastic constants, e.g. Lamé constants

$$\begin{cases} \lambda = c_{12} \\ \mu = c_{44} \end{cases}, \tag{3.9}$$

[1] $c_{ijkl} = c_{jikl} = c_{ijlk} = c_{jilk}$ and $c_{ijkl} = c_{klij}$.

connected to the longitudinal (c_L) and transversal (c_T) speed of sound via

$$c_L = \sqrt{\frac{\lambda + 2\mu}{\rho}} \qquad \text{and} \qquad c_T = \sqrt{\frac{\mu}{\rho}}\,, \tag{3.10}$$

or to the Young modulus (E) and Poisson's ratio (ν) speed of sound via

$$E = \mu\,\frac{3\lambda + 2\mu}{\lambda + \mu} \qquad \text{and} \qquad \nu = \frac{\lambda}{2(\lambda + \mu)}\,. \tag{3.11}$$

Combining Eq. (3.4), (3.6) and (3.7) for an elastically isotropic material, in the case $\vec{F} = \vec{0}$, yields the Navier equation

$$\rho\frac{\partial^2 \vec{u}}{\partial t^2} = (\lambda + 2\mu)\nabla(\nabla \cdot \vec{u}) - \mu\nabla \times (\nabla \times \vec{u})\,, \tag{3.12}$$

which is used in the following to describe the vibrations of metal nanoparticles. Despite neglecting the atomistic character of matter, this law has proved to be valid down to nanoparticles sizes of $\sim$1 nm [97, 98].

In addition to the elastic properties, a viscous damping can also be phenomenologically taken into account adopting the viscosity tensor $\mathbf{q}$

$$\mathbf{T} = \mathbf{c} : \mathbf{S} + \mathbf{q} : \frac{\partial \mathbf{S}}{\partial t}\,, \tag{3.13}$$

whose effects consist in the introduction of a frequency-dependent mechanical damping. At room temperature, two important physical mechanisms contributing to this viscous damping are the thermoelastic attenuation (due to the irreversible heat conduction from compressed to rarefied regions through longitudinal waves) and the Akhieser mechanism (lying on the passage of the coherently-excited acoustic wave that interacts with the equilibrium phonon distribution) [103]. These viscous effects introduce attenuations with a quadratic frequency dependence $\alpha \sim f^2$. However, other dissipation mechanisms may occur, introducing a wide variety in the attenuation-frequency curve. For instance, in polycrystalline materials, randomly oriented grains provoke scattering of acoustic waves. All these sources of attenuation are referred to as *intrinsic* damping, since they are independent on the particular geometry and are present in bulk systems. On the other hand, the configuration and composition considered could include other sources of relaxation (*extrinsic* damping). That is the case of the dissipation occurring at the interface between two different materials, introduced later through the infinite film example or when investigating confined nano-objects at nanoscale.

Eq. (3.4), (3.6) and (3.13), results in a system of three equations and three parameters ($\vec{u}$, $\mathbf{S}$, $\mathbf{T}$). Formally, the acoustic theory is very similar to the electromagnetic one, and by introducing the particle velocity $\vec{v} = \frac{\partial \vec{u}}{\partial t}$ and the momentum density $\vec{p} = \rho \vec{v}$, a parallelism can be established with the Maxwell's equations, considering

$$\mathbf{T} \iff \vec{E} \qquad \mathbf{S} \iff \vec{D} \qquad \vec{p} \iff \vec{B} \qquad \vec{v} \iff \vec{H}\,.$$

This comparison leads to the acoustic Poynting theorem: in any volume V with closed surface S [2], the energy balance is described by

$$\int_S \mathbf{P} \cdot \vec{n}\, dS = -\int_V \vec{v} \cdot \frac{\partial \vec{p}}{\partial t}\, dV - \int_V \mathbf{T} \cdot \frac{\partial \mathbf{S}}{\partial t}\, dV - \int_V \vec{v} \cdot \vec{F}\, dV\,, \tag{3.14}$$

where the tensor quantity

$$\mathbf{P} = -\vec{v} \cdot \mathbf{T} \tag{3.15}$$

is called the acoustic Poynting vector. [3]
Therefore, the total power flow outward through the surface S is the force applied times the velocity of the application point.

When a three dimensional linear elastic solid is subjected to point forces causing local displacements, the produced work is stored in the form of strain energy $\mathcal{E}$ (in absence of energy dissipation). The incremental strain energy, $d\mathcal{E}$, for the elementary volume dV can be written

$$d\mathcal{E} = \frac{1}{2}\, \mathbf{T} \cdot \mathbf{S}\, dV\,, \tag{3.16}$$

that, integrated over the entire volume V, yields the total strain energy $\mathcal{E}$

$$\mathcal{E} = \frac{1}{2} \int_V \mathbf{T} \cdot \mathbf{S}\, dV\,. \tag{3.17}$$

3.1.1 Eigenmodes and Q-factor

The vibrational eigenmodes of a nano-object are the harmonic solutions of Eq. (3.12) with complex frequency $\tilde{f}$, of the form [102]

$$\vec{u}(\vec{r}, t) = \vec{u}(\vec{r}) \exp\left(i 2\pi \tilde{f} t\right) + c.c. \tag{3.18}$$

It is possible to distinguish two important configurations satisfying the boundary conditions of the problem. For nano-objects in vacuum, these correspond to

[2] actually, there is no need of restricting the application of the Poynting vector to completly closed surfaces in the acoustic case.

[3] in complex notation it becomes $\mathbf{P} = -\frac{1}{2}\vec{v}^* \cdot \mathbf{T}$.

vanishing stress on the nanoparticle surface, yielding undamped vibrations modes, characterized by real frequencies $\tilde{f}$. For matrix-embedded nano-objects, the displacement field has to obey Navier equation in both the nanoparticle and its environment (where it should correspond to a purely diverging acoustic wave) with continuity of displacement and stress at their interface. Damped modes characterized by complex frequencies ($\tilde{f}$) are obtained in this case, with damping associated to the emission of acoustic waves in the environment.
The frequency $\tilde{f}$ has real part $f = 1/T$, where T is the oscillation period, and imaginary part $\alpha = 1/\tau$, where τ is the lifetime of the vibration. Acoustic vibration associated to a given mode it thus characterized by this complex frequency ($\tilde{f}_n = f_n + i\alpha_n/(2\pi)$), the normalized displacement field ($\vec{U}_n(\vec{r})$) and its complex amplitude ($\tilde{A}_n$).

$$\vec{u}_n(\vec{r},t) = \frac{1}{2}\tilde{A}_n\vec{U}_n(\vec{r})\exp\left(i2\pi f_n t - \alpha_n t\right) + c.c. \tag{3.19}$$

A convenient parameter to characterize the damping of an acoustic mode is its quality factor Q_n, defined as

$$Q_n = \pi\frac{f_n}{\alpha_n}\,, \tag{3.20}$$

with α_n/π also corresponding to the bandwidth Δf_n of the n-th mode in the spectral domain

$$Q_n = \frac{f_n}{\Delta f_n}\,. \tag{3.21}$$

Over time, an oscillating object returns to equilibrium thanks to extrinsic (emission of acoustic waves in the environment, see Sections (3.1.2,3.1.3)) and intrinsic (see discussion in Section Section (3.1)) damping mechanisms. Since these damping channels are independent, the total quality factor can be decomposed as

$$\frac{1}{Q} = \frac{1}{Q_{extrinsic}} + \frac{1}{Q_{intrinsic}}\,. \tag{3.22}$$

where $Q_{extrinsic}$ and $Q_{intrinsic}$ are the quality factors associated to extrinsic and intrinsic damping mechanisms, respectively. $Q_{extrinsic}$ is discussed below in two simple cases: a film on an infinite substrate and a nanosphere in homogeneous environment.

3.1.2 Film on substrate: interface contribution to damping

Consider an infinite film of thickness h, perfectly attached to an infinite extended substrate. The geometry is outlined in Fig. (3.3). Analyzing the longitudinal

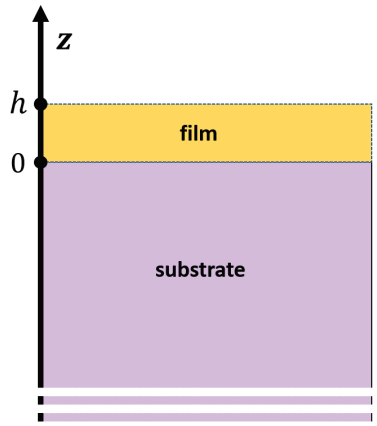

Figure 3.3: Slab of thickness h is spread over a semi-infinite substrate.

waves along the vertical direction ($\vec{u}(z,t) = u(z,t)\vec{z}$), Eq. (3.12) reduces to the wave equation

$$\frac{\partial^2 u}{\partial t^2} = c_L^2 \frac{\partial^2 u}{\partial z^2}\,. \tag{3.23}$$

The perfect contact film/substrate translates in two boundary condition at the interface: continuity of the acoustic displacement and acoustic pressure. This implies at the interface

$$\begin{cases} u[\mathrm{F}] = u[\mathrm{S}] \\ \rho[\mathrm{F}]\, c_L^2[\mathrm{F}]\, \frac{\partial u}{\partial z}[\mathrm{F}] = \rho[\mathrm{S}]\, c_L^2[\mathrm{S}]\, \frac{\partial u}{\partial z}[\mathrm{S}] \end{cases}, \tag{3.24}$$

where ρ is the density, and the letters "F" and "S" indicate the film and the substrate, respectively.
Assuming a free boundary condition (i.e. vanishing pressure) at $z = h$, one gets

$$\left.\frac{\partial \vec{u}}{\partial z}\right|_{z=h} = 0 \tag{3.25}$$

and imposing propagation through the substrate in the $-z$ direction only (without reflection components) complex frequencies of oscillation ($\tilde{f}_n$) are obtained. $\tilde{f}_n$ depend on the acoustic impedance of the materials ($Z = \rho\, c_L$), and in the $Z_F > Z_S$ case it results [104]

$$\tilde{f}_n = \frac{c_L[\mathrm{F}]}{2\,h} n + \frac{i}{2\pi} \frac{c_L[\mathrm{F}]}{4\pi\, h} \ln\left(\frac{Z_F - Z_S}{Z_F + Z_S}\right) \qquad \text{with} \quad n{=}1,2,3\ldots\,. \tag{3.26}$$

This results in Q-factors

$$Q_n = \frac{2\pi^2 n}{\ln\left(\frac{Z_F - Z_S}{Z_F + Z_S}\right)} \tag{3.27}$$

independent from h, the geometrical parameter characterizing this mono-dimensional system.

3.1.3 Spherical nano-objects embedded in an homogeneous environment

The acoustic modes of an elastic homogeneous and isotropic sphere can be obtained from the resolution of Eq. (3.12) in spherical coordinates. They were originally computed by Lamb [105] in the case of a sphere in vacuum, before being extended to spheres embedded in an elastic homogeneous and isotropic environment [106]. The solutions of the Navier equation in spherical coordinates consist in two types of displacements: spheroidal, characterized by a local variation of the volume (i.e. with $\nabla\cdot\vec{u}\neq 0$) and torsional, where the volume does not change (i.e. with $\nabla\cdot\vec{u}=0$). The radial and angular variations of displacement are respectively described by Bessel spherical functions $j_1(kr)$ and $y_1(kr)$ (for the radial component) and spherical harmonics $Y_l^m(\theta,\phi)$ (for the angular component), with angular momentum $l\geq 0$ and azimuthal number $m\in[-l,l]$. In time-resolved experiments, only the isotropic $l=0$ modes, associated to purely radial displacement field are detected. A schematic of the mode displacements is displayed in Fig. (3.4).

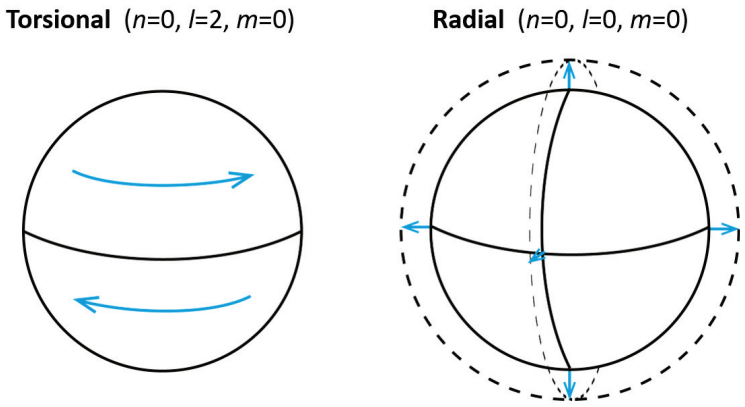

Figure 3.4: Schematic of the vibrational modes of a sphere: the blue arrows indicate the superficial deformation occurring in a torsional and radial mode.

In the case of a sphere of radius R in vacuum, undamped modes are obtained with frequencies

$$f_n=\frac{c_L\xi_n}{2\pi R}\approx\frac{c_L(n{+}1)}{2R}\qquad\text{with}\quad n{=}0,1,2\ldots, \tag{3.28}$$

where the coefficients ξ_n are the solutions of

$$\tan(\xi_n)=\frac{\xi_n}{1-\left(\frac{c_L\xi_n}{2c_T}\right)^2}. \tag{3.29}$$

In the case of an elastic homogeneous and isotropic infinite matrix, stress-free boundary has to be replaced by the imposition of a purely diverging acoustic wave in the environment, yielding to the complex $\tilde{f}_n$

$$\tilde{f}_n = \frac{c_L}{2\pi R}\,\mathrm{Re}\{\tilde{\xi}_n\} + \frac{i}{2\pi}\frac{c_L}{R}\,\mathrm{Im}\{\tilde{\xi}_n\} \;\approx\; \frac{c_L(n{+}1)}{2R} + \frac{i}{2\pi}\frac{c_L}{R}\,\frac{Z_s}{Z_m} \tag{3.30}$$

with Z_s and Z_m the acoustic impedances of the sphere and of the matrix respectively (the approximation of Eq. (3.30) is valid when the values of impedances are not too close.).
Remarkably, this mono-dimensional system defined by the radius R, has Q-factors

$$Q_n = \frac{\pi}{2}\frac{Z_m}{Z_s}(n{+}1) \tag{3.31}$$

independent from R (periods and damping time being both proportional to R), a result thus similar to the previously considered nanofilm case.

The goal of experiments performed in this thesis will be to investigate more complex systems, where the acoustic damping through the environment could be tuned by modifying the morphology of the nano-object (e.g. its aspect ratio).

3.1.4 Numerical modeling

The acoustic modes can be analytically calculated only for isotropic highly symmetric geometries (sphere or infinite cylinder in a uniform matrix or infinitely extended film attached on substrate). In all the other cases, their numerical computation is required. In this work, the finite-element method (FEM) was adopted to simulate a nanodisk (ND) on an infinite substrate.
It has been realized in the experimentally relevant configuration reported in Fig. (3.5), where an individual Au-ND of diameter D, thickness h and aspect ratio $\eta{=}D/h$, is perfectly attached to a sapphire substrate, much thicker than the ND. This translates in two boundary conditions at the gold/sapphire interface: continuity of displacement and stress. The system is characterized by the densities ρ and the Lamé constant of gold and sapphire.

Numerical simulation were performed using a frequency-domain approach consisting in calculating the forced vibrations of the ND induced by a given periodical excitation. Vibrational spectra were then obtained by plotting physically relevant quantities (such as the strain energy stored in the ND) as a function of excitation frequency, leading to resonances each associated to a specific excited vibrational

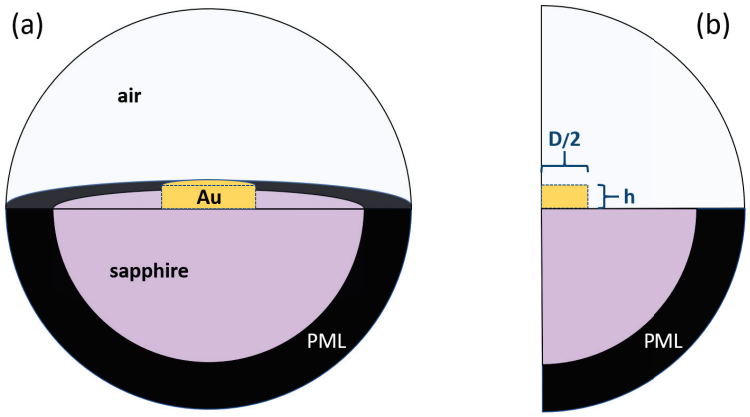

Figure 3.5: Configuration adopted for the FEM simulations. The geometry of the problem has a circular symmetry (a). This feature was exploited in the simulations, where only a section of the system was actually considered, reducing the computational time (b). A PML layer was introduced between two virtual spheres of fixed radii (120 and 160 nm).

mode and yielding its frequency and damping time (see pages 126-130). To avoid contamination effects associated to acoustic wave reflection at the domain border, a perfectly matched layer (PML) was introduced, an approach also used for optical simulations. In this work, ND excitation consists of uniform stress with the aim of simulate the effect of a femtosecond pulse laser (namely a uniform dilatation) used in the experiences illustrated later on.

Simulations show the general result that rescaling both the dimensions of the ND (D, h) by a factor M (η being unchanged) will not affect the nature of the modes, but simply reduce by M their complex frequency (the Q-factor remains unchanged, as it depends only on the specific considered mode and on the aspect ratio η). Such rescaling will be exploited later to compare frequencies of the same mode from ND of different sizes.

3.2 Experimental measurements on single gold nanodisks

The previous section has introduced two nano-resonators (film, sphere), showing that the Q-factor of their acoustic modes does not depend on the system dimension (thickness, radius). In order to understand whether this is also the case for more complex nanostructures with a geometry characterized by two or more parameters, an in-depth study on cylindrical nano-resonators was carried out. These

oscillators consist in isolated gold nanodisks (ND), geometrically characterized by their thickness (h) and diameter (D) and coupled with a thick sapphire substrate.

3.2.1 Investigated samples

Two ND samples, referred to as S1 and S2 in the following, were realized via electron lithography (collaboration with F. Banfi in Cattolica univeristy of Brescia and F. Rossella in Pisa university). Their layout is illustrated in Fig. (3.6). The

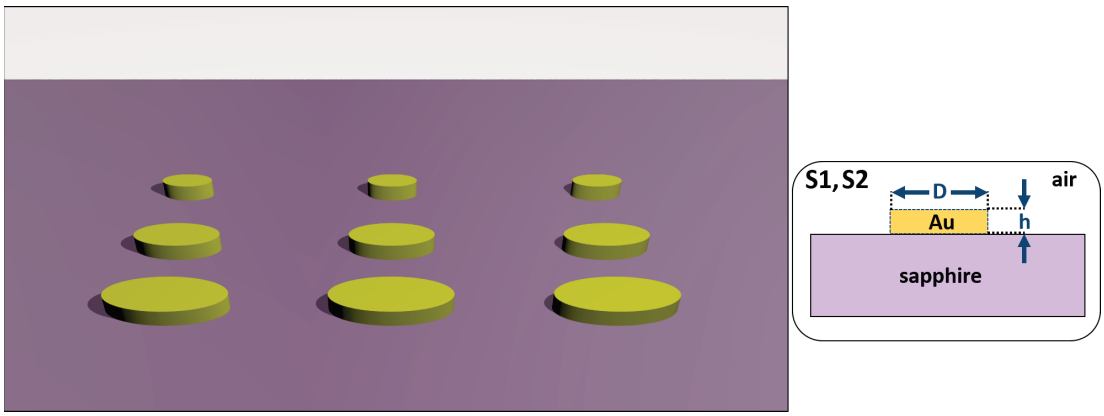

Figure 3.6: Left: schematics of the studied samples (not in scale), consisting in NDs with same thickness and different diameters. Right: composition of the samples: Au-ND of thickness h and diameter D are attached to a sapphire substrate.

samples were produced using a sapphire substrate of thickness 0.5 mm on which a multitude of NDs were lithographed. The NDs are well isolated from each other (10 µm apart) to permit single particle investigations. Constant thickness h and variable diameter D were targeted during the fabrication process for the different NDs forming each sample. This introduces a wide variety of aspect ratios $\eta = D/h$ per sample, each of them being repeated on 48 NDs. Dimensions of the NDs are reported in Tab. (3.1).
In order to precisely check the actual morphology of the produced NDs, atomic force microscope (AFM) and scanning electron microscopy (SEM) characterizations were performed by the collaborators. AFM measurements were performed on NDs located in diametrically opposed zones of the sample, demonstrating that h was constant over the whole sample, as shown in Fig. (3.7).
It follows that $h = (19 \pm 3)$ nm for S2 and $h = (40 \pm 5)$ nm for S1. SEM characterization of the NDs was also performed, allowing to identify and discard NDs with visible imperfections. However, precise D estimations via SEM are challenging, due to the limited resolution of this technique (degraded by charge accumulation on the sapphire substrate).

SAMPLES	S1	S2
NOMINAL THICKNESS (nm)	30	15
AFM THICKNESS "h" (nm)	40	19
NOMINAL DIAMETER RANGE "D" (nm)	60−180	60−400
DIAMETER STEP (nm)	5	10
ASPECT-RATIO RANGE "η" (nm)	1.5−4.5	3−20

Table 3.1: Geometry of the studied samples: the NDs aspect ratio η has been obtained using the thickness h, measured via AFM, and the diameter D, target of the electron lithography.

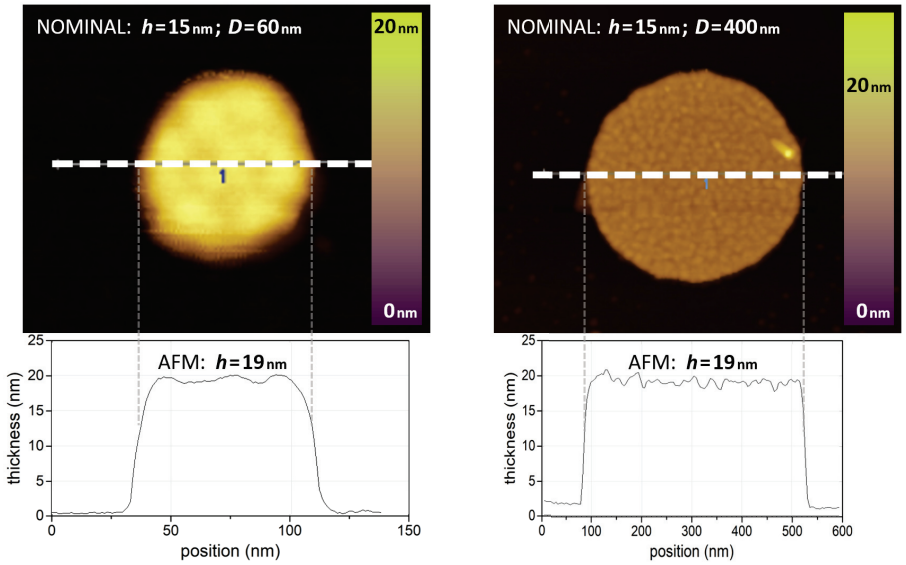

Figure 3.7: AFM measurements performed on sample S2 on two ND with very different diameters and locations. The thickness h remains equal in different regions. Note that precise D measurements by AFM are hampered by tip convolution effects.

3.2.2 Optical characterization of a single gold nanodisk

ND morphology characterizations were complemented by a linear optical characterization of single ND. Using the spatial modulation spectroscopy (SMS) technique, extensively described in Section (1.4.2) of Chapter 1, the absolute extinction spectrum of individual NDs, as well as the polarization dependence of extinction were measured.

EXTINCTION SPECTRUM

The extinction cross-section σ_{ext} spectrum, dominated by the surface plasmon resonance (SPR) of the gold nano-objects, provides information on η, as discussed in detail in Fig. (3.8).

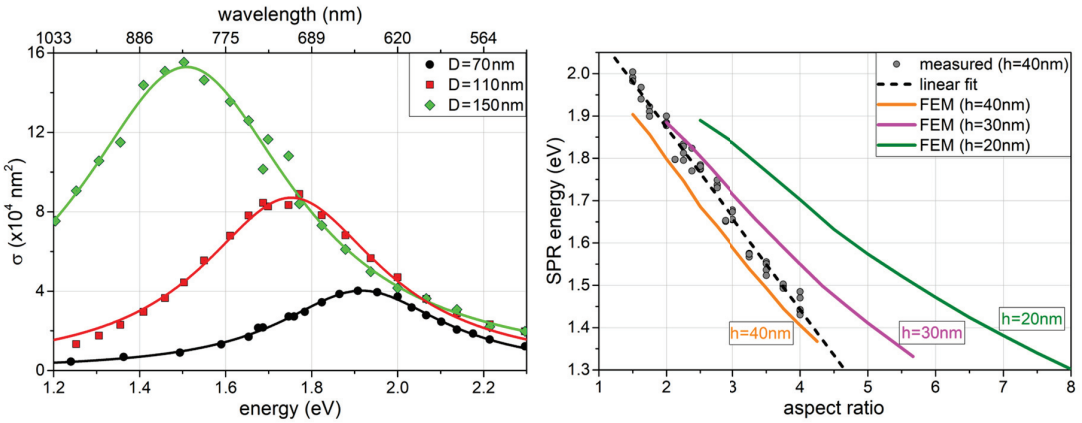

Figure 3.8: Examples of extinction spectra obtained on NDs from S1, all exhibiting clear SPR peaks. The experimental cross-section σ (dots) are well fitted by Lorentzian distributions (solid lines). Increasing the diameter yields a redshift of the SPR peak, whose energies are plotted in the second graph (dots). These data were compared with the optical FEM calculations including the sapphire substrate (solid lines). FEM calculations were performed for several h values, confirming that the (40 ± 5) nm value determined by AFM also leads to a good reproduction of the measured SPR positions.

POLARIZATION RESPONSE

Polarization measurements are extremely sensitive to shape anisotropy, allowing to identify and discard elliptical NDs. Indeed σ_{ext} is independent on the laser polarization for a circular symmetric ND, while a longitudinal and a transversal SPR emerge if the symmetry is broken, as in the case of the ellipsoid described in Section (1.3.4) of Chapter 1. A comparison between the response of an elliptical and a circular ND is proposed in Fig. (3.9).

The polarization selection is complementary to the SEM screening, since the latter cannot discern between small ellipticity or mis-calibrations. Note that for strong deviations from the circular shape, however, the polarization response may remain constant. For instance, in equilateral nanotriangles σ_{ext} is independent on the polarization [108], meaning that non-circular NDs with triangular shape cannot be distinguished from circular ones.

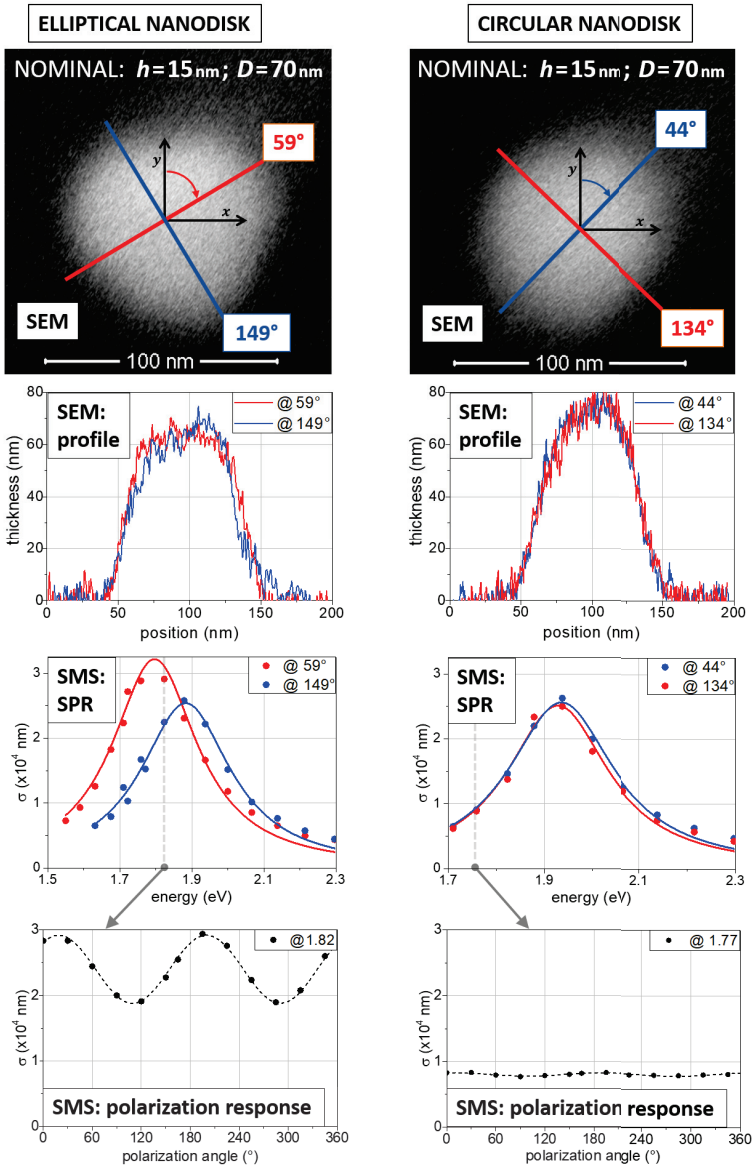

Figure 3.9: SEM-SMS characterization performed on two different ND from sample S2, with same nominal thickness h and diameter D. Left: the SEM profiles show that the diameter is slightly larger in the 59° direction; the SPR is clearly red-shifted and enhanced when measured along 59° (continuous lines are Lorentzian data fits), confirming the ND ellipticity suggested by SEM observations. Right: similar characterization with another more circular ND, that was identified as a suitable candidate for subsequent acoustic experiments. In the lower graphs, the angle-dependent and constant response as a function of the light polarization direction measured at a fixed wavelength confirm the two different geometries.

FURTHER APPLICATIONS OF SMS EXPERIMENTS

The linear optical characterization of the NDs by SMS provides other benefits when *pump&probe* (P&P) experiments are subsequently performed. In P&P spectroscopy, two pulsed laser beams of different colors are focused on the nano-object under investigation. Therefore, the SMS technique helps superposing spatially the two laser beams, by overlapping their SMS images from the same nano-object. Furthermore, the knowledge of the extinction spectrum of NDs allows to select an appropriate probe frequency maximizing the detection efficiency of an acoustic mode in ultrafast experiments. Finally, after a P&P experiment, where a ND has been repeatedly excited, a novel SPR measurement permits to verify the nanoparticle integrity.

3.2.3 Excitation and detection of acoustic modes in a single gold nanodisk by time-resolved spectroscopy

Acoustic vibrations of nano-objects can be detected through spectroscopy techniques, such as Raman and P&P. The latter is the most suitable choice for this work, since allows to study single (higher signal over noise ratio) and relatively large nanoparticles (Raman spectroscopy is well adapted to detect vibrational modes of small size objects, typically less than 20 nm, as larger sizes are associated to lower frequency vibrations difficult to detect [109]).

TIME-RESOLVED PUMP-PROBE EXPERIMENTS

In optical time-resolved P&P experiments, energy is deposited into a nano-object via a "pump" light pulse and its ultrafast response is monitored via a time-delayed "probe" pulse. The two-colors P&P setup used during this study is sketched in Fig. (3.10). It is based on a Ti:Sa laser source delivering 100 fs pulses at a repetition rate of 80 MHz in the frequency range $[690-1040\,\text{nm}]$. The output pulse train is split in two parts to generate the pump and the probe beams, a different wavelength being generated for one of them through second harmonic generation $[390-520\,\text{nm}]$ or with an optical parameter oscillator $[540-700\,\text{nm}]$. In the context of the experiments reported here, the two beams are focused on the single ND using an apochromatic objective, by combining the P&P setup with the SMS microscope. The time delay between the pump and the probe pulses is changed by means of a mechanical delay stage. The high sensitivity detection of the pump-induced time-dependent relative change in transmission $\Delta T/T$ of the probe beam through the sample is achieved by chopping the pump beam at 30 kHz and detecting the induced probe beam transmission change using a lock-in amplifier.

In the context of noble metal nanoparticles, the pump absorption initially gener-

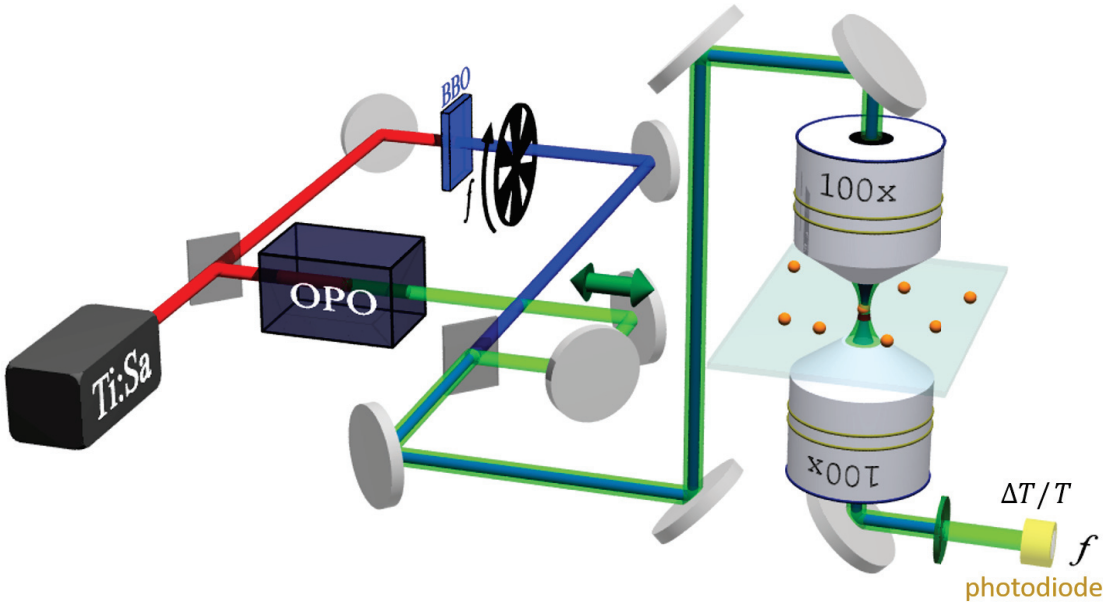

Figure 3.10: Setup for P&P experiments on single nano-objects. In the configuration illustrated here, pump and probe beams are respectively generated by frequency doubling (blue beam) and optical parametric oscillator (green beam) from the red/infrared output of the tunable Ti:Sa laser source. After filtering the pump, the ultrafast response is characterized by monitoring the relative transient change of probe beam transmission $\Delta T/T$, which is a function of the delay between the pump and probe pulses (controlled through the mechanical delay stage on the probe beam path). In order to achieve high sensitivity, the pump beam is mechanically modulated (chopper) at the frequency f, and the pump-induced probe beam power fluctuations are detected via lock-in amplification at the same frequency.

ates non-thermal electronic distributions [110]. Electron-electron scattering leads to electronic thermalization within a few hundred of fs [110, 111], while electron-phonon coupling leads to complete nanoparticle thermalization in a $\sim$1 ps timescale [81, 112]. This is followed by the cooling of the excited nanoparticle, i.e. the transfer of energy injected by the pump beam towards the surrounding. This process takes several ps-ns depending on the nanoparticle size, the composition and geometry of the interface nanoparticle/matrix, the thermal resistance at the interface (Kapitza resistance) and on the environment thermal conductivity [113, 114, 115].

More precisely, the coupling between hot electrons and phonon modes of the nanoparticle is described by the two-temperature model (TTM), which describes

the rate of energy exchange between electrons and phonons in the system [81]

$$\begin{cases} C_e(T_e)\frac{dT_e}{dt} = -g(T_e - T_l) \\ C_l\frac{dT_l}{dt} = g(T_e - T_l) \end{cases}, \tag{3.32}$$

where T_e and T_l are the electronic and lattice temperatures, $C_e(T_e) = cT_e$ is the temperature dependent electronic volumetric heat capacity, C_l is the lattice volumetric heat capacity and g is the electron-phonon coupling constant. Calling T_0 the ambient temperature and ΔT_e the increase in the electronic temperature due to the pump pulse, in the low excitation limit ($\Delta T_e \ll T_0$) the relaxation time is given by $\tau_B = c(T_0 + \Delta T_e)/g$. P&P measurements leads to $\tau_B \sim 1\,\mathrm{ps}$ for bulk gold. At 300 K, $C_e \ll C_l$, meaning the initial electronic temperature after laser excitation is much higher than the equilibrium temperature of whole nanoparticle after internal thermalization. The increase in lattice temperature from optical excitation is typically a few K to tens of K. Higher lattice heating is avoided in the following single particle experiments as it may cause nanoparticle melting.

The global cooling of the thermalized nanoparticle at temperature $T_s = T_e = T_l > T_0$ (and T_m being the surrounding matrix temperature) is then ruled by two main mechanisms: the heat transfer across the particle/matrix interface and the heat diffusion in the matrix itself [4]. Therefore, for a nanosphere of radius R embedded in a matrix of thermal diffusivity α_m ($\alpha_m = \Lambda_m/C_m$ considering the environment thermal conductivity Λ_m and volumetric heat capacity C_m) one has

$$\begin{cases} \frac{\partial T_s}{\partial t} = -\frac{3G}{RC_l}(T_s(t) - T_m(R,t)) \\ \frac{\partial^2(rT_m)}{\partial r^2} = \frac{1}{\alpha_m}\frac{\partial(rT_m)}{\partial t} \end{cases}, \tag{3.33}$$

where T_s and T_m are the temperatures of the nanosphere and of the matrix and G is the interface thermal conductance (typical order of magnitude $100\,\mathrm{MW\,m^{-2}\,K^{-1}}$). The system can be solved using Laplace transform techniques to determine the rate of cooling of the nanosphere, treating G as an adjustable parameter [81]. In the limiting case where the interface conductance mechanism is slow compared to the heat dissipation in the surrounding, T_s decays exponentially with a characteristic time of $\tau_C = C_l R/3G$. Considering a small gold nanosphere with $R = 10\,\mathrm{nm}$ and $G = 150\,\mathrm{MW\,m^{-2}\,K^{-1}}$, it results $\tau_C \approx 60\,\mathrm{ps}$. On the other hand, if heat dissipation in the matrix is the slowest process, then the timescale is given by $\tau_D = (C_l R)^2/(9C_m\Lambda_m)$, that results in $\tau_D \approx 50\,\mathrm{ps}$ for glass [121]. The similar magnitudes show that, generally, both interface resistance and environment diffusion have to be taken into account. However, considering a sapphire matrix and

[4] heat diffusion within nanoparticle can be neglected, as it is much faster than the surrounding matrix

$R = 10\,\text{nm}$, the diffusion timescale becomes much smaller, $\tau_D \approx 1\,\text{ps}$, due to the high diffusivity of sapphire, nanoparticle cooling being then mostly limited by interfacial thermal transfer. Note that, due to the different scaling with nanoparticle size of the relaxation times associated to diffusion and interface, heat diffusion in sapphire becomes again relevant for larger nanoparticles. For instance, a nanosphere with $R = 100\,\text{nm}$ embedded in sapphire presents $\tau_C \approx 600\,\text{ps}$ and $\tau_D \approx 100\,\text{ps}$.
This thermal relation induces a long-time $\Delta T/T$ signal which will be subtracted, as well as the electronic contributes, in order to focus the attention on the acoustic component of the signal investigated in this work.

In this frame, acoustic vibrations are launched via lattice dilation upon heating (heating modifying the equilibrium configuration of the nanoparticle), and thus, acoustic modes with displacement field similar to the particle dilatation can be

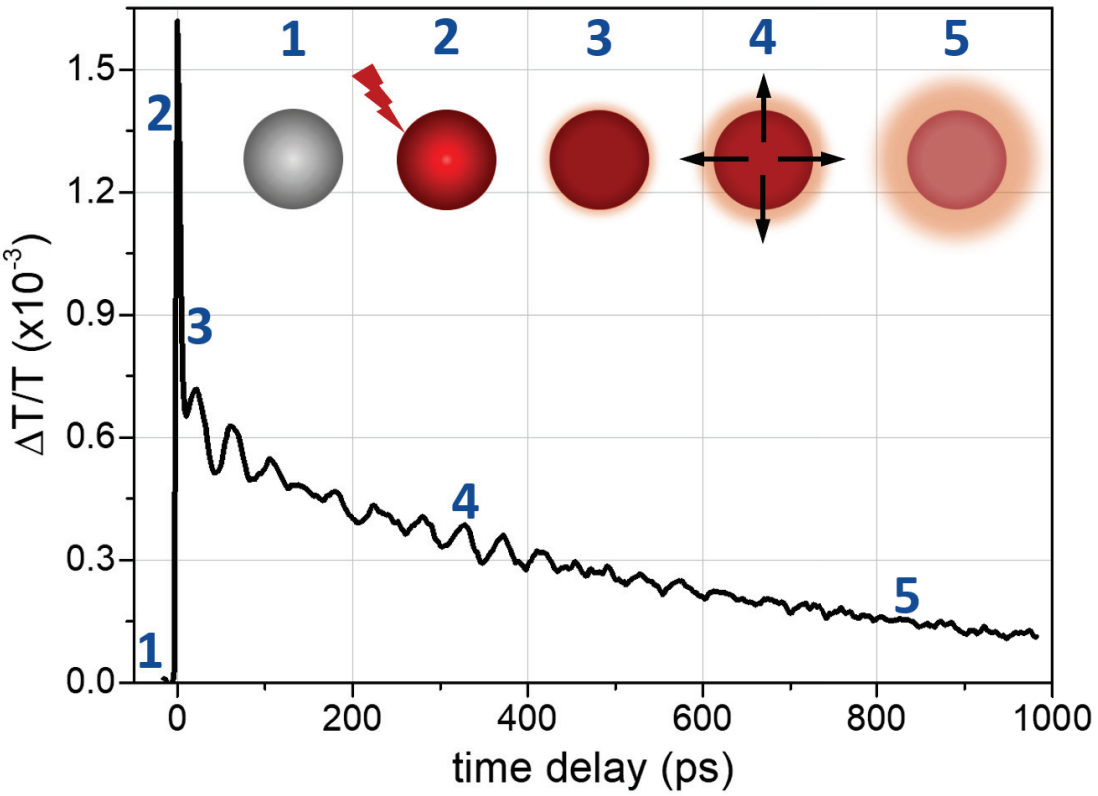

Figure 3.11: Ultrafast response of the asymmetrical ND presented on the left hand side of Fig. (3.9). The P&P signal is usually described through several time domain events: particle equilibrium (1); electron heating by a femtosecond pump pulse and thermalization of the electron gas (2); electron-lattice thermalization (3); damped acoustic vibrations (4); cooling (5).

excited. They are damped through intrinsic processes discussed in section (3.1) [116, 117, 118] and by mechanical energy dissipation towards the environment [119, 120], with a rate dependent on the nanoparticle size and on the composition and geometry of the nanoparticle/matrix interface.

All the mechanisms described above temporally modify the dielectric function of the nanoparticle ($\epsilon = \epsilon_1 + i\epsilon_2$), affecting the observed probe transmission. In particular, an acoustic vibration corresponds to a specific harmonic displacement of the nanoparticle interatomic distances. This locally induces a periodic variation of ϵ that reflects into a periodical SPR shift for metal nanoparticles. When the probe frequency ω_{pr} is chosen in the flanks of the SPR, the spectral oscillations of σ_{ext} induced by a vibration mode can be detected at fixed ω_{pr}, as it manifests with a temporal modulation of the observed probe transmission (its complex frequency $\tilde{f}$ directly reflecting that of the related acoustic mode [119]).
An example of the transmission change $\Delta T/T$ as a function of the P&P time delay is reported in Fig. (3.11). The experimental signal is firstly characterized by a sharp peak close to the origin that corresponds to the electronic excitation and to the relaxation via electron-electron and election-phonon coupling. This ultrafast response can be well fitted through the convolution between a Gaussian and a decaying exponential, whose lifetime τ_B is the characteristic time for the electron-phonon scattering. Afterwards, the signal returns globally to the zero because of the cooling mechanisms. In most of the reported cases, this trend is empirically well reproduced by the sum of one (or two) decaying exponential with lifetime τ_C (and τ_D). When acoustic vibrations are detected, sinusoidal damped oscillations are superposed to the quasi-decaying exponentials. Globally, the decaying part of the experimental signal can be fitted using

$$\frac{\Delta T}{T} = \sum_{i=1}^{N} A_i e^{-\frac{t}{\tau_i}} \cos\left(2\pi f_i t + \phi_i\right) + B e^{-\frac{t}{\tau_B}} + C e^{-\frac{t}{\tau_C}} + D e^{-\frac{t}{\tau_D}} , \tag{3.34}$$

where A_i, τ_i, f_i, ϕ_i are fit parameters setting out the i-th mode oscillation amplitude, lifetime, frequency and phase; B, C, D, τ_B, τ_C, τ_D are fit parameters describing the decaying exponentials amplitudes and lifetimes.

DATA ANALYSIS

The experimental P&P signal of each investigated ND has been analyzed following the protocol described in Fig. (3.12). In this way, the i-th acoustic mode of a ND is characterized by its frequency $f_i = 1/T_i$, attenuation $\alpha_i = 1/\tau_i$, phase ϕ_1 and amplitude A_i (note that the two former are intrinsic to vibrational modes, while the two later depend on the way they are excited, and, for A_i, detected). To count the number of oscillations carried out by a mode before its attenuation, the Q-factor

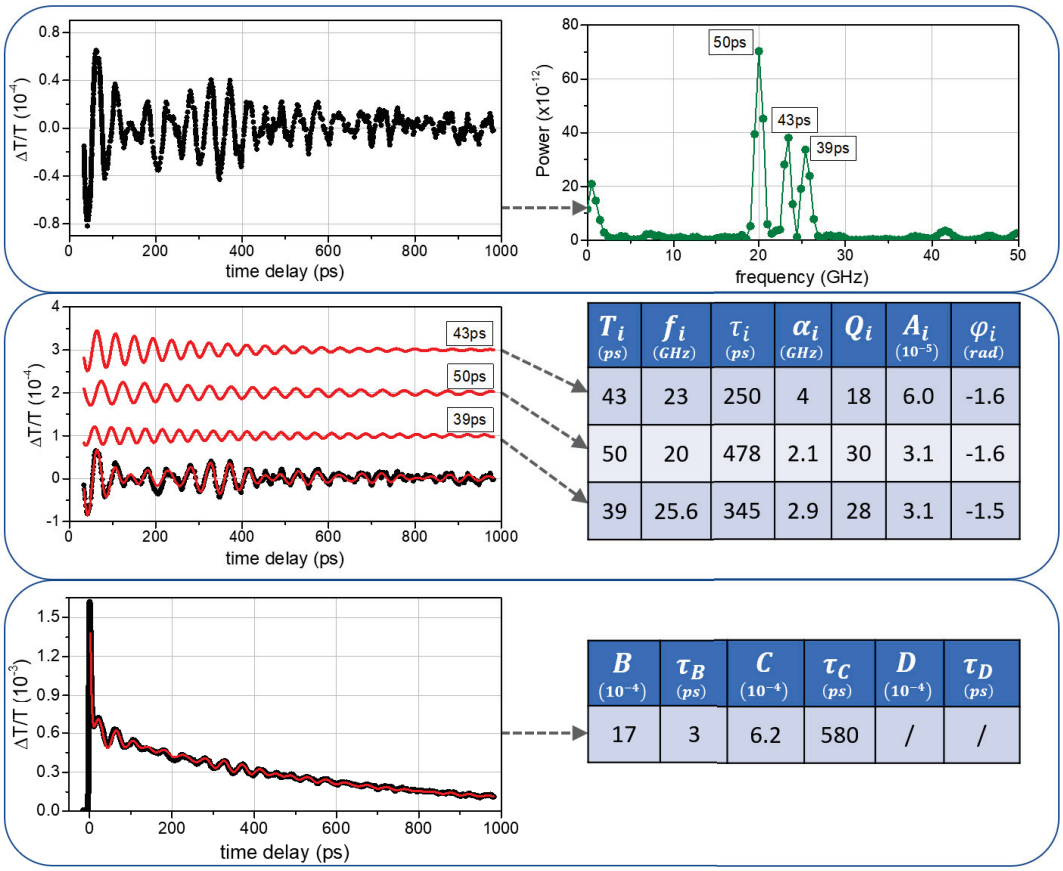

T_i (ps)	f_i (GHz)	τ_i (ps)	α_i (GHz)	Q_i	A_i (10^{-5})	φ_i (rad)
43	23	250	4	18	6.0	-1.6
50	20	478	2.1	30	3.1	-1.6
39	25.6	345	2.9	28	3.1	-1.5

B (10^{-4})	τ_B (ps)	C (10^{-4})	τ_C (ps)	D (10^{-4})	τ_D (ps)
17	3	6.2	580	/	/

Figure 3.12: Illustration of the analysis of P&P experiments realized on the NDs. In this example, the ultrafast response of Fig. (3.11), related to the asymmetrical ND characterized on the left hand side of Fig. (3.9), is the starting point. Upper panel: by subtracting the electronic and thermal exponential decays only the acoustic component remains (black) and a Fourier transform is realized to help identifying the modes frequencies (green). Central panel: oscillating part of the P&P signal is fitted using three damped sinusoids (red); above this fit, the three sinusoids are presented separately; in the table are reported the useful parameters of every mode (respectively: period, real frequency, lifetime, attenuation, Q-factor, amplitude, phase). Lower panel: the total P&P signal (black) is accurately reproduced by Eq. (3.34), using the sum of three damped sinusoidal function and two decaying exponentials (red), whose amplitudes and lifetimes are summarized in the table besides.

is also considered following the definition of Eq. (3.20): $Q_i = \pi f_i/\alpha_i$. Furthermore, for each ND the cooling dynamics has been monitored measuring the lifetime τ_C (and, in some cases, τ_D if another decaying exponential is needed to properly fit the data).
It might be pointed out that after 1 ns (the maximal P&P delay available in ex-

periments previously performed in our group on single nanoparticles, including those on the S2 sample) some experimental signals have not relaxed to their initial values (Fig. (3.11)). This usually does not affect much frequency determination. However, in order to achieve more reliable values of Q_i and τ_C it was worthwhile to extend the P&P time delay further during this thesis. This was accomplished by extending the delay line maximum range from 1 ns to 3 ns, introducing some back and forward paths that make the probe beam of Fig. (3.10) passing three times through the delay stage. This improvement has been exploited to study NDs from sample S1.

EXPERIMENTAL RESULTS

Shape effects have first been investigated by measuring the acoustic response of circular and elliptical NDs, as shown in Fig. (3.13). As illustrated in Fig. (3.13a), P&P experiments on the circular ND of Fig. (3.9) enable the detection of a single acoustic mode. Similar observations were made for several NDs, showing that circular symmetry breaking leads to the replacement of the dominant mode by two or three modes with close frequencies. These results are in line with the free ND eigenmodes evolution with ellipticity deduced from the FEM study presented in in Fig. (3.14).
In the specific case of the NDs from Fig. (3.12) and (3.13a), characterized by $D = 70\,\text{nm}$ and $h = 19\,\text{nm}$, the circular ND presents a dominant mode with frequency $f_1 = 23\,\text{GHz}$ and the elliptical one shows a mode at same frequency f_1 (with similar damping) and two different modes with frequencies within the range $f_1 \pm 3\,\text{GHz}$. Typically the frequencies exhibited by the circular NDs are detected also in elliptical ones, with very small deviations. However, their damping times and Q-factors present large fluctuations, as illustrated in Fig. (3.13b), where another elliptical ND (with yet same nominal dimensions), shows a dominant frequency close to f_1, but with Q-factor 40% higher. Therefore, reliable Q estimation is challenging for non-circular NDs. The detection of several vibration modes with close frequencies and similar lifetime generally induces a beating pattern which can be fitted by several damped sinusoids with exchangeable damping times, precluding from a precise attribution of lifetime for each mode. As the primary goal of this investigation was the determination of the Q-factor dependence on the aspect ratio, the subsequent investigations were therefore limited to circular NDs, identified from their quasi-polarization independent σ_{ext} in SMS measurements.

Some representative oscillating P&P components of circular NDs from samples S1 and S2 are presented in Fig. (3.15). As described in detail in its caption, every oscillation trace has been centered on the η of the related ND (vertical axis) and compressed along the time delay axis getting unitary periods (horizontal axis).

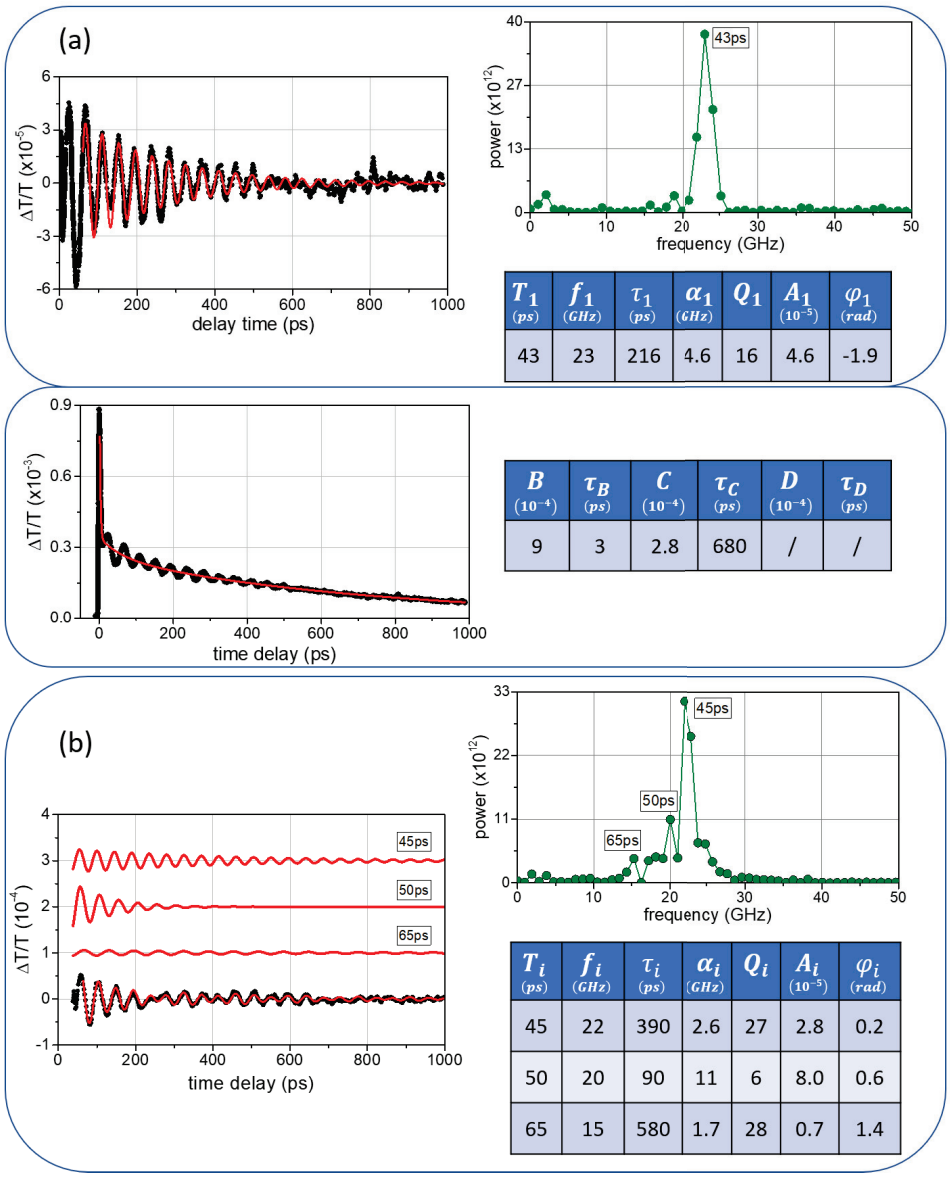

T_1 (ps)	f_1 (GHz)	τ_1 (ps)	α_1 (GHz)	Q_1	A_1 (10^{-5})	φ_1 (rad)
43	23	216	4.6	16	4.6	-1.9

B (10^{-4})	τ_B (ps)	C (10^{-4})	τ_C (ps)	D (10^{-4})	τ_D (ps)
9	3	2.8	680	/	/

T_i (ps)	f_i (GHz)	τ_i (ps)	α_i (GHz)	Q_i	A_i (10^{-5})	φ_i (rad)
45	22	390	2.6	27	2.8	0.2
50	20	90	11	6	8.0	0.6
65	15	580	1.7	28	0.7	1.4

Figure 3.13: (a) Analysis of P&P experiments performed on the circular ND described in Fig. (3.9). Top panel: the data (black) are fitted using a simple damped sinusoid (red), whose parameters are reported in the table below the Fourier transform graph. Bottom panel: the signal (black) descent is reproduced using the sum of two decaying exponentials (red), whom amplitudes and lifetime are summarize in the table. (b) Analysis of acoustic trace obtained from P&P experiment performed on another elliptical ND of similar size. The data (black) are fitted using three damped sinusoid (red), whose parameters are reported in the table below the Fourier transform graph. This enlightens that anisotropy may affect the estimated Q-factor of similar modes (43 and 45 ps).

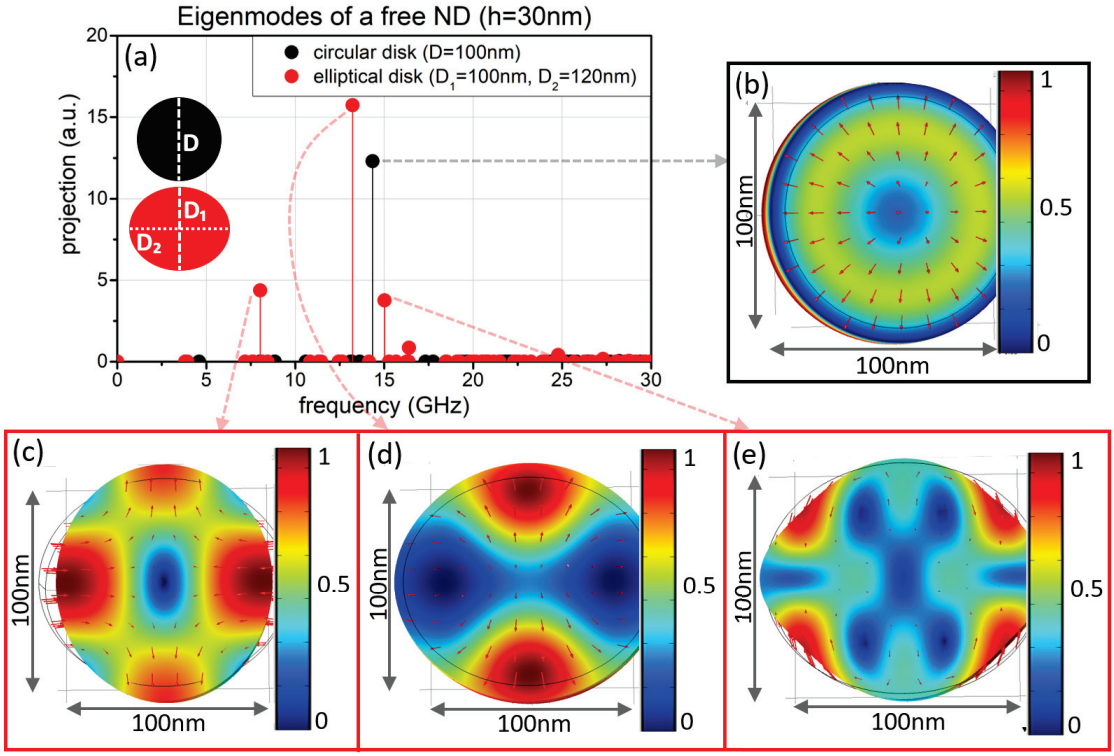

Figure 3.14: (a): computed acoustic excitation spectra (obtained by the computation of vibrational modes and their projection on the displacement field associated to a dilation) of eigenmodes of a free circular disk of thickness $h = 30\,\text{nm}$ and diameter $D = 100\,\text{nm}$ (black dot) and eigenmodes of a free elliptical disk of thickness $h = 30\,\text{nm}$, short axis $D_1 = 100\,\text{nm}$ and long axis $D_2 = 120\,\text{nm}$ (red dots). For the circular disk, a single mode is excited, with a 14.3 Hz frequency and a radial breathing-like normalized displacement profile (b). For the elliptical one, three modes are predicted to be excited, with 8.0 Hz, 13.3 Hz and 15.0 Hz frequencies and the normalized displacement profiles indicated in panels c-e.

This normalization allows to visually compare the Q-factors of the long-lasting mode for several η. Since Q is roughly the number of visible oscillations, its typical value is about 15, but an enhancement can be noticed at $\eta = 2.5$ ($Q \sim 50$), while a second broader and weaker enhancement seems to occur around $\eta = 6$ ($Q \sim 30$).

Acoustic P&P traces associated to η in the range $[3.2 - 8.5]$ are accurately fitted with a single damped vibrational mode, which is referred to as *mode1*. It is characterized by its frequency f_1, phase ϕ_1, lifetime τ_1 and amplitude A_1. An example is reported in the graph (a) of Fig. (3.16). f_1 decreases with the ND di-

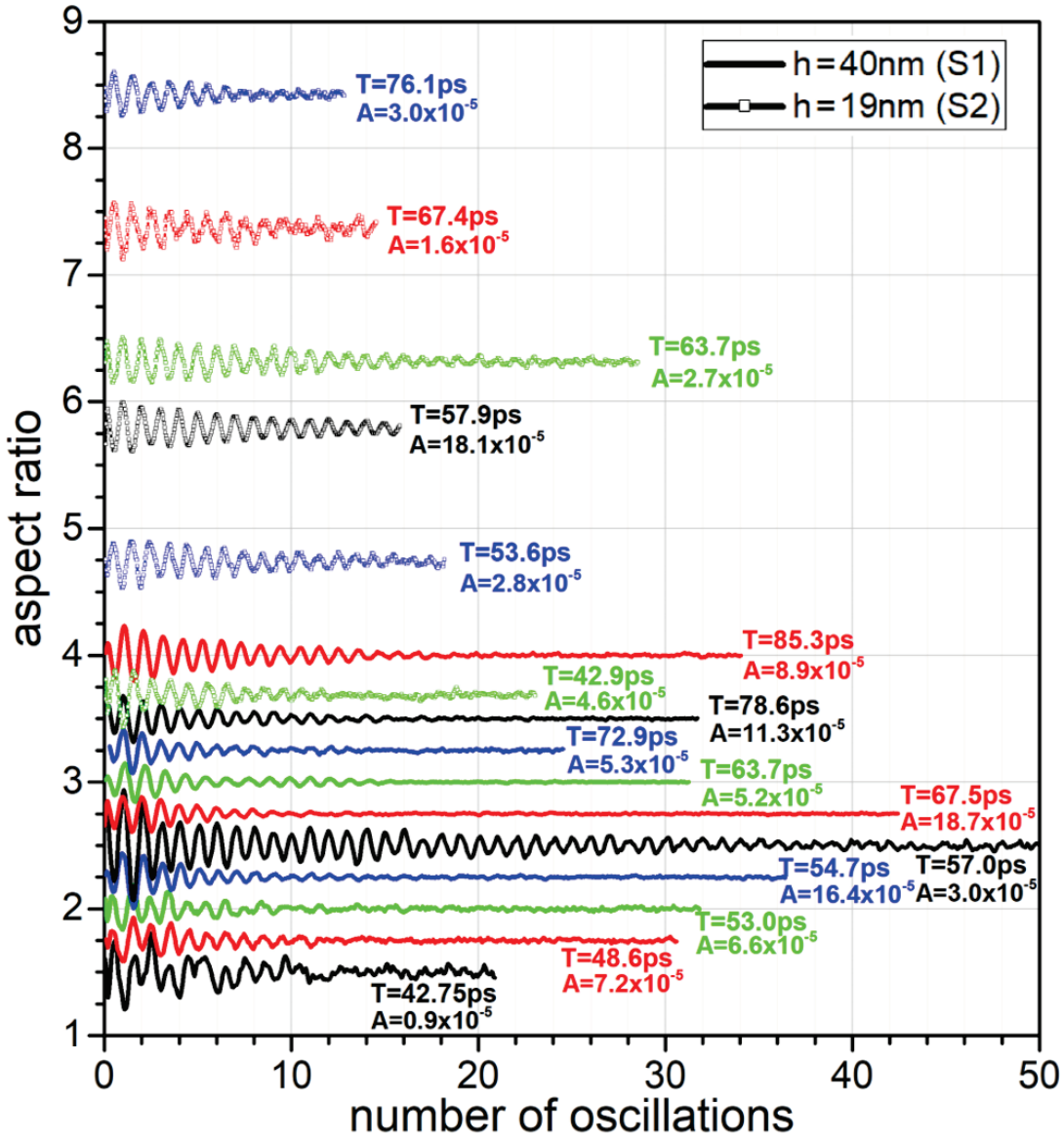

Figure 3.15: Representative acoustic P&P traces of circular NDs from samples S1 (solid lines) and S2 (dotted lines). In order to compare the different curves, some changes were made to the original data. Firstly, they have been vertically translated in order to match with the aspect ratio of the related ND (vertical axis), and then colored and rescaled to make them visible. Period T and amplitude A reported beside each curve correspond to the mode with higher Q-factor (identified by two-sinusoidal fits realized on every acoustic trace). The delay time axis of each acoustic trace was normalized over the period T yielding the number of oscillations (horizontal axis). This allows to visually compare the Q-factors of the most long-lasting mode for several aspect ratios η.

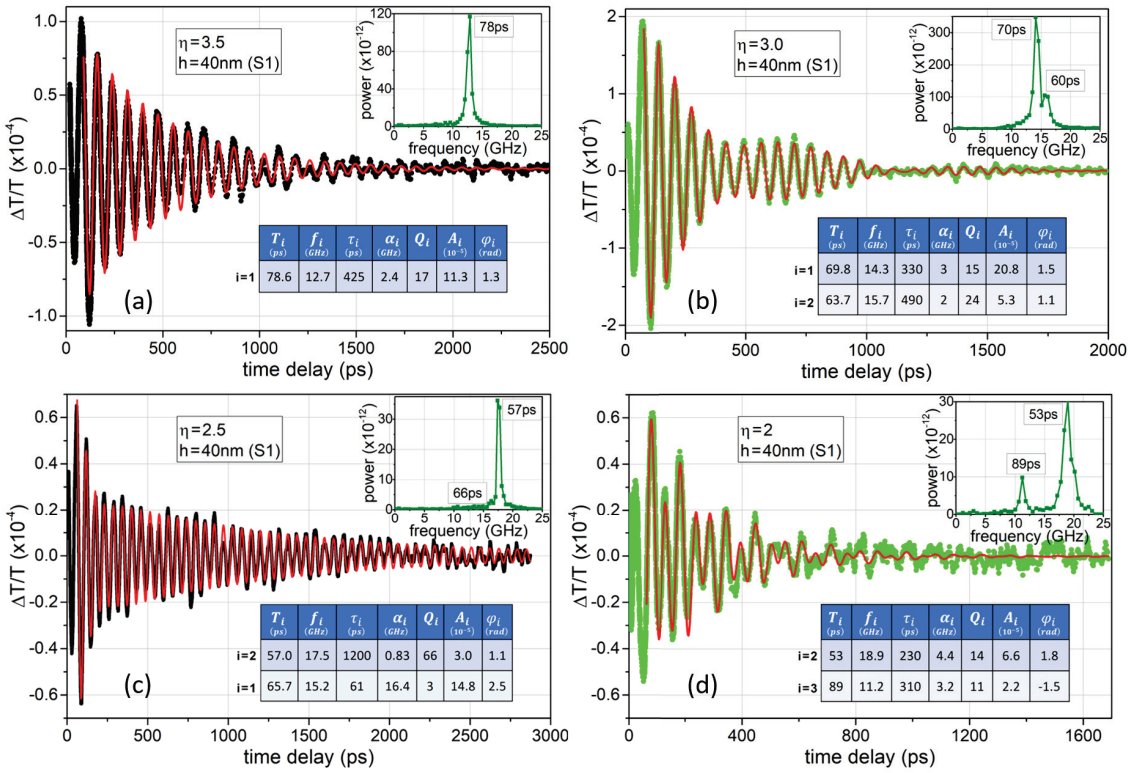

Figure 3.16: Four P&P acoustic traces (green and black) are fitted using one or two damped sinusoid (red). Each graph contains the Fourier transform and a table with the fitting parameters. The first table line describes the dominant mode of the Fourier transform. Overall, three different modes ($i = 1, 2, 3$) are detectable. Typically *mode1* and *mode2* are in phase $\phi_1 \sim \phi_2 \sim \pi/2$ (except when $\eta = 2.5$, i.e. Q is enhanced), while *mode3* is always in antiphase $\phi_3 \sim -\pi/2$.

ameter, while ϕ_1 remains constant [5], as shown later in the summary of Fig. (3.18). For smaller η, two modes are commonly detected. In particular, within the interval $[2.2-3.2]$ the acoustic traces still exhibit *mode1* (whose frequencies smoothly match with the *mode1* from the previous range) and a second relevant mode, called *mode2*, whose frequency f_2 reduces almost linearly with the ND diameter similarly to f_1. Its phase ϕ_2 is independent from η and close to ϕ_1. On the other hand, A_2 and τ_2 are remarkably dependent on η, and often completely different from A_1 and τ_1. Examples are shown in the graphs (b) and (c) of Fig. (3.16).
Within the range [1.5–2.2] the acoustic traces consist in the *mode2* and the *mode3* a new vibrational mode with frequency f_3 quasi-independent of ND diameter. Again, the phase ϕ_3 is independent from η, but this time is shifted of π with re-

[5] as long as the experimental probe wavelength is kept in the same SPR flank, as illustrated in Fig. (3.17).

spect to ϕ_2. An example is reported in the graph (d) of Fig. (3.16).

Overall, for η scaling from 1.5 to 8.5, three different vibrational modes are detected via P&P (see Fig. (3.18), discussed later, for details). Oscillations called *mode1* and *mode2* are most likely associated to radial displacements of the ND, since their frequencies decrease with the diameter and they tend to be in phase. On the contrary, *mode3* should be associated to a thickness displacement of the ND,

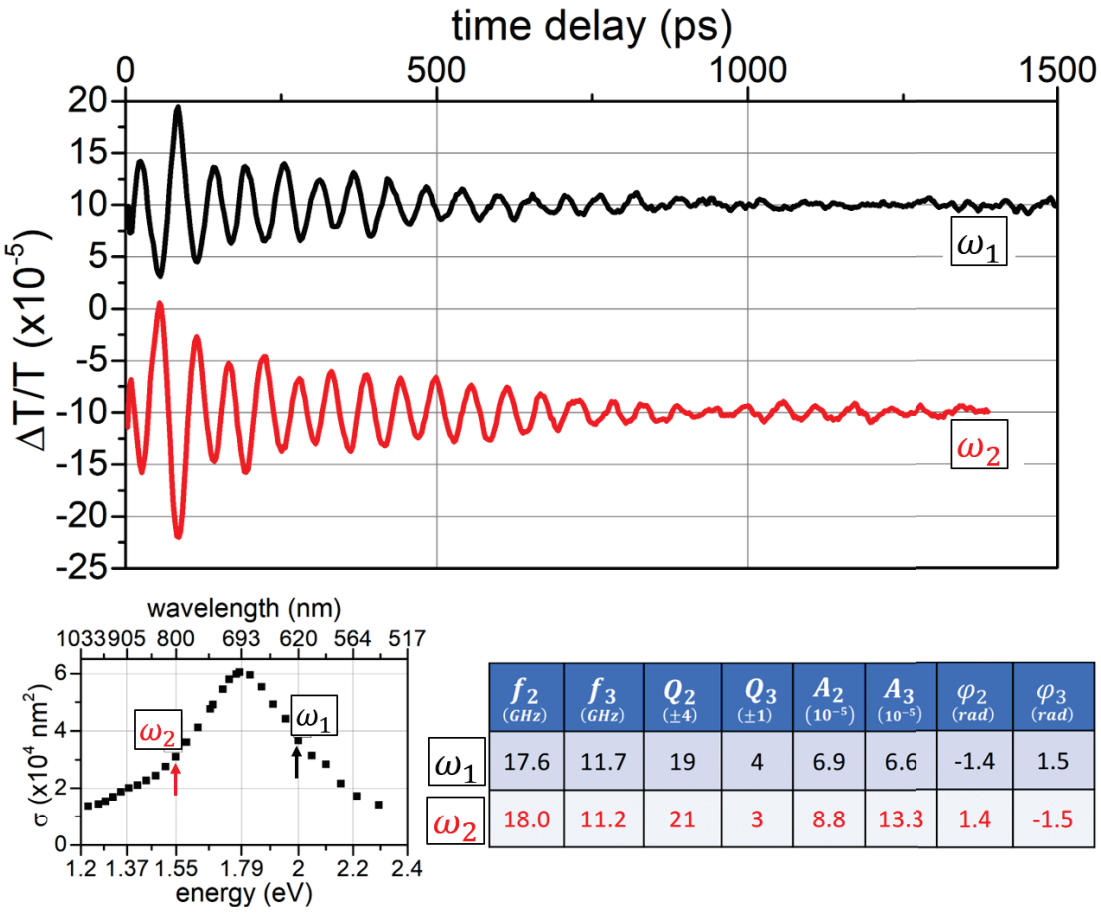

	f_2 (GHz)	f_3 (GHz)	Q_2 (±4)	Q_3 (±1)	A_2 (10^{-5})	A_3 (10^{-5})	φ_2 (rad)	φ_3 (rad)
ω_1	17.6	11.7	19	4	6.9	6.6	-1.4	1.5
ω_2	18.0	11.2	21	3	8.8	13.3	1.4	-1.5

Figure 3.17: Verification of the effect of pump and probe frequencies on the determined acoustic mode parameters. Two P&P acoustic traces (shifted for clarity) are obtained on the same ND (D=85 nm) from S1, using very different combination of probe ω_{pr} and pump ω_{pump} wavelengths: in the first case $\omega_{pr} = \omega_1 = 620$ nm and $\omega_{pump} = 820$ nm; in the second configuration $\omega_{pr} = \omega_2 = 800$ nm and $\omega_{pump} = 400$ nm. One may observe that in the second case the acoustic trace has larger amplitudes and is in antiphase with respect to the first. However, frequencies and Q-factor remain unchanged, within the experimental error bars.

given that its frequency does not change with the diameter and it is in antiphase with *mode1* and *mode2* (a thickness increase inducing a SPR blueshift, opposite to the redshift induced by a diameter increase).

As already mentioned, frequencies f_i and Q-factors Q_i are intrinsic to the i-th vibrational mode, and therefore independent on the excitation and detection conditions. This aspect is a key point that allows to compare frequencies and Q-factors obtained probing different NDs at different frequencies ω_{pr}. This property has been experimentally verified for a couple of NDs, repeating the P&P experiment with very different ω_{pump} and ω_{pr}. The results, reported in Fig. (3.17), show little fluctuation in f_i and Q_i attributed to their incertitudes. The phases ϕ_i are simply shifted of π when the probe wavelength passes in the other SPR flank. On the other hand, A_i exhibit strong variations, which make unsuitable a quantitative comparisons between mode amplitude of different NDs.
The results of the study performed on circular NDs from S1 and S2 are summarized in Fig. (3.18). The frequencies from S2 have been multiplied by 19/40 in order to compensate the difference in h with S1 (see Section (3.1.4)). Overall, three different modes (*mode1*, *mode2*, *mode3*) have been detected. For aspect ratio η in the range $[2.4-3]$, each NDs exhibit *mode1* and *mode2* with similar frequencies and phases. In order to distinguished between them, they were classified in accordance to the criterion $A_1 > A_2$ and $Q_1 < Q_2$ [6] (comparisons with frequencies, Q-factors and amplitudes computed in FEM simulations, reported later in Fig. (3.22), also helped to distinguish the nature of these three modes). A salient result of the experiments reported here is the enhancement of Q_1 and Q_2 around specific ND aspect ratios, with Q_2 presenting a sharp peak near $\eta = 2.5$ ($\max\{Q_2\} = 66$) and Q_1 a broader one about $\eta = 6$ ($\max\{Q_1\} = 31$). In order to clarify the nature of the detected modes, to model their frequencies and damping rates and to understand the origin of these Q-factor amplifications, a comparison with FEM simulations were carried out.

COMPARISON WITH NUMERIC MODELING

To better understand the origin of the observed acoustic modes, FEM simulations (Section (3.1.4)) were realized on single NDs of several η (ranging from 1.4 to 9) and $h = 40\,\text{nm}$, in the configuration shown in Fig.(3.5). The ND excitation consists in a uniform and periodic stress at a frequency f (chosen in the interval $0 - 25\,\text{GHz}$). For each η and f, the ND strain energy was deduced from the computed displacement field (accordingly with Eq. (3.16) of Section (3.1)). In Fig. (3.19) the ND strain energy is plotted as a function of η and f (and normalized to 0.5 for visualization purposes). The Lorentzian peaks appearing in

[6] although at $\eta = 3$ this distinction becomes vague.

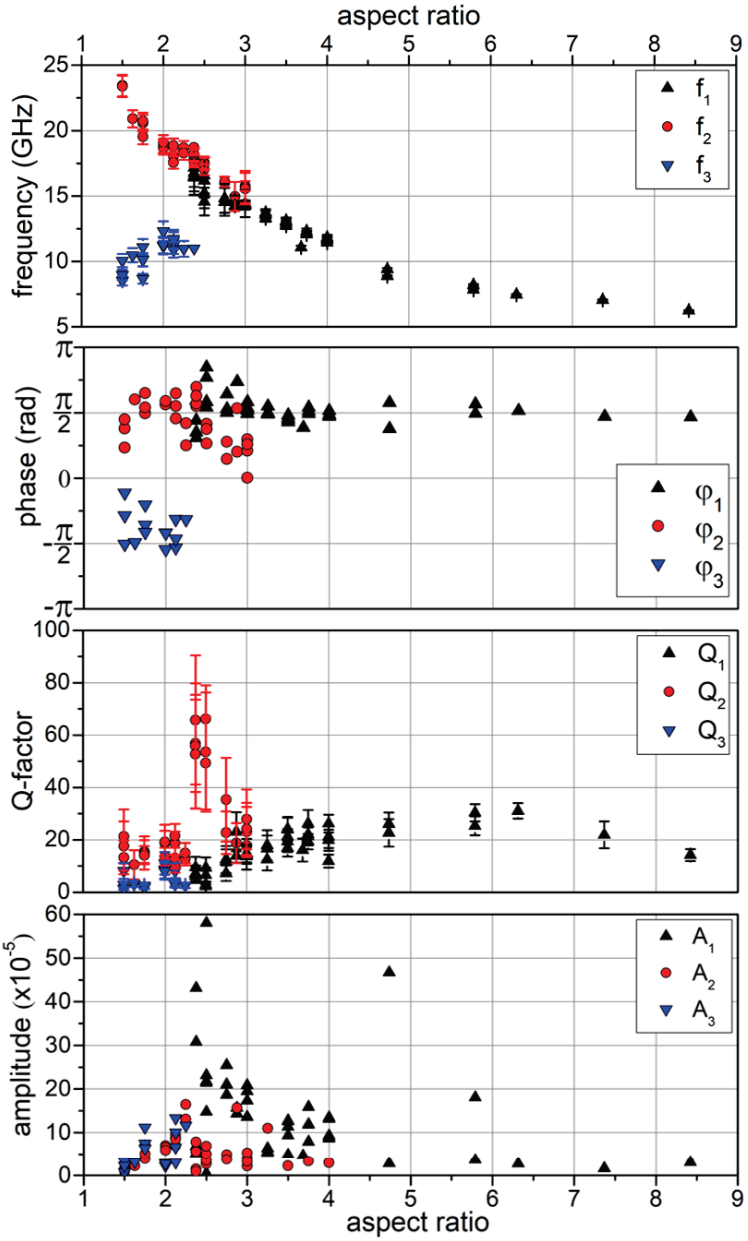

Figure 3.18: Extracted parameters of the detected modes for all the circular investigated single NDs from samples S1 and S2. The frequencies from S2 have been multiplied by 19/40 in order to compensate the difference in h with S1. *mode1* and *mode2* present frequencies that decrease with the diameter, while *mode3* has a constant frequency. *mode3* is in antiphase with respect to *mode1* and *mode2*. *mode2* exhibits an enhancement of Q at $\eta = 2.5$, while *mode1* shows a broader and weaker amplification of Q around $\eta = 6$. *mode1* also presents relative strong amplitude about $\eta = 2.5$.

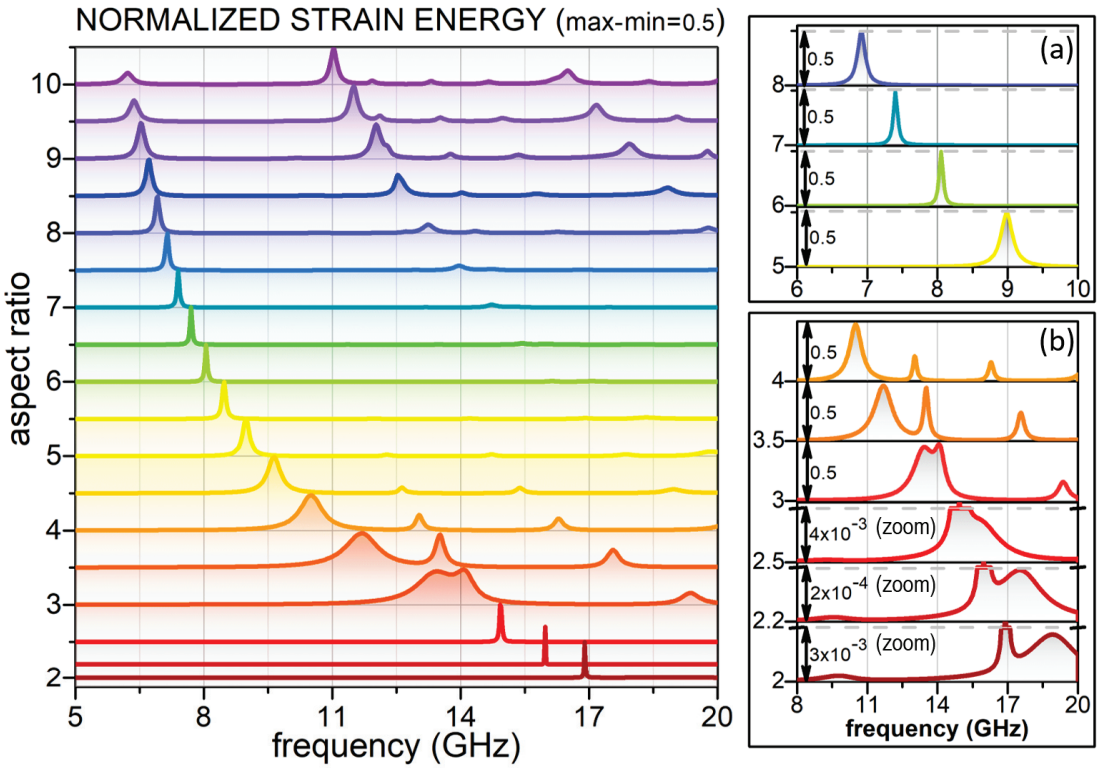

Figure 3.19: Normalized strain energies spectra computed for NDs of several η and $h=40\,\text{nm}$. The frequency response allows to identify the excited ND modes frequencies and Q-factors. Right: (a) in the η range $[5-8]$ and f interval $[6-10]$GHz an enhancement of Q may be noticed, since the Lorentzian peaks are sharper around $\eta=6$. This mode corresponds to *mode1* from the experimental results. (b) In the η range $[2-4]$ and f interval $[8-20]$GHz two dominant modes are crossing each other around $\eta=2.5$. *mode1* is the broader, while the second shall corresponds to *mode2* and its maximal Q enhancement takes place at $\eta=2.2$. At lower frequencies, about $9\,GHz$, *mode3* can be observed.

the graphs correspond to excitation-frequencies for which the ND reacts with an acoustic eigenmode. The Q-factor of each mode is directly evaluated as defined in Eq. (3.21), considering the frequency over bandwidth ratio $Q=f_n/\Delta f_n$, where f_n is the central frequency and Δf_n is its linewidth. The computed excitation spectra exhibit vibrational modes at frequencies close to those measured experimentally. For instance, the graph (a) and (b) on the right of Fig. (3.19) focuses on the modes observed in P&P experiments: in graph (a) *mode1* exhibit a high Q-factor at $\eta=6$ (with $f_1\approx 8\,\text{GHz}$); in graph (b) *mode1* is crossing *mode2* about $\eta=2.5$, which in turn present a maximal Q-factor at $\eta=2.2$ (with $f_1\approx 16\,\text{GHz}$). In the 10 GHz range, *mode3* may also be noticed for aspect ratios between 2 and 2.5 (its computed excitation amplitude becomes negligible for larger aspect ratios).

The frequencies f_n are rearranged in a more convenient way on the graph of Fig. (3.20). A visual comparison with the top graph of Fig. (3.18) is now straightforward. Frequencies corresponding to *mode1*, *mode2* and *mode3* have been enlightened using gray, red and blue lines respectively. *mode1* and *mode2* are crossing each other at $\eta = 2.7$, where only one frequency is observed. In order to individually understand the nature of *mode1* and *mode2*, their associated displacement fields and averaged energy fluxes were computed for $\eta = 4$, where the two modes are spectrally well separated (i.e., they do not significantly hybridize, as seen Fig. (3.19b)). As shown in the lower panel of Fig. (3.20), *mode1* exhibits a radial-like displacement. Its energy flux is mostly vertical and unidirectional and intense at the ND/substrate interface, associated to an efficient energy transfert to the environment (poor Q-factor). *mode2* presents a torsional-like displacement. The acoustic Poynting vector shows vortex patterns at the interface, meaning that the emission of acoustic waves in the sapphire substrate can be partly compensated by the reentrance of some of the emitted energy in the ND, suggesting possible higher quality factors for this mode. *mode3* has been characterized at $\eta = 2$. It is dominated by a thickness deformation and the energy flux is mainly vertical and intense at the interface, accounting for the poor quality factor of this mode.

According to the simulations, a maximal Q-factor enhancement for *mode2* occurs at $\eta = 2.2$. At this aspect ratio, relative displacement field and energy flux have been computed for *mode1* and *mode2* and the results are illustrated in Fig. (3.21). At $\eta = 2.2$ the modes are close in frequency and a hybridization of their displacement fields takes place. In particular, *mode1* presents some torsional deformations characteristic of *mode2*. On the other hand, *mode2* does not exhibit displacement in the region close to the interface, in contrast to what seen in Fig. (3.20). This lack of deformation can be visually obtained superposing the relative displacements fields of *mode1* and *mode2* from Fig. (3.20). As a results, the vortex patterns present in the energy flux of *mode2* are getting further apart from the interface, being higher into the ND. This effect reduces even more the energy flux intensity through the interface, and thus, strongly increases the Q-factor of *mode2*. It can be therefore concluded that the Q-factor enhancement is mainly caused by a mode hybridization that reduces the energy loss towards the substrate for one of the hybridized modes. This mode hybridization occurs when two modes intersect in frequency. The mode crossing thus requires a 2D system with two different geometrical dimensions (or higher), since in 1D systems all the mode frequencies scale with the size parameter in the same way.
Following this argument, the Q-factor enhancement observed in *mode1* at $\eta = 6$ could be attributed to an hybridization between *mode1* and *mode3*. Indeed, ob-

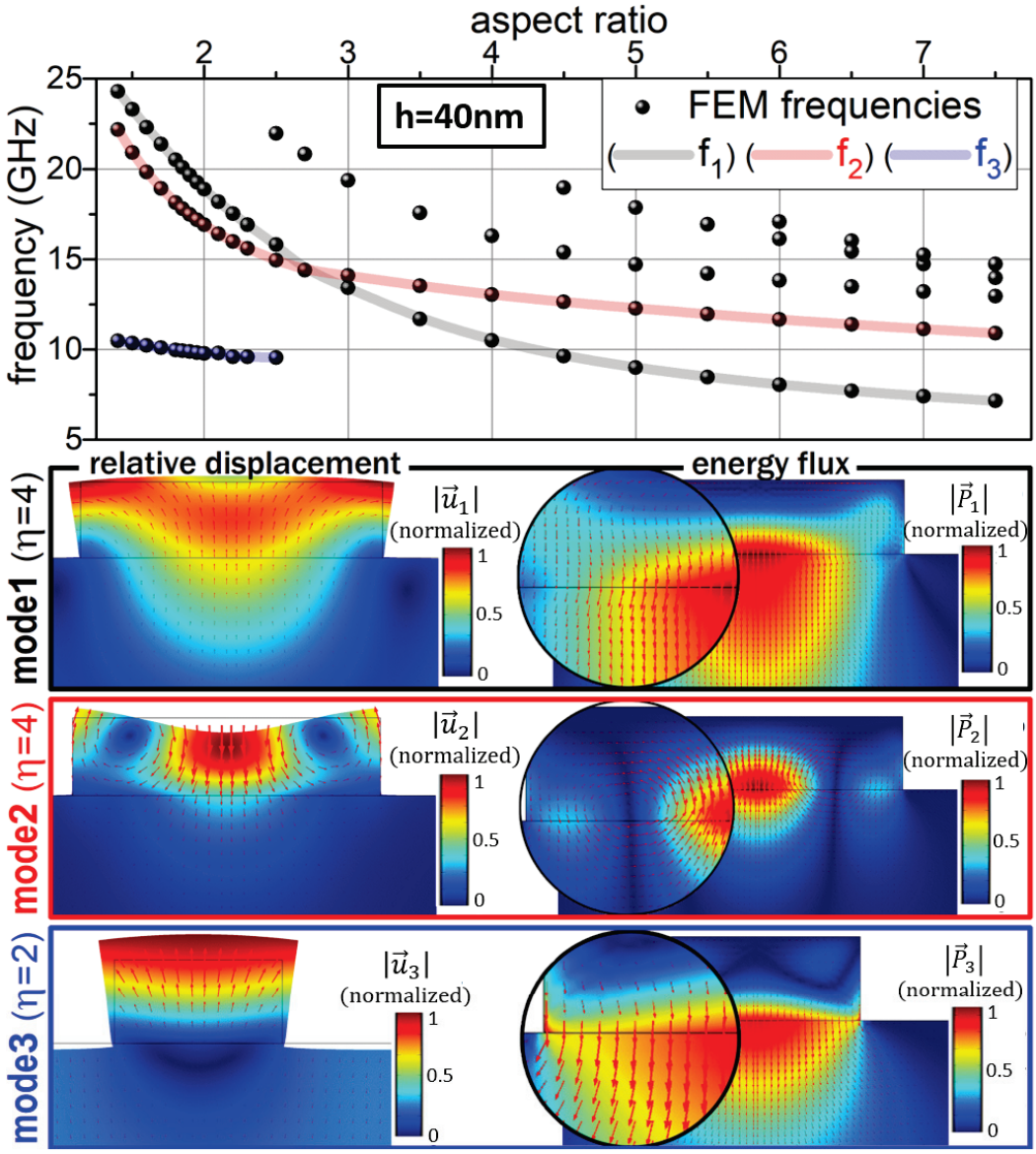

Figure 3.20: In the graph: ND frequencies calculated via FEM. Frequencies corresponding to *mode1*, *mode2* and *mode3* have been enlightened using gray, red and blue lines respectively. *mode1* and *mode2* are crossing each other at $\eta = 2.7$. Below: *mode1*, *mode2* and *mode3* example of normalized displacements field and energy flux (evaluated at η far away from the modes interception). *mode1* is radial-like, *mode2* is torsional-like and *mode3* is thickness-like.

serving the graph of Fig. (3.20), a prolongation of f_3 would cross f_1. The weak displacement of *mode3* (difficult to detect when other modes are present) together with the fact that f_1 and f_3 have similar slopes at $\eta = 6$ would explain why the

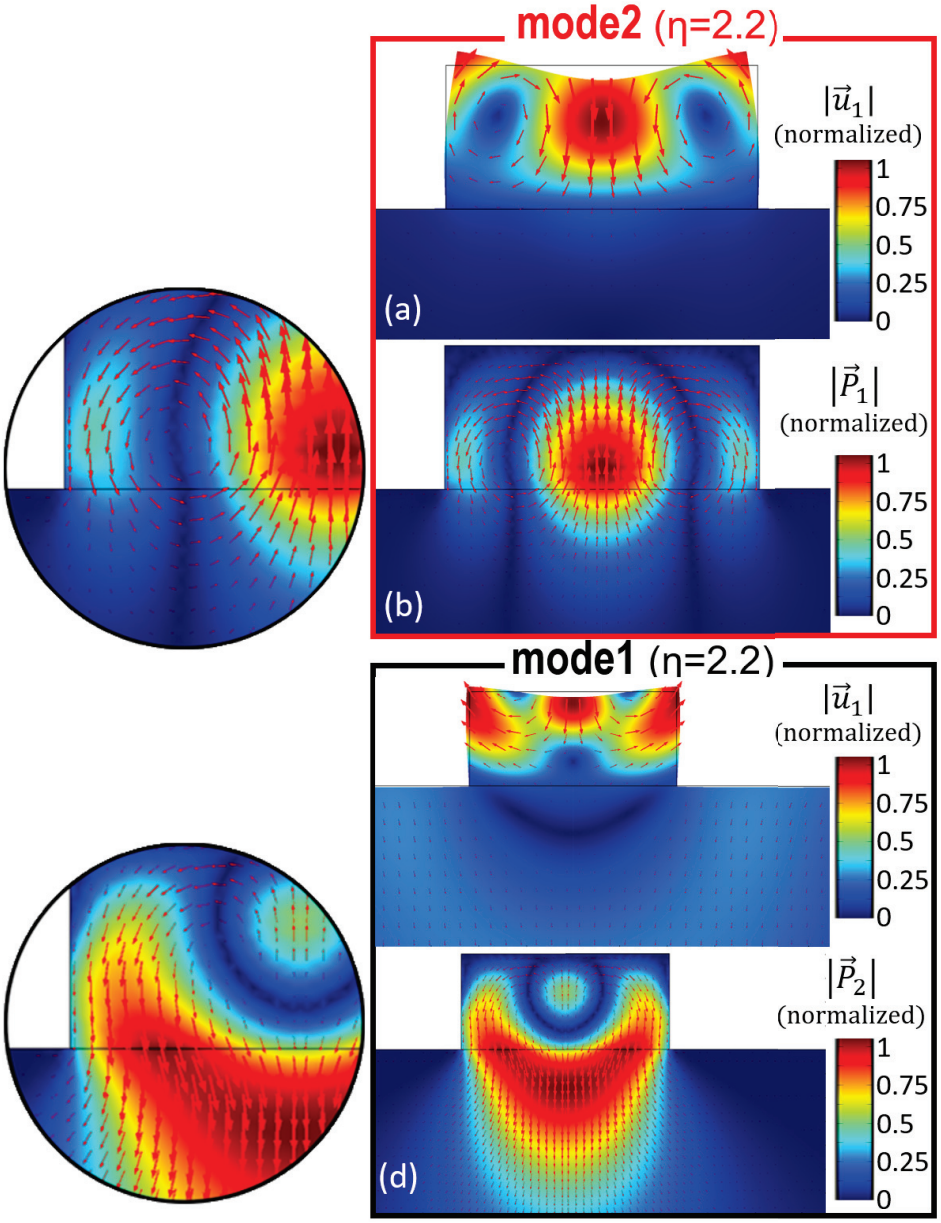

Figure 3.21: Normalized displacement field and energy flux computed for *mode1* and *mode2* at $\eta = 2.2$. The modes have difference appearance in respect to the ones illustrated in Fig. (3.20) at $\eta = 4$. The proximity to the mode frequencies intersection provokes an hybridization, which results in a reduction of energy loss throughout the interface in the case of *mode2*.

Q-factor peak of *mode1* is broader and weaker with respect to the one of *mode2*.

A direct comparison between the experimental and numerical results is proposed in Fig. (3.22). The modes frequencies are plotted using different symbols to distin-

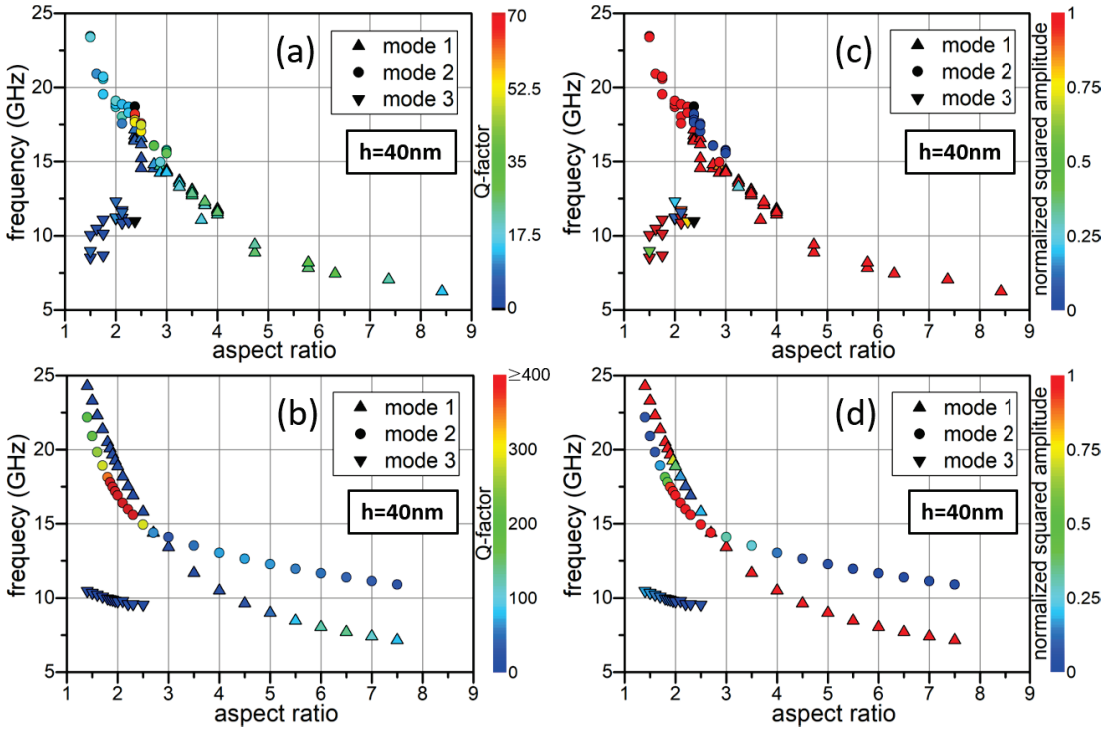

Figure 3.22: The mode frequencies are plotted using different symbols to distinguish between *mode1*, *mode2* and *mode3* and colors to indicate the experimental (a) and the numerical Q-factor (b), or the experimental (c) and numerical (d) normalized squared amplitude. Black points correspond to measured frequencies where the uncertainties are too big to establish a Q-factor (or an amplitude). These graphs allow to compare measured and modeled frequencies, Q-factors and amplitudes.

guish between *mode1*, *mode2* and *mode3* and colors to indicate the local Q-factor in panels (a) and (b), or the normalized squared amplitude in panels (c) and (d). The comparison between the measured (a) and computed (b) Q-factors, shows a general agreement, although in the experimental case the Q-factors enhancement are lower, and the peak of $\eta = 2.2$ is shifted towards $\eta = 2.5$ (which could be ascribed to a slight deviation in the effective aspect ratios). The frequencies have similar arrangements, despite the intersection is not clearly visible experimentally. Another difference is that when the experimental Q amplification occurs at $\eta = 2.5$, *mode2* has higher frequency than *mode1*, while in the simulations the opposite is expected.

The comparison between the measured (c) and computed (d) normalized squared amplitudes cannot be performed quantitatively, since experimentally the amplitudes depends on the detection configuration. However, observing numerical amplitudes and Q-factors allows to understand that at certain η some modes are not detectable, since both their Q-factor and amplitude are negligible (dark blue). This is the case for *mode1* at $\eta < 2.3$ and *mode2* at $\eta > 3$, as experimentally absent.

In Fig. (3.23) the computed Q-factors are plotted for the three modes as a function of the aspect ratio. FEM simulation takes into account only the acoustic damping coming from the propagation of acoustic waves throughout the interface, yielding extrinsic Q with important enhancement at $\eta = 2.2$ ($Q_2 \geq 2250$, where the "$\geq$" is due to discreteness of computed points) and $\eta = 6$ ($Q_1 \approx 120$). On the other hand, P&P measurements gives the total acoustic damping of the detected mode, meaning intrinsic damping and/or morphology imperfections also play a role. For this reason the experimental Q exhibits much weaker enhancements (with maximal values of $Q_2 = 66$ and $Q_1 = 31$) seen in Fig. (3.18) and Fig. (3.22).

Acoustic energy is efficiently conserved within the ND at $\eta = 2.5$ and $\eta = 6$, where

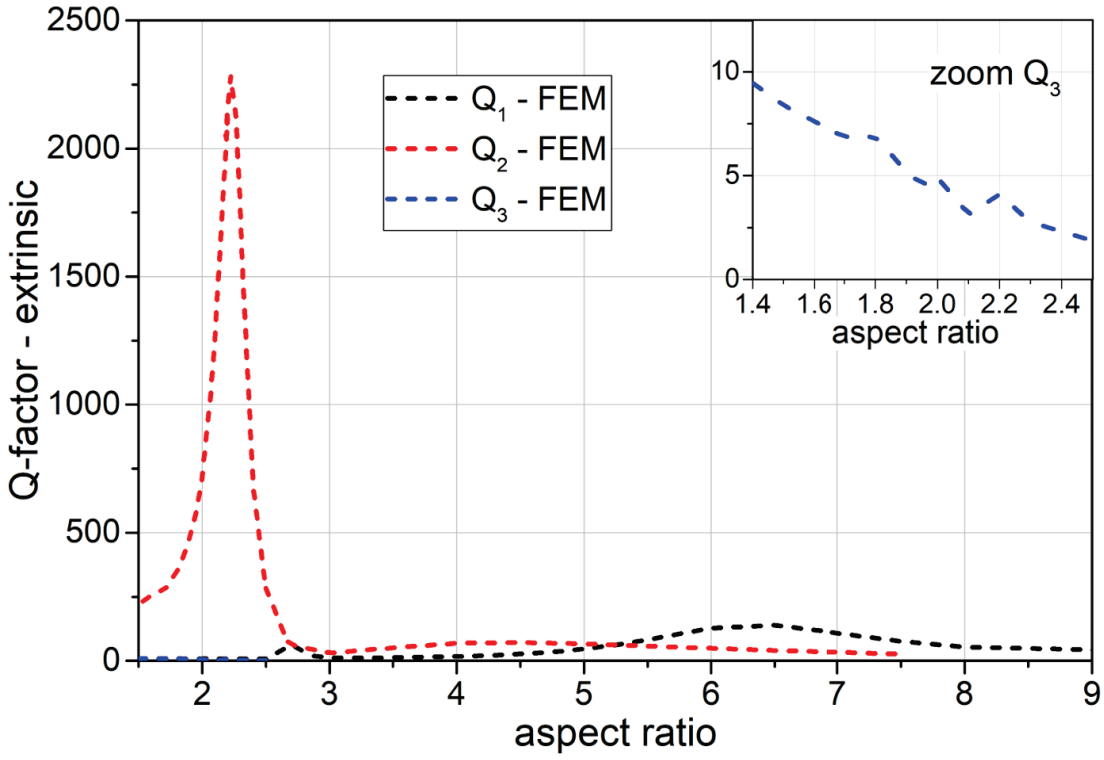

Figure 3.23: Numerically computed Q-factors. Inset: zoom of the region with Q_3.

Q-factor enhancements takes place. This raises the question of whether even the heat transfer towards the environment is slowed down. The nanoparticle cooling has been investigated in the NDs of S1, where the P&P delay time was extended to 3 ns. Using Eq. (3.34) to fit the NDs ultrafast responses, two exponential decays were usually required to follow the cooling process, and thus, two time constants τ_C and τ_D were extracted. Typically, τ_D results of the order of 200 ps, while τ_C is higher, being around 2 ns (therefore always well distinguishable from τ_D and being the limiting slower process due to heat transfer at interface). Its value has been extracted for different aspect ratio η, as illustrated in the graph of Fig. (3.24). Conversely to acoustic damping of one specific mode, the value of τ_C, associated to incoherent heat transfer, seems to be independent on η and centered around the average value of ≈ 1.8 ns. The variations present in Fig. (3.24) are mainly associated to the relatively high incertitudes. Furthermore, the use of different

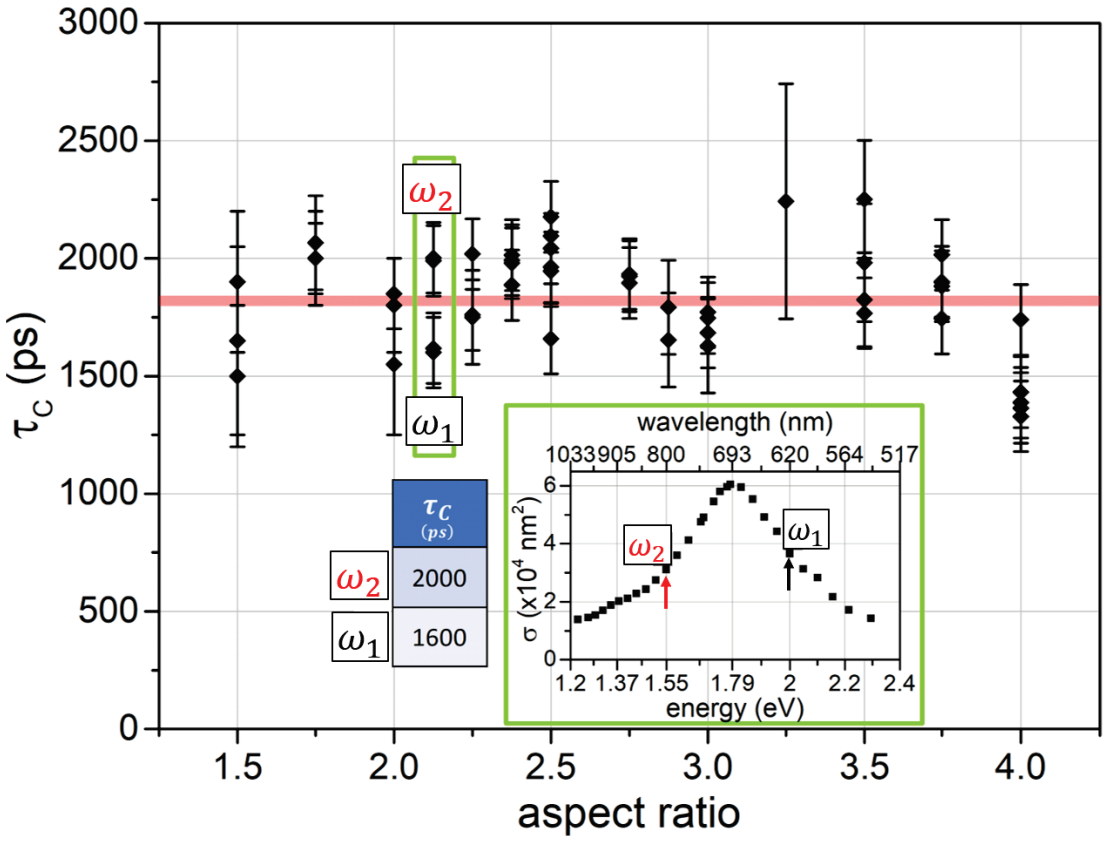

Figure 3.24: The value of τ_C (black diamonds) does not shows any dependence on η and its average value is $\approx$1.8 ns (red line). The fluctuations are mainly attributed to the important experimental incertitudes. In the green box: τ_C obtained on the same ND ($D = 85$ nm) from S1 repeating the experiment at a different ω_{pr}.

probe frequencies ω_{pr} could introduce additional fluctuations (the time constant τ_C may be influenced by the detection frequency, because, depending on ω_{pr}, the sensibility to the variations of the ND and environment dielectric functions changes [122]).

3.3 Conclusions and perspectives

By combining the spatial modulation microscopy with the *pump&probe* utrafast spectroscopy technique, the linear and ultrafast properties of single gold NDs deposited on a sapphire substrate have been investigated, with a focus on their acoustic properties. A campaign of time-resolved measurements on Au-ND of various aspect ratio η has been accomplished. Three different acoustic modes have been detected and called *mode1*, *mode2* and *mode3*. The former two exhibit a Q-factor enhancement, reaching $Q_1 = 66$ at $\eta = 2.5$ and $Q_2 = 31$ at $\eta = 6$ respectively. Conversely, the analysis of the slow relaxation of the signal shows that the thermal energy transfer at the interface (involving all vibrational modes of the ND) is not influenced by the phenomenon, being independent from η.
In order to understand the physical origin of the Q-factors enhancements, numerical simulation based on FEM computations has been achieved. In this way the NDs modes activated from a uniform and periodic stress has been traced and characterized in terms of Q-factor, amplitude, relative displacement field and energy flux.
The numerical simulations confirm en enhancement of Q-factor at similar η, but with higher intensity, strongly resulting in maximal values of $Q_1 \geq 2250$ and $Q_2 \approx 120$. This difference probably originates from the lack of intrinsic damping in the FEM computation and/or from the presence of geometrical imperfections and uneven contacts in the lithographed NDs.
The relative displacement field shows that the *mode1* is radial-like, *mode2* has some torsional components and *mode3* has a thickness nature. Typically, their energy flux are maximal at the ND/sapphire interface.
When approaching the Q_2 resonance, i.e. $\eta = 2.5$, the relative displacement shows an hybridization between *mode1* and *mode2*, reducing the energy losses of *mode2* throughout the interface. Therefore, Q-factor enhancements can be obtained by exploiting such mode hybridization that reduces the energy loss towards the substrate. This mode hybridization occur when two modes intersect in frequency. In practice, one can make two modes cross each other by tuning the morphology of the nano-object, as the aspect ratio of the ND. This phenomenon takes place for complex geometries, which involves at least two dimensional parameters, and could be exploited to optimize the geometry for high quality resonator or nanobalances. [123]

Extension of these studies to similar samples with different interfaces, including adhesion layers between NDs and substrate, could allow to improve the ND/substrate contact and investigate configurations with different interface properties. An attempt with chrome adhesion layer NDs was unsuccessful, because its presence broadens the NDs SPRs [124], reducing the P&P signal amplitude of one order of magnitude (compensating with higher pump powers caused NDs irreversible damage) and because at optical frequencies the chrome light absorption is one order of magnitude higher than the gold one, meaning the excitation mechanism is radically different and difficult to compare with the former samples results. In this contest, polymeric adhesion layers should be considered, having the advantage of avoiding SPR broadening [125].

In order to be quantitative, a study on the differences observed between measured and simulated Q-factors is necessary. A possible model system to study $Q_{intrinsic}$ would be a free-standing nano-object, as long nanowires (high aspect ratio) deposed on large holes, where the contact with the substrate occurs only in two remote regions. This kind of configuration has already been experimentally studied via P&P spectroscopy [126, 127] and a Q-factor of the order of 100 was observed. However, in such measurements the pump beam was focused on relatively little fractions of the suspended nanowire, exciting acoustic propagating longitudinal waves that contributed to the acoustic damping. In order to reduce this contribution, the system will be further investigated exciting the entire nanowire, providing values for $Q_{intrinsic}$ and a more complete insight of the damping processes at the nanoscale.

Conclusions and perspectives

In this thesis, the optical and acoustic properties of a single metal nanoparticle have been tuned by altering its environment and morphology.

In a first part, the impact of a pressurized environment on the linear optical response of individual gold bipyramids has been quantitatively studied. In order to follow the evolution of the single-particle extinction spectrum under high pressure, a challenging combination of a spatial modulation spectroscopy (SMS) microscope with a diamond anvil cell has been achieved. The characteristic longitudinal surface plasmon resonance (SPR), dominating the optical response of single gold bipyramids, has been experimentally monitored by measuring its energy position, spectral linewidth and area.
Rising the pressure results in nonlinear red-shift, broadening and area increases. The SPR red-shift has been successfully modeled numerically, using the finite-element method (FEM), and then analytically, showing that this behavior is essentially the result of two phenomena: the change in environment refractive index, which causes a strong nonlinear red-shift, and the metal compression, which translates in a weaker linear blue-shift.
The spectral area dependence on pressure has also been explained through a simple model for elongated morphologies and, again, the observed increases are mainly attributed to the environment refractive index changes.
The spectral linewidth rise with pressure contains multiple contributions, including modifications of the electronic scattering processes. An important term affected by pressure is the electron-surface scattering contribution which, according to merely theoretical quantum models, is sensitive to the environment refractive index. In that respect, pressure measurements on single nanoparticles can be considered as a first experimental evidence supporting these theories. Precise interpretation of the physical mechanisms at the origin of this phenomenon requires further investigations at different sizes and environments, that will be performed in the future.
The high-pressure SMS microscope also opens many perspectives for investigating other nanomaterials at single particle level under extreme conditions (e.g. nanotubes).

In the second part of this thesis, the morphology of a single nanoparticle on a substrate has been correlated to its acoustic properties. Specifically, two lithographed samples composed of gold nanodisks of various aspect ratios on a sapphire substrate were produced and characterized. SMS has been consistently exploited to select the most circular nanodisks. The combination of the SMS microscope with an ultrafast *pump&probe* (P&P) setup allowed to realize time-resolved measurements on single nanodisks.
Considering the acoustic components of the ultrafast responses, a few dominant vibrational modes could be optically excited and detected for each single nanodisk, and experimentally characterized providing access to their frequency, damping rate and quality factor (Q-factor). A particular attention was devoted to the dependence of these parameters on the aspect ratio. In the investigated region, three different modes were detected in total, two of them exhibiting a Q-factor enhancement at specific aspect ratios. Acoustic FEM simulations has allowed to precisely identify the three modes, confirming the presence of these Q-factor enhancements. The origin of the phenomenon has been clarified by looking at the displacement and energy flux fields computed in the nanodisk-substrate system.
Q-factor enhancements are induced by a mode hybridization that results in a reduction of the energy loss to the environment (through the interface with the substrate). Such hybridization can be achieved by tuning the nanodisk aspect ratio until two acoustic modes cross each other, and can be exploited for applications requiring high Q-factor acoustic resonators. This is not possible in monodimensional systems, such as films or spheres, where all the mode periods identically rescale with the object dimension.
Q-factor enhancements expected from FEM simulations occur for similar nanodisks aspect ratios, however they are much larger than the experimental ones. This difference is attributed to intrinsic vibrational damping and possibly to defects in the nanodisk morphology, not considered in computations. For a quantitative comparison with theory and a complete understanding of the physical phenomena at the origin of the acoustic damping, further investigations focused on the characterization of the intrinsic damping are required, and will be developed in the future (e.g. ideally studying quasi-free standing nano-objects).
Conversely to acoustic damping rates, the long time thermal components of the ultrafast relaxation were found to be independent from the aspect ratio of this specific system. A complete thermo-optical modeling is currently under development in the group, and more detailed investigations will be performed on the thermal relaxation of nano-objects, including morphological and environment-dependent effects and any possible connection with acoustic relaxation.

Appendices

Appendix A

Gaussian beam diffraction limit

When a lens is illuminated by a Gaussian beam, the diffraction-limited diameter of the image spot has the form [128]

$$\oslash_{spot} = \frac{K\lambda}{N.A.}\,, \tag{A.1}$$

where K is a constant dependent on the pupil illumination and on the definition of diameter, λ is the wavelength and $N.A.$ the numerical aperture. The intensity profile of the spot is strongly dependent on the radiation profile at the entrance pupil of the lens. If the pupil illumination has a Gaussian profile, the image spot has a Gaussian profile:

$$I_G = \frac{4\ln(2)W_0}{\pi FWHM^2}\exp\left[-\frac{4\ln(2)(r-r_0)^2}{FWHM^2}\right], \tag{A.2}$$

where W_0 is the total beam spot power that coincides with the incident one ($W_0 = W_i$), $FWHM$ is the full width at half maximum, and (r–r_0) the radial distance from the optical axis. On the other hand, if the pupil is brightened with a plane wave top uniform illumination, obtained for example by a strongly truncated Gaussian profile, the spot results in an Airy disc:

$$I_A = \frac{AW_0}{FWHM^2}\left\{\frac{2\,\mathrm{bessel}_{j1}\left[\frac{B(r-r_0)}{FWHM}\right]}{\left[\frac{B(r-r_0)}{FWHM}\right]}\right\}^2, \tag{A.3}$$

where W_0 is a fraction of the incident power ($W_0 = W_i(1-w_L)$, with w_L being the entrance pupil power loss ratio of Eq. (A.7) below ($w_L = 0$ when no truncation occurs), $\mathrm{bessel}_{j1}[...]$ stands for the Bessel function of first kind and first order, A and B are numerical constant ($A = 0.83159179$; $B = 3.23266$). When the pupil illumination is between these two extremes, a hybrid intensity profile occurs.

In the case of the Airy disc, the diameter of the spot can be defined considering the first dark ring:

$$\oslash_A = 2.44\lambda N \approx \frac{1.22\lambda}{N.A.}\,. \tag{A.4}$$

However, when the pupil illumination is not uniform, the image spot intensity never falls to zero making it necessary to define the spot size differently. Commonly it is considered as the diameter at the half intensity point, the so called full width at half maximum ($FWHM$), or the radius at the $1/e^2$ intensity point, the beam waist w. When the image spot has an ideal Airy disc intensity profile, the diffraction limit of Eq. (A.4) can be rewritten as

$$\text{Airy disc:}\quad \begin{cases} FWHM = \frac{0.515\lambda}{N.A.} \\ w = \frac{0.411\lambda}{N.A.} \end{cases}\,. \tag{A.5}$$

An alternative characterization of the Airy disc intensity profile is made approximating the central lobe with a Gaussian profile with same central amplitude or with free amplitude. The fitting width results

$$\text{Gaussian (max-fixed)}\quad \begin{cases} FWHM = \frac{0.501\lambda}{N.A.} \\ w = \frac{0.426\lambda}{N.A.} \end{cases}\,,\quad \text{(max-free)}\quad \begin{cases} FWHM = \frac{0.496\lambda}{N.A.} \\ w = \frac{0.421\lambda}{N.A.} \end{cases}\,. \tag{A.6}$$

In the second case, where the amplitude is treated as a free parameter, the width is smaller because the maximum amplitude is overestimated. This introduces a systematic error if one tries to fit an experimental Airy profile with a Gaussian function.
The constant K of Eq. (A.1) is a function of the truncation ratio

$$T = \frac{2w_G}{D}\,,$$

where w_G is the waist of the incident Gaussian beam and D the limiting aperture diameter of the lens. If $T \geq 2$ (high truncation) the image spot intensity profile approaches the Airy pattern, whilst when $T \leq 0.5$ (low truncation) it is closer to a Gaussian function. The $FWHM$ of the spot can be expressed as a function of K

$$FWHM = \frac{K\lambda}{N.A.}\,,$$

with

$$K = 0.515 + \frac{0.35625}{(T-0.2161)^{2.179}} - \frac{0.32225}{(T-0.2161)^{2.221}}\,,$$

plotted in the graph of Fig. (A.1)).

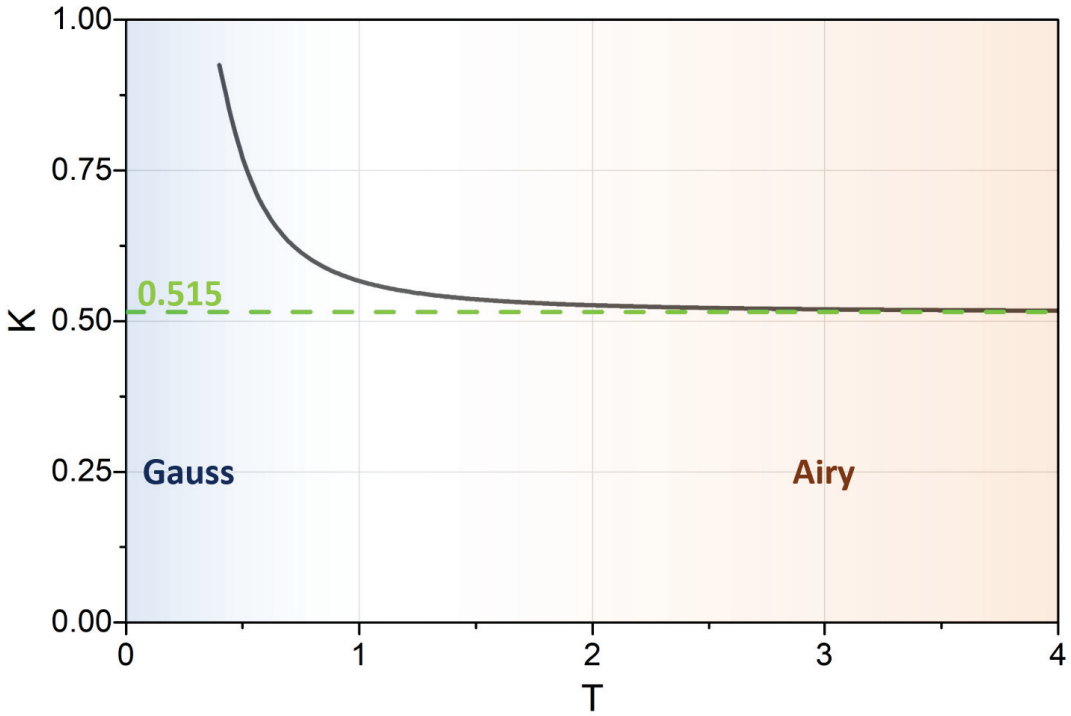

Figure A.1: Constant K as a function of the truncation ratio T.

The optimal choice for truncation ratio depends on the relative importance of spot size, shape and power loss ratio that, for a truncated Gaussian beam, decreases exponentially with T:

$$w_L = e^{-2/T^2} . \tag{A.7}$$

Typically, in SMS experiments the required powers are very modest and it is therefore possible to work in the $T \geq 2$ regime, where the incoming laser Gaussian beam is strongly truncated, the pupil is uniformly illuminated and the image spot approaches the ultimate focusing limit due to Airy pattern. In reverse, during *pump&probe* measurements on single nanoparticles the required pump power can be higher and, for certain wavelengths, w_L must be kept small (low truncation). However, in these kinds of experiments, reducing the size of the pump beam spot close to the diffraction limit is less critical, allowing a choice of smaller T.

Appendix B

Diamond properties under high pressure

The refractive index of the diamond n_d is a function of the wavelength λ as well as the pressure P.
In standard condition, the dependence of n_d on λ was studied by Edwards et al. [129]. Previous data from the UV to the near IR region were reviewed and collected, and a phenomenological formula to estimate n_d in the far IR region was obtained

$$n_d(\lambda, P=0) = n_d(\lambda=\infty, P=0) + A_1 L + A_2 L^2 + A_3 L^3 + A_4 L^4 \qquad \text{(B.1)}$$

with $L=(\lambda^2 - 0.028\,\mu\text{m}^2)^{-1}$, $n_d(\lambda=\infty, P=0)=2.37553$, $A_1=3.36440\times10^{-2}\,\mu\text{m}^2$, $A_2=-8.87524\times10^{-2}\,\mu\text{m}^4$, $A_3=-2.40455\times10^{-6}\,\mu\text{m}^6$, $A_4=2.21390\times10^{-9}\,\mu\text{m}^8$. The resulting graph of n_d as a function of λ is displayed in Fig. (B.1). These data are well fitted by a decreasing three-exponential function with offset equal to the asymptotic limit of Eq. (B.1)

$$n_d(\lambda, P=0) = n_d(\lambda=\infty, P=0) + \Lambda_1 e^{-\lambda/\lambda_1} + \Lambda_2 e^{-\lambda/\lambda_2} + \Lambda_3 e^{-\lambda/\lambda_3}\,, \qquad \text{(B.2)}$$

where $\Lambda_1 = 5.2$, $\lambda_1 = 72\,\text{nm}$, $\Lambda_2 = 0.226$, $\lambda_2 = 312\,\text{nm}$, $\Lambda_3 = 0.0076$, $\lambda_3 = 2785\,\text{nm}$. This expression is valid in the whole range $400 - 4000\,\text{nm}$.
The diamond refractive index is also pressure dependent. This aspect was studied in the range $0-40\,\text{GPa}$ for several wavelength ($400-900\,\text{nm}$) by Eremets et al., [74] resulting to be a quasi-linear function of the pressure. Realizing a linear approximation of these data in the range 0–20 GPa allows to estimate the pressure dependence

$$dn_d(\lambda, P) = p(\lambda)\, dP\,. \qquad \text{(B.3)}$$

The slope coefficient $p(\lambda)$ is always negative and is reported in Fig. (B.2) as a function of the wavelength. Linear fits were performed on these data obtaining

$$n_d(\lambda, P) = n_d(\lambda, P=0) + p(\lambda) P\,, \qquad \text{(B.4)}$$

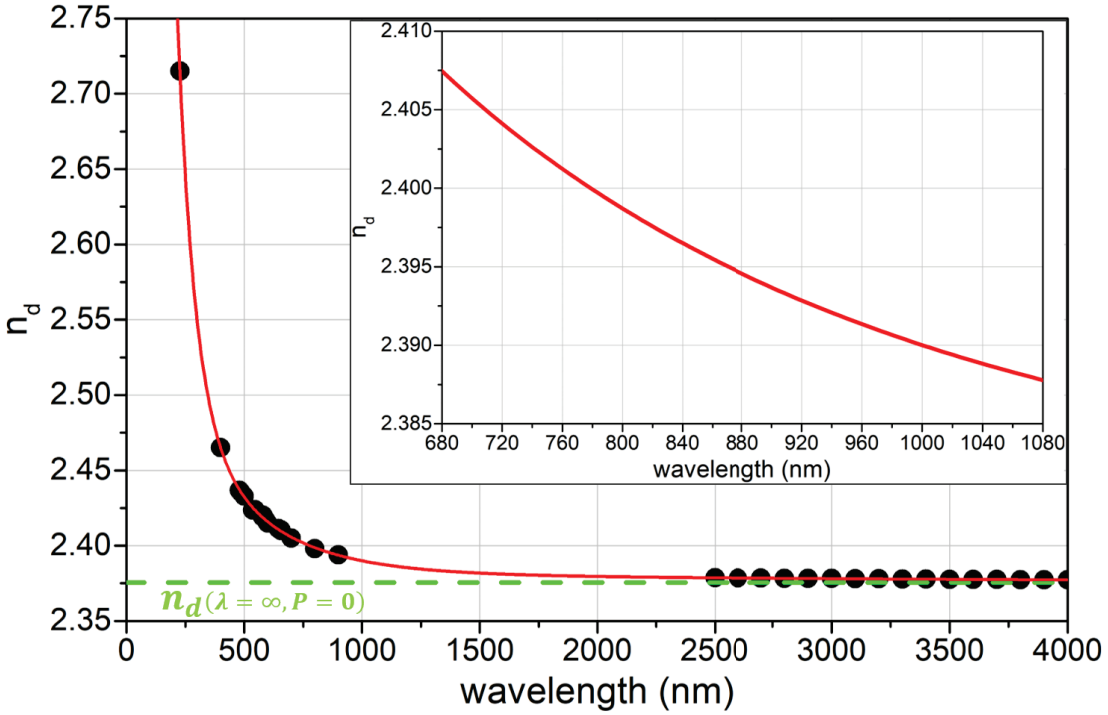

Figure B.1: Refractive index of the diamond at standard pressure as a function of the wavelength. The data in the far-IR region are calculated using Eq. (B.1), while the others come from the literature. The red solid curve is the decreasing three-exponential fit of Eq. (B.2) and the inset drawn the attention to the wavelengths available in the "Transmission SMS setup" of Fig. (2.14).

with

$$p(\lambda) = \begin{cases} p_0 + p_1 P & \text{if } x \leq 703\,\text{nm} \\ p(\lambda=\infty) & \text{if } x > 703\,\text{nm} \end{cases} \tag{B.5}$$

$p(\lambda=\infty) = -5\times10^{-4}\,\text{GPa}^{-1}$, $p_0 = -8.472\times10^{-4}\,\text{GPa}^{-1}$, and $p_1 = 4.94\times10^{-7}\,\text{GPa}^{-2}$. Considering the "Transmission SMS setup" of Fig. (2.14), where the available wavelength range is $680-1080\,\text{nm}$, Eq. (B.5) can be simplified

$$n_d(\lambda, P) = n_d(\lambda, P=0) + p(\lambda=\infty)P\,. \tag{B.6}$$

The thickness h of a diamond slab contained in a DAC pressure chamber can be studied using the experimental diamond equation of state [129]

$$h(P) = h_0 \left[1 + 4.28\left(\frac{\lambda(P)}{\lambda_0} - 1\right)\right]^{-\frac{1}{3}}, \tag{B.7}$$

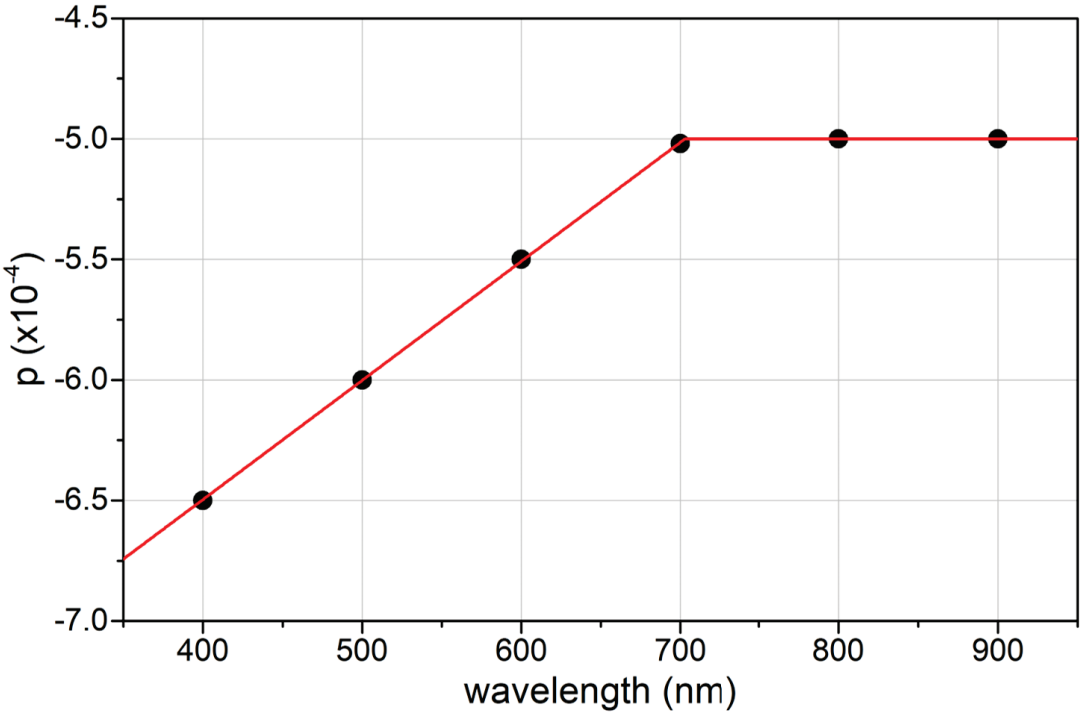

Figure B.2: The refractive index of the diamond decreases linearly with the pressure through the coefficient $p(\lambda)$, which is wavelength dependent. A linear fit was realized using the formula Eq. (B.5) to estimate the coefficients $p(\lambda=\infty)$, p_0 and p_1. For the wavelengths available in the "Transmission SMS setup" of Fig. (2.14) $p=p(\lambda=\infty)=-5\times10^{-4}$ can be used.

where h_0 is the thickness at 0 GPa, $\lambda(P)$ is the R1 ruby line position at the pressure P and $\lambda_0=\lambda(P=0)$. Injecting the ruby pressure dependence of Eq (2.2) of Chapter 2, Eq. (B.7) becomes

$$h(P) = h_0 \left[1 + 4.28 \left[\left[1 + \frac{B}{A}P\right]^{\frac{1}{B}} - 1\right]\right]^{-\frac{1}{3}}, \tag{B.8}$$

where $A = 1904$ and $B = 7.665$. The pressure dependence of the ratio h/h_0 is reported in Fig. (B.3). Eq. (B.8) is a quasi-linear function in the regime 0–10 GPa and can be approximated to

$$h(P)/h_0 = 1 - 7.315\times10^{-4}P\,. \tag{B.9}$$

Alternatively, the thickness h can be calculated directly from the diamond elastic moduli (experimentally determined using ultrasonics, X-rays and Brillouin scattering). Considering one of the most reliable value, $c_{11} = 1080.4 \pm 0.5$ GPa, [130]

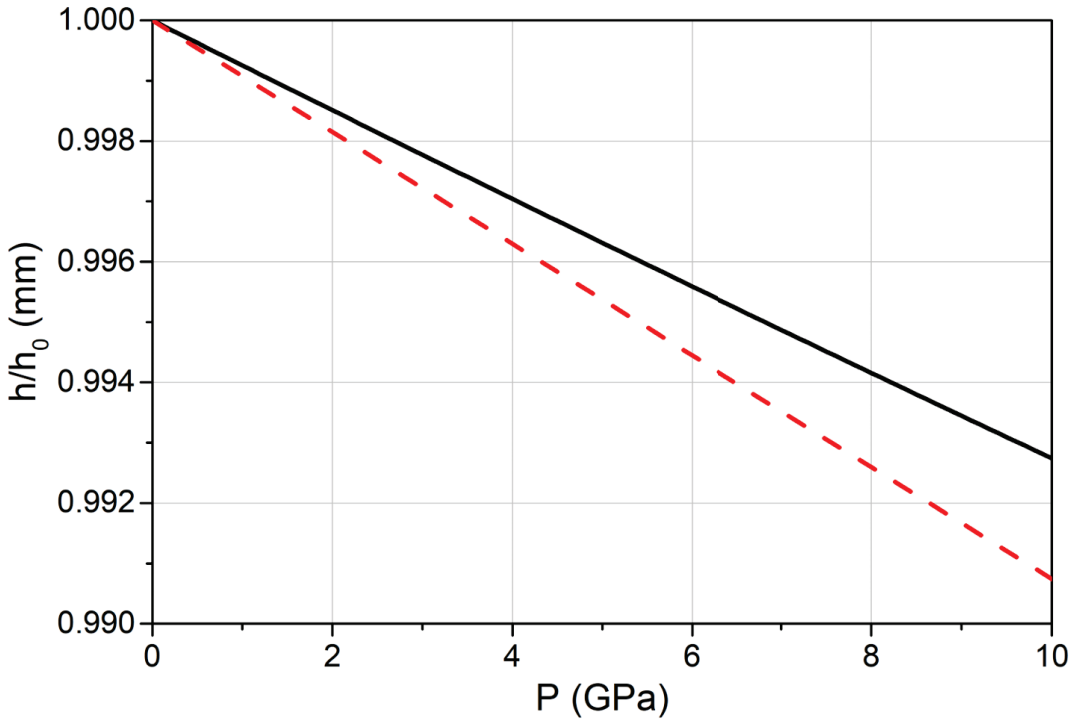

Figure B.3: Relative thickness of bulk diamond as a function of the pressure. The solid black line results from the DAC approach of Eq. (B.8); the dash red line correspond to the Young modulus calculation from Eq. (B.11).

one obtains

$$h(P) - h_0 = \frac{T}{c_{11}} h_0 \,, \tag{B.10}$$

where T, the stress component normal to the diamond surface [100], matches $-P$. Eq. (B.10) can be reformulated as

$$h(P)/h_0 = 1 - 9.256 \times 10^{-4} P \,, \tag{B.11}$$

and is shown in Fig. (B.3) as well.

Appendix C

4Me:1Et properties under high pressure

4Me:1Eth is a common pressure transmitting medium, composed in four parts of methanol (CH_3OH) and one part of ethanol (C_2H_5OH), which remains liquid and hydrostatic until 10.4 GPa. [64] [65] Concerning the methanol, the refractive index dispersion in the range 450−1550 nm, at standard pressure and 27°C can be approximated as [131]

$$n_{Me}^2 = 1.745946239 - 0.005362181\lambda^2 + \\ + 0.004656355\lambda^{-2} + 0.00044714\lambda^{-4} - 0.000015087\lambda^{-6}\,, \tag{C.1}$$

where λ is the light wavelength expressed in µm. For the the ethanol, in the range 500−1600 nm and at 20°C, the dispersion takes the form [132]

$$n_{Et}^2 = 1 + \frac{0.83189\lambda^2}{\lambda^2 - 0.00930} - \frac{0.15582\lambda^2}{\lambda^2 + 49.45200}\,. \tag{C.2}$$

The imaginary part κ_{Et} remains always within the range 10^{-6}−10^{-8} in the region 600−1100 nm, and hence the absorption is negligible. The refractive index of the PTM mixture 4Me:1Et can be estimated combining Eq. (C.1) and (C.2)

$$n_{PTM}(\lambda, P{=}0) = (4n_{Me} + n_{Et})/5 \tag{C.3}$$

whose dispersion in the range 680−1080 nm is plotted in Fig. (C.1).
The refractive index of the hydrostatic PTM 4Me:1Et has been measured by Eggert et al. [68] in the region of low viscosity 0.5−11.5 GPa in the wavelength range 415–830 nm. The data are fitted by a simple formula that depends on the pressure P and light wavelength λ

$$n_{PTM}(\lambda, P) = \sqrt{1 + \frac{E_d\, E_0}{E_0^2 - \epsilon^2}}\,, \tag{C.4}$$

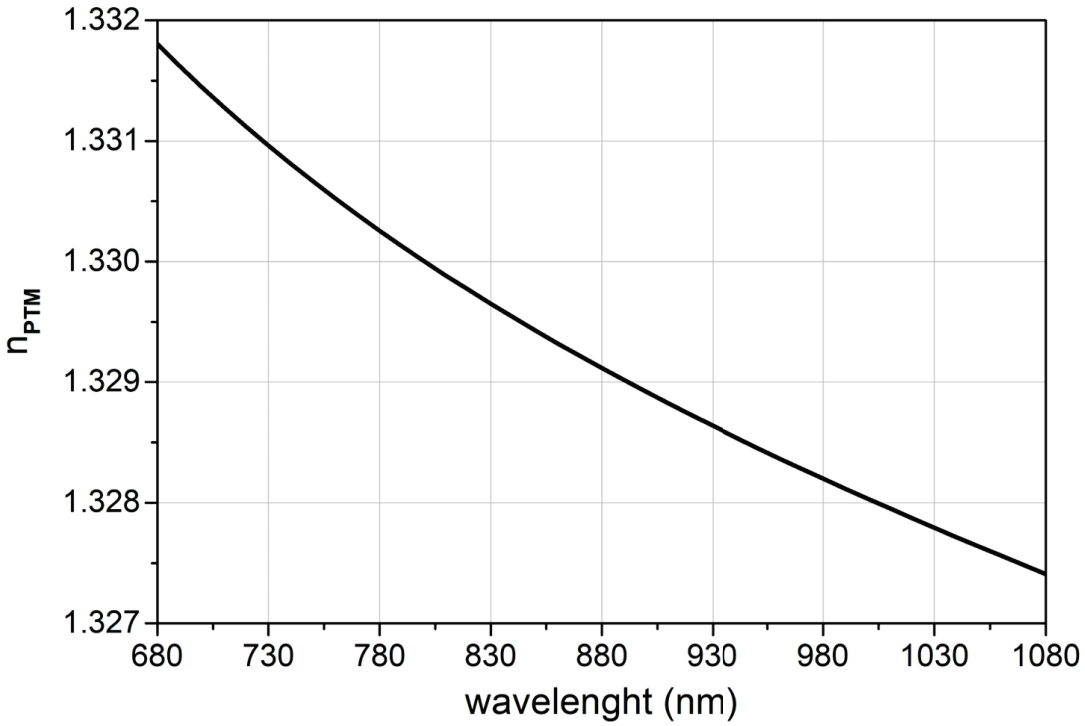

Figure C.1: Modest dispersion of the 4Me:1Et refractive index in standard condition.

where

$$E_d = 10.58\,(\rho/\rho_0)^{1.31}\,, \quad E_0 = 13.38\,(\rho/\rho_0)^{0.07}\,, \quad \epsilon = hc/\lambda \qquad \text{are in eV}$$

and

$$\rho/\rho_0 = [1 - 0.0894\ln(1 + 14.37\,P)]^{-1}\ .$$

The evolution of the refractive index as a function of the pressure is illustrated in Fig. (C.2). Despite Eq. (C.4) has been developed in the range $415-830\,\text{nm}$, it is reasonable to make an extension until 1080 nm, as the chromatic dispersion is small. Moreover, the imaginary part of the PTM refractive index k_{PTM} is negligible in the interval $680-1080\,\text{nm}$, hence the PTM permittivity is simply $\epsilon_1 = n^2_{PTM}(\lambda, P)$.

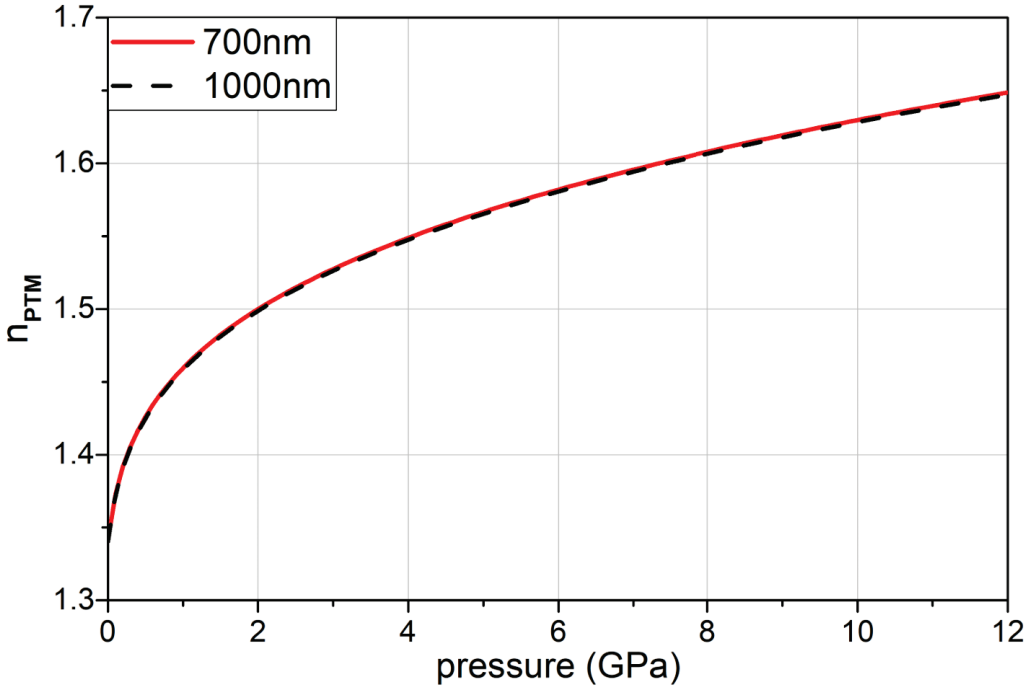

Figure C.2: Pressure dependence of the 4Me:1Et refractive index. The difference between 700 and 1000 nm is negligible.

Appendix D

SPR optical modifications under high pressure: from numerical to semi-analytical model

Each small isotropic change in pressure dP modifies the dielectric functions of the metal and the environment, as well as the volume of the object. This yields a variation in the BP cross-section $\sigma(\omega)$, where $\omega = \frac{2\pi c}{\lambda}$ is the photon frequency. Therefore, its peak position, which occurs at the resonant frequency ω_R, will undergo a shift induced by these variations

$$d\omega_R = \frac{\partial \omega_R}{\partial \epsilon_m}\frac{\partial \epsilon_m}{\partial P}dP + \frac{\partial \omega_R}{\partial \epsilon_1}\left(\frac{\partial \epsilon_1^D}{\partial P} + \frac{\partial \epsilon_1^{ib}}{\partial P}\right)dP + \frac{\partial \omega_R}{\partial \epsilon_2}\left(\frac{\partial \epsilon_2^D}{\partial P} + \frac{\partial \epsilon_2^{ib}}{\partial P}\right)dP\,, \qquad \text{(D.1)}$$

where $\epsilon_{1,2}(\omega) = \epsilon_{1,2}^D + \epsilon_{1,2}^{ib}$ are respectively the real and imaginary parts of the gold dielectric function which must be evaluated at ω_R, $\epsilon_{1,2}^D$ indicates the Drude components and $\epsilon_{1,2}^{ib}$ the interband contributions. $\epsilon_m(\omega)$ is the environment dielectric function (including both the PTM and the diamond substrate), which is a real number and weakly dispersed in the SPR region (see Appendix (B) and (C)). In order to evaluate the peak position change $d\omega_R$ induced by a pressure variation dP, all the partial derivatives in Eq. (D.1) shall be determined. The term $\partial\epsilon_m/\partial P$ can be calculated using Eq. (C.4) of Appendix (C), which defines the pressure and frequency dependence of the PTM refractive index. The diamond contribution, determined by Eq. (B.6), can be neglected as in the $0-10$ GPa range the variation of its refractive index is 60 times smaller. Moreover, the frequency dependence of ϵ_{PTM} can be neglected, as shown Fig. (C.2) of Appendix (C). The derivatives of the Drude terms $\epsilon_{1,2}^D$ with respect to the pressure are analytically determined from

the Eq. (1.13) of Chapter 1

$$\begin{cases} \epsilon_1^D(\omega, V) \approx -\frac{\omega_p^2}{\omega^2} \\ \epsilon_2^D(\omega, V) \approx \frac{\omega_p^2 \gamma}{\omega^3} \end{cases} . \tag{D.2}$$

Pressure derivatives of $\epsilon_{1,2}^D$ can be expressed as

$$\frac{\partial \epsilon_{1,2}^D}{\partial P} = \frac{\partial \epsilon_{1,2}^D}{\partial V}\frac{\partial V}{\partial P} = -k_{Au} V \frac{\partial \epsilon_{1,2}^D}{\partial V} , \tag{D.3}$$

where $k_{Au} = 5.77 \times 10^{-3}\,\mathrm{GPa}^{-1}$ is the bulk gold isothermal compressibility at 300 K [80]. By taking into account the modifications of the plasma frequency ω_p, due to a change of the nano-object volume V ($\omega_p \sim V^{-0.5}$) and therefore of the conduction electron density. At 1.55 eV

$$\begin{cases} V\frac{\partial \epsilon_1^D}{\partial V} = \frac{\omega_p^2}{\omega^2} \\ V\frac{\partial \epsilon_2^D}{\partial V} = \frac{\gamma}{\omega} V \frac{\partial \epsilon_1^D}{\partial V} \approx \frac{1}{10} V \frac{\partial \epsilon_1^D}{\partial V} \end{cases} . \tag{D.4}$$

This correspond to

$$0.02\,\mathrm{GPa}^{-1} \sim \frac{\partial \epsilon_2^D}{\partial P} < \left|\frac{\partial \epsilon_1^D}{\partial P}\right| \sim |-0.2\,\mathrm{GPa}^{-1}| . \tag{D.5}$$

ϵ_2^D is also dependent on γ which increases with the pressure as seen in the experiments reported. Keeping the volume constant $V_0 = V(P = 0\,\mathrm{GPa})$, an increment of γ of 15% induces

$$\left.\frac{\partial \epsilon_2^D}{\partial P}\right|_{V_0} \sim 0.04\,\mathrm{GPa}^{-1} . \tag{D.6}$$

For elongated gold BPs the frequencies of resonance ($\omega_R < 1.5\,\mathrm{eV}$) are far from the gold interband transition region ($\omega_{ib} > 2.5\,\mathrm{eV}$): $\omega_R \ll \omega_{ib}$. As a consequence, $\epsilon_2^{ib}(\omega_R) = 0$ and $\epsilon_1^{ib}(\omega)$ is weakly dispersed, their derivatives with respect to P will be negligible. To be more quantitative and estimate the order of magnitude of these derivatives one can consider the measurements of Garfinkel et al. [133] on the bulk gold reflectivity subjected to biaxial pressure, or the temperature dependent ellipsometric measurements in bulk gold of Winsemius et al. [134], analyzed by Stoll et al. [122], using

$$\frac{\partial \epsilon_{1,2}^{ib}}{\partial P} = \frac{\partial \epsilon_{1,2}^{ib}}{\partial T}\frac{\partial T}{\partial V}\frac{\partial V}{\partial P} = -\frac{k_{Au}}{\alpha_{Au}}\frac{\partial \epsilon_{1,2}^{ib}}{\partial T} , \tag{D.7}$$

where $\alpha_{Au} = 4.3 \times 10^{-5}\,\mathrm{K}^{-1}$ is the bulk gold volumetric thermal expansion coefficient at 0 GPa [80]. The two approaches gives similar results and in the domain 1.2 − 1.8 eV one finds

$$0 \sim \frac{\partial \epsilon_2^{ib}}{\partial P} < \frac{\partial \epsilon_1^{ib}}{\partial P} < 0.04\,\mathrm{GPa}^{-1} . \tag{D.8}$$

As for a quasi-Lorentzian SPR in the dipolar regime

$$0 \sim \left|\frac{\partial \omega_R}{\partial \epsilon_2}\right| < \left|\frac{\partial \omega_R}{\partial \epsilon_1}\right|, \tag{D.9}$$

one may use Eq. (D.5), (D.8) and (D.9) to simplify Eq. (D.1) in the form

$$d\omega_R \approx \frac{\partial \omega_R}{\partial \epsilon_{PTM}} \frac{\partial \epsilon_{PTM}}{\partial P} dP + \frac{\partial \omega_R}{\partial \epsilon_1} \frac{\partial \epsilon_1^D}{\partial P} dP\,, \tag{D.10}$$

where the partial derivatives must be evaluated at $\omega = \omega_R$. Taking into account that at $\omega = \omega_R$

$$\begin{cases} \left.\frac{\partial \omega_R}{\partial \epsilon_1}\right|_{\omega_R} \approx -\frac{1}{2}\frac{\omega_R^3}{\omega_p^2} \\ \left.\frac{\partial \epsilon_1^D}{\partial V}\right|_{\omega_R} = \frac{\omega_p^2}{V\omega_R^2} \\ \frac{\partial V}{\partial P} = -k_{Au} V \end{cases}, \tag{D.11}$$

the simplified formula of the main text is recovered

$$\frac{d\omega_R}{dP} = \frac{1}{2} k_{Au}\, \omega_R + \frac{\partial\, \omega_R}{\partial \epsilon_{PTM}} \frac{d\, \epsilon_{PTM}}{d\, P}\,, \tag{D.12}$$

with its two main contributions due to the pressure-induced changes in the metal (Drude) and environment dielectric functions.

Bibliography

[1] R.W.G. Wyckoff, Crystal Structures, Volume 1, R.E. Krieger Pub. Co. (1982) 467.

[2] N.W. Ashcroft, N.D. Mermin, Solid State Physics, EDP Sciences (2002) 986.

[3] P.B. Johnson, R.W. Christy, Optical constants of the noble metals, Physical Review B 6 (1972) 4370–4379.

[4] P. Drude, Zur Elektronentheorie der Metalle, Annalen der Physik 306 (1900) 566–613.

[5] T. Rangel, D. Kecik, P.E. Trevisanutto, G.-M. Rignanese, H. Van Swygenhoven, and V. Olevano, Band structure of gold from many-body perturbation theory, Physical Review B 86 (2012) 125125.

[6] K.D. Sattler, Handbook of Nanophysics: Nanoelectronics and Nanophotonics, CRC Press (2011) 24-4.

[7] C.F. Bohren, D.P. Gilra, Extinction by a spherical particle in an absorbing medium, Journal of Colloid and Interface Science 72 (1979) 215-221.

[8] C.F. Bohren, D.R. Huffman, Absorption and Scattering of Light by Small Particles, Wiley-VCH Verlag GmbH (2008) 544.

[9] A. Lebedev, M. Gartz, U. Kreibig, O. Stenzel, Optical extinction by spherical particles in an absorbing medium: Application to composite absorbing films, The European Physical Journal D 6 (1999) 365–373.

[10] C.F. Bohren, D.R. Huffman, Absorption and scattering of light by small particles, John Wiley ed., 1998.

[11] K.D. Sattler, Handbook of Nanophysics: Nanoelectronics and Nanophotonics, CRC Press (2011) 24-6.

[12] G. Mie, Beiträge zur Optik trüber Medien, speziell kolloidaler Metallösungen, Annalen der Physik 330 (1908) 377–445.

[13] H. Horvath, Gustav Mie and the scattering and absorption of light by particles: Historic developments and basics, Journal of Quantitative Spectroscopy and Radiative Transfer 110 (2009) 787–799.

[14] P. Billaud, J.-R. Huntzinger, E. Cottancin, J. Lermé, M. Pellarin, L. Arnaud, M. Broyer, N. Del Fatti et F. Vallée, Optical extinction spectroscopy of single silver nanoparticles, The European Physical Journal D 43 (2007) 271–274.

[15] U. Kreibig, Anomalous frequency and temperature dependance of the optical absorption of small gold particles, Journal de Physique Colloques 38 (1977) C97–C103.

[16] V. Juvé, Spectroscopie linéaire et ultra-rapide de nanoparticules métalliques : de l'ensemble au nano-objet individuel, PhD thesis, Université Claude Bernard Lyon 1 (2011).

[17] P. Billaud, J.-R. Huntzinger, E. Cottancin, J. Lermé, M. Pellarin, L. Arnaud, M. Broyer, N. Del Fatti, and F. Vallée, Optical extinction spectroscopy of single silver nanoparticles, European Physical Journal D 43 (2007) 271–274.

[18] M. Grzelczak, L.M. Liz-Marzán, Colloidal nanoplasmonics: from building blocks to sensing devices, Langmuir 29 (2013) 4652–4663.

[19] R. Gans, Über die Form ultramikroskopischer Goldteilchen, Annalen der Physik 342 (1912) 881–900.

[20] R. Gans, Über die Form ultramikroskopischer Silberteilchen, Annalen der Physik 352 (1915) 270–284.

[21] O.L. Muskens, G. Bachelier, N. Del Fatti, F. Vallée, A. Brioude, X. Jiang, M.P. Pileni, Quantitative absorption spectroscopy of a single gold nanorod, Journal of Physical Chemistry C 112 (2008) 8917–8921.

[22] M. Kauranen, A.V. Zayats, Nonlinear plasmonics, Nature Photonics 6 (2012) 737–748.

[23] P. Zijlstra, J.W.M. Chon, M. Gu, Five-dimensional optical recording mediated by surface plasmons in gold nanorods, Nature 459 (2009) 410–413.

[24] H.A. Atwater, A. Polman, Plasmonics for improved photovoltaic devices, Nature Materials 9 (2010) 205–213.

[25] I.H. El-Sayed, X. Huang, M.A. El-Sayed, Surface Plasmon Resonance Scattering and Absorption of anti-EGFR Antibody Conjugated Gold Nanoparticles in Cancer Diagnostics: Applications in Oral Cancer, Nano Letters 5 (2005) 829–834.

[26] M. Dahan, S. Lévi, C. Luccardini, P. Rostaing, B. Riveau, A. Triller, Diffusion dynamics of glycine receptors revealed by single-quantum dot tracking, Science 302 (2003) 442–445.

[27] K.A. Willets, R.P. Van Duyne, Localized surface plasmon resonance spectroscopy and sensing, Annual Review of Physical Chemistry 58 (2007) 267–297.

[28] E. Ringe, B. Sharma, A.-I. Henry, L.D. Marks, R. P. Van Duyne, Single nanoparticle plasmonics, Physical Chemistry Chemical Physics 15 (2013) 4110–4129.

[29] A. Crut, P. Maioli, N. Del Fatti, F. Vallée., Optical absorption and scattering spectroscopies of single nano-objects, Chemical Society Reviews 43 (2014) 3921–3956.

[30] E.H. Synge, A suggested method for extending microscopic resolution into the ultra-microscopic region, Philosophical Magazine Series 6 (1928) 356–362.

[31] Y. Oshikane, T. Kataoka, M. Okuda, S. Hara, H. Inoue, M. Nakano, Observation of nanostructure by scanning near-field optical microscope with small sphere probe, Science and Technology of Advanced Materials 8 (2007) 181–185.

[32] A. Liu, A. Rahmani, G.W. Bryant, L.J. Richter, S.J. Stranick, Modeling illumination-mode near-field optical microscopy of Au nanoparticles, Journal of the Optical Society of America A 18 (2001) 704.

[33] M. Hu, C. Novo, A. Funston, H. Wang, H. Staleva, S. Zou, P. Mulvaney, Y. Xia, G.V. Hartland, Dark-field microscopy studies of single metal nanoparticles: understanding the factors that influence the linewidth of the localized surface plasmon resonance, Journal of Materials Chemistry 18 (2008) 1949–1960.

[34] C. Sönnichsen, T. Franzl, T. Wilk, G. von Plessen, J. Feldmann, O. Wilson, P. Mulvaney, Drastic reduction of plasmon damping in gold nanorods, Physical Review Letters 88 (2002) 077402.

[35] C. Sönnichsen, S. Geier, N.E. Hecker, G. von Plessen, J. Feldmann, H. Ditlbacher, B. Lamprecht, J.R. Krenn, F.R. Aussenegg, Z.-H. Chan, J.P. Spatz, M. Möller, Spectroscopy of single metallic nanoparticles using total internal reflection microscopy, Applied Physics Letters 77 (2000) 2949–2951.

[36] S. Berciaud, L. Cognet, G.A. Blab, B. Lounis, Photothermal heterodyne imaging of individual nonfluorescent nanoclusters and nanocrystals, Physical Review Letters 93 (2004) 257402.

[37] D. Boyer, P. Tamarat, A. Maali, B. Lounis, M. Orrit, Photothermal imaging of nanometer-sized metal particles among scatterers, Science 297 (2002) 1160–1163.

[38] S. Berciaud, D. Lasne, G.A. Blab, L. Cognet, B. Lounis, Photothermal heterodyne imaging of individual metallic nanoparticles: theory versus experiment, Physical Review B 73 (2006) 045424.

[39] A. Arbouet, D. Christofilos, N. Del Fatti, F. Vallée, J. R. Huntzinger, L. Arnaud, P. Billaud, M. Broyer, Direct measurement of the single-metalcluster optical absorption, Physical Review Letters 93 (2004) 127401.

[40] W.E. Moerner, L. Kador, Optical detection and spectroscopy of single molecules in a solid, Physical Review Letters 62 (1989) 2535–2538.

[41] C.R. Carey, T. Lebel, D. Crisostomo, J. Giblin, M. Kuno, G.V. Hartland, Imaging and absolute extinction cross-section measurements of nanorods and nanowires through polarization modulation microscopy, Journal of Physical Chemistry C. T. 114. 38. (2010) 16029–16036.

[42] M. Husnik, S. Linden, R. Diehl, J. Niegemann, K. Busch et M. Wegener, Quantitative experimental determination of scattering and absorption cross-section spectra of individual optical metallic nanoantennas, Physical Review Letters 109 (2012) 233902.

[43] D. Christofilos, S. Assimopoulos, N. Del Fatti, C. Voisin, F. Vallèe, G.A. Kourouklis, S. Ves, High pressure study of the surface plasmon resonance in Ag nanoparticles, High Pressure Research 23 (2003) 23–27.

[44] D. Christofilos, C. Voisin, N. Del Fatti, F. Vallèe, Femtosecond Nonlinear Optical Spectroscopy of the Acoustic Vibration of Metal Nanoparticles Under High Pressure, High Pressure Research 22 (2002) 277–281.

[45] Y. Bao, B. Zhao, D. Hou, J. Liu, F. Wang, X. Wang, T. Cui, The redshift of surface plasmon resonance of colloidal gold nanoparticles induced by pressure with diamond anvil cell, Journal of Applied Physics 115 (2014) 223503.

[46] L. Dubrovinsky, N. Dubrovinskaia, V.B. Prakapenka, A.M. Abakumov, Implementation of micro-ball nanodiamond anvils for high-pressure studies above 6 Mbar, Nature Communications 3 (2012) 1163.

[47] L. Dubrovinsky, N. Dubrovinskaia, E. Bykova, M. Bykov, V. Prakapenka, C. Prescher, K. Glazyrin, H.-P. Liermann, M. Hanfland, M. Ekholm, Q. Feng, L.V. Pourovskii, M.I. Katsnelson, J.M. Wills, I.A. Abrikosov, The most incompressible metal osmium at static pressures above 750 gigapascals, Nature 525 (2015) 226–229.

[48] R. Boehler, Temperatures in the Earth's core from melting-point measurements of iron at high static pressures, Nature 363 (1993) 534–536.

[49] Y. Fei, Simulation of the Planetary Interior Differentiation Processes in the Laboratory, Journal of Visualized Experiments 81 (2013) e50778.

[50] D. Kraus, J. Vorberger, A. Pak, N.J. Hartley, L.B. Fletcher, S. Frydrych, E. Galtier, E.J. Gamboa, D.O. Gericke, S.H. Glenzer, E. Granados, M.J. MacDonald, A.J. MacKinnon, E.E. McBride, I. Nam, P. Neumayer, M. Roth, A.M. Saunders, A.K. Schuster, P. Sun, T. van Driel, T. Döppner, R.W. Falcone, Formation of diamonds in laser-compressed hydrocarbons at planetary interior conditions, Nature Astronomy 1 (2017) 606–611.

[51] R. Boehler, Diamond cells and new materials, Materials Today 8 (2005) 34–42.

[52] P.F. McMillan, New materials from high-pressure experiments, Nature Materials 1 (2002) 19–25.

[53] A.F. Goncharov, V.V. Struzhkin, M.S. Somayazulu, R.J. Hemley, H.K. Mao, Compression of Ice to 210 Gigapascals: Infrared Evidence for a Symmetric Hydrogen-Bonded Phase, Science 273 (1996) 218–220.

[54] M.I. Eremets, R.J. Hemley, H.K. Mao, E. Gregoryanz, Semiconducting nonmolecular nitrogen up to 240 GPa and its low-pressure stability, Nature 411 (2001) 170–174.

[55] W.A. Caldvvell, J.H. Nguyen, B.G. Pfrommer, F. Mauri, S.G. Louie, R. Jeanloz, Structure, bonding and geochemistry of xenon at high pressures, Science 277 (1977) 930–933.

[56] D. Castelvecchi, Physicists doubt bold report of metallic hydrogen, Nature 542 (2017) 17.

[57] R. Miletich, D.R. Allan, W.F. Kuhs, High-Pressure Single-Crystal Techniques, Reviews in Mineralogy and Geochemistry 41 (2000) 445–519.

[58] M.H. Nazaré, A.J. Neves, Properties, growth and applications of diamond, Institution of Engineering and Technology, INSPEC (2001) 28–31.

[59] A. Jayaraman, Ultrahigh pressures, Review of Scientific Instruments 57 (1986) 1013–1031.

[60] R. Kinslow, High-Velocity Impact Phenomena, Academic Press (1970).

[61] R.A. Forman, G.J. Piermarini, J.D. Barnett, S. Block, Pressure Measurement Made by the Utilization of Ruby Sharp-Line Luminescence, Science 176 (1972) 284–285.

[62] H.K. Mao, P.M. Bell, Specific volume measurements of Cu, Mo, Pd, and Ag and calibration of the ruby R1 fluorescence pressure gauge from 0.06 to 1 Mbar, Journal of Applied Physics 49 (1978) 3276.

[63] R. Boehler, K.D. Hantsetters, New anvil designs in diamond-cells, High Pressure Research 24 (2004) 391–396.

[64] S. Klotz, J.-C. Chervin, P. Munsch, G. Le Marchand, Hydrostatic limits of 11 pressure transmitting media, Journal of Physics D 42 (2009) 075413.

[65] 1973 G.J. Piermarini, S. Block, J.D. Barnett, Hydrostatic limits in liquid and solids to 100 kbar, Journal of Applied Physics 44 (1973) 5377–5382.

[66] K. Takemura, O. Shimomura, T. Sawada, A diamond anvil cell for advanced microscopic observations and its application to the study of crystal growth under pressure, Review of Scientific Instruments 60 (1989) 3783.

[67] Y. Sato-Sorensen, Measurements of the lifetime of the ruby R1 line and its application to high-temperature and high-pressure calibration in the diamond-anvil cell, High-pressure Research in Mineral Physics (1987) 53–59.

[68] J.H. Eggert, L. Xu, R. Che, L. Chen, J. Wang, High pressure refractive index measurements of 4:1 methanol:ethanol, Journal of Applied Physics 72 (1992) 2453–2461.

[69] A.D. Chijioke, W.J. Nellis, A. Soldatov, I.F. Silvera, The ruby pressure standard to 150 GPa, Journal of Applied Physics 98 (2005) 114905

[70] Y.M. Gupta, X.A. Shen, Potential use of the ruby R2 line shift for static high-pressure calibration, Applied Physics Letters 58 (1991) 583.

[71] D.M. Adams, R. Appleby, S.K. Sharma, Spectroscopy at very high pressures. X. Use of ruby R-lines in the estimation of pressure at ambient and at low temperatures, Journal of Physics E 9 (1976) 1140.

[72] W.L. Vos, J. Schouten, On the temperature correction to the ruby pressure scale, Journal of Applied Physics 69 (1991) 6744–6746.

[73] D.D. Ragan, R. Gustavsen, D. Schiferl, Calibration of the ruby R1, and R2 fluorescence shifts as a function of temperature from 0 to 600 K, Journal of Applied Physics 72 (1992) 5539–5544.

[74] M.I. Eremets, V.V. Struzhkin, J.A. Timofeev, I.A. Trojan, A.N. Utjuzh, A.M. Shirokov, Refractive index of diamond under pressure, High Pressure Research 9 (1992) 347–350.

[75] N.M Balzarzetti, J.A.H. da Jornada, Pressure dependence of the refractive index of diamond, cubic silicon carbide and cubic boron nitride, Solid State Communications 99 (1996) 943–948.

[76] W.J. Smith, Modern Optical Engineering: The Design of Optical Systems, SPIE Press, 3rd edition (2000) 100–102.

[77] M.J. Riedl, Optical Design Fundamentals for Infrared Systems, 2nd edition, SPIE Press (2001) 83–86.

[78] A. Lombardi, M. Loumaigne, A. Crut, P. Maioli, N. Del Fatti, F. Vallée, M. Spuch-Calvar, J. Burgin, J. Majimel, M. Tréguer-Delapierre, Surface Plasmon Resonance Properties of Single Elongated Nanoobjects: Gold Nanobipyramids and Nanorods, Langmuir 28 (2012) 9027–9033.

[79] E. Pertreux, A. Lombardi, M. Hettich, P. Maioli, A. Crut, F. Vallée, N. Del Fatti, Surface Plasmon Resonance of an Individual Nano-Object on an Absorbing Substrate: Quantitative Effects of Distance and 3D Orientation, Advanced Optical Materials 4 (2016) 567–577.

[80] C. Kittel, Introduction to Solid State Physics, 8th edition, John Wiley & Sons, Inc, (2005).

[81] G.V. Hartland, Optical Studies of Dynamics in Noble Metal Nanostructures, Chemical Reviews 111 (2011) 3858–3887.

[82] R. Gurzhi, M. Azbel, H. Lin, Surface effects in infrared optics, Soviet Physics-Solid State 5 (1963) 554–559.

[83] C.-Y. Tsai, C.-H. Chen, T.-L. Sung, T.-Y. Wu, F.-P. Shih, Theoretical model for intravalley and intervalley free-carrier absorption in semiconductor lasers: beyond the classical Drude model, IEEE Journal of Quantum Electronics 34 (1998) 552–559.

[84] D. Mongin, Spectroscopie ultrarapide de nanoparticules métalliques et hybrides, PhD thesis, Université Claude Bernard Lyon 1 (2012).

[85] N. Del Fatti, Dynamique électronique femtoseconde dans les systèmes métalliques massifs et confinés, PhD thesis, Ecole polytechnique (1999).

[86] N. Del Fatti, C. Voisin, M. Achermann, S. Tzortzakis, D. Christofilos, F. Vallée, Nonequilibrium electron dynamics in noble metals, Physical Review B 61 (2000) 16956–16966.

[87] N. Del Fatti, F. Vallée, C. Flytzanis, Y. Hamanaka, A. Nakamura, Electron dynamics and surface plasmon resonance nonlinearities in metal nanoparticles, Chemical Physics 251 (2000) 12.

[88] A. Kawabata, R. Kubo, Electronic properties of fine metallic particles, Journal of the Physical Society of Japan 21 (1966) 1765–1772.

[89] H. Baida, P. Billaud, S. Marhaba, D. Christofilos, E. Cottancin, A. Crut, J. Lermé, P. Maioli, M. Pellarin, M. Broyer, N. Del Fatti, F. Vallée, Quantitative Determination of the Size Dependence of Surface Plasmon Resonance Damping in Single Ag@SiO2 Nanoparticles, Nano Letters 9 (2009) 3463–3469.

[90] H. Baida, D. Christofilos, P. Maioli, A. Crut, N. Del Fatti, F. Vallée, Surface plasmon resonance spectroscopy of single surfactant-stabilized gold nanoparticles, European Physical Journal D 63 (2011) 293–299.

[91] V. Juvé, M.F. Cardinal, A. Lombardi, A. Crut, P. Maioli, J. Jérez-Juste, L.M. Liz-Marzán, N. Del Fatti, F. Vallée, Size-Dependent Surface Plasmon Resonance Broadening in Nonspherical Nanoparticles: Single Gold Nanorods, Nano Letters 13 (2013) 2234–2240.

[92] J. Lermé, Size Evolution of the Surface Plasmon Resonance Damping in Silver Nanoparticles: Confinement and Dielectric Effects, Journal of Physical Chemistry C 115 (2011) 14098–14110.

[93] J. Lermé, H. Baida, C. Bonnet, M. Broyer, E.l Cottancin, A. Crut, P. Maioli, N. Del Fatti, F. Vallée, Michel Pellarin, Size Dependence of the Surface Plasmon Resonance Damping in Metal Nanospheres, Journal of Physical Chemistry Letters 1 (2010) 2922–2928.

[94] A. Crut, P. Maioli, F. Vallée, N. Del Fatti, Linear and ultrafast nonlinear plasmonics of single nano-objects, Journal of Physics: Condensed Matter 29 (2017) 123002.

[95] S. Ogata, J. Li, N. Hirosaki, Y. Shibutani, S. Yip, Ideal shear strain of metals and ceramics, Physical Review B 70 (2004) 104104.

[96] J.-Y. Kim, J.R. Greer, Tensile and compressive behavior of gold and molybdenum single crystals at the nano-scale, Acta Materialia 57 (2009) 5245–5253.

[97] V. Juvé, A. Crut, P. Maioli, M. Pellarin, M. Broyer, N. Del Fatti, F. Vallée, Probing Elasticity at the Nanoscale: Terahertz Acoustic Vibration of Small Metal Nanoparticles, Nano Letters 10 (2010) 1853–1858.

[98] H.E. Sauceda, D. Mongin, P. Maioli, A. Crut, M. Pellarin, N. Del Fatti, F. Vallée, I.L. Garzón, Vibrational Properties of Metal Nanoparticles: Atomistic Simulation and Comparison with Time-Resolved Investigation, Journal of Physical Chemistry C 116 (2012) 25147–25156.

[99] J. Burgin, P. Langot, N. Del Fatti, F. Vallée, W. Huang, M.A. El-Sayed, Time-resolved investigation of the acoustic vibration of a single gold nanoprism pair, Journal of Physical Chemistry C 112 (2008) 11231–11235.

[100] P.V. Ruijgrok, P. Zijlstra, A.L. Tchebotareva, M. Orrit, Damping of acoustic vibrations of single gold nanoparticles optically trapped in water, Nano Letters 12 (2012) 1063–1069.

[101] H. Staleva, G.V. Hartland, Vibrational dynamics of silver nanocubes and nanowires studied by single-particle transient absorption spectroscopy, Advanced Functional Materials 18 (2008) 3809–3817.

[102] A. Crut, P. Maioli, N. Del Fatti, F. Vallée, Acoustic vibrations of metal nano-objects: Time-domain investigations, Physics Reports 549 (2015) 1–43.

[103] B.A. Auld, Acoustic Fields and Waves in Solids, Volume 1, John Wiley & Sons (1973) 1–167.

[104] S. Peli, E. Cavaliere, G. Benetti, M. Gandolfi, M. Chiodi, C. Cancellieri, C. Giannetti, G. Ferrini, L. Gavioli, F. Banfi, Mechanical Properties of Ag Nanoparticle Thin Films Synthesized by Supersonic Cluster Beam Deposition, Journal of Physical Chemistry C 112 (2016) 4673–4681.

[105] H. Lamb, On the vibrations of an elastic sphere, Proceedings of the London Mathematical Society s1-13 (1881) 189–212.

[106] V. Dubrovskiy, V. Morochnik, Natural vibrations of a spherical inhomogeneity in an elastic medium, Izvestiya, Physics of the Solid Earth 17 (1981) 494–504.

[107] M. Hu, X. Wang, G.V. Hartland, P. Mulvaney, J.P. Juste, J.E. Sader, Vibrational Response of Nanorods to Ultrafast Laser Induced Heating: Theoretical and Experimental Analysis, Journal of the American Chemical Society 125 (2003) 14925–14933.

[108] J. Burgin, P. Langot, N. Del Fatti, F. Vallée, W. Huang, M.A. El-Sayed, Time-resolved investigation of the acoustic vibration of a single gold nanoprism pair, Journal of Physical Chemistry C 112 (2008) 11231–11235.

[109] H. Portales, L. Saviot, E. Duval, M. Gaudry, E. Cottancin, M. Pellarin, J. Lermé, M. Broyer, Resonant Raman scattering by quadrupolar vibrations of Ni–Ag core–shell nanoparticles, Physical Review B 65 (2002) 165422.

[110] C. Voisin, N. Del Fatti, D. Christofilos, F. Vallée, Ultrafast electron dynamics and optical nonlinearities in metal nanoparticles, Journal of Physical Chemistry B 105 (2001) 2264–2280.

[111] C. Voisin, D. Christofilos, N. Del Fatti, F. Vallée, B. Prével, E. Cottancin, J. Lermé, M. Pellarin, M. Broyer, Size-dependent electron–electron interactions in metal nanoparticles, Physical Review Letters 85 (2000) 2200–2203.

[112] A. Arbouet, C. Voisin, D. Christofilos, P. Langot, N. Del Fatti, F. Vallée, J. Lermé, G. Celep, E. Cottancin, M. Gaudry, M. Pellarin, M. Broyer, M. Maillard, M. Pileni, M. Treguer, Electron–phonon scattering in metal clusters, Physical Review Letters 90 (2003) 177401.

[113] A. Crut, V. Juvé, D. Mongin, P. Maioli, N. Del Fatti, F. Vallée, Vibrations of spherical core–shell nanoparticles, Physical Review B 83 (2011) 205430.

[114] D.G. Cahill, W.K. Ford, K.E. Goodson, G.D. Mahan, A. Majumdar, H.J. Maris, R. Merlin, S.R. Phillpot, Nanoscale thermal transport, Journal of Applied Physics 93 (2003) 793–818.

[115] Z. Ge, D.G. Cahill, P.V. Braun, AuPd metal nanoparticles as probes of nanoscale thermal transport in aqueous solution, Journal of Physical Chemistry B 108 (2004) 18870–18875.

[116] M. Pelton, J.E. Sader, J. Burgin, M. Liu, P. Guyot-Sionnest, D. Gosztola, Damping of acoustic vibrations in gold nanoparticles, Nature Nanotechnology 4 (2009) 492–495

[117] P.V. Ruijgrok, P. Zijlstra, A.L. Tchebotareva, M. Orrit, Damping of acoustic vibrations of single gold nanoparticles optically trapped in water, Nano Letters 12 (2012) 1063–1069.

[118] T.A. Major, A. Crut, B. Gao, S.S. Lo, N. Del Fatti, F. Vallée, G.V. Hartland, Damping of the acoustic vibrations of a suspended gold nanowire in air and water environments, Physical Chemistry Chemical Physics 15 (2013) 4169–4176.

[119] N. Del Fatti, C. Voisin, F. Chevy, F. Vallée, C. Flytzanis, Coherent acoustic mode oscillation and damping in silver nanoparticles, Journal of Chemical Physics 110 (1999) 11484–11487.

[120] C. Voisin, D. Christofilos, N. Del Fatti, F. Vallée, Environment effect on the acoustic vibration of metal nanoparticles, Physica B: Condensed Matter 316–317 (2002) 89–94.

[121] V. Juvé, M. Scardamaglia, P. Maioli, A. Crut, S. Merabia, L. Joly, N. Del Fatti, F. Vallée, Cooling dynamics and thermal interface resistance of glass-embedded metal nanoparticles, Physical Review B 80 (2009) 195406.

[122] T. Stoll, P. Maioli, A. Crut, N. Del Fatti, F. Vallée, Advances in femto-nano-optics: ultrafast nonlinearity of metal nanoparticles, The European Physical Journal B 87 (2014) 1.

[123] J. Chaste, A. Eichler, J. Moser, G. Ceballos, R. Rurali, A. Bachtold, A nanomechanical mass sensor with yoctogram resolution, Nature Nanotechnology 7 (2012) 301–304.

[124] D.T. Debu, P.K. Ghosh, D. French, J.B. Herzog, Surface plasmon damping effects due to Ti adhesion layer in individual gold nanodisks, Optical Materials Express 7 (2017) 73–84.

[125] T.G. Habteyes, S. Dhuey, E. Wood, D. Gargas, S. Cabrini, P.J. Schuck, A.P. Alivisatos, S.R. Leone, Metallic Adhesion Layer Induced Plasmon Damping and Molecular Linker as a Nondamping Alternative, ACS Nano 6 (2012) 5702–5709.

[126] C. Jean, L. Belliard, T.W. Cornelius, O. Thomas, M.-E. Toimil-Molares, M. Cassinelli, L. Becerra, B. Perrin, Direct Observation of Gigahertz Coherent Guided Acoustic Phonons in Free Standing Single Copper Nanowires, Journal of Physical Chemistry Letters 5 (2014) 4100–4104.

[127] T.A. Major, A. Crut, B. Gao, S.S. Lo, N. Del Fatti, F. Vallée, G.V. Hartland, Damping of the acoustic vibrations of a suspended gold nanowire in air and water environments, Physical Chemistry Chemical Physics 15 (2013) 4169–4176.

[128] Melles-Griot, All Things Photonic: Gaussian Beam Optics, 2.2–2.9.

[129] D.F. Edwards, E. Ochoa, Infrared refractive index of diamond, Journal of the Optical Society of America 71 (1981) 607–608.

[130] M.H. Nazaré, A.J. Neves, Properties, Growh and Applications of Diamond, INSPEC (2001) 28.

[131] K. Moutzouris, M. Papamichael, S.C. Betsis, I. Stavrakas, G. Hloupis, D. Triantis, Refractive, dispersive and thermo-optic properties of twelve organic solvents in the visible and near-infrared, Applied Physics B 116 (2014) 617–622.

[132] S. Kedenburg, M. Vieweg, T. Gissibl, H. Giessen, Linear refractive index and absorption measurements of nonlinear optical liquids in the visible and near-infrared spectral region, Optical Materials Express 2 (2012) 1589.

[133] M. Garfinkel, J.J. Tiemann, W.E. Engeler, Piezoreflectivity of the Noble Metals, Physical Review 148 (1966) 695–706.

[134] P. Winsemius, M. Guerrisi, R. Rosei, Splitting of the interband absorption edge in Au: Temperature dependence, Physical Review B 12 (1975) 4570.

Summary

In this thesis, the properties of a single metal nanoparticle have been tuned by altering its environment and its morphology. Specifically, in the first part of this work, the surface plasmon resonance of individual gold nanobipyramids has been experimentally studied under a pressure-adjustable surrounding, and its evolution physically interpreted through theoretical modeling. In order to access to the optical response under high-pressure at single-particle level, a challenging combination of a *spatial modulation spectroscopy* (SMS) microscope with a diamond anvil cell has been achieved. In the second part of the thesis, the acoustic vibrations of individual gold nanodisks on sapphire substrate have been experimentally characterized by combining the SMS microscope with an ultrafast *pump&probe* setup. The dependence of their damping on the disk morphology has enlightened the presence of quality-factor enhancements. Numerical modeling has provided a physical insight for the observed phenomena, showing that mode hybridizations occur at specific aspect ratios, reducing the acoustic energy loss through the nano-object/environment interface.

Résumé

Dans cette thèse, les propriétés d'une nanoparticule métallique unique ont été contrôlées en modifiant son environnement et sa morphologie. Plus spécifiquement, dans la première partie de ce travail, la résonance plasmon de surface de nanobipyramides d'or individuelles a été étudiée expérimentalement dans un milieu sous pression contrôlable, et son évolution interprétée à l'aide de modélisations théoriques. Afin d'accéder à la réponse optique d'une nanoparticule unique à haute pression, la combinaison d'un microscope de *spectroscopie à modulation spatiale* (SMS) avec une cellule à enclume de diamant a été réalisée. Dans une seconde partie, les vibrations acoustiques de nanodisques d'or individuels sur un substrat en saphir ont été caractérisées en combinant le microscope SMS avec un dispositif de spectroscopie ultrarapide *pompe-sonde*. L'étude de leur amortissement en fonction de la morphologie des disques a permis de démontrer d'exaltations des facteurs de qualité mécaniques. Les modélisations numériques ont fourni un aperçu physique du phénomène observé, montrant qu'une hybridation entre modes se produit pour des rapports d'aspect spécifiques, réduisant ainsi les pertes en énergie acoustique à travers l'interface disque/environnement.